Design and Control of a Dexterous Anthropomorphic Robotic Hand

Giulio Cerruti

To cite this version:

Giulio Cerruti. Design and Control of a Dexterous Anthropomorphic Robotic Hand. Robotics [cs.RO]. École centrale de Nantes, 2016. English. ⟨NNT : 2016ECDN0009⟩. ⟨tel-01396616v2⟩

HAL Id: tel-01396616
https://hal.science/tel-01396616v2

Submitted on 24 Jul 2019

L'UNAM l'université nantes angers le mans
COMMUNAUTÉ D'UNIVERSITÉS ET ÉTABLISSEMENTS

ECN Centrale Nantes

Thèse de Doctorat

Giulio CERRUTI

Mémoire présenté en vue de l'obtention du
grade de Docteur de l'École centrale de Nantes
sous le label de l'Université de Nantes Angers Le Mans

École doctorale : Sciences et technologies de l'information, et mathématiques

Discipline : Robotique
Unité de recherche : Institut de Recherche en Communications et Cybernétique de Nantes

Soutenue le 17/10/2016

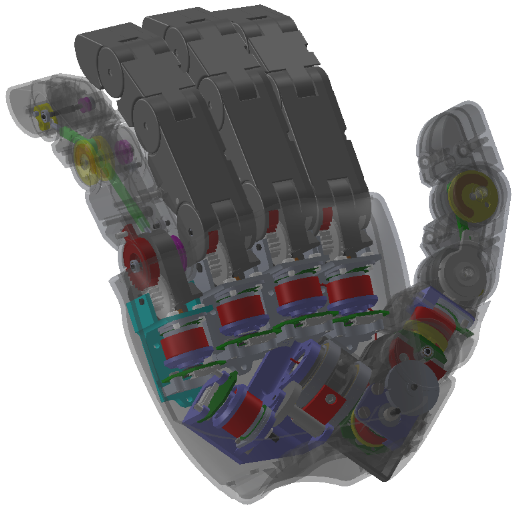

Design and Control of a Dexterous Anthropomorphic Robotic Hand

JURY

Président :	**M. Bruno SICILIANO**, Professeur, Université de Naples Federico II
Rapporteurs :	**M. Jean-Pierre GAZEAU**, Ingénieur de Recherche HDR, CNRS
	M^{me} Véronique PERDEREAU, Professeur, Université Pierre et Marie Curie (UPMC), Sorbonne universités
Examinateur :	**M. David GOUAILLIER**, Ingénieur de Recherche, Aldebaran - SoftBank Group

* * *

Directeur de thèse :	**M. Damien CHABLAT**, Directeur de Recherche, CNRS
Co-encadrante de thèse :	**M^{me} Sophie SAKKA**, Maître de Conférence, Ecole Centrale de Nantes

Contents

List of Figures

Ch 1 - Designing a robotic hand **1**

List of Tables

Acknowledgment

This research has been supported by the French Ministry of Higher Education and Scientific Research through a CIFRE contract (Conventions Industrielles de Formation par la REcherche) which permitted the establishment of a fruitful collaboration between IRCCyN and Aldebaran - SoftBank Group. To them, I would like to express my gratitude for the extraordinary opportunity they gave me.

This work has been possible thanks to the professional and personal support of various people. Among them I would like to especially thank my supervisor Damien Chablat. Your suggestions and questions stimulated me to widen my research and your encouragements to remain motivated all the time, particularly during the writing of this thesis. Thanks to my co-supervisor Sophie Sakka for her advice and insightful comments. You pushed my criticism and introspection. I would like to express my special appreciation and thanks to Lionel Birglen for his valuable recommendations and warm welcome in Montreal. I would like to express my sincere gratitude to David Gouaillier. I could not have imagined having a better mentor. Your guidance and support have been precious and your transparency, dynamism and open-mindedness priceless. My sincere thanks also goes to Florian Armange and Thibault Davasse who respectively contributed to the implementation of the control and mechanics of the hand. Thanks for all the stimulating discussions, your constant curiosity and willingness to help. Thanks to this wonderful trio without which it would have been impossible to conduct this research in time. Working with you has been extremely motivating and pleasant. You have been more than colleagues and I do consider myself very lucky for this.

Furthermore, my gratitude goes also to the amazing people I met in these years. Each of you enriched my life with something special. In particular, I would like to thank the ones who left an indelible mark. First of all, I would like to thank Andrea. Your ever-ready smile, kindness and carefulness have cheered me up this last year. You are a wonderful person, patient and trustful. Thanks to you and to your parents for having welcomed as part of your family. You made me feel home and allowed me to truly understand and embrace the French culture. I know, I still do not eat salty butter for breakfast but some things are hard to change. Doubtlessly, my experience in France would have been much harder without the support of my current and old flatmates. In particular, I would like to thank Yohann for his energy and nice attitudes. You are a good listener and you are constantly ready to help everybody. Please do not change. How not to thank Kim, for her authentic and creative personality. If it wasn't for you the flat would be still bare and colorless. Thanks for our chats in Italian and the wonderful dinners you made. Be careful not to become a real "ritale". Thanks to Eloise, who taught me to be always positive, proactive and to always do something different. Thanks to my dear friends Abdoulaye, who showed me how simple it can be to make people happy, and Alexandra, who never stopped to correct my French and my accent. I'm sorry but I still do not pronounce "u" as I should. Thanks to Adèle for having managed the French-Italian café with me all along last year. It was not an easy task. Thanks to all of you. You made me spend a fantastic time here in the dynamic, young and evergreen Nantes.

I would like to express my profound gratitude to my closest friends who were always by my side, no matter the distance. I hope you'll always be part of my life. Last but not the least, I would like to thank my parents, who supported, advised, encouraged and trusted me. You are a fundamental pillar in my life. A special thank you is dedicated to my mother who put some of her artistic talent in this work.

Merci beaucoup.

Introduction

Motivation. At present, the fast-growing robotics community is progressively pushing toward autonomous and dexterous machines capable of operating in various environments. The ambitious challenge is to transfer the operative conditions from well-structured surroundings to unstructured and unpredictable ones, where knowledge relies on exteroceptive sensors and few generic assumptions. Both industrial and scientific societies are following this trend. Robots are required to operate outside of specific frameworks, such as to cross hazardous terrains of different nature (sometimes changeable and difficult to access) or handle and manipulate different types of objects. Moreover, they must safely cooperate and interact with people while working in their surroundings. Such robots must perform precise motions and be sufficiently compliant to handle external contact at the same time.

Task-oriented physical interaction mainly involves robot end-effectors. These are grippers or more complex manipulators when objects have to be grasped or manipulated, and human-inspired multi-fingered manipulators (or hands) when human-likeness is desired. Two-fingered robotic manipulators are limited to pick and place tasks, during which the object needs to be displaced and reoriented from one position to another. These are typically used in industrial applications but they are not restricted to them (e.g. HRP2 hands). Manipulators with three or four fingers can perform in-hand manipulation, if properly designed, which consists in changing the object configuration within the hand by means of its fingers only. Multi-fingered hands, with up to four fingers, solve object handling and manipulation problems but still present some limitations in applications which involve human perception. Prosthetic hands, for example, are hardly accepted by users if they present less than five fingers or their anthropomorphism is not evident. To a lower extent, the same applies to humanoid robots which can be barely considered human-like if they present simple grippers. Human-likeness imposes several constraints to the hand design. Particularly, in terms of geometry, kinematics and aesthetics. In addition, it inherently implies functional abilities that do not only refers to grasp and manipulation skills, but also to non-verbal communication capabilities.

Robotic hands mounted either on a humanoid robot or on a person present two particular challenges: they must be limited in size and must be lightweight. Furthermore, they need to be easy to carry and be proportioned to the connected body. An effective way to limit weight and size is to reduce the number of actuators. This is challenging as current technology lack actuators with high power-to-weight ratios, except for hydraulic actuation which, on the other hand, requires noisy (and often heavy) pumps. The noise produced by actuators and transmission mechanisms is often neglected in most hand designs. Indeed, it is irrelevant for industrial manipulators or for artificial limbs working far from people, on the contrary, it is a significant factor for automata operating in our every-day life. In such a context, actuation power is highly bounded by mechanical and functional constraints which induce human-like hand designs with simplified kinematics and reduced capabilities. In fact, prosthetic hands mainly focus on providing reliable grasping capabilities, while humanoid robot hands target specific services. In brief, the main difficulty in designing these devices consists in finding the best trade-off between human-likeness and mechanical feasibility.

In literature, robotics hands only meant for grasping are often designed to mechanically self-adapt to the object shape. These hands are commonly called *under-actuated* and are characterized by transmission mechanisms which allow power distribution to phalanges even when the motion of some links are hindered by external forces. A classical solution adopted by these artifacts consists in placing single acting actuators in the palm or in the forearm and distributing the grasping force through pulleys and cables to the fingertips. The pulling force moves the fingers according to the restorative forces provided by elastic elements normally placed at the finger joints, and any external force applied to the phalanges. Their mechanical parameters are challenging to size but, once chosen, self-adaptable mechanisms prove to be simple and effective manipulators. By properly distributing actuation forces, this type of hand can grasp a large variety of objects with only one motor. This solution is extremely effective for grasping, but it is obviously inadequate to manipulate or simply perform expressive gestures. De facto, for a minimal set of European common gestures at least seven independent DoFs are required: one per finger and three for the thumb. Even abandoning force distribution and adopting a sufficient number of actuators, self-adaptable fingers require high reduction ratios to act against elastic restoring forces. These take space, add weight and often increase the noise. In addition, they weaken backdrivability and prevent contact force estimation from motor current readings, imposing additional exteroceptive sensors to ensure safe human-robot interaction.

Alternatively, multi-purpose hands preserve the highest feasible number of actuators and couple the reminder DoFs. The number varies according to the task to be performed and the context of application. Apart from robotic hands mounted on industrial arms or fixed platforms, which can be designed with relaxed weight and size constraints, prosthetic and humanoid robot hands have limited dexterity with respect to the human hand. In general, they can express basic gestures (with enough DoFs) but they require complex control strategies during pre-grasp and grasping phases to firmly hold an object. Furthermore, they still need high reduction ratios to provide sufficient grasp forces.

In this work, a novel anthropomorphic robotic hand which mixes the advantages of both self-adaptable and fully-coupled hands is proposed. The hand is sized to be mounted on *Romeo*, a 1.4 [m] tall humanoid robot produced by Aldebaran - SoftBank Group. Its design is characterized by two distinct actuation systems which coexist in parallel within the palm and the fingers. The first actuation system is characterized by seven low-power motors: one per finger and three for the thumb. These are embedded within the palm and thumb and are characterized by low gear reduction ratios. Remainder DoFs are driven by 4-bar linkage mechanisms which non-linearly couple adjacent links. Low reduction ratios reduce volume, weight, noise and cost. In addition, they provide high backdrivability and allow sensor-less force feedback. Their output torques grant gesture capabilities but lack in adequate grasping force. The second actuation system is composed by a single motor placed in the forearm, 50 times more powerful than the ones embodied in the palm. Its pulling force is transmitted to the fingertips through a series of cables and pulleys placed in the palm, to distribute the input force to each finger base, and then each fingers. This actuation system replaces the first one to grasp objects that would be otherwise ejected. The second actuation system does not only strengthen the grip but also improves grasping performance by implementing self-adaptation among fingers and phalanges. This is done by means of a differential mechanism in the palm and by implementing 4-bar linkages with elastic bars, which also provide mechanical protection in the presence of external forces applied to the phalanges. Differently from classic self-adaptable mechanisms, passive elements restore couplings among phalanges rather than recalling fingers back to straight configurations. This implies that stronger forces are provided to the grasp since minor force is lost in deviating the passive elements from their equilibrium position. In conclusion, the hand can be regarded as *hybrid*, in the sense that it behaves as a fully-coupled or self-adaptable hand by alternatively activating the two distinct actuation systems. The hand can perform common gestures with the first actuation system and grasp objects of different shapes with the second one, while simultaneously limiting its size, weight, noise and cost.

Thesis goal and research problems. This thesis focuses on the design and control of a humanoid robot anthropomorphic hand able to perform common gestures and to grasp light objects. Great importance is placed on its human-likeness, safety, weight, noise and cost. To achieve these goals different problems have to be solved:

Problem 1:

There is scarce integration and acceptance of social humanoid robots in our society. Currently these robots are extremely expensive, or present limited motion performance and dexterity. Social humanoid robots generally only provide restricted services and, more importantly, disregard the importance of non-verbal communication, such as body language and manual communication (hand signs and gestures), which can enhance empathy with people.

Problem 2:

The identification of objective anthropomorphic criteria and their application to the geometric and kinematic conception of the robotic hand are often disregarded. Differently from some artificial hands, whose design only shares five fingers with that of the human hand, the intention is to transpose anthropomorphism and dexterity to the artifact.

Problem 3:

There is a discrepancy among compactness, lightweight and (sensorless) safety properties and the dexterity and power of the hand. A trade-off between the number of actuators and relative reduction ratios to fulfil important mechanical constraints and functional objectives must be found.

Problem 4:

The integration of a lightweight, proportioned robotic hand on a existing humanoid robot. The hand must contain most of its mechanical and hardware components within its structure taking into account the limited space in the forearm. Its actuation technology must be coherent with the one already present in the robot and require a reasonable amount of energy. Its cost has to be moderate and adequate to the price of the whole robot.

Thesis Structure. To address these problems and achieve the desired objectives the thesis is organized as follows.

Chapter 1:

This chapter introduces the human hand anatomy and its natural dexterity, which represents the main source of inspiration for all anthropomorphic hand makers. It reviews the current state of the art of five-fingered robotic hands, highlighting their major strengths and weaknesses and analyzing their suitability and efficacy to be mounted on a service humanoid robot supposed to safely operate in our surroundings. Aspects like anthropomorphism, expressiveness, compactness, weight, safety, grasping capabilities, noise and cost are adopted as criteria of comparison and they are used to empathize the problem of designing a dexterous robotic hand for a humanoid robot. Finally, the goal of the thesis is presented and the chosen strategy outlined.

Chapter 2:

This chapter defines the geometric and kinematic models of the robotic hand devised to obtain an anthropomorphic and dexterous design. The kinematic model reduces the independent DoFs to the minimum number required to perform common gestures and simple grasps. This is done to achieve a compact and lightweight hand able to reproduce basic human hand capabilities. Artificial finger lengths, widths and base configurations are established according to human-inspired heuristic methods. Particular focus is given to the thumb base, placed to enhance hand dexterity and thumb opposability to the other fingers. A numerical method is implemented to find the best configuration of the thumb base which satisfies the surgical tests known as the *Kapandji* test and to preserve the most equilibrated interaction with the opposite fingers.

Chapters 3, 4, 5:

These chapters describe the mechanical design and control of the robotic hand. Since gesturing and grasping capabilities are provided by two distinct actuation systems, three chapters are presented. The first two outline the transmission, actuation and control of each system as if it was the only one embedded in the hand. The third considers the problems arising from their coexistence and presents the design solutions adopted.

Chapter 3 presents the gesture-oriented design in which finger configurations are always known at any time instant (even in presence of external forces). This is referred as the *e-motion* system (a pun between emotion and motion) since it enhances human-robot interaction through non-verbal communication (emotional counterpart) and allows independent finger movements (motion counterpart). The chapter details the finger models based on the joint coupling mechanism. Then, it explains the actuation requirements and choices. Finally, it describes the control strategies adopted in motor and joint spaces.

Chapter 4 presents a grasp-oriented design capable of adapting to different object shapes. This is referred to as the *grasp* system and it is inspired by classical self-adaptable finger designs which present "smart" mechanics and do not require complex grasping strategies. Firstly, the chapter outlines the transmission design within the fingers and the palm. Then, it describes the actuation requirements and choices based on the heaviest object to be grasped: a full soda can. Finally, it presents the current-based force control to handle the grasp force.

Chapter 5 is devoted to merge the two designs into one: the *ALPHA* (ALdebaran Parallel HAnd). Focus is given to the internal forces at the e-motion transmission mechanism to open its closed loop kinematic chain. Among different analyzed and implemented mechanical solutions, a decoupling elastic mechanism is finally chosen and embodied in the finger structures. Finally, the chapter shows the final finger prototypes, addresses their validation and draws some conclusions about the chosen design.

Chapter 6:

This chapter is devoted to analyze and evaluate the ALPHA prototype. Firstly, the control strategies adopted to test the hand are briefly introduced. Then, the tests performed to analyze its anthropomorphism, gesture and grasping capabilities are presented. These are intended to both check mechanical and functional requirements and to characterize its general performance. Finally, some conclusions are drawn about experimental results. The hand design is validated in terms of the thesis objectives and the limits of its implementation are highlighted.

Chapter 7:

This chapter shortly resumes the motivation and summarizes the main contributions of this work. Finally, it outlines suggested future work and possible research directions.

Main contributions. There are three main relevant original contributions disclosed in this work. A brief summary is presented below.

Contribution 1:

A numerical methodology to compute finger and thumb geometries and base placements for a human-like dexterous robotic hand. In literature, there are few numerical methods for the finger placement of human-inspired robotic hands. In particular, there are no numerical methods for the thumb placement that aim to improve the hand dexterity by keeping the hand design close to the human one. While existing models are usually the result of successive parameter adjustments, the proposed method determines the fingers placements by mean of empirical tests. Moreover, a surgery test and the workspace analysis of the whole hand are used to find the best thumb position and orientation according to the hand kinematics and structure.

Contribution 2:

A novel approach to design a compact and lightweight robotic hand able to perform common gestures and self-adaptable grasps. The proposed solution mixes a fully-coupled hand and a self-adaptable hand in a unique design, answering the need for precise finger postures and sensorless force feedback when gesturing and for finger adaptation when grasping. Up to the author's knowledge, in literature, robotic hands which embody dual actuation systems are driven by different objectives from the one presented in this context (e.g. gross and fine manipulation) and their coexistence (actuation cooperation or independence) is often solved by control. Elastomers, rather than classical tension springs, are used as passive elements in the fingers thanks to their high elastic coefficients at reduced sizes and strains. The proposed solution significantly reduces the weight and the size of the hand by the use of small low-power actuators.

Contribution 3:

The realization of a first functional prototype which globally respects the design constraints and achieves the required objectives (and even more). The prototype is developed to safely interact with people and to preserve its mechanical integrity. Safe human-robot interaction is guaranteed by impedance control during normal motions and by a bounded actuation force (by current limits) during grasp. In addition, the actuation system adopted for gesturing is conceived to be highly backdrivable (barely no reduction ratio) and weak, with just sufficient power to counterbalance the effects of gravity. Finally, mechanical integrity is provided by the elastic elements in the transmission mechanisms which protect the actuation system from shocks and erratic interactions far from the joint limits. The prototype still needs some improvements to effectively pass to production but it represents an important step toward an enhanced human-likeness and functional capabilities for compact, lightweight and low-cost robotic hands.

1

Designing a robotic hand

This chapter empathizes the problem of designing a human-like robotic hand for a social humanoid robot. At first, it introduces the human hand anatomy and its natural dexterity, which are the main sources of inspiration for all human-like robotic hand makers. Then, it reviews the current state of the art of five-fingered robotic hands and classifies them according to their functional capabilities. The difficulties of designing a biologically-inspired design are introduced and the thesis objectives are presented. Finally, the chapter outlines the limits of current robotic hands on the base of weight, cost, noise, compactness, anthropomorphism and dexterity criteria and summarizes the proposed solution.

1.1 The human hand

The human hand is a marvellous machine of great complexity. It is endowed with gross and fine motor skills which provide high manual dexterity to perform *non-prehensile* movements, *prehension* and *manipulation*. Non-prehensile movements involve *gestures*, made to enrich communication or to replace a spoken language, and actions which not involve holding an object, such as switching on a light. Prehension refers to the action of reaching and *holding* an object, while manipulation refers to the process of *changing the object configuration* within the grasp. Human hand performance allows the realization of a wide number of motor-based tasks of different natures and difficulty, such as smoothly drawing a painting, precisely passing a thread through a needle eye, painstakingly carving a sculpture, gently petting an animal or repeatedly typing on a keyboard. The human hand is the prime mean to *express feelings*, thoughts and intentions, both through manual gestures or tools. Thanks to richly innervated fingerprints, which are the parts of our body with the densest nerve endings, the human hand is capable of actively (active haptic) and passively (tactile) sense the environment to identify objects and detect information about them (e.g. their weight, size, shape, temperature and surface texture). Human hand primary manual functions can be divided into four main activities (Figure 1.1); from tactile sensing to non-prehensile movements on a sensorimotor continuum [1].

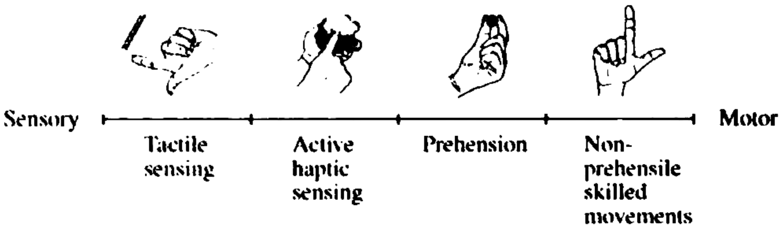

Figure 1.1 – Primary manual functions on a sensorimotor continuum - picture taken from [1].

The human hand has a more sophisticated structure and capabilities compare to the primate hand, evolving from a locomotion support to a manipulation tool. This transition took millions of years to complete, and was mainly promoted by the development of an opposable thumb, improving hand dexterity and encouraging bipedal locomotion. Nowadays, the human hand shares the opposable thumb only with some primates [2] (the others have no opposable thumb or are even thumb-less), while it presents unique characteristics which improve its manipulation capabilities. These are mainly a longer thumb, whose base is placed far from the opposing digits, shorter fingers and large areas of contact between the soft fingertip of thumb and index [3] which distribute pressure during grasp, even on irregular surfaces [4].

1.1.1 Anatomy

The anatomy of the human hand has been studied for centuries. One of the first scientific works, still considered valid and accurate despite the limited technology and lack of contemporary medical knowledge, dates to the XV and XVI century with the human hand sketches of Leonardo da Vinci (Figure 1.2a).

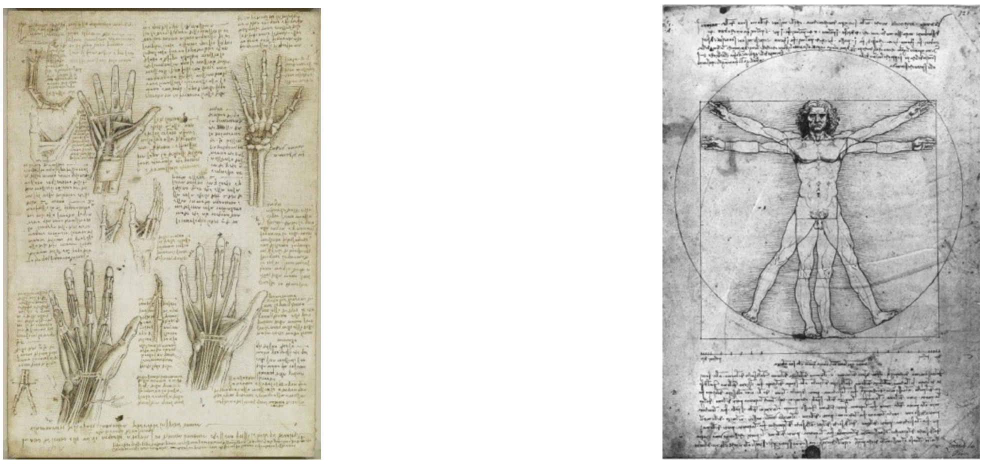

(a) Human hand sketches - picture taken from [5].

(b) Proportional study of human body - picture taken from [6].

Figure 1.2 – Pen and ink sketches of Leonardo da Vinci.

These drawings belong to a series of anatomical representations of the human body that Leonardo painted during a meticulous analysis of corpses which remained hidden up to the XX century [5]. The sketches depict the bones, sinews and muscles of different parts of the human body (comparable to current CT - Computed Tomography - and MRI - Magnetic Resonance Imaging - scans), enriching the anatomical studies that Leonardo already started with the analysis of the body proportions represented in the well-known Vitruvian man (Figure 1.2b).

The human hand can be analyzed from several perspectives: bones, joints, ligaments, tendons, muscles and nerves. From a robotic point of view, the structure of the hand is defined by bones, its kinematics by joints and ligaments, its motion by tendons and muscles and its control by nerves. In other words, the bones are the links of this perfect machine, the joint and ligaments are its DoFs and joint limits, tendons and muscles are its transmission and actuation mechanisms while the nerves are its buses through which data are sent. Since more importance is given to the hand aesthetics and dexterity, all these aspects are not treated in this context. Hereafter, the structure and kinematics of the human hand, namely bones, joints and ligaments are presented.

1.1.1.1 Bones and joints: nomenclature

The human hand is composed of 27 bones [7] which make up its three main parts: wrist, palm and fingers (Figure 1.3). The wrist is formed by 8 small bones (arranged in two rows) called carpals, which join the ulna and radius bones of the forearm to the hand. The palm is composed by 5 bones called metacarpals which connect the fingers and the thumb to the wrist. The joints between the wrist and the finger metacarpals are called the carpometacarpal (*CMC*) joints while the one linking the metacarpal of the thumb is called the radiocarpal (RC) joint. Each finger is composed by 3 long bones called phalanges whose names are given according to their distance to the palm: proximal, middle and distal. The proximal phalanx (*PP*) is linked to the metacarpal bone through the metacarpophalangeal joint (*MCP*) while the remaining phalanges are connected to each other through the interphalangeal joints. The joint between the proximal and the middle phalanx is the proximal interphalangeal joint (*PIP*) while the joint closest to the end of the finger is the distal interphalangeal joint (*DIP*). The thumb has one bone less with respect to the fingers (no middle phalanx) and it consequently has one interphalangeal joint plus the *MCP* joint.

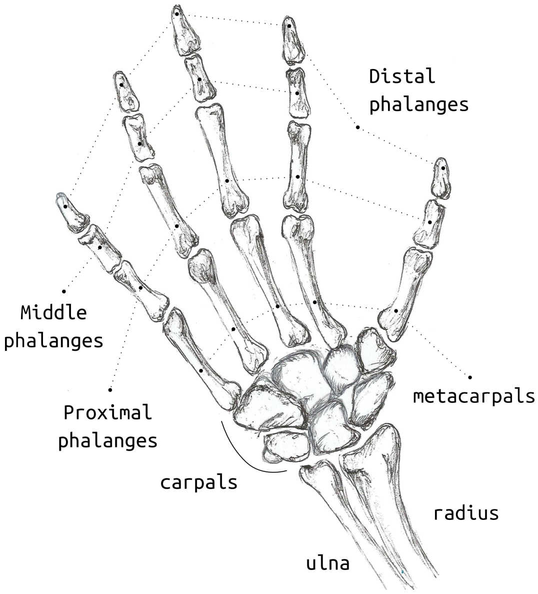

Figure 1.3 – Human hand skeleton - drawn by Cristina Botto.

1.1.1.2 Hand DoFs

At their ends, bones have articular cartilage which absorbs shocks and smooths the contact surfaces to reduce motion friction. Relative motion between adjacent bones is constrained by hand ligaments which consequently define the DoFs of each joint. These avoid, for example, middle and distal phalanges to abnormally bend sideways with respect to their precedent phalanges (collateral ligaments). In addition, they delineate the maximal extension angle of each joint, preventing the fingers to bend too far or hyper-extend (volar plate ligaments), and serve as pulleys to guide the tendons through fingers [8] (annular and cruciate). According to the shape of the contact surface and the motion constraints imposed by ligaments, hand joints are classified into three main types shown in Figure 1.4: hinge (1 DoF), condyloid (2 DoFs) and saddle (2 DoFs). The hinge joints on the human hand are the *CMC*, *PIP* and the *DIP* joints. They allow the fingers to flex (move toward the palm) and to extend (move further from palm). The condyloid joints are the finger *MCP* joints which allow flexion/extension and abduction/adduction of the fingers, the latter being the motion of spreading and gathering them. Hence, each finger can be represented as a kinematic serial chain of 5 DoFs: 1 at the *CMC*, 2 at the *MCP*, 1 at the *PIP* and a last one at the *DIP*. Finger *PIP* and *DIP* joints are orthogonal to the bone axis when the phalanx is fully extended and they progressively bend toward the center of the palm (due to the bone surface) while flexing. As a result, all fingers converge to a common point improving the opposition of the thumb to the ring and little fingers. The thumb has the same number of DoFs of fingers but differently distributed: the *RC* joint is a saddle joint, the *MCP* is a condyloid joint and the *IP* joint is a hinge joint [9]. The thumb is the only finger able to turn and oppose to the other four fingers. Opposition is provided by one DoFs of the *RC* joint while the inward rotation, called pronation (see Figure 1.5), is attributed to one DoFs of the *MCP* joint [10]. In general, pronation is not independently controlled and increases with the opposition angle of the *RC* joint. The opposability of the thumb enables humans to grip and hold objects that they would not be able to take otherwise.

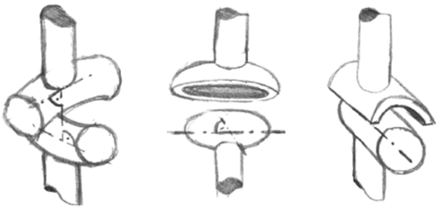

Figure 1.4 – Joints types: saddle, condyloid and hinge - picture taken from [11].

Figure 1.5 – Thumb inward orientation according to its opposition to the reminder fingers. Two grasping configurations are taken as example: the pinch grasp (left) and the key grasp (right). These pictures are taken from [12].

Figure 1.6 shows the summarized DoFs of the human hand plus additional DoFs in the palm that represent the small motions that occur among the carpal bones while flexing the wrist. In principle, *CMC* joints provide 5 DoFs to the fingers and the intra-carpal motions add one DoF after the wrist. However, their movements are highly constrained (relatively immobile) by inter-osseous ligaments that stabilize the hand joints. The *CMC* joints at the bases of the index, middle and ring metacarpals can be neglected and the small intra-carpal motions can be collected into the wrist motion. The *CMC* joint of the little finger is not omitted since it forms the hollowed shape of the palm [13] when the little finger moves in opposition to the thumb.

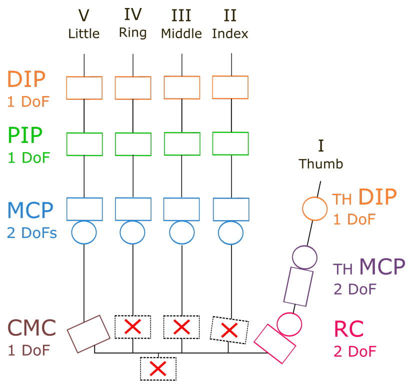

Figure 1.6 – Dorsal view of the simplified human hand kinematic model (22 DoFs).

1.1.1.3 Motion constraints

Despite the high number of DoFs the hand cannot perform arbitrary gestures. Indeed, hand kinematics are characterized by bounded motions and some joint angle dependences. Natural finger motions are defined by static and dynamic constraints. Static constraints refer to anatomical bounds at the finger joints which limit their range of motion (RoM). Dynamic constraints refer to joint angle dependences imposed by intra-finger and inter-finger couplings during motion [14]. Intra-finger constraints represent couplings between joints of the same finger, such as the one existing between *PIP* and *DIP* joints (Figure 1.6) of the four digits opposing the thumb. In literature [14], the relation is written as:

$$\theta_{DIP} = \frac{2}{3}\theta_{PIP} \tag{1.1}$$

These fingers present another intra-finger constraint at the *MCP* joints between flexion and abduction capabilities. In fact, abduction/adduction movements decrease in range as the finger bending angle increases. Inter-finger constraints refers to dependences among fingers, such as the flexion angle of an *MCP* joint that affects the neighboring *MCP* bending angles and abduction/adduction capabilities. Other examples and cases of dynamic constraints are defined in [15].

Range of Motion (RoM). Joint range of motion defines the minimum and maximum angles that can be attained by the human joints. Its breadth can be affected by injuries (mechanical problems) or diseases, consequently limiting joint motions and the global hand dexterity. Joint RoM measurements are characterized by several factors:

- measurement tool - e.g. universal goniometer;
- testing position - the subject posture during the measure;
- stabilization methods - how sensible parts are immobilized during the measure;
- measured axes - which anatomical landmarks are chosen to realize the measure;
- movement nature - performed by the subject (active) or by an external source (passive).

Even though common practices are currently supported and encouraged by researchers [16], these factors differ among studies due to the absence of accepted shared conventions. In light of this, some sources are reported in Table 1.1 and 1.2 to show some examples of joint RoMs.

Finger	Joint	Flexion	Extension	Abduction	Adduction
I	*RC*	20°	-38°	80°	-7°
I	*MCP*	40°	-15°	-	-
I	*DIP*	70°	-10°	-	-
II - V	*MCP*	90°	-20°	(20°)[i] 15°	(-20°)[i] -30°
II - V	*PIP*	100°	-2°	-	-
II - V	*DIP*	70°	-2°	-	-

[i] digit II only

Table 1.1 – 50^{th} percentile Joint RoM taken from CATIA v5 2012 based on [17].

Finger	Joint	Flexion	Extension	Abduction/Adduction[i]
I	*RC*	50° ÷ 90°	-15°	45° ÷ 60°
I	*MCP*	75° ÷ 80°	0°	-
I	*DIP*	75° ÷ 80°	-5° ÷ -10°	-
II - V	*MCP*	90°	-30° ÷ -40°	45° (60°)[ii] (50°)[iii]
II - V	*PIP*	110° (120°)[iv] (135°)[iii]	0°	-
II - V	*DIP*	80° ÷ 90° (90°)[iii]	-5°	-

[i] not given separately [ii] digit II only [iii] digit V only [iv] digit IV only

Table 1.2 – Simplified joint RoM from [18].

1.1.1.4 Finger geometries

Global dimensions of the hand are defined by its length and width. The hand length is the distance between the last crease (visible in Figure 1.5) of the wrist and the tip of the third digit (defined in Figure 1.6). The hand width is the maximum distance between the lateral borders of the palm at the level of the index and little finger bases. The ratio between hand length and width is proven to be very close among healthy people (2.26 with standard deviation 0.14 for Europeans). Indeed, Galea *et al.* [19] measured 60 healthy people (38 males and 32 females) between 25 and 85 years old and 60 patients (similar gender proportions and age ranges) affected by carpal tunnel syndrome and found out that the latter group presents smaller hand ratios (and wrist ratios) with respect to the former. The hand length can be determined by summing up the palm length and the length of the third digit, or it can be estimated from the overall height of the human body [5].

Finger lengths. Sources about finger lengths are scattered and most of the time do not include the measurements of all phalanges, metacarpals and thicknesses of the soft tissues at the tip of the five fingers. Finger lengths are not easy to measure and their values are rather different between studies, due to diverse analysis objectives, measurement methods and disparate subject ethnics. Hereafter, some examples are presented.

The most common method to evaluate finger lengths consist in identifying finger joints through anatomical landmarks, such as prominences and ridges, and directly measure their distances to estimate the bone lengths. This offers a good estimate of finger lengths for a given hand length. Table 1.3 shows the phalanges length measured from 32 subjects (15 men and 17 women) [20]. Another method consists in placing passive markers in correspondence of anatomical landmarks and estimate finger lengths from specific motion trajectories. Van der Hulst *et al.* [7], for example, updates table 1.3 by additional experimental data collected through an optical motion capture system. This method confirms finger lengths of the thumb, ring and little fingers while it changes the lengths of the index and middle phalanges. Table 1.4 shows phalanges lengths which differ from previous data. A recent work [21] measures bones lengths using X-rays images, which allow a clearer distinction of the bones with respect to other body scan techniques. Bone lengths of 66 European adults from 19 to 78 years old (without anatomical pathologies) are collected and represented as scaling factors (corrected to the nearest tenths) with respect to distal phalanges (Table 1.5). Differently from the previous methods, this approach allows the detection of metacarpal lengths and the thickness of finger pulps at the tips. Its estimations are fundamental for medical applications but less relevant to robotic ones since it identifies bone edges rather than distances between centers of rotation.

Finger	DP	MP	PP
I	12.1	-	17.1
II	8.6	14.1	21.8
III	9.8	15.8	24.5
IV	9.7	15.3	22.2
V	8.6	10.8	17.7

Table 1.3 – Directly measured phalanx lengths expressed as a percentage of the hand length [20].

Finger	DP	MP	PP
II	9.3	15.2	23.5
III	10.4	16.8	26.0

Table 1.4 – Phalanx lengths values updated by [7] through a motion capture system. These are expressed as a percentage of the hand length.

Finger	DP	MP	PP	MC
I	1	-	1.5	2.1
II	1	1.4	2.5	4.3
III	1	1.5	2.6	3.7
IV	1	1.5	2.4	3.4
V	1	1.1	2.1	3.4

Table 1.5 – Bones lengths estimated from X-ray images and expressed in function of distal phalanx lengths [21].

Finger basis. MCP joints represent the point of connection between fingers and the palm. Their positions can be estimated by knowing the length of the metacarpal bones, their orientations with respect to the wrist and their position at the carpal bones. Since no reliable quantitative information about these two last parameters are available, this method has more incorrect results than those of empirical approaches, like the one proposed by Isobe [22] which observes that the fingertips of the four digits opposed to the thumb approximatively lie on a common circle when abducted. This method places a circle of radius equivalent to the middle finger length at the MCP of the middle finger and determines the finger bases by imposing additional constraints (e.g. fixing the angle between the line passing through the index and little finger basis and the medial line passing through the middle finger).

Finger widths. Sources which relate finger widths with respect to the dimensions of the hand are scarce. The ones found by the author analyze finger widths at the *PIP* joints and mainly focus on the second digit. These studies estimate finger widths on the base of empirical linear equations which take the hand width as input. Greiner [23] defines two distinct equations (in [mm]) according to the gender. For men:

$$II_w = 1.5H_w + 7.91 \tag{1.2}$$

For women:

$$II_w = 1.6H_w + 8.79 \tag{1.3}$$

where II_w is the index finger (second digit) width and H_w is the hand width. These equations come from the hand analysis of 63 men and 63 women of the U.S. army personnel based on high resolution images. Buchholz and Armstrong [24] define a single equation for both genders based on the right hands of 30 subjects (15 man and 15 women) measured with a 300 [mm] caliper with resolution of 0.02 [mm]:

$$II_w = 2.15H_w \tag{1.4}$$

In [25] previous studies are compared with respect to an additional dataset obtained from measuring with a standard caliper the width of the hand and the index *PIP* joint of 19 adults (11 men and 8 women) ranging between 20 and 57 years old. The comparison shows that Greiner model is consistent with female measurements while it predicts larger values for men. On the contrary, it shows that Buchholz and Armstrong equations always estimate smaller values with respect to the analyzed subjects, concluding that both models can be used to predict finger widths as upper and lower bounds respectively.

1.1.1.5 Thumb opposability

The most important, complex and dexterous finger of the human hand is the thumb. It can operate within the frontal (coronal) plane of the palm beside the radial side of the index, and in opposition to the reminder fingers. It can easily interact with each digit, from the base to the fingertip, thanks to its articulated chain and placement on the palm. Opposability is also enhanced by the previously mentioned finger flexing motions, which do not lie on planes orthogonal to the palm (or frontal plane) but on surfaces which bend toward the middle of the palm. In this way, digits are straight when stretched and point toward a common point below the wrist when flexed. In the case of thumb loss, hand functional capabilities drastically drop and require a surgical intervention to be fixed. The surgery, called pollicization, normally consists in replacing the missing finger with one of the remaining digits (normally the index). After this medical procedure, a dexterity test is performed to investigate whether the "new" thumb preserves the natural capabilities of its predecessor. This test, called Kapandji test [26] in honor of its inventor, contains specific motion directions and a set of positions on the opposite fingers to check the thumb mobility and the range of motion of its joints. The thumb is asked to reach 11 positions: base, *PIP* joint, *DIP* joint and fingertip of index and little fingers and the fingertips of the digits in between, plus a point on the palm close to the little finger base. According to the achieved configurations a score is assigned to determine the final thumb dexterity. Figure 1.7 shows the mentioned configurations with the relative scores.

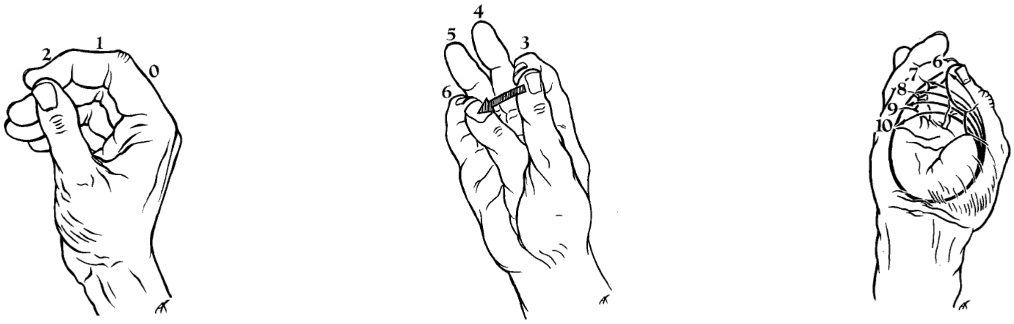

Figure 1.7 – Set of configurations on the opposing fingers that the thumb has to reach to be fully functional. These are selected to check thumb dexterity after surgery or important physical injuries. Figures are taken from [26].

1.1.2 Motion capabilities

An extensive classification of human hand task-oriented motion capabilities is proposed by Bullock and Dollar [27]. This work characterizes basic hand motion behaviors according to the existence of contact with external objects, prehension, and the object motion relative to the hand. Figure 1.8 shows the hand behaviors ordered by precision and dexterity during the execution of various simple tasks. To clarify the tree-structured taxonomy, few definitions are necessary:

- *Prehensile grasp* - contact forces stabilize the grasp and more than one independent contact is involved;
- *Motion* - the hand moves with respect to the human body frame (e.g. torso frame);
- *Within hand* - fingers move with respect to the palm frame;
- *Motion at contact* - the object is significantly reconfigured (translated and/or rotated) with respect to the contact frames. This does not consider small motions due to skin deformation but substantial relative object motions.

Complex tasks involving a series of time-separated motions, two hands and simultaneous functions can be regarded as a combination of distinct sub-tasks performed. Time-separated motions refer to a sequence of movements evolving in time, such as picking a key and opening a lock. This can be divided in a sequence of three simple tasks: lifting the key from the pocket (contact/prehensile/motion/not within hand), reorienting the key within hand (contact/prehensile/motion/within hand/motion at contact) and turning the key in the lock (contact/prehensile/motion/not within hand). Two-hand tasks are operations which require the simultaneous and correlated use of two hands, such as sewing. In this case, each hand perform an independent task which can be either a simple or complex operation. Tasks which require simultaneous functions to a single hand are frequent in our everyday life. These combine more skills at the same time, such as thumb-typing on a phone which requires to hold the object (contact/prehensile/no motion) and repeatedly touch the screen (non-prehensile/motion/not within hand).

1.1.2.1 Hand gestures

Hand motions convey information analogously to a spoken language: "As the tongue speaketh to the ear, so the gesture speaketh to the eye" [28]. They can be generally divided between *communicative* and *non-communicative* gestures [29]. Communicative gestures are intentionally directed toward one or more interlocutors while non-communicative ones are not addressed to specific individuals. The former contribute to express the speaker's intended meaning (semantic information) while the latter normally enrich the communication by providing additional information not strictly related to the main subject. Hand motions are distinguished in three main categories according to their lexicality [30], i.e. their ability to concisely express a concept or, equivalently, their transparency in providing lexical meaning and conceptual symbolism. Figure 1.9 introduces the lexicality continuum of hand movements.

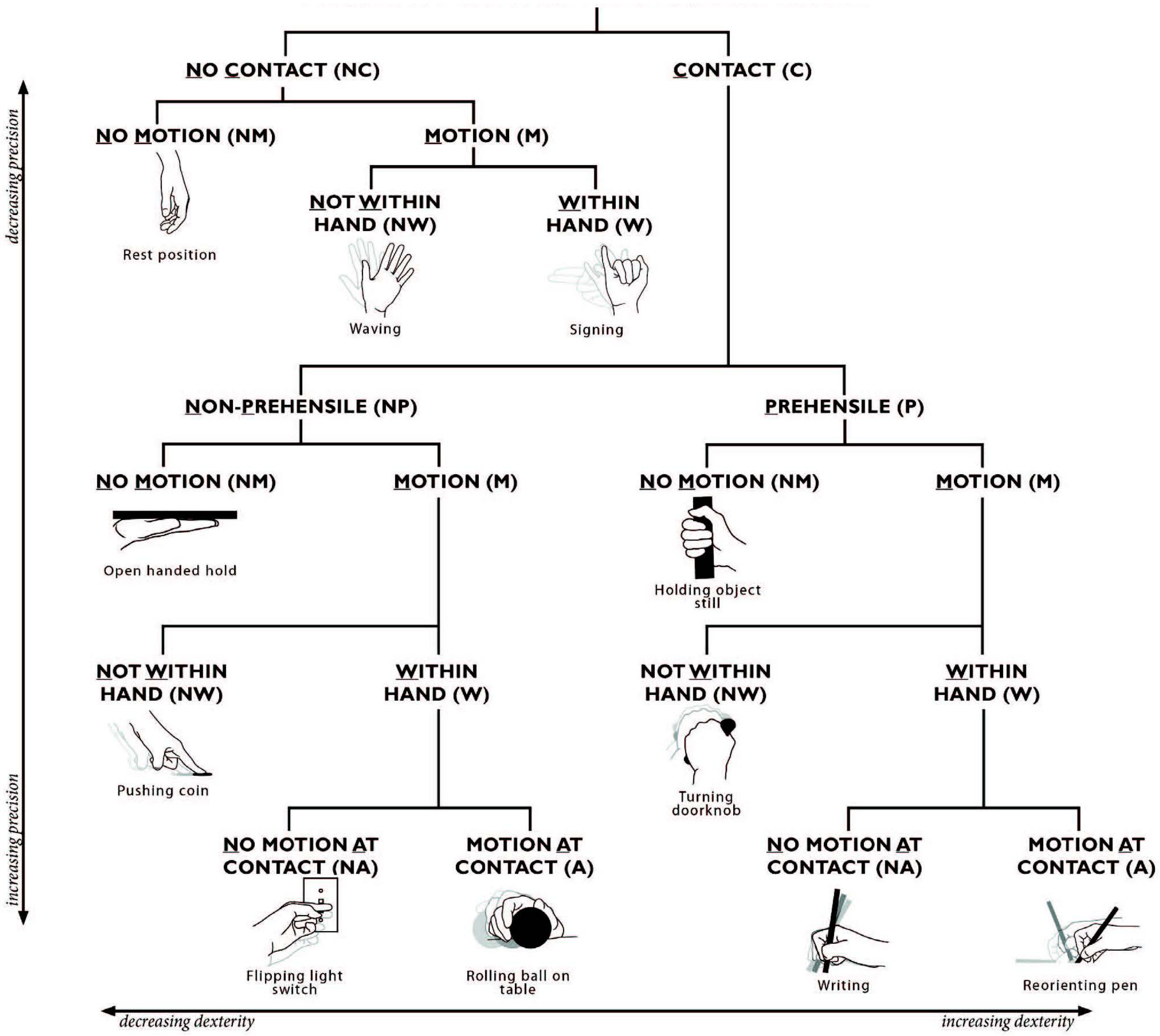

Figure 1.8 – Human hand taxonomy of task-oriented motion capabilities - adapted from [27].

Figure 1.9 – Lexicality continuum of hand movements.

At the bottom of the continuum, *adapters* [31] are hand movements not related to the meaning of the speech they accompany and they are not perceived as part of the communication. They are not considered as gestures but as involuntary expressions of thoughts and feelings that the speaker unconsciously has [32] or is trying to hide (e.g. upset, worried, disinterested). Adapters include self-addressed (self-touching), object-addressed and person-addressed (body-focused) touching movements. Simple examples are actions like tapping on a table or scratching the back of our head. *Conversational gestures*, also called gesticulations or illustrators, are a heterogeneous set of hand movements synchronized and apparently related to speech. They do not take place in absence of speech and they are only made by the speaker. They are coordinated with the oral communication and appear to be in-line with the meaning of the talk. Two main types are distinguished [33]: motor and lexical movements. The former are simple, rhythmic and repetitive motions that do not explicitly support the semantic content of the speech. The latter are changing, non-repetitive and complex movements which meaningfully support, at least from a naive point of view, the discussion. *Expressive gestures*, also called illustrators, emblems or conventionalized signs, are word-like hand movements with specific agreed meanings. They are intentionally used to communicate and always express a semantic content. Differently from adapters and conversational gestures, they are often used in absence of speech. When they accompany oral communication they are sometimes adopted to strengthen a word or replace an unspoken one. The meaning of expressive gestures is based on shared agreement about their semantic content. There exists some conventionalized signs which are familiar to almost everyone, such as "thumbs-up", the "raised fist" and the impolite straight middle finger sometimes called the "flipping the bird". In general, however, each culture has a set of expressive gestures whose meaning might change from one group to another. Some communities may also adopt special signs unknown to outer members. Expressive gestures can be distinguished in four categories according to their communicative function. Table 1.10a describes each category and provides some example according to [34]. Symbolic gestures concisely express a concept with simple gestures or signs but requires semantic agreement among speakers. Deictic (or indexic) gestures rely on the environment to convey information. Iconic gestures represent objects or actions by sketching them, while pantomimic gestures by miming or acting out their meaning. From this perspective, expressive gestures can be ordered according to their conventionalized semantic content (see Figure 1.10b). The more unconventional, the more exaggerated to convey the intended meaning.

Types	Meaning	Examples
Symbolic Gesture	Gestures have a single meaning within each culture.	Sign Language, Command Gesture
Deictic Gesture	Gestures direct the listener's attention to specific events or objects in the environment.	Pointing Gesture
Iconic Gesture	Gestures represent meaningful objects or actions.	Predefined Gesture
Pantomimic Gesture	Gestures that depict objects or actions, with or without accompanying speech.	Mimic Gesture

(a) Taken from [34]

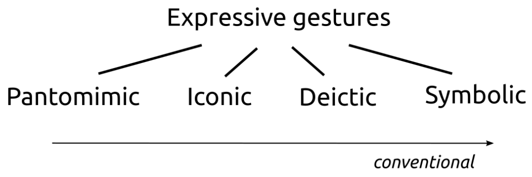

(b)

Figure 1.10 – Expressive gestures taxonomy.

1.1.2.2 Grasp types

Moving the perspective from the hand capabilities to the objects being grasped, prehensile tasks which involve no finger motions at contact can be classified into different *grasp types*. An early and general distinction proposed by Schlesinger [35] recognizes six main grasp categories: cylindrical, tip, hook, palmar, spherical and lateral. These are typical hand postures adopted to grasped objects according to their shapes and sizes. However, the way objects are grasped not only depends on their physical characteristics but also on the task to be performed. Napier suggests this by dividing the grasps between power and precision grasps [36]. A clear example is given by mugs: grasped with large contact surfaces involving the palm (power grasp) for drinking, and grasped with limited contact surfaces offered by fingertips (precision grasp) for displacement. Power and precision grasps do not cover all grasp capabilities of the human hand, leaving some grasps not clearly identified. Cutoski adopts both Schlesinger and Napier perspectives by organizing human grasps in a tree [37], firstly divided according to power and precision grasps and then expanded according to object shapes and weights. A more recent and detailed taxonomy collects and compares grasp types coming from different field of studies, such as medicine, biomechanics and robotics [38]. It defines 33 valid grasps arranged in a matrix-like taxonomy presented in Figure 1.11. Three main columns divide the grasps among power, intermediate and precision types. A finer sub-division distinguish grasps according to the opposition type: palm, pad and side. The opposition type defines the first virtual finger (*VF1*), which in case of pad and side type normally corresponds to the thumb. A virtual finger is the abstraction of a set of forces synchronously acting in a similar direction. In function of the grasp, it can include one or more fingers and parts of the hand [37]. As it can be seen in Fig. 1.11, two opposing virtual fingers (*VF1* and *VF2*) are required to define a grasp, while sometimes a third is added in presence of one or more fingers opposing a task related force or torque. An additional characterization is based on the thumb position determined by the abduction/adduction angle of the RC joint. According to this classification, grasp types can be reduced to 17 if object shapes are not taken into account.

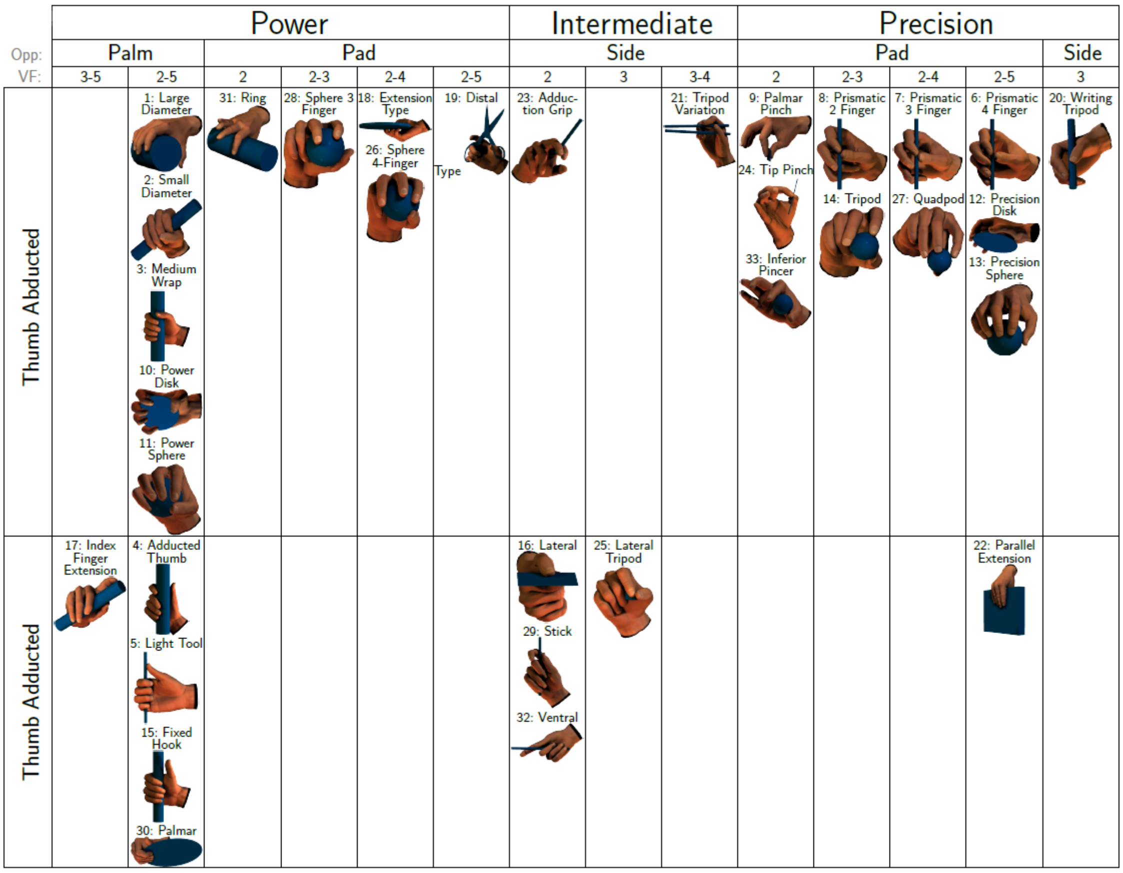

Figure 1.11 – Grasp taxonomy of the human hand - taken from [39].

1.1.2.3 Motor primitives

Neuroscientific studies show that the nervous system does not control each muscle and joint as independent units, but as a whole of coordinated and coherent motions. These are generated by specific muscular activation patterns among which a set of motor primitives, called *synergies*, can be identified. From this perspective the human hand appears to have more independent DoFs than the ones effectively required. Synergies can be interpreted as the basis (set of linearly independent components) of a vector space, where any element in the space can be obtained as a linear combination of the basis vectors. In this sense, synergies allow the control the hand, characterized by a large number of independent DoFs, in a dimensionally reduced space. From the analysis of the hand shape adopted by five subjects to grasp imagined objects of different shapes and sizes, Santello *et.al.* [40] identifies a small set of synergies (or "principal components") among which the first three components are sufficient to reconstruct most of the hand configurations, while the reminders only provide additional information about the object. In particular, at least 80% of the hand posture variance involves the first two synergies while 87% is covered by the first three. This suggests that reach-to-grasp motions, or motions performed to approach the grasp (pre-shape phase), can be generally obtained by controlling two independent control inputs. These generally shape the hand, while higher order components allow finer kinematic adjustments. These synergies are often called kinematic [41] or postural synergies [42], since they define the hand posture in function of the object shape and size, rather than the physical interaction with the object. These have been recently adopted in robotics either to simplify the control of robotic hands [43] [44] [45] (software synergies), or to reduce the number of actuators at the design stage (hardware synergies) [46]. Extrapolating the same concept in the force domain, different grasp types can be achieved on the base of a reduced set of control inputs, called force synergies [47] or soft synergies [48]. Soft synergies control the grasp force by means of the hand mechanical compliance, which can be varied by changing hand stiffness or driving its grasp reference posture. The reference posture is defined as a virtual hand in the synergy space to which the real hand is attracted in function of the hand stiffness. The posture of the physical hand is determined by the equilibrium between the attraction force toward the reference configuration and the opposing force offered by the object. Indeed, in absence of contact, the virtual and physical hands coincide, leading soft synergies back to postural synergies. In conclusion, synergies simplify motion and force control of multi-digit robotic hands for grasping tasks, limiting the full utilization of the hand capabilities - such as the individual control of finger movements.

1.2 Robotic hands

Over the last decades, robotic hands have been studied and developed to replace conventional grippers: parallel jaws with limited dexterity and range of motions, normally adopted for specific industrial applications. Nowadays, there exists a large variety of robotics hands. According to the context and the type of tasks they are supposed to perform, they normally present different number of digits. Three-fingered hands are commonly adopted for pick and place tasks which require stable grasps and limited in-hand manipulation. Four-fingered hands offer more dexterity and can be used for fine manipulation if properly designed [49]. For applications concerning humanoid robots and amputees, five fingers are compulsory. Indeed, both require human-like aesthetics and functional capabilities to enhance user acceptance and interaction. Several dexterous hands have been developed to replicate the human hand aspect and performance. In this section, a subset of them is presented and characterized on the base of their Degree of Motion (DoM) - wrist excluded.

1.2.1 Highly dexterous hands

The most intuitive method to develop a highly dexterous robotic hand is to create a pragmatic replica of the human hand, i.e. an artificial upper limb with a number of DoFs and motion capabilities coherent with the human hand kinematics. The main challenge in designing such devices consists in preserving the highest number of actuators while respecting the hand shape and size close to the human hand. Some of them are presented hereafter (see Table 1.6).

Name	Year	Joints	Ind. DoFs	Actuators	Self-contained	Size [mm]	**Weight** [Kg]
DLR Hand Arm System [50]	2011	21	19	38	no	n/a	13.5[i]
Robonaut 2 hand [51]	2012	18	12	17[ii]	no	l: 304 ∅: ≤ 127[iii]	9
Shadow hand [52]	2006	22	18	36[iv] 18[v]	no	l: 448 ∅: ≤ 135	4.2
CEA hand [53]	2014	22	18	18	no	n/a	4.2
DLR/HIT hand II [54]	2008	20	15	15	yes	l: 169.1	1.5
Gifu hand III [55]	2002	20	16	16	yes	251.3 x 95 x 41	1.4
UB hand IV [56]	2013	20	15	20[vi]	no	l ≈ 330[vii]	n/a
SBC [57]	2007	20	16	32	no	n/a	0.8
Sonoda and Golder hand [58]	2010	18	14	15	yes	238 x 116 x 72	0.8

[i] arm included [ii] 16 declared but not coherent with the total number of tendons [iii] from the base to the center of the palm
[iv] Air Muscles [v] Smart Motors [vi] wrist not considered [vii] forearm excluded

Table 1.6 – General characteristics of highly actuated robotic hands. Further DoFs and actuation details are provided in Tables A.1 and A.2

DLR Hand Arm System. The DLR Hand Arm System [50] consists in a 5-DoFs arm, a 2-DoFs wrist and a 21-DoFs hand. It is conceived to reproduce the human hand kinematic, dynamic and force properties. The system is driven by 52 embedded variable stiffness actuators (VSA) able to adjust joint stiffnesses on-line, avoiding the trade-off between robustness and accuracy typical of serial elastic actuators (with predetermined and fixed stiffnesses). With respect to active compliance, they offer high robustness and dynamic performances absorbing violent shocks at the first control cycle and storing energy. Three different types of VSA are adopted in the system, according to the actuation requirements and available space. The hand (shown in Figure 1.12) is driven by 38 actuation modules, called ServoModules, located in the forearm. Each ServoModule is composed of one motor, the electronics to control it and the wave generator of the harmonic drive gear. Each DoF is actuated by pairs of antagonist modules which control its position and stiffness by moving in the same and opposing direction respectively [59]. Joints are remotely controlled through Dyneema® tendons, routed to minimize joint couplings and guided by custom-made sliding surfaces to reduce friction. Fingers have four independent DoFs, except for the ring and the little fingers which presented coupled PIP and DIP joints. Also the thumb has four independent DoFs, eliminating the 5^{th} DoF of the human thumb dedicated to the in-ward orientation of the serial chain on the opposing fingers during abduction. The overall systems weighs 13.5 [Kg].

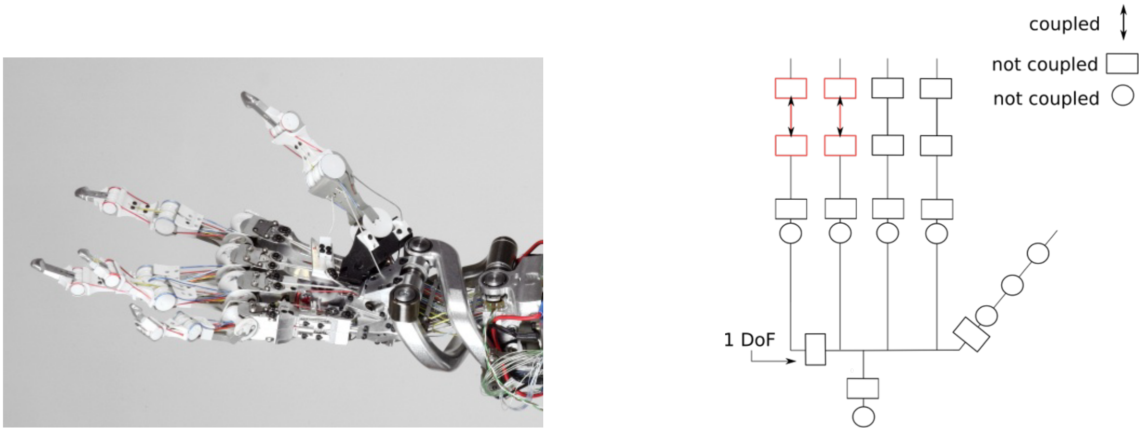

(a) Picture taken from [50]. (b) Kinematic structure.

Figure 1.12 – The hand of the DLR Hand Arm System.

Shadow hand. The Shadow hand [52] has 22 DoFs, 18 of which are directly driven. The thumb is the most articulated among robotic hands with five independent DoFs, like the human counterpart. Fingers are endowed with four DoFs, one for abduction/adduction and three for flexion/extension. Like the human hand, PIP and DIP joints are coupled, reducing finger DoMs to three. Fingers all have the same lengths but are attached to the palm at different heights. The palm presents one DoF below the little finger to improve its opposition to the thumb. Figure 1.13 shows the hand and its kinematic model. The Shadow hand can be actuated by two different actuation systems. One based on rotary electric motors, called Smart Motors, and one based on McKibben-type pneumatic actuators [60], called Air Muscles or artificial muscles [61]. These are only able to pull by contraction, consequently requiring antagonist actuation (36 artificial muscles are required). All actuators are embodied in the hand support (forearm) and remotely control the hand joints through tendons. The hand and the forearm weigh, in total, 4.2 [Kg]. Its price (updated in 2009) is about 75000 £ for the muscle actuated version and 115000 £ for the motor actuated version.

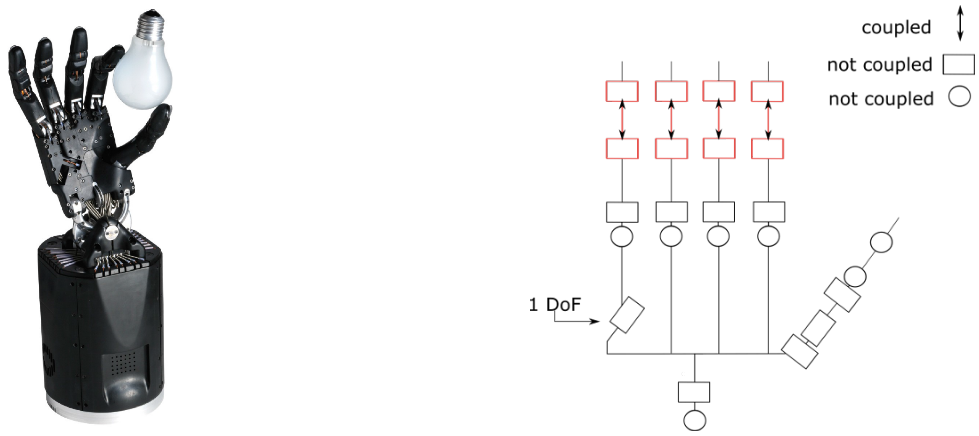

(a) Picture taken from [52]. (b) Kinematic structure.

Figure 1.13 – The Shadow hand.

CEA hand. The CEA hand [53] adopts the same kinematic structure of the Shadow Hand but embeds a completely different actuation system (see Figure 1.14). All DoFs are driven by custom backdrivable mechanisms based on rotary DC motors coupled to a ball-screw transmission (with high pitch-to-radius ratio). These are implemented either as double acting actuators (bi-directional) or as single-acting actuators (mono-directional) with return springs to guarantee one motor per DoF. Modularity is encouraged by 3-DoFs sub-mechanisms, called "three-axis units", which include actuation, transmission and hardware components (remotely located). The three DoFs consist in two orthogonal axis which provide abduction/adduction and flexion/extension motions and one successive axis allowing flexion/extension. Actuators are placed in the palm and thumb to limit tendon lengths and redirections, consequently reducing friction losses and tendon elasticities. Electronic components (power boards and low-level control units) are left in the forearm. The total weight of the CEA hand is 4.2 [kg], exactly like the Shadow Hand.

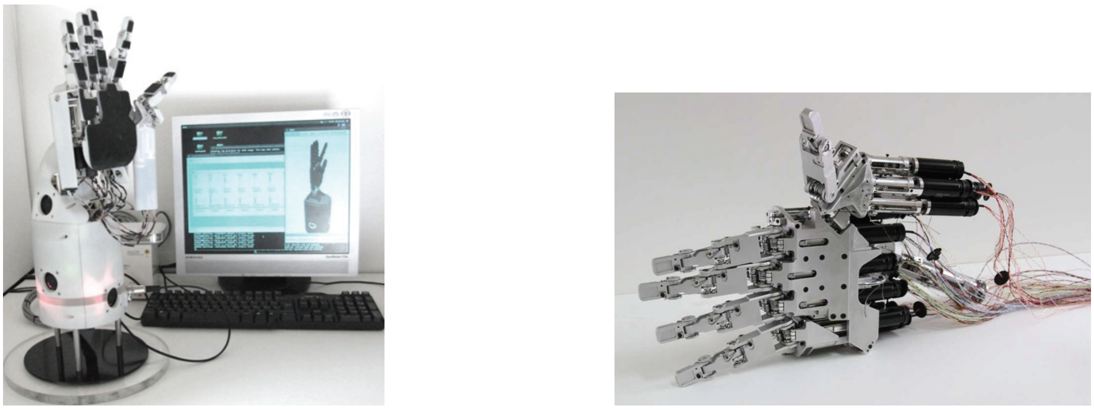

Figure 1.14 – The CEA dexterous hand. Pictures taken from [53].

Gifu Hand III. Gifu Hand III [55] has 20 DoFs driven by 16 built-in servomotors. The thumb has four independent DoFs like the DLR Hand Arm System. Fingers have four DoFs, the first three directly actuated and the last coupled through planar 4-bar linkages with the PIP joints. Actuators are all embedded in the hand and placed close to the driven joints. Indeed, no tendons are required. The first two DoFs of each digit are driven by two independent motors and asymmetrical differential gears placed in the palm. The third (and fourth for the thumb) is driven by a small motor arranged inside the proximal (and middle) phalanx. The hand is characterized by a high thumb opposability, enhanced on the base of its intersection space with the other digits. Gifu III hand (shown in Figure 1.15) is the last of the Gifu hand series (I [62], II [63]) after which a new hand, called the "Kinetic humanoid hand" [64], has been designed. The last preserves Gifu hand III kinematics and introduces hardware and actuation improvements (ad-hoc BLDC motors) to reduce the size of the robotic hand. This hand weighs 1.09 [Kg] with respect to 1.4 [Kg] of the Gifu Hand III.

(a) Picture taken from [55]. (b) Kinematic structure.

Figure 1.15 – The Gifu Hand III.

SBC hand. The SBC (Segmented Binary Control) hand [57] has 16 independent DoFs controlled by 32 Shape Memory Alloy (SMA) actuators placed in the forearm (as shown in Figure 1.16a). Each finger is endowed with four DoFs, three of which are independently actuated. The first two drive the abduction/adduction and flexion/extension motions of the proximal phalanx. The third actuates PIP and DIP joints at the same time, allowing self-adaptation (defined in Section 1.2.2.2) of the distal phalanx during grasp. Finger joints are controlled by antagonist SMA wires heated according to a segmented activation principle. On the base of Joule's effect, specific areas are heated by running currents between desired couples of points on the wires. Electrical connectors are placed at regular interval to supply voltage at each segment (see Figure 1.16b). These are activated through a binary control and coordinated to reproduce desired human hand postures. To preserve antagonist wires in tension a compression spring is attached in series of each actuation pair. Thanks to the lightweight type of actuation the overall weight of the hand is less than 0.8 [Kg]. No information is provided about the achievable motion speeds. It is likely, however, that such a system is affected by slow dynamics due to the heating and cooling phases.

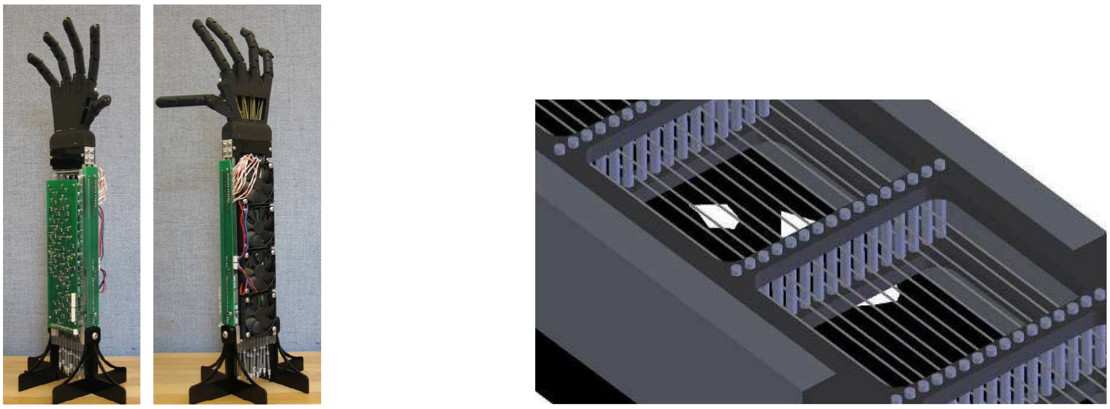

(a) The SBC hand.

(b) Segmented activation of SMA wires.

Figure 1.16 – The SBC hand and the SMA segmented activation principle. Pictures taken from [57].

UB hand IV. The UB hand IV [56], also called DEXMART Hand [65], is realized to explore alternative solutions to conventional hand structures and sensorimotor systems, with the objective to simplify the design, reduce the cost and improve the performance of next-generation robotic hands. Its design (shown in Figure 1.17) is the result of nearly three decades of research in the field of robotic hands which produced different hand prototypes (UB I-II-III) [66]. Its structure is characterized by an endoskeletal finger model, an optimized cable routing and an easy-to-control compliant actuation. The endoskeletal finger model consists of a bio-inspired finger structure, stiff inside and compliant outside. Indeed, the hand adopts external soft covers to increase impact robustness and designs the internal stiff links as the human bones. After the investigation of different types of joints [67], revolute joints consisting in a plastic shaft sliding on a cylindrical surface are adopted. The hand presents modular 4-DoFs fingers with 3 DoMs. Each finger is driven by four actuators according to the N+1 configuration [68] (where N is the number of independent DoFs): three agonists and one antagonist. The first two tendons attached to the proximal phalanx control the MCP joint. The third tendon actuates the PIP joint, while the fourth tendon passes on the back on the finger up to the distal phalanx. A fifth tendon internally routed between middle and distal phalanges couples the DIP and PIP joints. Dyneema®-based Fast-Flight tendons are adopted to reduce friction within fingers and on sliding paths. In addition, cable redirections are minimized between the actuators and the fingers to preserve the pulling forces. Finger joints are driven by 24 twisted-string actuators [69] (four dedicated to the antagonist actuation of the 2-DoFs wrist) which offer direct rotative to linear transformation, high reduction and natural compliance. Furthermore, they do not need additional mechanical components (e.g. pulleys or ball-screws) which increase frictional losses.

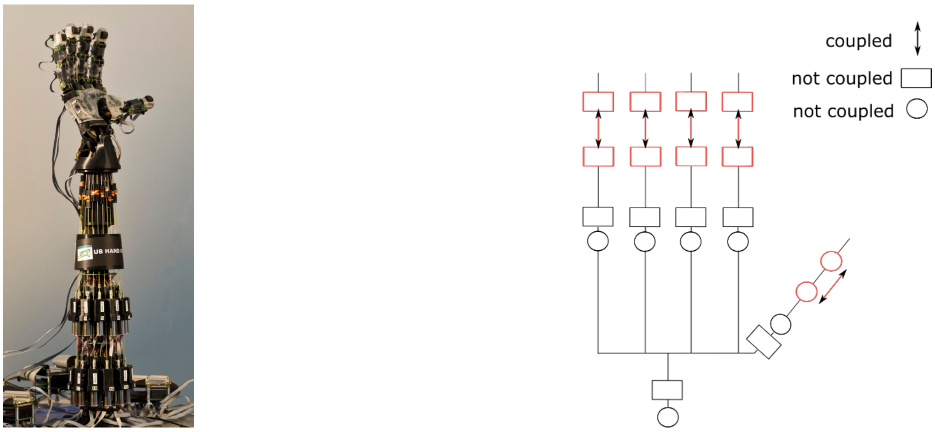

(a) Picture taken from [56]. (b) Kinematic structure.

Figure 1.17 – The UB hand IV.

DLR/HIT II hand. The DLR/HIT II hand [54] improves the four-fingered DLR/HIT I hand [70] reducing finger sizes by one third. In addition, it eliminates the first thumb DoF, used to change the palm opposition angle, by properly fixing the thumb base orientation. The hand (shown in Figure 1.18a) has modular 4-DoFs fingers with three DoMs. Modularity is also applied to the actuation system, where each actuation mechanism is composed of a flat BLDC motor, a tiny harmonic driver with 100:1 of reduction ratio and custom flexible circuits. The motor and the gearbox together weighs 30 [g]. Their axes are mounted in parallel and are connected by a timing belt with a reduction of 1:2.1. Each finger is composed by two main parts: a body unit and a base unit. In the body unit, a single actuation mechanism is adopted to drive the PIP joint while the DIP joint is mechanically coupled to the previous one with a steel wire (1:1 of reduction ratio). In the base unit, a differential mechanism is used to control the abduction/adduction and flexion/extension motions. Both DoFs are independently actuated by two actuation units embedded in the palm whose torques are transmitted to the differential inputs via additional timing belts. The hand self-contains all actuators, gears and electronics, weighing in total 1.5 [Kg]. As it can be seen in Figure 1.18b, the DLR/HIT II hand is mounted on the DLR's JUSTIN robot.

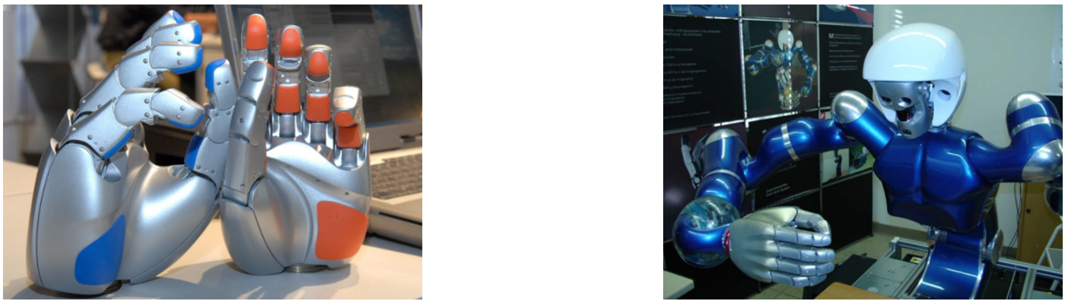

(a) Picture taken from [71]. (b) DLR's humanoid robot: JUSTIN.

Figure 1.18 – The DLR/HIT hand II and JUSTIN.

Sonoda and Golder hand. Among the nearly full-actuated robotic hands reported in this context, the Sonoda and Godler hand [58] (shown in Figure 1.19) is the lightest. Indeed, it weighs approximately 0.8 [Kg] including the actuation system and relative driver boards. Even though it presents less DoMs with respect to the robotic hands previously introduced, the weight is quite low considering that the hand embeds 15 actuators. Each finger has four DoFs except the Middle finger and the thumb. The former has no abduction/adduction motion at the MCP joint while the latter presents only three directly actuated joints. All fingers have PIP and DIP joints non-linearly coupled by a fixed-length string forming a 4-bar linkage structure. BLDC motors drive finger joints by mean of the same transmission principle adopted by the UB IV hand: twisted strings. In this case, however, twisted strings (called *Twist Drive*) are short in length and connect the actuators directly to the finger links (rather than on pulling tendons). This is encouraged by the fact that motors are placed within the palm and the fingers, close to the driven phalanges. The direct connection to the finger links leads to variable joint torques which depend on phalanx configurations. Each independent DoF is controlled by one actuator and a torsion spring, which provides the return motion. Only the first thumb joint is actuated by two antagonist Twist Drives, to provide active control while moving in and from palm opposition.

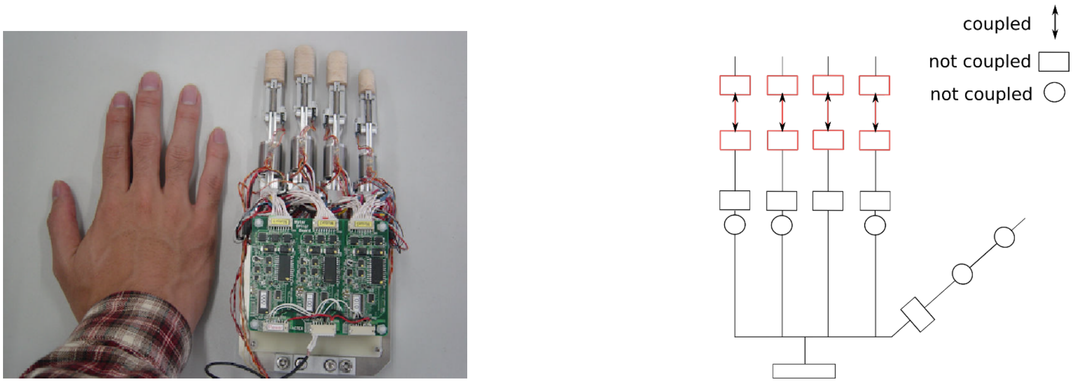

(a) Picture taken from [58]. (b) Kinematic structure.

Figure 1.19 – The Sonoda and Godler hand.

Robonaut 2 hand. The Robonaut II hand [51] (Figure 1.20) is characterized by two types of fingers called primary and secondary fingers. These are designed according to the tasks they are supposed to perform. Primary fingers are used for manipulation tasks and have the classic human-inspired 4-DoFs kinematic structure. Each primary finger has the first three joints independently actuated while it has the DIP joint rigidly coupled with the precedent one by a four-bar linkage transmission mechanism. Secondary fingers have structures similar to the primary ones but present no abduction/adduction DoF at the MCP joints and self-adaptable (or *loosely-coupled*) MCP and PIP joints. Index and middle fingers are primary fingers, while ring and little fingers are secondary fingers. The thumb does not belong to any finger type. It has four phalanges and four independently controlled DoFs. Its kinematics simplifies the structure of the human thumb by replacing the re-orienting passive capability with a fixed angular twist between the second and the third joints. Joints are controlled by modular actuation units composed of a motor, a gearbox and a ball-screw assembly placed in the forearm, and a Vectran tendon. The last is routed within a flexible conduit up to the target link. In total, the hand has 12 independent DoFs driven by 17 actuators. Primary fingers and the thumb are controlled according to the N+1 rule to reduce the number of tendons and, consequently, the number of actuators. Secondary fingers are driven by one tendon per independent DoF. The overall structure of the Robonaut II hand weighs more than 9 [Kg].

1.2.2 Hands with reduced DoMs

Highly actuated robotic hands slightly simplify the kinematic structure of the human hand, eliminating certain DoFs which marginally impact grasping and in-hand manipulation capabilities. To preserve human hand proportion and size, some of the designs embed the actuators in the forearm, while others adopt small motor sizes within the hand. The former generally end up being bulky while the latter weak. In addition, both are heavy with respect to the human hand, which weighs on average 0.4 [Kg] excluding the muscles in the forearm [72].
Another approach to design robotic hands consists in limiting weight and size by reducing the number

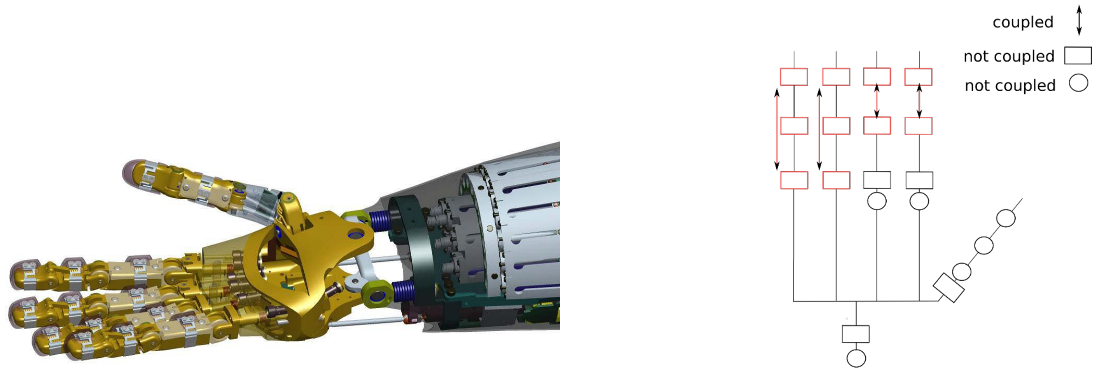

(a) Picture taken from [51]. (b) Kinematic structure.

Figure 1.20 – The Robonaut II hand.

of independent DoFs and, consequently, the number of actuators. This method leads to simplified kinematic structures with lower functional capabilities. Nonetheless, for the same volume, less actuators means larger motors and, consequently, more power. Indeed, some highly actuated robotic hands (such as the DLR/HIT hand II) have less grip force of simpler hands (such as the FluidHand III), as highlighted by [72]. Robotic hands with a reduced number of actuators have different natures. Some are embedded on humanoid robots and others are used as prosthetic devices. All share common objectives such as to preserve human aesthetics and provide fundamental functional capabilities. Some of them limit the number of actuators to accommodate durability (energy-consumption) and reduce costs. This is done in particular for prosthetic hands whose autonomy is pushed by non-backdrivable mechanisms which allow grasped objects to be held without actuation power. Independent DoFs are reduced by decreasing the number of joints and introducing additional joint couplings according to the task to be performed. Joints are coupled with (linear or non-linear) fixed transmission ratios or loosely coupled with self-adaptable transmission mechanisms. In the first case, complex control strategies and sensors are needed to grasp objects while, in the second, grasp is directly solved by mechanical design. Hereafter, robotic hands with a reduced number of actuators and simplified kinematics are presented according to the adopted coupling method.

1.2.2.1 Fixed joint couplings

Joints coupled with fixed transmission ratios simultaneously move as a single unit. Their relative motion can be linear or non-linear but always known within the joint range of motions. Joint configurations are determined by the actuator (or the master link) position, which becomes the only variable required to describe distinct finger postures. Highly actuated robotic hands normally use this kind of coupling since it is more suited for generic manipulation tasks. Hereafter, some robotic hands (see Table 1.7) with reduced DoMs and fixed joint couplings are presented.

Schunk Dexterous Hand. The Schunk Dexterous Hand [73] is a commercially available robotic hand previously developed by Elumotion LDT. Limited information is available about its design and actuation system. The hand has 20 joints driven by 9 electromagnetic actuators. All its electronics and actuation components are embedded within the palm and the fingers. Its circular base provides easy connection to different robotic arms. The hand (shown in Figure 1.21) has human-like proportions but a size larger than the average human hand. It weighs 1.3 [Kg] and costs 39900 € (price updated on November 2014).

HRP-4C hand. The HRP-4C hand [74] has a completely different purpose with respect to the hands previously presented. Rather than focusing on dexterity and general manipulation capabilities, this hand is designed for pure entertainment. In particular, the hand is required to imitate basic human-like motions while dancing (which reduce the desired hand postures to few configurations). The HRP-4C hand (shown

Name	Year	Joints	Ind. DoFs	Actuators	Self-contained	Size [mm]	**Weight** [Kg]
Schunk Gripping hand [73]	2010	20	9	9	yes	242.5 x 92 x (<) 65[i]	1.3
HRP-4C hand [74]	2011	13	2	2	yes	184 x 80.5 x 27	n/a

[i] estimated from the smallest base diameter

Table 1.7 – General characteristics of robotic hands with fixed joint couplings. Further DoFs and actuation details are provided in Table A.3.

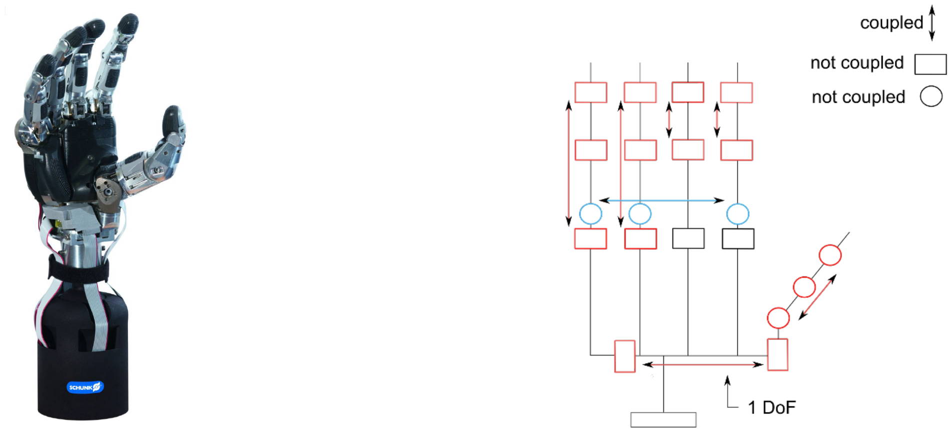

(a) Picture taken from [73]. (b) Kinematic structure.

Figure 1.21 – The Schunk Dexterous hand.

in Figure 1.22) is actuated by only 2 servomotors embedded in the palm. One drives the thumb while the other actuates the remaining fingers. The thumb has only one joint which enables palm opposition. Each finger has three DoFs tightly coupled into one DoM. Their motions are synchronized by a parallel crank mechanism at the output of the planetary gear of the second servomotor. The hand size respects the average of young Japanese females but, in some cases, it is perceived to be disproportionate with respect to its body.

Figure 1.22 – HRP-4C hand and humanoid robot. Pictures taken from [74].

1.2.2.2 Adaptive couplings within fingers

As the number of actuators decreases, fixed joint couplings are often replaced by adaptive mechanisms to provide autonomous force distribution on grasped objects. Robotics hands designed to mechanically self-adapt to different object shapes [75] are commonly called *under-actuated*. These hands are characterized by transmission mechanisms which allow power distribution to fingers and phalanges even when some link motions are hindered by external forces. The term under-actuated is not always used by hand designers to identify self-adaptable mechanisms, creating ambiguities about its meaning. In this context, they are named *self-adaptable* to avoid confusion, leaving the sense of under-actuated to its classic connotation. A typical solution adopted by self-adaptable hands consists in placing the actuators in the palm or in the forearm and distributing their forces to the fingertips via linkages or pulleys and cables. In such hands, finger motions depend on the actuation forces, the restorative forces provided by elastic elements placed within fingers and to the external forces applied on phalanges. This means that fingers can reach different configurations for the same number of actuators but, at the same time, specific finger configurations can only be attained through object contacts. In this case, actuators cannot be used to determine joint angles since they depend on the presence of external contacts. The geometric parameters of self-adaptable hands are challenging to design but, once determined, they provide simple and effective manipulators. Robotic hands which embed adaptive transmission mechanisms can grasp unevenly shaped objects with the entire finger surface and their multi-DoFs structure can be controlled with few control signals. Hereafter, some robotic hands (see Table 1.8) which exclusively embed self-adaptable mechanisms within fingers are presented.

CyberHand. The CyberHand [76] is conceived to provide dexterous sensorimotor control to human amputees. The name comes from *cybernetic*, which means connected by a neural interface to a human. Only a few control signals are required to drive the hand to preshaped configurations and grasp forces. This is thanks to a simplified kinematics and self-adaptable actuation mechanism. The hand has 16 DoFs and 6 DC motors. Each finger has three DoFs loosely coupled into one flexion/extension DoM. The thumb has an additional motor driving its opposition to the palm. Five motors equipped with planetary gear heads (14:1) are remotely placed in the forearm (in a socket of $\approx$ 250 [cc]), while the motor dedicated to thumb opposition is embedded in the palm with a reduction ratio of 64:1. Finger joints are driven by nylon-coated steel tendons pulled by non-backdrivable lead screws, to preserve desired configurations with no power supplied. The same behavior is achieved in the thumb opposition driven

Name	Year	Joints	**Ind. DoFs**	Actuators	Self-contained	Size [mm]	Weight [Kg]
CyberHand [76]	2006	16	6	6	no	50[i]	1.8
Alpes Instruments hand [77]	2015	15	6	6	yes	n/a	0.62
InMoov hand [78]	2012	17	5	5	no	196 x 74	0.75[ii]
Harada hand [79]	2001	14	5	5	yes	201.5 x 92.3 x 33.5[iii]	0.369

[i] volume of the hand only, expressed in [cc] [ii] forearm included [iii] thumb base excluded

Table 1.8 – General characteristics of robotic hands with self-adaptable fingers. Further DoFs and actuation details are provided in Table A.4.

by a non-backdrivable worm-based gear transmission. The weight of the hand only is about 0.36 [Kg] while, the whole system, including the external motors and the artificial forearm, weighs 1.8 [Kg].

Alpes Instruments hand. The Alpes Instruments hand [77] embeds 6 DC electric motors in the palm to actuate a total of 15 joints. Fingers have three DoFs with no abduction/adduction motion to reduce the mechanical complexity of the hand and limit the weight. Each finger is driven according to a classical tendon-based adaptable transmission mechanism: a pulling tendon is routed up to the fingertip to flex the finger and tension springs are placed at each joint to stretch it back. The single DoM precludes in-hand manipulation since PIP and DIP joints are loosely coupled with the MCP joint. The thumb has three DoFs, one to move in opposition to the palm and two to flex and extend the phalanges. The first joint is bidirectionally actuated by one motor, while the reminders are loosely coupled and driven as the finger joints. Motor torques are amplified by planetary gears with 256:1 of reduction ratio. The hand length is designed on the base of the average size of male human hands. The total weight of the hand is 0.62 [Kg].

InMoov hand. InMoov [78] is the first open source humanoid robot (see Figure 1.23). It can be quickly built at home with off-the-shelf 3D printers. The robot is an affordable research platform [80] supported by a constantly increasing community. InMoov hand has 17 DoFs actuated by 5 servomotors placed in the forearm. Each finger is controlled by one servo DC motor and two pulling tendons routed up to the fingertip which provide loosely coupled finger joints. At present, InMoov hand performance are limited but impressive considering the manufacturing process. The price of the hand is estimated to 350 € while its weight is about 0.75 [Kg] with the forearm included.

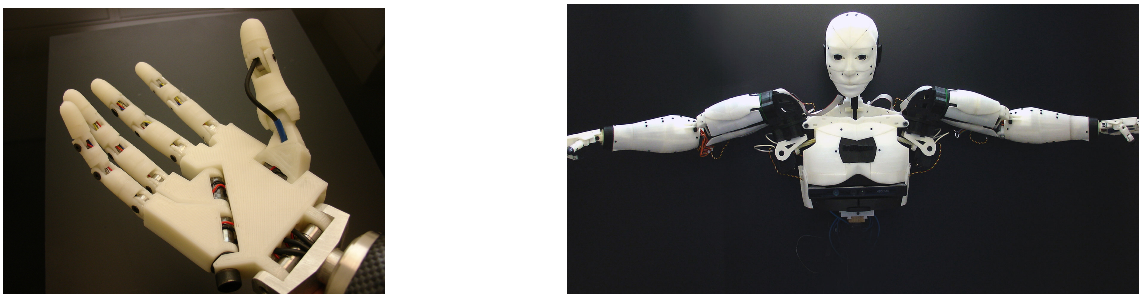

Figure 1.23 – The InMoov hand and 3D printed humanoid robot. Pictures taken from [78]

Harada hand. The Harada hand [79] is a 5 DoFs robotic hand produced by Harada Electric Industry. The hand (shown Figure 1.24) presents a simplified kinematic structure: 3-DoFs fingers and a 2-DoFs thumb. Fingers have no abduction/adduction motion and their joints are loosely coupled by a single tendon, which approximately bends each phalanx to equal angles in absence of contact. Flexing motion is driven by one motor while extension is provided by loaded springs placed at each joint. The thumb has two DoFs and it is simply composed of two links. Similarly to the fingers, it is driven by only one motor but, this time, the transmission mechanism is designed to span the opposing motion before bending the thumb toward the palm. This strongly reduces thumb dexterity and potential grasping performance.

(a) Picture taken from [79]. (b) Kinematic structure.

Figure 1.24 – The Harada hand.

1.2.2.3 Adaptive couplings within and among fingers

Adaptive couplings can be extended among fingers by properly distributing actuation forces within the palm. This is done through one or multiple differential mechanisms which connect two or more fingers to a common source. Differential mechanisms in five-fingered robotic hands have been already adopted in the 90's. In the Belgrade USC hand [81], for example, each pair of fingers is loosely coupled by a differential mechanism in the palm. This consists in a rocker arm designed so that if one finger enters in contact with the object the second one continues to move. The robotic hands presented hereafter (see Table 1.9) are characterized by different adaptive transmission mechanisms, some of which optimized to improve specific performance indexes or implement human grasp synergies.

iCub hand. The iCub hand [82] presents 19 joints driven by 9 DC motors. To save space in the hand, seven actuators are placed in the forearm while the remaining two are embedded in the palm. Finger joints are remotely controlled by stainless steel tendons routed in a closed-loop or open-ended fashion. Closed-loop tendons are routed up to the joints and back to the motor and provide bi-directional actuation. Open-ended tendons drive the joints in one direction while the return motion is offered by torsional springs. Each finger (thumb included) has four classical DoFs. The thumb has two independent DoFs at the RC opposition and flexion joints driven by closed-loop tendons, while it presents loosely coupled MCP and DIP joints driven by a common open-ended tendon. Abduction/adduction finger motions are coupled by a single closed-loop tendon with fixed transmission ratio. Flexion/extension motions are differently addressed according to the finger. Index and middle fingers present independent MCP flexing motions and adaptive couplings between DIP and PIP joints. On the contrary, the ring and little fingers have flexing joints loosely coupled by an open-ended tendon. These are pulled at the same time by a common linear slider which offers self-adaptability among fingers. The hand (shown in Figure 1.25) weighs 1.02 [Kg] included the wrist and the actuators in the forearm. The price of the hand and the arm is approximately 75000 € (updated on January 2014).

Name	Year	Joints	**Ind. DoFs**	Actuators	Self-contained	Size [mm]	Weight [Kg]
iCub hand [82]	2010	19	9	9	no	155 x 75 x 40	1.3
FRH-4 hand [83]	2008	11	8	8	yes	149 x 93 x n/a	0.216
IH2 Azzurra hand [84]	2014	11	5	5	yes	213 x 102 x 45	0.640
Smart hand [85]	2011	16	4	4	yes	n/a	0.530
Nazarbayev Universtiy (NU) hand [86]	2013	10	4	4	yes	193 x 92 x 96	0.574
15-dof underactuated hand [87]	2008	16	1	1	yes	n/a	0.4
Pisa/IIT SoftHand [88]	2014	19	1	1	yes	235 x 230[i] x 40	n/a
The Delft Cylinder Hand [89]	2015	13	1	1	yes	n/a	0.217

[i] from the thumb to the little finger tips

Table 1.9 – General characteristics of robotic hands with adaptive actuation mechanism among and within fingers. Further DoFs and actuation details are provided in Table A.5.

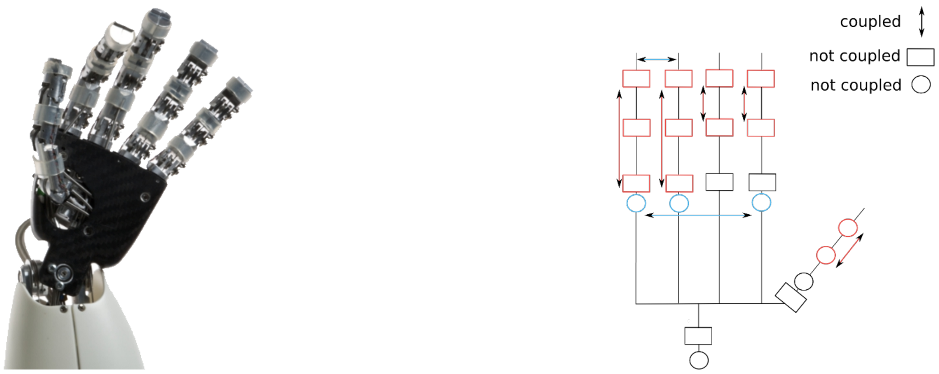

(a) Picture taken from [82].

(b) Kinematic structure.

Figure 1.25 – The iCub hand.

FRH-4 hand. The FRH-4 hand [83] is the last of the series of *Fluidhands* developed by Karlsruhe in the last two decades. The fluidhands are characterized by a human-like size and a very low weight, thanks to their custom made hydraulic actuation system. The pressure in the circuit is generated by a micro pump embedded in the palm and then distributed to the joint via ad-hoc valves optimized in size, flow rate, efficiency, liquid resistance and pressure stability. Hydraulic pressure at the joint is directly transformed to revolute motion through flexible fluidic actuators [90]. These consist in deformable chambers attached to the joints, which generate a flexing motion when inflated. By design they provide less torques as joint flexes, which imposes the augmentation of the pressure as bending angles increase. In the FRH-4 hand (shown in Figure 1.26) flexible fluidic actuators consist of bellows. Extension motion is provided by elastic elements, either rubber bands or tension springs. The same actuation structure can be driven by pneumatic actuation, however, hydraulic actuation reduces noise and requires less energy to be compressed. The first Fluidhand (2001), called the *New Ultralight Anthropomorphic hand* [91], is a prosthetic device composed of 16 joints and driven by 11 valves. Successive fluidhand versions, FRH II and III [92, 93] (2006-2009), reduce the number of joints and valves to eight and are designed to be mounted either on a human or robotic arm (e.g. on the ARMAR humanoid robot [94]). The FRH-4 hand differs from the previous versions in terms of kinematic structure. Its thumb does not have the opposition DoF (which hinders precise grasps in previous models), but it is directly mounted in opposition to the palm between the middle and index fingers. In addition, the hand differently distributes the 8 independent DoFs: two are dedicated to the thumb, index and middle fingers, one drives ring and little fingers and the last opens and closes the palm. The FRH-4 hand weighs, in total, 0.216 [Kg].

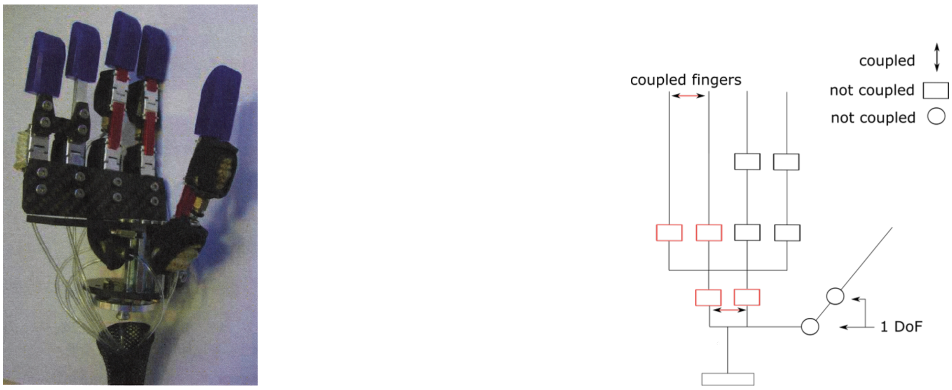

(a) Picture taken from [83]. (b) Kinematic structure.

Figure 1.26 – The FRH-4 hand.

SmartHand. The SmartHand [85] improves the CyberHand design by realizing a self-contained hand prosthesis. The hand preserves the tendon-based adaptive transmission mechanism adopted in the previous hand version, with pulley radii and torsion spring stiffness designed to imitate the natural finger closure in absence of contacts. The SmartHand (shown in Figure 1.27) fits four brushed DC motors within the palm to drive the five fingers [95]. One motor is dedicated to the thumb opposition while another one is employed for the thumb flexion/extension. The third motor drives the index flexion/extension while the last controls middle, ring and little fingers via a differential mechanism placed inside the palm. Thumb and index flexing motions are driven by small-sized Faulhaber Minimotors (model 1319) with planetary gear heads (491:1) and non-backdrivable transmissions, realized through miniaturized mechanisms based on wedge phenomena [96]. Thumb opposability is bi-directionally actuated by another Faulhaber minimotor (model 1016) with a reduction ratio of 1024:1, which ensures non-backdrivability by itself. The differential mechanism is composed of a lead screw and three compression springs. Each spring is connected to one finger by means of its flexion tendon. If no contact occurs, finger motions are synchronized. As soon as one finger enters in contact with the object the associated spring starts to compress, allowing the other fingers to continue their motion. As the lead screw (linear slider) keeps moving the compressed spring increasingly behaves as a rigid link, transmitting the force from the slider to the finger. The lead screw is controlled by a Faulhaber minimotor (model 1331) with a gearbox of 8:1 of reduction ratio. The hand is highly equipped with 40 redundant proprioceptive sensors (position, tactile/pressure and force) to provide automatic grasp control and sensory feedback to amputees. The hand weighs 0.530 [Kg] and it has a closing time of 1.5 [s]. A simplified version of this hand, called IH2 Azzurra, is commercially produced by Prensilia SRL [84]. This presents no DIP joints at the digits, embeds 5 motors and weighs 0.64 [Kg].

Figure 1.27 – The SmartHand. Pictures taken from [85].

Nazarbayev Universtiy (NU) hand. The Nazarbayev Universtiy hand [86] is a 3D printed hand designed for industrial and service robots. It has 10 DoFs, two per finger (thumb included), actuated by four servomotors embedded in the palm. Motor torques are transmitted to the fingers via tendons routed up to the fingertips except for the thumb abduction/adduction axis which is directly actuated in both directions. Flexing motions of thumb and index are driven by two independent motors, while the last three digits are actuated by one motor. Extension is provided by torsional springs. Middle, ring and little fingers are loosely coupled by series elastic elements placed at the end of their tendons. These offers limited force distribution (adaptability) among fingers while grasping an object [97]. The hand (shown in Figure 1.28) is easy and cheap to build, as it uses off-the-shelf servomotors and is fully 3D printed. To ease grasp tasks it embeds unconventional (for a five-fingered robotic hand) sensors which increase its weight and size: a LIDAR sensor, a digital camera and a non-contact temperature sensor used for object detection, recognition and pose estimation. The mass of the hand is 0.574 [Kg] including motors and sensor modules.

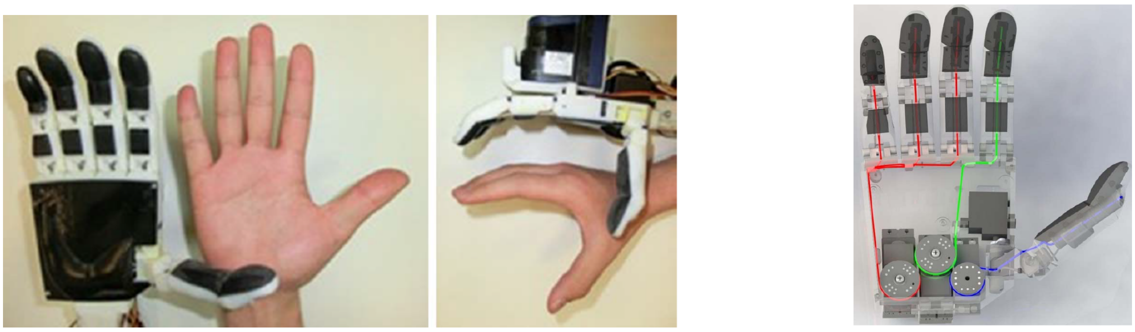

Figure 1.28 – The NU hand. Pictures taken from [86].

15-dof underactuated hand. The 15-dof underactuated hand [87] is the first five-fingered robotic hand designed to explore extreme under-actuation, driving all DoFs with only one motor. The hand (shown in Figure 1.29) is rapid prototyped (except some components) and actuated by a human (no motors adopted) to test the concept. Each finger has three DoFs loosely coupled by one tendon (kite cable) routed up to the fingertip. Fingers flex pulling the tendon and extend via torsion springs placed at the joint when the tendon is relaxed. The stretched configuration is achieved once joint limits are attained. Spring stiffnesses are chosen to limit their opposition to the actuation force and to be sufficiently stiff to open the finger. The thumb has one more DoF (for a total of 16 joints in the hand) to perform adduction/abduction motion. This is not actuated and can be locked in any arbitrary configuration within its RoM. The position of the tendon guides are optimized according to three performance indexes. The first improves grasp robustness encouraging net forces on the object to point toward the palm and the thumb. The second is used to uniformly distribute contact forces among phalanges to avoid high local pressures which might damage the grasped object. The third minimizes the probability of object ejection (grasp failure) [75] to occur. In the palm, a differential mechanism is implemented as a cascade of *sliding pulleys* stages which distribute the input force among fingers. Each differential stage equally splits the input force to the outputs, finally providing 50% of the actuation forces to the thumb and 12.5% to each digit. The first version of the 15-dof underactuated hand is affected by high friction forces which hinder the correct force distribution among fingers. This is mainly due to numerous cable redirections required to fit the differential mechanism within the hand. In order to reduce force losses, the second version eliminates the first stage, synchronizing the closure of the thumb and the fingers. The weight of the hand is approximately 0.4 [Kg].

Figure 1.29 – The 15-DoF underactuated hand. Pictures taken from [87].

Pisa/IIT SoftHand. The Pisa/IIT SoftHand [88] is a robotic hand designed to be robust, safe, easy to control and to effectively grasp a large variety of objects. Its self-contained structure is simple, lightweight and cheap (shown in Figure 1.30). One motor drives its 19 DoFs; four per finger and three for the thumb. Robustness and safety are inspired by *soft-robotics* approaches. The hand can safely interact with people, and bear strong impacts and joint overextension thanks to its unconventional joint design. Its grasp versatility is ensured by an adaptive transmission mechanism which implements the first soft synergy proposed by Santello *et al.* [40]. The transmission mechanism is composed of several pulleys and a closed-loop Dyneema® cable routed through all joints. When the last is pulled, fingers flex and adduct, while elastic elements restore fingers to a stretched configuration at rest. Finger joints for flexion/extension implement rolling contacts compliant in flexion and stiff in traction, inspired by Hillberry joints [98]. These consist of pairs of cylinders rolling at contact and an elastomer (polihuretane Shore 88 A) fixed on the dorsal side. The pre-tension of the elastomer and the joint profile are chosen to create an attractive equilibrium at rest. Joints present teeth to improve tangential load support and lateral edges on both sides to fit in predisposed sockets on adjacent phalanges. The last allows the autonomous recovery of its working configuration after disarticulations or violent impacts. The geometric parameters of the adaptive transmission mechanism, namely pulley radii and spring stiffnesses, are numerically determined to replicate the desired synergy. Thanks to its design, the hand is capable of achieving whole hand grasps and tip grasps with only one actuation source: a MAXON 6W RE-max21 with 84:1 of reduction ratio.

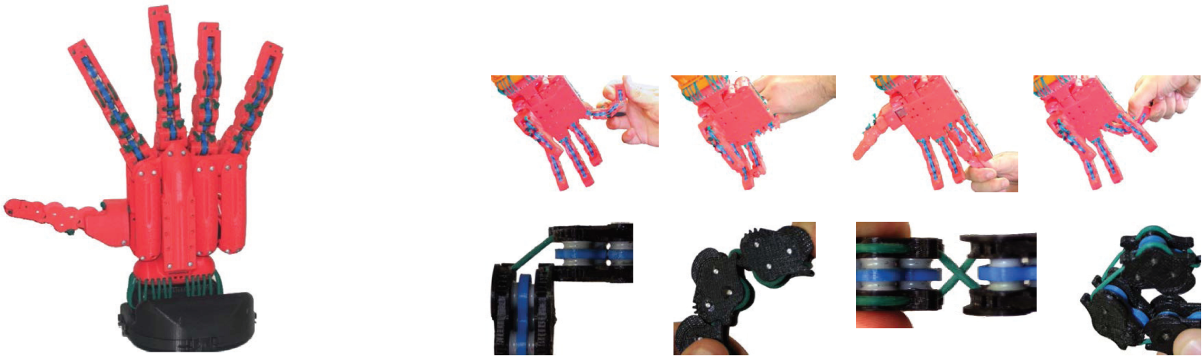

Figure 1.30 – The Pisa/IIT SoftHand. Pictures taken from [88].

Delft Cylinder Hand. The Delft Cylinder Hand [89] is a lightweight prosthetic hand designed to perform adaptive grasps by mean of one actuation source. Differently from the last two hands previously presented, self-adaptation within and among fingers is provided by a (body-controlled) hydraulic system (see Figure 1.31). The last is composed of one main cylinder and seven miniature hydraulic slave cylinders. These are placed in the fingers and in the palm, close to the joints they actuate. The main cylinder is directly controlled by the amputee through a shoulder harness. By pulling the harness, the user drives the main cylinder which, in turns, extends the miniature cylinders to close the fingers. The pressure among master and slave cylinders is uniform at any time instant. This allows the amputee to have force feedbacks about the grip strength and the object compliance while grasping. Since the main cylinder can be only controlled by pulling, finger extension is provided by springs and the stretched configuration by the joint limits. The Delft Cylinder Hand has 13 DoFs which allow precision and power grasps. Seven DoFs are loosely coupled by the slave cylinders which drive MCP flexing motion of all fingers plus the PIP flexing motion of index, middle and ring fingers. The PIP joint of the little finger is rigidly coupled by a four-bar linkage to the MCP joint. For simplicity the hand replaces movable DIP joints with rigid links bent of 15°. The thumb has no flexing motion and its only DoF is not controlled. To change its opposition the user has to manually adjust its orientation. Fingers have limited abduction/adduction capabilities (±8°) provided by passive elements at the CMC joints. The total weight of the hand is about 0.217 [kg], including the cosmetic glove.

(a) The Delft Cylinder Hand structure. In the picture: S(x) are the slave cylinders, OS are the opening springs, H are the hoses which connect the hydraulic cylinders and BL is the four-bar linkage in the little finger.

(b) Shoulder harness to actuate the prosthetic hand.

Figure 1.31 – The Delft Cylinder Hand structure and actuation. Pictures taken from [89].

1.2.2.4 Hybrid designs

Some robotic hands adopt more than one actuation system to differently actuate a desired set of joints. These are called *hybrid*, since they combine the advantages of distinct actuation mechanisms in one design. Their kinematic structure is arranged through the coordination and interaction of the embedded actuation systems. This can change the hand behavior according to the task to perform [99] [100]. Hereafter, three hybrid designs (see Table 1.10) are presented.

Name	Year	Joints	Ind. DoFs	Actuators	Self-contained	Size [mm]	Weight [Kg]
TUAT/Karlsruhe hand [101]	2013	24	6	6	yes	175 x 110 x n/a	0.49
			1	1			
RoboRay hand [102]	2014	20	12	12	no	346[i] x 80[ii] x 83[iii]	1.59
Crawford hand [103]	2010	20	10	10	yes	n/a	n/a
			5	5			

[i] hand plus forearm length [ii] hand width [iii] forearm max thickness, the hand is 45 [mm] thick

Table 1.10 – General characteristics of robotic hands with hybrid kinematics.

TUAT/Karlsruhe Humanoid Hand. The TUAT/Karlsruhe Humanoid Hand [104] is conceived to be mounted on artificial arms and amputees. It is designed to grasp everyday objects and tools (see Figure 1.32a) via automatic finger and palm adaptation. The hand provides stable grasps thanks to the differential mechanism developed in its first version [101]. Each finger is driven by a linkage-based transmission mechanism where PIP and DIP are rigidly coupled. As the proximal phalanx enters in contact with the object, a pulling rod transmits the force from the proximal to middle and distal phalanges. This is done through the rotation of a link-plate at the base of the proximal phalanx. The differential mechanism in the palm, called a harmonic linkage mechanism (shown in Figure 1.32b), distributes the main servomotor force to the fingers. It is composed of free-to-move interconnected floating plates, except the one driving the thumb which is only free to rotate. As the input rod of the differential mechanism is pulled, all plates move to preserve force balance on every link. This allows the motion of each finger until they either enter into contact with the object or reach their mechanical limit. Once the servomotor releases the input rod, springs restore the initial configuration of the fingers. The TUAT/Karlsruhe Humanoid Hand is controlled according to two working modes: the *auto operate mode* and the *manual operate mode*. The first drives all fingers at once via one main servomotor, while the second controls each fingers independently by means of six servomotors (called sub servomotors). All actuators are embedded in the palm. Each sub servomotor drives the link-plate at the base of the proximal phalanx through a cable. The two modes change the kinematic structure of the hand and the thumb, while they preserve the kinematic structure of each finger. The thumb has 5 DoFs, two of which actuated. Abduction/adduction of the RC joint is actuated in both directions by one sub servomotor placed in the dorsal size of the palm. The adaptive flexion motion of the RC, MCP and DIP joints plus the abduction of the MPC joint are driven by a second servomotor, placed in the dorsal side of the palm. In brief, the hand is capable of grasping objects with only one servomotor. Six more are added to pre-shape and achieve different grasp configurations which would be otherwise unreachable. The weight of the hand is 0.49 [Kg], while its size is based on a 27 year old Japanese male who is 1.65 [m] tall.

(a) TUAT/Karlsruhe Humanoid Hand.

(b) Harmonic linkage mechanism: a linkage-based differential mechanism adopted in the palm.

Figure 1.32 – The TUAT/Karlsruhe Humanoid Hand. Pictures taken from [104].

RoboRay hand. RoboRay is a service humanoid robot [102] conceived by Samsung Electronics. The robot has two five-fingered hands (shown in Figure 1.33), with 12 DoFs each (wrist excluded), designed to perform precise manipulation and versatile grasps. To achieve both functions, hands are actuated by two distinct actuation systems: one based on seven high torque motors (called grasp motors) placed in the forearm and, the other, based on five small-sized motors (called pose motors) embedded in the palm. The first actuation system is inspired by the mechanical intelligence and grasping versatility of self-adaptable hands, while, the second one is encouraged by in-hand manipulation capabilities of highly actuated robotic hands. Each hand is composed of 4-DoFs modular fingers, thumb included. The first three digits are driven by three actuators each and can perform in-hand manipulation tasks. PIP joints are loosely coupled to the flexing motion of MCP joints by means of a grasp-motor-controlled tendon, while 2-DoFs MCP joints are driven by two independent pose motors. PIP and DIP joints are coupled with a fixed transmission ratio by a 8-shaped tendon. The synchronization between flexing actuators characterizes the finger behavior. If the pose motor is turned off while the grasp motor is active, the finger undergoes an adaptive grasp. If the grasp motor is fixed and the pose is actuated, the configuration of the fingertip is precisely adjusted. Ring and little fingers are controlled by three high torque motors to provide only self-adaptation during grasping. One DoF per finger drives flexion and extension motions, while the third DoF provides adduction/abduction motion to both fingers. Finger joints are bi-directionally actuated by closed-loop steel tendons directly connected to linear ball screws placed at the motor outputs. Large high torque motors, rather than small motors with high reductions, are chosen to preserve speed and backdrivability. The last allows the sensing of external forces with no additional sensors but through motor current measurements. Pose motors are 1.8 W DC motors and 12 W BLDC motors. Grasp motors are 8 W BLDC motors. Reduction ratios are 47:1 for abduction/adduction, 57:1 for flexion/extension at MCP joints and 82:1 at the PIP joints. The hand weighs 1.59 [Kg] including the forearm which embeds the electronic boards plus 9 motors: 7 for the hand and 2 for the wrist.

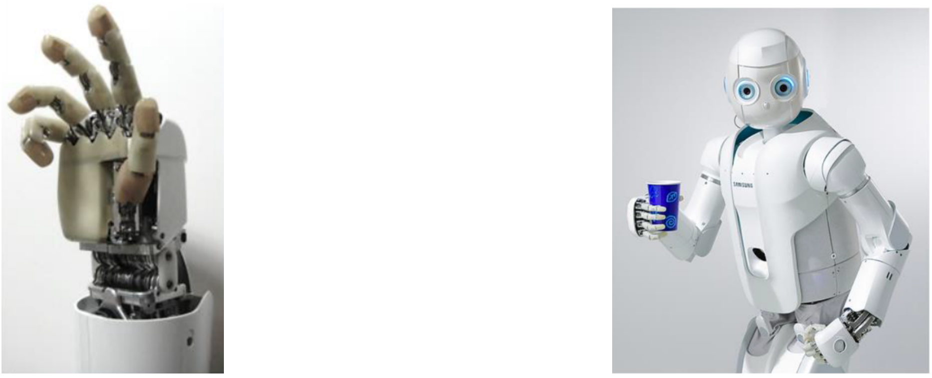

Figure 1.33 – RoboRay hand and humanoid robot. Pictures taken from [102].

Crawford hand. The Crawford hand [103] is an EMG-driven prosthetic hand characterized by two actuation systems of different nature. Similarly to the RoboRay hand, the actuation systems are intended to provide complementary functions. In this case, however, actuation systems are not coordinated to provide precise finger motions but to mimic the behavior of primary finger flexor muscles. Indeed, one actuation system ensures fine manipulation capabilities, while the other provides high forces to secure the grasp. The first is composed of small and fast electromagnetic motors which nearly fully actuate finger kinematic structures. The second consists of tendons connected to quiet, lightweight and slow Shape Memory Alloy (SMA) which allow finger self-adaptation. Each finger, thumb included, is a 4-DoFs serial chain where the last two joints are constantly coupled by a 8-shaped tendon. The electromagnetic motors are embedded in the palm hand proximal phalanges and are equally distributed among fingers. In each finger MCP and PIP flexing motions are actuated by two DC motors while, in the thumb, two DC motors control the RC opposition and MCP flexing motion (coupled with the DIP). Finger abduction/adduction DoFs are passive, while the RC flexing motion of the thumb is only actuated by the self-adaptable actuation system. The last adopts one tendon per finger to loosely couple joint flexing motions: MCP and PIP joints of each finger and RC and MCP joints of the thumb. Coexistence between the two systems is guaranteed by spring loaded cams. Information about the complete hand is not disclosed in [103], nevertheless, finger and thumb prototypes (shown in Figure 1.34) are presented and tested.

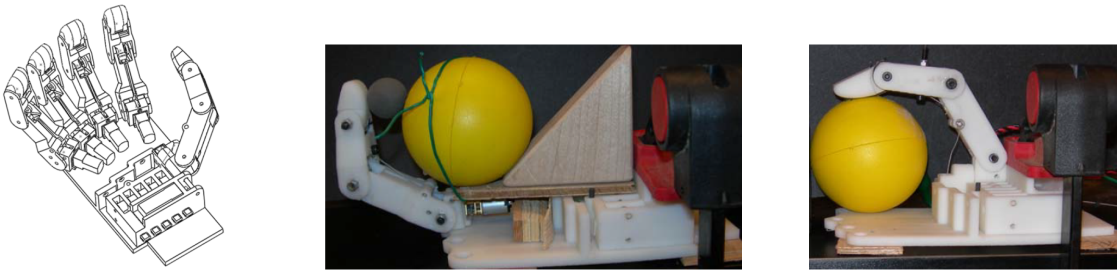

Figure 1.34 – The Crawford hand structure and finger prototypes. Pictures taken from [103].

1.3 Biologically-inspired design

The human hand is an astonishingly advanced mechanism which is too complicated to be faithfully replicated. It is the most dexterous part of our body and it is thanks to it that a great part of our physical interactions with the environment is ensured. Most five-fingered robotic hands aim to mimic its appearance and functional capabilities. Two main criteria can be used to describe human-likeness of robotic hands: *anthropomorphism* and *dexterity*. Both are often used by robotic hand designers, but with no clear reference to specific characteristics of the hand. Biagiotti *et. al.* [105] defines the difference and the meaning of these two concepts. Anthropomorphism is the capability to resemble the human hand in terms of shape, size, consistency (e.g. number of fingers) and other general aspects (e.g. fingertip shape). It is a qualitative consideration of perceivable properties which does not consider functional capabilities. Robotic hands need to be anthropomorphic to operate in every-day environments and in contact with people, for example to enhance acceptance or engage in non-verbal communication. Dexterity is the capability to provide functional expertises to the artifact (grasping and in-hand manipulation), which level differs according to the complexity of the achieved tasks. It is not trivial to measure, since it depends on how control algorithms exploit the mechanical structure and the sensory apparatus of the robotic hand. A rough distinction about the potential dexterity of an artifact in relation to its mechanical structure can be made - hands limited in grasping, such as ones which present simplified kinematics and a reduced number of actuators, and hands capable of performing some in-hand manipulation. These two can be further divided into higher or lower degrees of dexterity whether single fingertips and the whole hand can be involved in the task. Figure 1.35 shows how anthropomorphism and mechanical dexterity can be weighted to compare robotic hands on the basis of human-likeness [105].

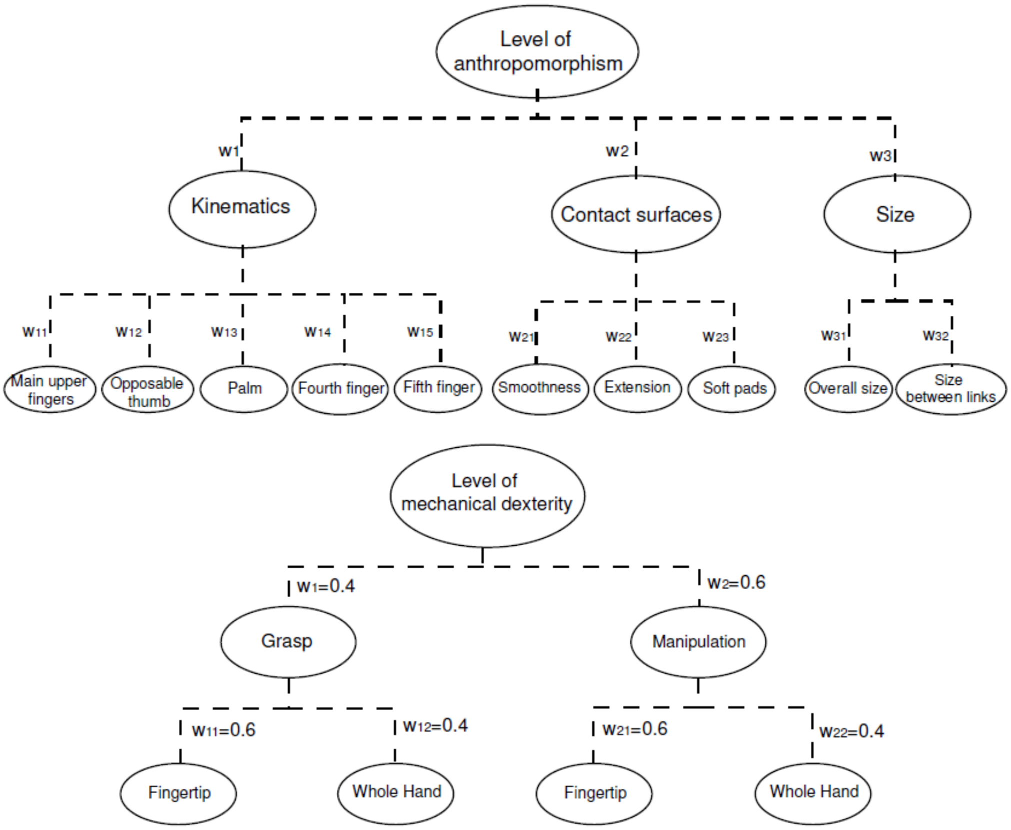

Figure 1.35 – Anthropomorphism and dexterity. Two criteria to determine human-likeness of robotic hands. Picture taken from [105].

Many techniques are used to model human hand kinematics, namely the number DoFs and the placement of their center of rotations. As presented in Section 1.1.1.4, some analyze the upper limbs through direct [9] or indirect measurement methods, such as motion capture [106], computed tomography scans [107] and radiography [108]. Others estimate its kinematic features by means of optimization algorithms [109], learning techniques [14], empirical observations and results present in literature [7, 18]. From these, robotic hands are designed. The most accurate robotic hand ever built is the anatomically-correct testbed (ACT) [110]. Its structure (shown in Figure 1.36) is machined with the same shape and mass of human bones, and its joints are designed to preserve the same DoFs and passive stiffness of the human ones. The ACT is conceived to deeply investigate the human hand structure, function and control for medical purposes. Indeed, its complexity hinders its practical use in robotics. In general, simplified joint structures and link shapes are commonly chosen by robotic hand designers. Furthermore, the number of independent DoFs is reduced due to technological limits (hardware and software) and mechanical constraints, not necessarily at the cost of a high level of anthropomorphism [111].

Each human hand has its own peculiarities, and yet, its functional capabilities do not significantly change from the others. This implies that different link lengths, width and joint placements do not greatly alter the hand performance. As a consequence, no true optimal design exists for the construction of a human-like robotic hand [11]. Nevertheless, an appropriate model has to be realized in order to provide important functional requirements, such as grasping objects and manipulating them. These abilities require high interaction among fingers, in particular between each finger and the thumb. Indeed, 40%

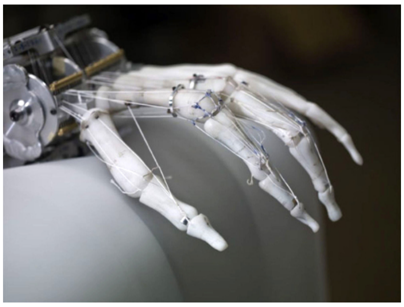

Figure 1.36 – The anatomically-correct testbed. Picture taken from [110].

of human hand functionalities are provided by the thumb [112]. Therefore, it is essential to properly design the thumb kinematics according to the opposing finger geometries and kinematics. The problem of thumb placement on robotic hands has already been addressed in literature. Grebenstein *et al.* [11] developed cardboard prototypes (Figure 1.37) to incrementally refine the hand kinematics in order to obtain thumb functionalities and hand aesthetics similar to the human one. Wang *et al.* [113] approached the problem using a numerical method based on the Euler rotation theorem. The thumb placement was computed passing from a lateral posture to an opposing one in order to ensure basic grasping modes.

Figure 1.37 – Cardboard prototypes. Picture taken from [11].

1.4 Thesis specifications

The objective of this thesis is to design and control a five-fingered robotic hand for *Romeo*, a humanoid robot 1.4 [m] tall produced by Aldebaran - SoftBank Group.
The hand has to be conceived according to the following mechanical specifications:

- respect human hand proportions and size;
- self-contained;
- weigh less than 600 [g];
- safe;
- back-drivable;
- open/close in less than 1[s];
- low-cost;
- robust;
- energy-efficient;
- preserve the same actuation technology adopted in the rest of the body;
- silent.

The size must respect the proportions of an equally tall child to enhance human acceptance and harmony with the rest of the body. The hand has to embed most of its actuation and control components in the

palm to ease integration on the robot arm. It has to be lightweight (less than 600 [g]) to reduce its impact on the robot dynamics, to be easy to carry and limit potential modifications to the arm actuation. Most of all, the hand must be safe to operate in our surroundings and to cooperate with people. Backdrivability has to be provided to ensure external force detection through current readings, so that no force and touch sensors are required. Fast movements are desirable for dynamic interactions. For that, open/close motion is required to take less than 1 [s]. To limit the overall price of the humanoid robot, the cost of production must be reasonable. The actuation system has to be robust against undesired mechanical stress (e.g. children playing with fingers). In addition, it has to be energy efficient to enhance robot autonomy. Its technology must be coherent with that already present in the rest of the body: electromagnetic actuators powered by an on-board battery. Finally, the hand must be silent to offer continuous operation while preserving user comfort, avoiding annoyance which might discourage its use and the use of the robot itself. The noise produced by actuators and transmission mechanisms is often ignored in most hand designs and, indeed, it is an irrelevant constraint for industrial manipulators and artificial limbs working in isolated environments. However, it is a significant factor for automata operating in our every-day life.
From the perspective of functional capabilities the hand has to:

- perform a chosen set of expressive hand gestures;
- grasp small and lightweight objects (no in-hand manipulation required).

To improve empathy and feeling between humans and robots, communication should rely not only on voice but also on body motions and gestures. For this reason, the hand has to be designed to express emotions and feelings and strengthen the communication through expressive hand gestures. Among them some symbolic, deictic and iconic (see Section 1.1.2.1) gestures are required: thumb up, OK, closed fist, cupped hand ("give me" gesture), "come here" movement, "stop" (with the hand at the level of the throat), count up to 5 in two different ways, point at and mimic the shape of a heart, a telephone and someone talking ("blah-blah", often used to indicate someone speaking too much). The hand is also demanded to shake and handle the hand of a man. These are not considered as grasping capabilities since the action is not performed on an object. Only one movement which might be considered more an adapter rather than a gesture is demanded: twiddling thumbs. This normally express boredom and it can be used by the robot to show its idle state, wishing for new tasks to perform. Figures 1.38 and 1.39 show the aforementioned gestures.

Figure 1.38 – Required hand gestures.

Gestures are fundamental to enhance empathy but social robots are not only supposed to engage and encourage conversations. If endowed with hands they are expected to provide some service by grasping. A minimum set of common small and lightweight objects it is demanded to be grasped (Figure 1.40): full beverage cans, small bottles (33 [cl]), glasses, pencils and pens, smartphones. In addition, the hand

Figure 1.39 – Counting up to five.

has to be capable of switching the light and holding a box in cooperation with another hand.

Figure 1.40 – Example of required objects to grasp and tasks to perform.

The relevance of each functional capability is shown in Figure 1.41.

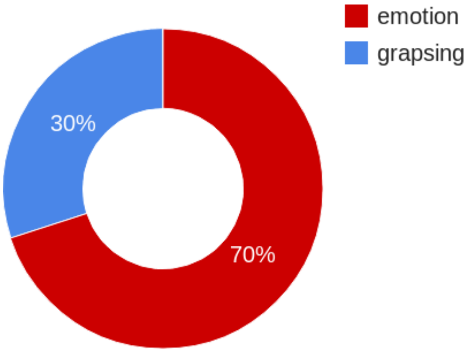

Figure 1.41 – Robotic hand functional requirements.

1.5 Positioning

The main challenge in designing a robotic hand with the requirements and constraints presented in Section 1.4 consists in finding the best trade-off between anthropomorphism, dexterity and mechanical feasibility. Robotic hands presented in Section 1.2 can be divided between self-contained and indivisible hand-arm systems. The first are independent artifacts which embed all required mechanical and control components within the palm and the fingers. The second are complete devices which place part of its actuation elements in the forearm, taking advantage of the additional space available. Highly actuated robotic hand present different level of dexterity and anthropomorphism. This generally depends on the type of actuation adopted and its facility to be integrated in narrow spaces. Self-contained hands normally embed motors of reduced sizes which provide weak forces to the fingers. On the contrary, hand-arm systems can adopt larger and stronger actuators in the forearm, but they often result in bulky designs and require transmission mechanisms through the wrist. Highly actuated robotic hands offer high manipulation capabilities, however, they are *heavy and expensive*. Only two of them present weights under 1 [Kg] regardless of the number of independent DoFs: the SBC and the Sonoda and Golder hands. The SBC hand is remarkably light, considered that it is driven by 32 actuators, thanks to its inherently lightweight actuators (SMA). However, these have low time responses and require high currents (if heated-up by Joule's effect) and cooling systems. Differently, the Sonoda and Golder hand use lightweight transmission mechanisms (twisted strings). These are designed to offer high reduction ratios in order to embed small motors within the palm and the fingers. However, this comes with the cost of slower motions and opposing springs to provide complementary motions. This, because the number of actuators is bounded to the number of independent DoFs to limit the weight and because twisted strings only drive by pulling.

Robotic hands with a reduced number of independent DoFs (< 10) and, consequently, of actuators have lower dexterity (generally no in-hand manipulation capabilities). Nevertheless, they are smaller, lighter and less expensive with respect to highly actuated hands. The lightest ones are based on hydraulic actuation systems. Regardless of the fact that they are characterized by high power-to-weight ratios, they are prone to leakage and often require noisy pumps. Robotic hands which have less than six independent DoFs generally provide good grasping capabilities, mostly based on adaptive actuation mechanisms, but have low thumb dexterity and insufficient gesture-based communication abilities. In fact, to the author's opinion, at least 7 independent DoFs, one DoF per finger and a minimum of two DoFs for the thumb, are necessary to perform the set of required gestures. The ones with at least 6 independent DoFs are either heavier than 0.6 [Kg] or adopt high reduction ratios. Gearboxes with high reduction ratios are often employed to fight against restoring forces within fingers (e.g. torsion springs). They limit fast finger motions, prevent backdrivability and hinder sensor-less contact detection (to ensure safety through active compliance). Hybrid robotic hands get closer to our needs, even though none of them satisfy all requirements. RoboRay hand is heavy. Crawford prosthetic design provides no info about final weight and size of the prototype, but it embeds a high number of actuators which would probably lead to a non-negligible payload. TUAT/Karlsruhe hand is exclusively conceived to perform self-adaptable grasps. Indeed, it presents a thumb with low dexterity (2 ind. DoFs) and its fingers are designed to autonomously adapt in case of contact during motion. Figure 1.42 shows the weights of the robotic hands presented in the Section 1.2 in function of their number of independent DoFs.

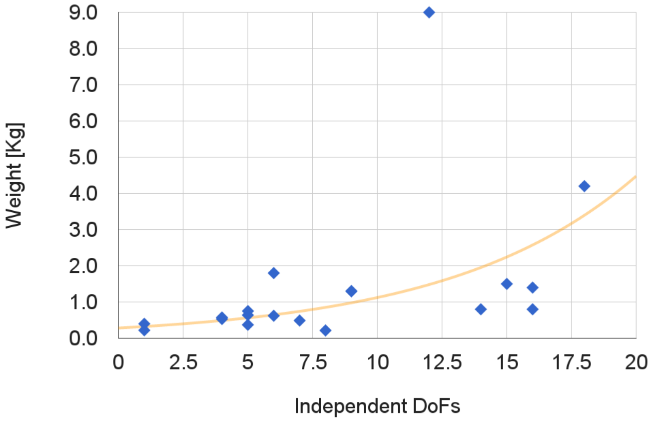

Figure 1.42 – Robotic hand weights with respect to their number of independent DoFs.

This thesis presents the design and control of a novel hybrid robotic hand for a humanoid robot 1.4 [m] tall. The hand is designed to be anthropomorphic by preserving some kinematic aspects of the human hand and by respecting its size and proportions. The hand kinematic is simplified to reduce the number of independent DoFs and actuators, so to minimize size, weight and cost. It is designed to guarantee gesture and grasping capabilities and optimized to preserve high thumb opposability. Two actuation systems are embedded in the hand. The first, called *e-motion*, grants gesture capabilities but lacks in adequate grasping forces. It is characterized by very low reduction ratios which reduce volume, weight, noise and cost. In addition, they encourage fast finger motions, backdrivability and sensor-less force feedback. The second actuation system, called *grasp*, provides the grasp force to the fingertips and implements self-adaptability among fingers and phalanges. In brief, the hand can perform the required gestures with the first actuation system and grasp objects of different shapes with the second one. This, by changing its kinematic structure when needed. Both systems preserve the actuation technology adopted in the rest of the body, and their electromechanical components are nearly full-embedded within the palm and the fingers - only the electronic boards and the grasp actuator are located in the forearm. Actuation coexistence is ensured by elastic transmissions designed to oppose the grasp power only when object adaptation occurs. These consume less energy than standard self-adaptable actuation mechanisms and improve finger robustness by protecting the mechanics from undesired stress. The hand offers different degrees of safety. Impedance control is implemented to provide safe interaction during natural motions while, during grasp, actuation force is limited by current.

2

Hand kinematics and geometry

This chapter defines the geometric and kinematic models of the robotic hand to obtain an anthropomorphic and dexterous design. The simplified kinematics models the DoFs as the minimum number sufficient to perform the required gestures and simple grasps. This is done to obtain a compact and lightweight hand able to reproduce basic human hand capabilities. Artificial finger lengths, widths and base configurations are established according to human-inspired heuristic methods. Particular focus is given to the thumb base, placed to enhance hand dexterity and thumb opposability. A numerical method is implemented to find the best thumb base configuration which satisfies the surgical tests known as "Kapandji test" and preserves the most equilibrated interaction with the opposite fingers.

2.1 Kinematic definition

To have a light and small hand the number of independent DoFs has to be as small as possible. A reduced number of independent DoFs means minor dexterity but, if the hand kinematic and actuation system are properly designed, fundamental functional capabilities can still be preserved with a limited number of actuators. As shown in Section 1.2, effective grasps can be achieved by means of an adaptable transmission mechanisms within the fingers, which provides autonomous adaptation to various object shapes. These loosely couple finger joints and allow to reduce the number of actuators. Thanks to differential mechanisms in the palm, self-adaptation can be extended among fingers and the number of actuators fixed to one. Another approach to reduce the number of actuators and still preserve good grasping capabilities consists in coupling finger joints to replicate a set of postural synergies (see Section 1.1.2.3). These mimic human hand reach-to-grasp motions and allow the control of the grasping force by means of a reduced set of inputs. These methods can be adopted together to implement self-adaptability and human-inspired grasp in the same design. In brief, grasp dexterity (distinguished between fingertip and whole hand) depends on the number of independent DoFs while its performance relies on the design of the actuation system. Indeed good grasp performance can be obtained with only one actuator. On the contrary, hand gestures requires a minimal set of independent DoFs which can be reduced only to a certain extent. Since in this context the main objective is to provide basic non-verbal communication, the kinematic model is primarily designed to satisfy the set of hand gestures presented in Section 1.4.

2.1.1 DoFs selection

The kinematic model of the robotic hand is determined starting from the highly articulated human hand kinematic structure (presented in Section 1.1.1). At first, all joints are considered coupled. Then, for each gesture, joint couplings are incrementally relaxed to minimally increase the number of actuators. Note that since specific configurations have to be attained, couplings are exclusively fixed to arbitrary constant ratios. Each gesture is evaluated starting from the open flat configuration (default position), with fingers slightly spread and the MCP joints not parallel, but converging to a common point below the wrist during flexion. Figure 2.1 shows the relaxation process on six randomly selected gestures. To perform the whole required gesture set, twelve independent DoFs are needed (see Figure 2.2): two per finger, one for a common abduction/adduction motion and three for the Thumb, one of which driving the CMC joint at the base of the little finger.

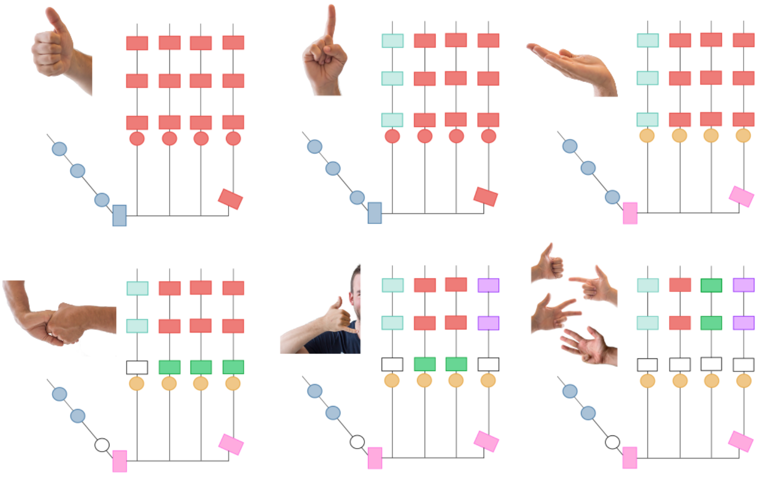

Figure 2.1 – Incremental joint coupling relaxation to minimally increase the number of independent DoFs. Each color refers to a single DoF.

Nevertheless, this number is still too high to conceive a self-contained, small-sized and lightweight robotic hand. Consequently, the number of joints is reduced to find an acceptable compromise between gestures capabilities and a specification-compliant mechanical structure. At this stage, gestures are classified according to the feelings they trigger: low priority is given to gestures inducing negative sensations, while, middle and high priorities are associated to the ones inspiring neutral and positive feelings respectively. Required gestures are divided as follows:

- *Positive*: thumb-up, OK, cupped hand, "come here" movement, point at and mimic the shape of a heart, handling and shaking a hand;
- *Neutral*: twiddling thumbs, counting and "calling" (hand shaped like a phone);

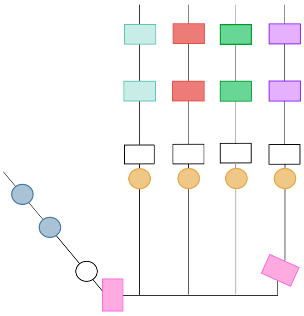

Figure 2.2 – 12-DoFs kinematic model. Each color refers to a single DoF.

- *Negative*: "blah-blah" movement, "stop" gesture (with the hand at the level of the throat), shouting and closed fist.

The importance of each joint is weighted according to its contribution to high, middle and low priority gestures. The ones mostly involved in low priority gestures and that slightly affect high and middle priority gestures are removed. Three main simplifications are adopted. The first couples MCP flexing motions to PIP and DIP joints. This impedes the hand to perform the "stop" (with the hand at the level of the throat) and the "blah-blah" gestures and imposes less natural hand-shakes and hand handling. The second eliminates finger abduction/adduction axes of MCP joints, imposing fixed finger abduction angles. Parallel fingers cannot be preserved during cupped hand, "come-here" and shouting gestures but their human-likeness can be improved by making fingers converge while flexing. The last simplification removes the CMC joint of the little finger in the palm. This affect the cupping motion and the thumb opposability to the little finger, which can still be ensured by properly placing the thumb base. Figure 2.3 shows the final 7-DoFs hand kinematic model composed of 1-DoF fingers (which can only flex and extend) and a 3-DoFs thumb.

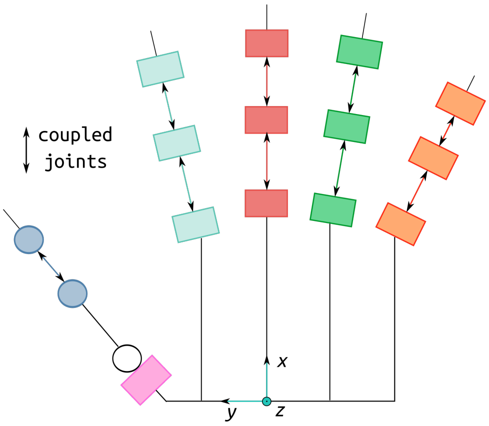

Figure 2.3 – 7-DoFs kinematic model. Each color refers to a single DoF. The dorsal side of the hand is shown.

2.1.2 Kinematic model

The hand is modeled as a tree structured robot. Each finger is considered as an independent serial chain with a common root. Reference frames are placed at each joint to characterize the kinematic model. Figure 2.4 shows their placements and orientations on a simplified 2D perspective. The hand Direct Geometric Model (DGM) is computed by means of the modified DH parameters [114] (γ_j, b_j, α_j, d_j, θ_j and r_j). These allow the description of complex kinematic chains (tree or closed loop robots) via transformation matrices (${}^{a_j}T_j$) between two consecutive reference frames (a_j, j) defined as follows:

$$ {}^{a_j}\boldsymbol{T}_j = \text{Rot}(\boldsymbol{z}, \gamma_j)\ \text{Transl}(\boldsymbol{z}, b_j)\ \text{Rot}(\boldsymbol{x}, \alpha_j)\ \text{Transl}(\boldsymbol{x}, d_j)\ \text{Rot}(\boldsymbol{z}, \theta_j)\ \text{Transl}(\boldsymbol{z}, r_j) \tag{2.1} $$

where a_j is the antecedent frame of frame j. Table 2.1 shows the kinematic parameters of the thumb and Table 2.2 presents the kinematic parameters of a generic finger. The root, alternatively called base frame or world frame (j = 0), is placed at the center of rotation of the wrist.

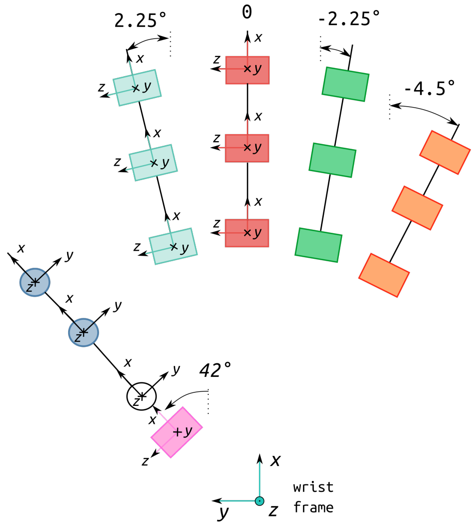

Figure 2.4 – Reference frame definition (dorsal view).

j	a_j	γ_j	b_j	α_j	d_j	θ_j	r_j
T_1	0	γ_{T1}	b_{T1}	α_{T1}	d_{T1}	q_{T1}	0
T_2	T_1	0	0	α_{T2}	d_{T2}	q_{T2}	r_{T2}[i]
T_3	T_2	0	0	0	d_{T3}	q_{T3}	0
T_4	T_3	0	0	0	d_{T4}	q_{T4}	0

[i] offset imposed by mechanical design

Table 2.1 – DH parameters of the thumb.

j	a_j	γ_j	b_j	α_j	d_j	θ_j	r_j
F_1	0	γ_{F1}	b_{F1}	α_{F1}	d_{F1}	q_{F1}	0
F_2	F_1	0	0	0	d_{F2}	q_{F2}	0
F_3	F_2	0	0	0	d_{F3}	q_{F3}	0

Table 2.2 – DH parameters of a generic finger.

2.1.3 Joint Range of Motions (RoMs)

All joints can rotate by 90° about their axes (Table E.1). Their range of motion goes from 0° to 90°, where 0° refers to the rest configuration at which all fingers are fully extended (all phalanges aligned) and lie on planes parallel to the palm. The only axis which presents a different RoM is the flexion/extension motion of the thumb RC joint which requires hyper-extension (with respect to the resting configuration) to perform an easy-to-recognize thumb-up gesture.

Finger	Joint	Extension/Flexion	Abduction/Adduction
Thumb	RC	-20° / 70°	0° / 90°
	MCP	0° / 90°	0°
	IP	0° / 90°	0°
I, M, R, L	MCP	0° / 90°	0°
	PIP	0° / 90°	0°
	DIP	0° / 90°	0°

Table 2.3 – Joint range of motions. I, M, R, L are respectively index, middle, ring and little fingers.

2.2 Geometry definition

The selected number of independent DoFs limits the mechanical dexterity of the robotic hand to only grasp. In fact, in-hand manipulation normally requires fingers with abduction/adduction motions and independent flexing motion at the MCP joints. This is coherent with the required functional capabilities required. However, from a kinematic perspective, the limited number of independent DoFs also reduces the degree of anthropomorphism of the robotic hand. Consequently, finger base positions and orientations must be properly designed to compensate the kinematic simplifications. Hereafter, finger placements and proportions are defined in order to ensure an anthropomorphic robotic hand design in terms of both kinematics and size.

2.2.1 Digit proportions

No best practice to define finger lengths, widths and placements exists. Modular designs of some or all fingers are often used to help mechanical modeling and construction. Each finger has the same link length, width, joint RoM and DoFs and their placement on the palm determines the similarity to the human counterpart. Nevertheless, a better affinity with the human hand is achieved respecting human finger diversities.

Proportion reference. Link lengths and widths are derived from body proportions under the assumption that the structure and bones proportions of hands are maintained despite their physical size [115]. Link lengths are commonly disclosed as percentage of the hand length (as shown in Section 1.1.1.4), therefore, they can be easily computed knowing the distance between the wrist and the middle fingertip. To determine the hand length, human body proportions are collected by crossing evidence already present in literature [116] with experimental measurements. The last are carried out on 10 subjects (5 men and 5 women) of different nationalities (Europeans, Asians, Central and South Americans), between 22 and 27 years old. From the cross averaged body proportions two coefficient are extracted: the ratio between the hand length and the body height (0.108) and the ratio between the upper arm length and the body height (0.153). Considering that the hand will be embedded on an existing forearm, hand proportions are initially computed in function of the forearm length in order to preserve a coherent appearance of the upper limbs. The hand length is obtained in function of both height-to-length anthropomorphic ratios. The forearm length is used to compute the correspondent human height and the resultant height is used to determine the relative hand length. Through these calculations, Romeo's forearm results to be 15% shorter than the forearm of a 1.4 [m] child, leading to tiny hands with respect to the rest of the body. Consequently, the idea to respect the proportions with the forearm is abandoned, taking the height of the humanoid robot as the main reference. This choice implies that the hand would respect anthropomorphic proportions but probably appears slightly disproportioned beside the forearm. A possible solution would consists in accordingly extending the forearm, gaining in anthropomorphism and available space for the actuation components. The palm width is computed from the hand length according to the ratio presented in [19]. Link lengths are computed according to Table 1.3, while link widths are determined as a function of the palm width using the linear equations 1.2 and 1.4 as lower and upper bounds. This approach takes inspiration from the comparison done by [25] between the Grainer model [23] and Buchholz and Armstrong model [24] presented in Section 1.1.1.4. The aforementioned equations give width boundaries of the index middle phalanx of a male, but provide no hints about the width of the reminder fingers. Since index, middle and ring fingers of the human hand do not remarkably change in width, their values are considered equivalent. The width of the middle phalanges is chosen as the mean value between the lower (14 [mm]) and upper (20 [mm]) boundaries. The widths of the proximal phalanges are set one millimeter bigger than the middle one and the widths of the distal phalanges one millimeter smaller. Considering that the little finger is the thinnest digit while the thumb the thickest, their widths are directly associated to the finger width boundaries. The width of the little finger middle phalanx is fixed to the lower boundary, while the width of the thumb is fixed to the upper boundary. Like other fingers the little finger presents a larger proximal phalanx and a smaller distal phalanx, while the thumb presents constant phalanx widths. Table 2.4 shows phalanx lengths and widths obtained from anthropomorphic data. Lengths are reported with 0.1 [mm] precision while widths with 1 [mm] precision.

Real proportions. To ease the design of the hand some simplifications are adopted. Modularity is adopted between the second and fourth digits (by averaging their phalanx lengths) and finger widths are chosen equal and constant among phalanges. In the final prototype, reference values are approximately respected, except for the distal phalanges augmented of about 50% for mechanical feasibility. Table E.2 shows link lengths and widths adopted on the robotic hand.

Finger	Link	Length [mm]	Width [mm]
Thumb	Carpometacarpal	n/a	20
	Proximal phx	25.9	20
	Distal phx	18.3	20
Index	Proximal phx	33.0	17
	Middle phx	21.3	16
	Distal phx	13	15
Middle	Proximal phx	37.0	17
	Middle phx	23.9	16
	Distal phx	14.8	15
Ring	Proximal phx	33.6	17
	Middle phx	23.1	16
	Distal phx	14.7	15
Little	Proximal phx	26.8	15
	Middle phx	16.3	14
	Distal phx	13.0	13

Table 2.4 – Link lengths and widths base on anthropometric data.

Finger	Link	Length [mm]	Width [mm]
Thumb	Carpometacarpal[i]	53[ii]	29
	Proximal phx	25.9	23
	Distal phx	28	20
Index and Ring	Proximal phx	33.3	18
	Middle phx	22.2	18
	Distal phx	21.8	18
Middle	Proximal phx	37.0	18
	Middle phx	24.0	18
	Distal phx	22.8	18
Little	Proximal phx	26.8	18
	Middle phx	20.0	18
	Distal phx	19.7	18

[i] separated into two links since abduction/adduction axes do no intersect but present an offset of 22 [mm] [ii] in default configuration: 22 (offset) + 31

Table 2.5 – Final link lengths and widths imposed by mechanical design.

2.2.2 Finger placement

Finger bases are computed using a circle centered at the MCP joint of the middle finger [22]. Fingers are considered lying on concurrent lines passing though a common point arbitrary placed along the line associated to the middle finger. This point (P) is chosen close to the center of the carpal bones and it is appointed as origin of the carpal frame, whose x axis divides the circle into two halves (see Figure 2.5). Finger bases are identified through simple geometric considerations based on the inclination of

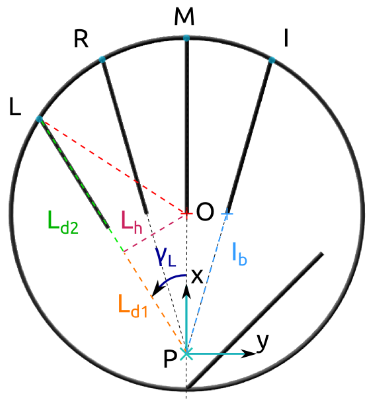

Figure 2.5 – Definition of finger base positions (palmar view).

each finger with respect to the x axis. Considering a generic finger f, its base is computed as follows:

$$\begin{aligned} f_{d1} =& |\overline{PO}| \cos(\gamma_f) \\ f_h =& |\overline{PO}| \sin(\gamma_f) \\ f_{d2} =& \sqrt{r^2 - f_h^2} \\ f_b =& f_{d1} + f_{d2} - f_l \\ f_{bx} =& f_b \cos(\gamma_f) \\ f_{by} =& - f_b \sin(\gamma_f) \end{aligned} \tag{2.2}$$

where γ_f is the angle between the x axis and the line passing through the f^{th} finger, f_b is the metacarpal bone length, f_l is the finger length (obtained from Table 2.4) and r is the circle radius equivalent to the middle finger length. To enhance symmetry $\gamma_L = \gamma_R = \gamma_I = \gamma$. Small angles return closer finger bases, with similar heights from the wrist (Figure 2.7a), while big angles locate finger bases at further distances and with various heights from the wrist (Figure 2.7c). Obviously, finger bases too close to each others are mechanically infeasible, while far finger bases result in an unaesthetic design. A compromise between the two is necessary in order to have a well-balanced anthropomorphic hand. Once determined, finger base positions are adjusted along the z axis, so that fingertips lie on a common xy plane when fingers are completely flexed. This allows the palm to have the same arched shape as the human hand.

Since the designed fingers can only flex and extend via three parallel hinge joints, MCP joints are inclined to preserve the finger convergence of the human hand towards the center of the palm. To determine the maximum angles of inclination of the finger bases, intra-finger collisions are checked while flexing the joints. For each finger, the inclination angle is increased starting from $0°$ until a collision is detected. At early design stages this check has been performed considering the distance between spheres placed at the DIP joints, since fingers had cylindrical shapes (Figure 2.6). After, intersection among rectangles circumscribing the real finger shapes at the DIP joints has been checked.

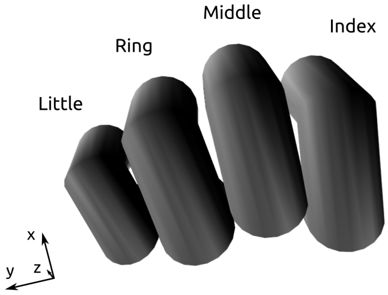

Figure 2.6 – Checking intra-finger collisions while flexing finger joints (palmar view).

Table E.3 shows the resulting finger base positions and orientations. Locations are expressed in the wrist frame, which is placed toward the little finger (along the y axis) and the forearm (along the x axis) with respect to the carpal frame.

2.2.3 Thumb placement

To approximately attain human hand performances the thumb geometry and kinematic need to be carefully designed. To gesture and grasp, 4 joints with 3 DoFs are chosen for the thumb kinematics (Figure 2.3). Its proportions are calculated as described in the previous Section 2.2.2. The thumb base configuration is computed following three criteria: dexterity, opposability and aesthetics. In order to imitate human thumb motions, the robotic thumb has to be able to reach a certain number of desired

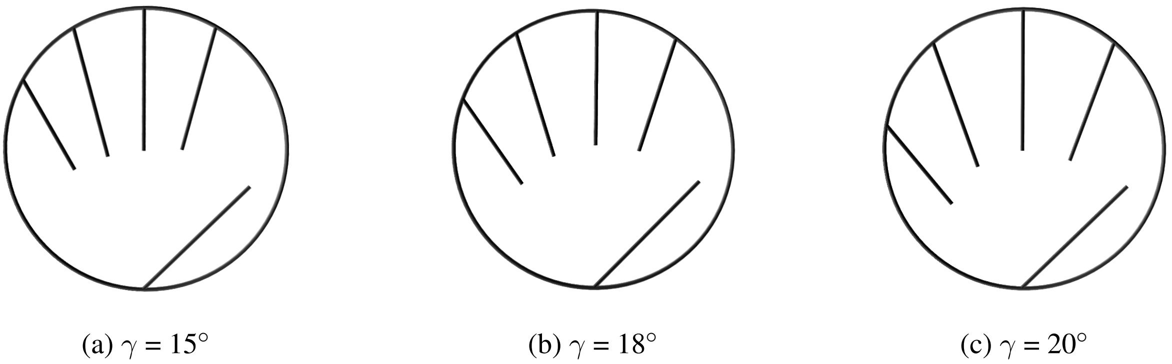
(a) γ = 15°

(b) γ = 18°

(c) γ = 20°

Figure 2.7 – Finger base placement variation according to the angle γ between concurrent finger lines.

Finger	**Base position [mm]** (x, y, z)	**Base orientation [deg]**
Index	(100, 26.7, -3.7)	2.25°
Middle	(102, 7, 0.0)	0°
Ring	(100, -12.7, -3)	-2.25°
Little	(94, -32.4, -8.5)	-4.5°

Table 2.6 – Finger base positions and orientations with respect to the wrist frame.

positions on the opposite fingers. These positions are defined by a surgery test, known as Kapandji test [26], described in Section 1.1.1.5. The test contains all motion directions and an interesting set of positions which are useful to check the thumb range of motion and dexterity. However, it does not provide information about thumb grasping abilities. Indeed, reaching all required positions does not imply that the thumb is effectively able to interact with the opposing fingers. Hence, an additional test is carried out to explore the physical interaction between the thumb fingertip and the reminder fingers. This test returns the intersection volume between the thumb and fingers as a thumb opposability index [55], which denotes the hand grasping abilities from a kinematics point of view. Note that no forces are considered in this context; an additional evaluation metric should be taken into account to determine finger forces and grasping stability.

In summary, the thumb base placement is the most delicate design step. In order to obtain the needed functionalities (gesturing and grasping) the thumb has to be dexterous and opposable. These two properties are achieved through:

- The Kapandji test;
- The thumb opposability index.

In addition, an aesthetic check is done to evaluate the overall hand appearance. This last test implies a cyclic design in which the intervals of search among the thumb base parameters are adapted at each iteration.

2.2.3.1 Thumb base selection

In this section the tests used to design a dexterous and opposable thumb are presented. According to the thumb geometry and kinematics, the thumb base configuration is determined by calculating the thumb base position (x, y, z) and orientation (θ_z) about the z axis with respect to the carpal frame (Figure 2.3). The orientations about x and y axes are not included because of the 2 DoFs of the base.

2.2.3.2 Problem formulation

The thumb and the fingers are treated as two independent serial chains attached to a common base. On each chain an end-effector is defined according to the desired position that has to be reached. The objective is to determine if both kinematic chains can converge to a common position.

Definitions:

— $j = t$ or f_i, respectively referring to the thumb fingertip and the i^{th} end-effector ($i =$ MCP, PIP, DIP and fingertip) on the f^{th} finger;

— $\mathbf{q}_j$ vector of the independent joint variables of the j^{th} chain;

— $T_j(\mathbf{q}_j)$ direct geometric model (DGM) of the j^{th} serial kinematic chain. It computes the end-effector configuration passing from the joint space to the Cartesian space;

— $J_j(\mathbf{q}_j)$ Jacobian matrix. It provides the j^{th} end-effector differential displacement (linear and angular) in terms of the differential variation of the joint variables. In this context, only its upper part is used in order to uniquely consider the linear displacement of the end-effector: $\mathbf{dP} = J_j(\mathbf{q}_j)\mathbf{dq}_j$.

The problem can be solved using the inverse geometric model where the desired frame changes at each iteration:

1. Initialization of current joint variables $\mathbf{q}_t^c$ and $\mathbf{q}_{f_i}^c$ to a random value or desired initial value within the joint domain;
2. Computation of the current end-effector transforms $T_t(\mathbf{q}_t^c)$ and $T_{f_i}(\mathbf{q}_{f_i}^c)$ of each chain (thumb and opposing finger);
3. Computation of the position error defined as:
   $\mathbf{dP} = P_t(\mathbf{q}_t^c) - P_{f_i}(\mathbf{q}_{f_i}^c)$, where $P_t(\mathbf{q}_t^c)$ and $P_{f_i}(\mathbf{q}_{f_i}^c)$ are the position vectors of $T_t(\mathbf{q}_t^c)$ and $T_{f_i}(\mathbf{q}_{f_i}^c)$ respectively;
4. If $||\mathbf{dP}||$ is as small as required:
   the algorithm stops;
   else:
   $\mathbf{dP}$ is scaled if it is too big to be used in the differential model $\mathbf{dP} = \mathbf{dP}/||\mathbf{dP}||dx$, where dx is a properly defined small displacement;
5. Computation of thumb and finger current Jacobians $J_t(\mathbf{q}_t^c)$ and $J_{f_i}(\mathbf{q}_{f_i}^c)$;
6. Calculation of joint variations $\mathbf{dq}_t = J_t(\mathbf{q}_t^c)^+\mathbf{dP}/2$ and $\mathbf{dq}_{f_i} = J_{f_i}(\mathbf{q}_{f_i}^c)^+(-\mathbf{dP}/2)$;
7. Updating joint configurations $\mathbf{q}_t^c = \mathbf{q}_t^c + \mathbf{dq}_t$ and $\mathbf{q}_{f_i}^c = \mathbf{q}_{f_i}^c + \mathbf{dq}_{f_i}$ within the joint domain;
8. Reiteration from step 2.

In our context, $\mathbf{q}_{f_i}$ is always a scalar for each finger f, independently from the chosen end-effector, since all finger joints are coupled. Note that, if more than 3 DoFs are available on a single chain, this algorithm can be extended when computing the joint displacements. Indeed, a correction in orientation, if desired, could be attained as a secondary objective, working in the null space of the Jacobian matrix of the serial chain. This iterative approach can return some undesired solutions: the thumb end-effector reaches the desired position colliding with the finger in opposition. Consequently, a non-linear optimization algorithm with collision avoidance constraints is used:

$$\begin{aligned}
&\min_{\mathbf{q}_t,\mathbf{q}_{f_i}} ||\mathbf{dP}(\mathbf{q_t},\mathbf{q_{f_i}})|| \\
&\text{s.t.} \\
&\quad q_{t_l\,\min} \leq q_{t_l} \leq q_{t_l\,\max}, \qquad \forall l \in [1, \text{DoFs}(\mathbf{q}_t)] \\
&\quad q_{f_{il}\,\min} \leq q_{f_{il}} \leq q_{f_{il}\,\max}, \quad \forall l \in [1, \text{DoFs}(\mathbf{q}_{f_i})] \\
&\quad d_{sph} \geq r_t + r_{f_i} - \epsilon
\end{aligned} \tag{2.3}$$

where r_t is the thumb radius at the fingertip (the half of the thumb fingertip width defined in Table E.2), r_{f_i} is the radius of the opposed finger at the desired point of interest (half of the joint or fingertip width defined in Table E.2), ϵ is an arbitrary fixed scalar (e.g. 0.5 [mm]) which defines the intersection acceptance between the two chains, considering that finger surfaces can be made of soft materials, and d_{sph} is the distance between two sphere centers, one located within the thumb and the other one within the opposed finger. Spheres are placed so that their surfaces overlap with the finger ones. Obviously, contour and constraining inequalities have to be adapted according to the finger shapes.

2.2.3.3 End-effectors definition

Since the objective is to mimic human thumb opposability, specific thumb end-effector positions are considered according to the target location on the opposing fingers. Figure 2.8 shows the thumb end-effector definitions in correspondence of the target digit. Frames are defined on finger surfaces, not displayed for clarity. Frame a at the thumb tip does not change from one finger to another. Frames b, c and d, instead, are jointly displaced by 30° over the thumb surface, from the thumb side to the center of its pad, as target finger varies from the second to the fifth digit.

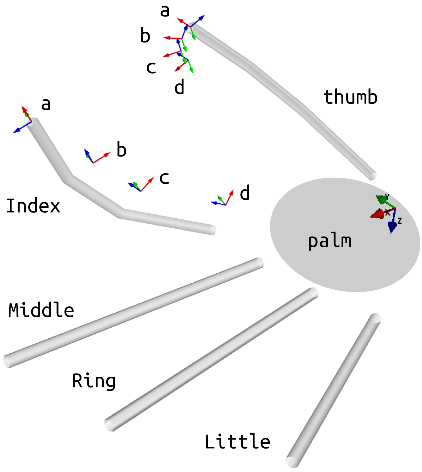

Figure 2.8 – Frames definition at the thumb fingertip and the opposing fingers.

2.2.3.4 Volume of intersection

Volumes of intersection among fingers discern their kinematic degree of interaction. Collision points are identified by exploring finger workspaces. To evaluate the thumb opposability a modified version of the performance index [55] is used:

$$I = \frac{1}{d_t^3} \sum_{i=1}^{k} \sum_{j=1}^{e} w_{ij} v_{ij} \tag{2.4}$$

where d_t is the thumb length, k is the number of fingers (thumb excluded), e is the number of end-effectors considered on each opposed finger, w_{ij} is a weighing coefficient, v_{ij} is the volume of intersection between the thumb and the finger end-effector. This performance index includes and weights the interaction between the thumb fingertip and each finger portions involved in the Kapandji test. Intersection volumes (v_{ij}) are computed sampling the Cartesian space in x, y and z. The number of cells which compose the grid strictly depends on the hand workspace boundaries and the size of the sampling interval (set to 2 [mm]). Each contact is checked by visiting the thumb and finger joint spaces and it is stored in the corresponding cell. Consequently, the number of cells holding collisions reveals the intersection volume per finger:

$$v_{ij} = n_{ij} \Delta V \tag{2.5}$$

where n_{ij} is the number of cells in which the thumb fingertip and the j^{th} end-effector of the i^{th} finger intersect and ΔV is the volume of a cell.

Differently from [113], the end-effector is not considered as a single point. Indeed, a single point does not determine the potential grasping capabilities of the hand. For this reason, a cloud of points within the finger and thumb structures is taken into account (see Figure 2.9a). In this case, v_{ij} approximatively discloses the amount of effective interaction between the thumb and the fingers close to the Kapandji positions (Figure 2.10).

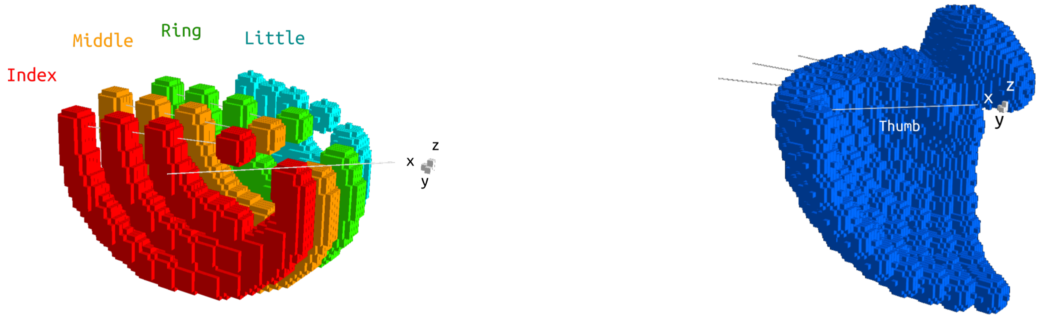

(a) Finger augmented workspaces.

(b) Thumb augmented workspace.

Figure 2.9 – Analysis of finger and thumb augmented workspaces (dorsal view).

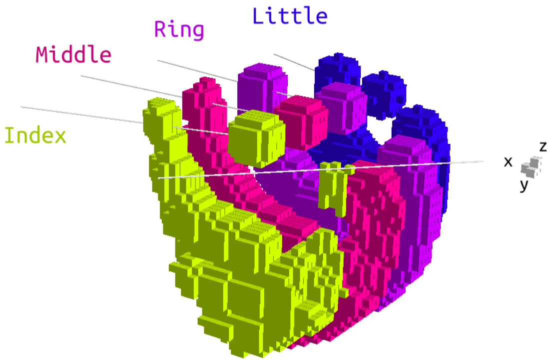

Figure 2.10 – Intersection between thumb fingertip and all fingers end-effectors.

2.2.3.5 Solution selection

To select the best position and orientation of the first joint of the thumb the following algorithm is implemented:

1. Thumb bases are generated using a brute force exploration. Intervals are defined according to aesthetics and mechanical constraints;
2. For each base the Kapandji test is performed;
3. If the candidate passes the Kapandji test: the thumb opposability index is computed beside the relative standard deviation (σ_r) of the intersection volume:

$$\sigma_r = \frac{\sigma^2}{\bar{v}} 100 \tag{2.6}$$

where $\sigma^2 = \sum_{i=1}^{k} (v_i - \bar{v})^2 / k$, $v_i = \sum_{j=1}^{e} v_{ij}$ and $\bar{v}$ is the mean value of v_i.

4. If the relative standard deviation is lower than a desired threshold (in our case set to 20%) the candidate is stored (the thumb opposability is considered equilibrated).
5. The solution is selected picking the stored candidate with the highest thumb opposability index.

Table 2.7 lists some stored candidates for the right hand.

position [mm] (x, y, z)	**orientation [deg]**	**TOI**	$\sigma_{\mathbf{r}}$ [%]
(8, 11, -9)	45°	0.167	19.693
(8, 11, -5)	40°	0.169	17.421
(8, 2, -5)	50°	0.177	6.705
(12, 2, -5)	45.0°	0.196	12.252

Table 2.7 – Thumb bases candidates expressed with respect to the carpal frame. TOI is the Thumb Opposability Index.

2.2.3.6 Problem reformulation

Finger joint couplings influence the thumb base selection since end-effector trajectories change. At early stages, transmission ratios were set to 1:1 to test the algorithm and provide a first version of the hand geometry. Once completed the mechanical design of fingers (presented in the next chapters), the thumb placement is recomputed according to the non-linear coupling ratios. The fact that middle and distal joints close faster than the proximal ones at small MCP angles leads thumb base candidates to be placed closer to the finger bases. This results in an anesthetic and mechanically infeasible design which requires the problem to be reformulated. First of all, end-effectors at the opposing fingers are reduced from 16 to 8, getting rid of locations at the PIP and DIP joints which are less interesting for precise (pinch) grasps and gestures. Secondly, the objective function is changed redefining $\mathbf{dP}$ as the distance between the center of the sphere within the thumb fingertip and the i^{th} end-effector position on the f^{th} opposing finger. This completely changes the problem formulation which presents a larger number of solutions (thumb base candidates). Indeed, the redefinition allows the thumb to reach the desired locations with different configurations and unconstrained points of contacts. However, it reintroduces the problem of undesired finger intersections. In fact, the introduced collision avoidance constraint allows the convergence between the point of interest and the surface of the sphere, but no longers hinders intersection among digits.

To limit the solution set to a specific portion of the sphere surface, frame orientations are added to the problem:

$$\begin{array}{ll} \displaystyle\min_{\mathbf{q}_t,\mathbf{q}_{f_i}} ||\mathbf{dP}(\mathbf{q_t},\mathbf{q_{f_i}})|| & \\ \text{s.t.} & \\ \quad q_{t_l\,\min} \leq q_{t_l} \leq q_{t_l\,\max}, & \forall l \in [1, \text{DoFs}(\mathbf{q}_t)] \\ \quad q_{f_{il}\,\min} \leq q_{f_{il}} \leq q_{f_{il}\,\max}, & \forall l \in [1, \text{DoFs}(\mathbf{q}_{f_i})] \\ \quad d_{sph} \geq r_t + r_{f_i} - \epsilon & \\ \quad -\pi/2 \geq d\theta_y \geq 0 & \\ \quad 0 \geq d\theta_z \geq \pi/2 & \end{array} \tag{2.7}$$

where $d\theta_y$ and $d\theta_z$ belong to the orientation difference vector ($d\theta_x$, $d\theta_y$, $d\theta_z$) containing the RPY angles of $R_t(\mathbf{q}_t^c)^T(R_{f_i}(\mathbf{q}_{f_i}^c)R_z(\pi))$, where $R_z(\pi)$ is used to reorient the end-effector frame at the point of interest so that its x axis points inward the finger. According to the frame definitions, the constraints on $d\theta_y$ and

$d\theta_z$ restrict the solutions to the eighth of the sphere coinciding with the palmar side of the thumb tip and pad (Figure 2.11).


(a) (b)

Figure 2.11 – Selected sphere surface at the thumb tip.

Apart from the collection process of thumb base candidates, the rest of the algorithm remains unchanged. Figure 2.12 shows one of the thumb base candidates solving the reformulated problem. The final thumb base is placed at (32, 24, -2) [mm] and oriented of 42° about z with respect to the wrist frame.

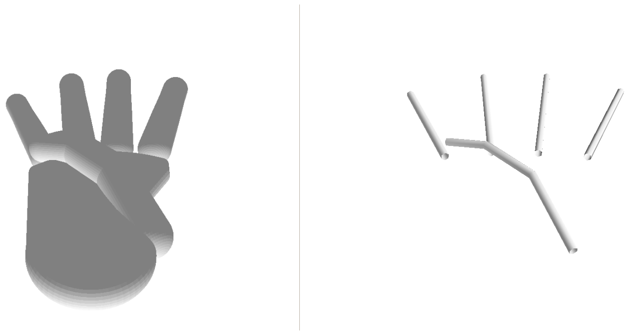

Figure 2.12 – Example of thumb base candidate solving the reformulated problem at the little finger MCP joint.

2.3 Validation and discussion

The hand model is designed and simulated using Python and *NAOqi* [117] APIs. Geometric and kinematic parameters are inspected by direct visualization of the final robotic hand model. The Kapandji test is verified by moving the fingers and thumb in the configurations collected during the algorithm execution and it is checked that the hand is able to reach the desired list of positions within the demanded precision. Figure 2.13 shows the furthest (a) and the closest (b) positions involved in the test. Hand grasping capabilities have been examined on various objects (e.g. soda can and a smartphone) using CAD software. However, no conclusions can be drawn on the grasping success since only a kinematic analysis has been conducted at this stage. The hand is capable of performing all one-hand gestures with high and middle priorities, such as "pointing" (Figure 2.14-a), "thumb-up", "ok" gestures and counting up to five. For example, Figure 2.14-b shows the number three in the European counting. In addition, half of the low priority hand gestures can be performed (no "stop" and "blah-blah" gestures). Note that, in order to give more emphasis to the finger kinematics, a simplified palm is represented.

2.4 Conclusions

A simple and effective method for designing dexterous anthropomorphic robotic hands has been presented. The method is conceived to realize a small sized and lightweight hand for a social humanoid robot

(a) (b)

Figure 2.13 – Thumb opposition on the little fingertip 2.13a and the index MCP 2.13b: two out of the 8 positions demanded in the implemented Kapandji test.

(a) (b)

Figure 2.14 – Two examples of gestures that can be performed by the hand: pointing (a) and counting (b).

1.4 [m] tall. It consists in a design tool that generates a minimal kinematic model to perform expressive gestures and grasps. Hand geometry has been conceived using anthropometric data and heuristics methods which preserve a hand structure close to that of a human hand. Main focus has been given to the thumb base position and orientation, since its interaction with the opposed fingers strongly affects the hand performance. Three tests drove its selection: aesthetic, surgical and interaction tests. The first played a relevant role to obtain a fairly equilibrated hand, the second provided a human-like opposable thumb, while the third defined its potential mechanical dexterity for grasping. Hand designers can follow this methodology to immediately obtain the hand kinematic model and structure.

Hand design: Preface

Actuation selection. Different types of actuators have been used in robotic hands (see Chapter 1.2). The main ones are pneumatic, hydraulic, Shape Memory Alloy (SMA) and electromagnetic. Pneumatic actuators (e.g. Pneumatic Artificial Muscles [61]) are interesting for safe physical human-robot interaction thanks to their natural compliance, however, they have low power efficiency, their motion trajectories are difficult to control and they need an air-compressor that would be cumbersome to be embodied in the robot palm or forearm. Hydraulic actuators have high power-to-weight ratios but their pumps are often bulky, noisy and prone to leakages. SMAs are capable of memorizing or retaining their previous shape when subjected to thermo-mechanical or magnetic variations [118]. This type of actuation is silent and smooth and has a high power-to-weight ratio which allows the development of compact and lightweight hands. However, it presents limited strain and a slow response time since its transformations depend on thermodynamic processes. Even if the last drawback can be improved by hybrid actuation system designs (e.g. connecting DC motors in series to SMA [119]) or specific actuation units, SMAs still present a very low power efficiency (<10%) [120]. Electromagnetic motors represent the most reliable and effective solution. They have a lower power-to-weight ratio with respect to hydraulic actuators but they are lighter and present no leakage issues. They are rigid with respect to pneumatic actuators but their stiffness can be arranged by adding to the actuation system passive elements or by actively controlling the rotor impedance. Their motion trajectory can be precisely controlled together with their response time and their power efficiency (which obviously depends on the motor quality and the adopted transmission) is normally higher than the power efficiency of SMA. There exists several types of electromagnetic actuators: brushed DC motors, brushless DC motors (BLDC), reluctance motors, step motors and inductance motors. Brushed DC motors are easy to control but short in lifetime due to the mechanical commutation between the rotor and the stator. BLDC motors are more difficult to control, since they require electronic commutation and additional sensors if no back-EMF (electromotive force) is used to estimate the rotor position. On the other hand, they have an interesting long lifetime. Reluctance motors have high torque ripple (difference between the maximum and the minimum torque during one revolution) when operated at low speed and they are noisy. Step motors are easy to control (open-loop control) and no sensors are needed. Yet, they are merely useful for holding precise positions. Inductance motors (asynchronous motors) are slower and develop higher torques than classical (synchronous) motors. Nevertheless, to our knowledge, they do not exist at diameters under 50 [mm]. In view of the core design specifications of the hand, actuators must be small and lightweight to be embodied in the robot hand or forearm. They have to move smoothly and quietly in order to be installed on a social humanoid robot. In addition, external force estimation from current readings rather than additional sensors is required. This strong constraint imposes small reductions after the motor shaft, in a mechanical system which requires high torque-to-volume ratio. According to these characteristics, BLDC motors emerge among all, even though they are more complex to control. They are efficient, they have a higher power-to-weight ratio with respect to DC motors (see example in the table below) and have a longer lifetime, that is fundamental to improve the final product reliability.

Parallel actuation systems. Seven small BLDC motors are placed in the hand to drive finger motions according to the robotic hand kinematic (Chapter 2). Five are embodied within the palm, while the reminder are installed in the first and second phalanges of the thumb to control its flexing motions. These

	DC	BLDC
Motor size [mm]	⌀ 29 x 45	⌀ 30 x 47
Power/Weight [W]/[Kg]	22 / 0.15 $\approx$ 147	100 / 0.21 $\approx$ 476
Price	DC_{price}	$\approx$ 4 x DC_{price}

DC motors and BLDC motors comparison taking the MAXON catalog as example.

seven independent DoFs provide the *e-motional* essence of the hand. The word gathers two fundamental concepts together: emotion and motion. The former refers to engaging communication that the robot has to perform to create empathy with people through natural language, body language and gestures. The latter refers to the fact that phalanges position, velocity and acceleration have to be precisely known and controlled to track desired motion trajectories. The limited volume within the palm and the small reduction ratio demanded, impose small "e-motion motors" with restrained torques at finger joints. More energy demanding tasks are left to another actuation system which acts independently and in parallel to the previous one. It consists in a single BLDC motor connected to a differential mechanism that distributes the pulling force from the motor shaft to the fingers. The force is transmitted through Fast-Flight cables (Section 4.1.1) and a series of bearings and pulleys (Sections 4.1.2 and 4.1.3) that route the cables until the end of each finger. This actuation system provides the *grasping* capability of the hand, sized to develop, at most, the force required to hold a full soda can within all fingers (Chapter 4.2). The BLDC motor, that will henceforth be addressed as "grasp motor", is placed in the robot forearm and it represents the only independent DoF of the mechanism. Phalanges are all *loosely coupled* so that fingers can adapt their postures according to the object shape.

These two actuation systems can actually be considered as two completely different hands. The first, with seven DoFs, is capable of performing desired motion and gestures. The second, with one DoF, is able to grasp and autonomously adapt to different object shapes. Since their designs and functionalities are diverse and self-reliant, the two systems are presented in two distinct parts (Chapter 3 and Chapter 4). Directly after these two chapters, the mechanical systems are merged in a unique design (Chapter 5) that creates the coexistence of both functionalities in one hand: the ALdebaran Parallel HAnd (ALPHA). The name derives from the two actuation systems embodied in parallel within the hand. In addition, it underlines the current design stage of the prototype: a proof of concept.

3

Hand design: E-motion

In this chapter the hand is designed to perform a specific set of gestures. Fingers are rigidly coupled with non-linear transmission mechanisms which interconnect MCP, PIP and DIP finger joints and the MCP-IP joints of the thumb. Their design is presented in Section 3.1 together with the geometric, kinematic and dynamic models of thumb and fingers. Section 3.2 outlines the actuation choice dictated by the compromise between mechanical constraints and required joint torques. Then, Section 3.3 introduces the joint-level control based on the FoC (Field oriented Control) and active compliance. Finally, Section 3.4 closes the chapter by showing finger and thumb designs.

3.1 Transmission

3.1.1 Joint coupling mechanism

To analyze coupling mechanisms three links are considered: a fixed frame, a master link and a slave link. The fixed frame is the motionless link considered as the ground. The master link is the directly actuated link, while the slave link is the one driven by the transmission mechanism (see Figure 3.1). There exists several types of transmission mechanisms: gear train, pneumatic/hydraulic pipes, cables, linkages etc. Gear train drives the slave link through a series of gears connected to the ground frame.

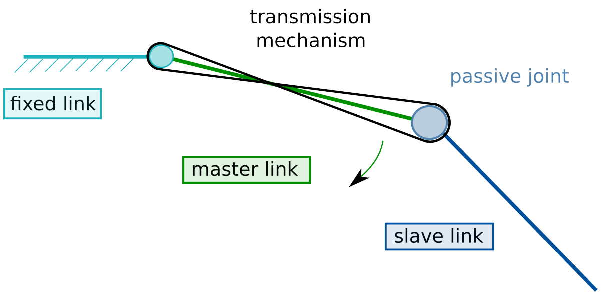

Figure 3.1 – Transmission mechanism terminology.

It is simple to conceive but it kinematically couples the links with a constant ratio and its mechanical efficiency decreases proportionally to the number of gears. Hydraulic pipes do not need intermediary stages like gear trains, but they introduce potential leakages after repeated operations. Cables are light and reliable (if their material is properly selected) but they need a pretensioning system. A linkage-based transmission system results to be the most interesting solution: more efficient than gear train, no potential leakages, no pretensioning systems needed and it can provide a non-linear coupling ratio if appropriately designed. For these reasons, finger joints are coupled using a 2D inverted four-bar linkage as shown in Figure 3.2. The last is designed to drive the output angle faster than the input one, at the beginning of a closing motion, and slower at the end of it. Each finger is driven by a series of two inverted four-bar linkages, except for the thumb which presents only one coupling mechanism between its last two joints.

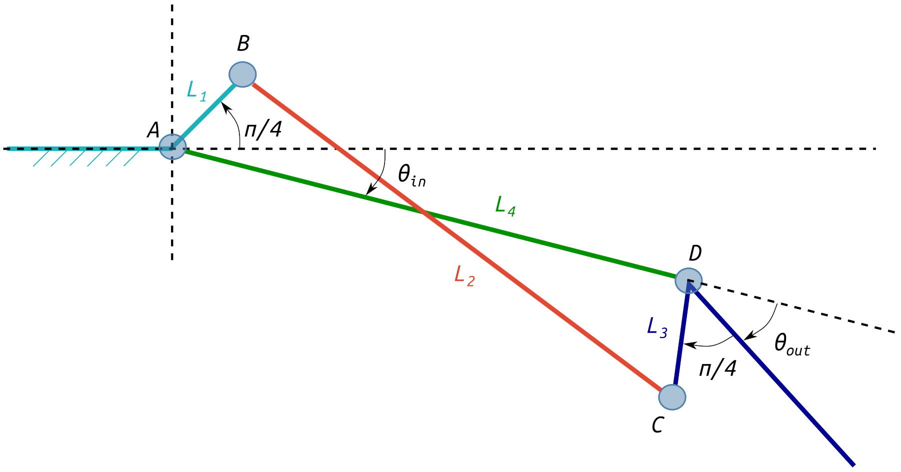

Figure 3.2 – Four-bar linkage notations.

3.1.1.1 Inverted four-bar linkage model

The geometric parameters of the four-bar linkage are bounded by mechanical constraints. L_4 coincides with the phalanx length while L_3 is imposed equal to L_1. The four-bar linkage has to be designed so that fingers can properly stretch and close. In other words, the output angles must coincide with input ones ($\theta_{in} = \theta_{out}$) at the joint boundaries (0° and 90°). This is obtained imposing the angle between *AB* and the precedent phalanx and the angle between *DC* and the successive phalanx equal to $\pi/4$ (Figure 3.2). The length of L_1 is bounded between avoiding collision with the joint axis and the available space in the finger, and it is chosen so that the successive phalanx closes faster than the precedent one from stretched configurations. To resume, the four-bar linkage lengths are defined as follows:

$$\begin{aligned} L_1 &= \text{const} \\ L_4 &= L_{phalanx} \\ L_3 &= L_1 \\ L_2 &= \sqrt{L_4^2 + 2L_1^2} \end{aligned} \tag{3.1}$$

A four-bar linkage structure can be studied as a closed chain: a set of links and joints that form at least a closed loop. In general, a closed chain is composed by L joints and $n+1$ links (ground included), where $L > n$. The number of independent closed loops (B) is defined by:

$$B = L - n \tag{3.2}$$

which is trivial for the simple four-bar linkage case: $B = 4 - 3 = 1$. Differently from a classical serial chain, not all joints are active in a closed chain. The complex chain imposes kinematic constraints between the joints, reducing the structure mobility: the number of active joints (DoFs) required to control the whole structure. Chebychev-Grübler-Kutzbach criterion defines the mechanism DoFs on the base of the number of joints, links and closed loops:

$$N = L - \sum_{j=1}^{B} c_j \tag{3.3}$$

where c_j is the number of independent kinematic constraint equations of loop j. For a spatial loop $c_j \leq 6$ while for a planar loop $c_j \leq 3$. In this context, the loop is planar and the revolute joints fully span the space, consequently the structure mobility is $N = 4 - 3 = 1$. Chebychev-Grübler-Kutzbach criterion represents the easiest way to determine the mobility of a mechanism but it is not the most reliable. An alternative approach that always returns a correct result is the so called Gogu's method. Its formulation for a single loop chain consists in splitting the loop around an arbitrary joint $k < L$, dividing the structure in two simple serial chains with n_1 and n_2 joints respectively. The mobility is computed in function of the number of joints and the DoFs that are lost due to the loop closure (rank(J_L)):

$$N = L - \text{rank}(\boldsymbol{J}_L) \tag{3.4}$$

The number of joints that lose their independence is given by:

$$\begin{aligned} \text{rank}(\boldsymbol{J}_L) &= \dim(\boldsymbol{E}_1) + \dim(\boldsymbol{E}_2) - \dim(\boldsymbol{E}_1 \cap \boldsymbol{E}_2) \\ &= \dim(\boldsymbol{J}_{n_1}) + \dim(\boldsymbol{J}_{n_2}) - \dim(\boldsymbol{E}_1 \cap \boldsymbol{E}_2) \end{aligned} \tag{3.5}$$

where $\boldsymbol{E}_j$ is the operational space of the j^{th} serial branch and $\boldsymbol{E}_1 \cap \boldsymbol{E}_2$ is the common operational space that the two branches share. In case the two chains do not contain any redundant DoF the formula turns to:

$$N = L - \text{rank}(\boldsymbol{J}_L) = L - n_1 - n_2 + \dim(\boldsymbol{E}_1 \cap \boldsymbol{E}_2) = \dim(\boldsymbol{E}_1 \cap \boldsymbol{E}_2) \tag{3.6}$$

If the four-bar linkage is opened at joint D (Figure 3.2) the structure becomes a tree robot with two non-redundant serial chains with $n_1 = 2$ and $n_2 = 2$ joints respectively. Their common operational space has dimension one as the four-bar linkage mobility (Equation 3.6), confirming the result given by the Chebychev-Grübler-Kutzbach criterion. Hence, the four-bar linkage is fully driven by a single motor placed at joint A, considering link L_1 fixed to ground.

Modified Denavit-Hartenberg notations. Modified DH parameters are identified transforming the closed loop structure in an equivalent tree robot (a set of serial chains whose bases converge to a common structure). The chain can be opened either cutting links or passive joints. Joint frames are numbered starting from the ground up to the multiple serial chain end-effectors so that a child frame always has a frame number greater than its parent. To reduce computational complexity in the dynamic model, the cut joint in the four-bar linkage is selected minimizing the difference of links forming the two serial chains between the root of the loop and the links connected to the cut joint. Figure 3.3 shows the frame numbers and their x axes. Since the four-bar linkage is defined on a plane, all joint axes (z) are parallel to z_0, while y axes are obtained according to the right hand rule. Joint angles are defined positive when clockwise. For each frame number the color in the background coincides with the link connected to the joint while the color of the square recalls the parent frame. Table 3.1 collects the DH parameters of the inverted four-bar linkage. For each frame j the antecedent joint (a_j) and the nature of the joint (σ_j) are defined. The last can be:

$$\sigma_j = \begin{cases} 0 : \text{if } j \text{ is revolute} \\ 1 : \text{if } j \text{ is prismatic} \\ 2 : \text{if the current frame is fixed w.r.t. its antecedent} \end{cases} \tag{3.7}$$

The third case normally occurs if j is cut or if a redundant frame is added. The parameters μ_j denotes an active joint if equal to 1 and a passive joint if 0. The reminder values (γ_j, α_j, d_j, θ_j are r_j) are the DH parameters that define the transformation matrix between two consecutive reference frames (Equation 2.1). Since the model is planar b_j is always zero for all frames. For this reason the parameter is not inserted in Table 3.1 and it is not reported in the tables presented in this chapter.

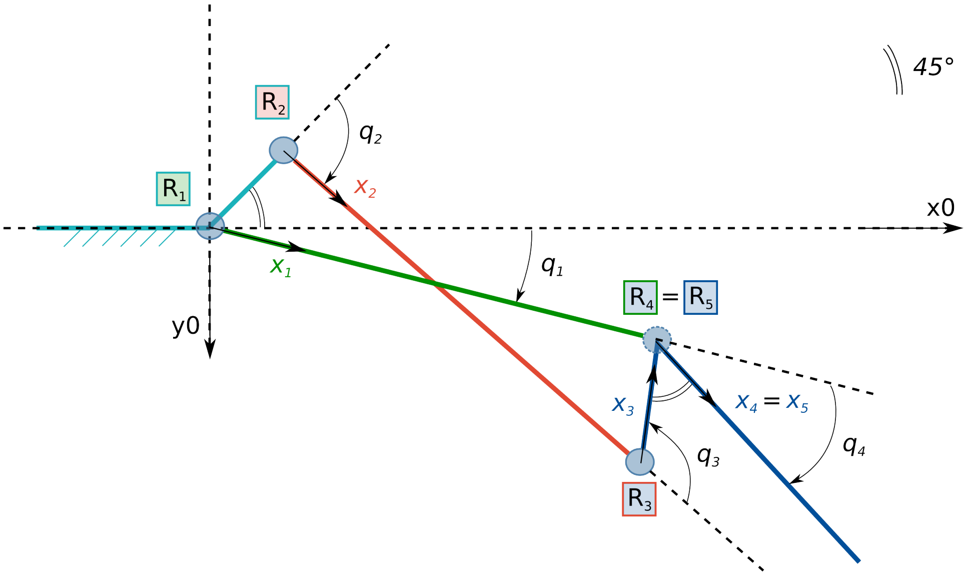

Figure 3.3 – Reference frame definition of the four-bar linkage geometric model using the modified Denavit-Hartenberg notations.

3.1.1.2 Direct geometric model

The relation between the actuated input angle ($\theta_{in} = q_1$) and the driven output angle ($\theta_{out} = q_4$) can be computed using different approaches. In this context, two methods are presented. One solves the geometric model by mean of the cosine rule while the other on the base of the modified DH parameters.

Law of cosines. Given two sides (a and b) of a generic triangle and the angle contained between them (γ), the side opposite to the angle (c) can be computed as follows:

$$c^2 = a^2 + b^2 + 2ab\cos(\gamma) \tag{3.8}$$

j	a_j	μ_j	σ_j	γ_j	α_j	d_j	θ_j	r_j
1	0	1	0	0	0	0	q_1	0
2	0	0	0	$-\pi/4$	0	L_1	q_2	0
3	2	0	0	0	0	L_2	q_3	0
4	1	0	0	0	0	L_4	q_4	0
5	3	0	2	0	0	L_3	$3/4\pi$	0

Table 3.1 – Modified DH parameters of the four-bar linkage.

As shown in Figure 3.4, in the inverted four-bar linkage three triangles ABC, CBD and ADC can be identified. Thanks to them, the direct geometric model (DMG) can be solved in few steps:

$$\begin{aligned}
s_1 &\triangleq |\overline{BD}(q_1)| = \sqrt{L_4^2 + L_1^2 - 2L_1L_4\cos\left(\frac{\pi}{4} + q_1\right)} \\
\beta_1 &= \cos^{-1}\left(\frac{L_1^2 + s_1^2 - L_4^2}{2L_1 s_1}\right) \\
\beta_2 &= \cos^{-1}\left(\frac{L_2^2 + s_1^2 - L_3^2}{2L_2 s_1}\right) \\
\eta_2 &= \beta_1 - \beta_2 \\
s_2 &\triangleq |\overline{AC}(q_1)| = \sqrt{L_1^2 + L_2^2 - 2L_1L_2\cos(\eta_2)} \\
\eta_4 &= \cos^{-1}\left(\frac{L_4^2 + L_3^2 - s_2^2}{2L_4 L_3}\right) \\
q_4 &= \frac{3}{4}\pi - \eta_4
\end{aligned} \tag{3.9}$$

where:

- — L_1, L_2, L_3 and L_4 are the four-bar linkage lengths;
- — q_1 is the active input angle;
- — q_4 is the passive output angle.

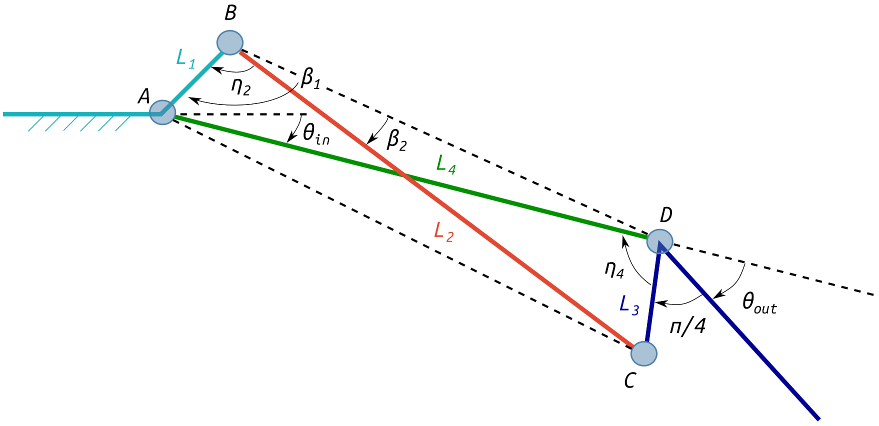

Figure 3.4 – Four-bar linkage geometric model using the Law of cosines.

DH parameters. As previously mentioned, DH parameters represent a closed loop as an equivalent tree robot with two serial chains. To mathematically reconstruct the loop, geometric constraint equations are computed at the virtually cut joint (highlighted in Figure 3.3 with a dashed circle) imposing the following condition:

$$\begin{aligned} {}^0\boldsymbol{T}_5 &= {}^0\boldsymbol{T}_4 \\ {}^0\boldsymbol{T}_2{}^2\boldsymbol{T}_3{}^3\boldsymbol{T}_5 &= {}^0\boldsymbol{T}_1{}^1\boldsymbol{T}_4 \end{aligned} \tag{3.10}$$

Developing matrices in Equation 3.10 rotation and translation constraint equations are derived.

Rotation constraint:

$${}^0\boldsymbol{R}_5 = \begin{bmatrix} \cos(\pi/2 + q_2 + q_3) & -\sin(\pi/2 + q_2 + q_3) & 0 \\ \sin(\pi/2 + q_2 + q_3) & \cos(\pi/2 + q_2 + q_3) & 0 \\ 0 & 0 & 1 \end{bmatrix} \tag{3.11}$$

$${}^0\boldsymbol{R}_4 = \begin{bmatrix} \cos(q_1 + q_4) & -\sin(q_1 + q_4) & 0 \\ \sin(q_1 + q_4) & \cos(q_1 + q_4) & 0 \\ 0 & 0 & 1 \end{bmatrix} \tag{3.12}$$

Imposing ${}^0\boldsymbol{R}_5 = {}^0\boldsymbol{R}_4$ we get:

$$\pi/2 + q_2 + q_3 = q_1 + q_4 \tag{3.13}$$

Translation constraints:

$${}^0\boldsymbol{p}_5 = \begin{bmatrix} L_1\cos(\pi/4) + L_2\cos(\pi/4 - q_2) + L_3\cos(\pi/4 - q_2 - q_3) \\ -L_1\sin(\pi/4) - L_2\sin(\pi/4 - q_2) - L_3\sin(\pi/4 - q_2 - q_3) \\ 0 \end{bmatrix} \tag{3.14}$$

$${}^0\boldsymbol{p}_4 = \begin{bmatrix} L_4\cos(q_1) \\ L_4\sin(q_1) \\ 0 \end{bmatrix} \tag{3.15}$$

Imposing ${}^0\boldsymbol{p}_5 = {}^0\boldsymbol{p}_4$ we get:

$$\begin{cases} L_1\cos(\pi/4) + L_2\cos(\pi/4 - q_2) + L_3\cos(\pi/4 - q_2 - q_3) = L_4\cos(q_1) \\ -L_1\sin(\pi/4) - L_2\sin(\pi/4 - q_2) - L_3\sin(\pi/4 - q_2 - q_3) = L_4\sin(q_1) \end{cases} \tag{3.16}$$

These equations solve the four-bar linkage direct geometric model. Developing the translation constraint equations, passive joint angles (q_2 and q_3) are expressed in function of the active joint $q1$, while the cut joint angle (q_4) is obtained thanks to the rotation constraint.

The presented methods represent two reliable approaches to solve the direct geometric problem of a closed loop structure. The first method is fast and effective for simple mechanisms while it could be more problematic for complicated robots. On the contrary, the second approach is methodical and applicable at any degree of complexity. However, it is more laborious to be employed on simple structures and its constraint equations are not always analytically solvable.

In the next sections, equations 3.9 are used to develop the first and second order kinematic constraints and the dynamic model. The cut joint is not reported hereafter since its position, velocity and acceleration can be determined using Equation 3.13 and its time derivatives.

3.1.1.3 First and Second order kinematic constraints

Distinguishing the joint variables (shown in Figure 3.3) among active (q_a), passive (q_p) and cut (q_c), the joint vector can be written as follows:

$$\boldsymbol{q} = \begin{bmatrix} q_a \\ \boldsymbol{q}_p \\ q_c \end{bmatrix} = \begin{bmatrix} q_1 \\ q_2 \\ q_3 \\ q_4 \end{bmatrix} \tag{3.17}$$

Due to the geometric constraints, passive (q_2 and q_3) and cut (q_4) joint angles depend on the active joint (q_1). Thanks to the rotation constraint the cut joint is easily obtained in function of active and passive joints while, the last, are computed as follows:

$$\begin{aligned} q_2 &= \pi - \eta_2 = \pi - \beta_1 + \beta_2 \\ q_3 &= -\pi + \eta_3 \end{aligned} \tag{3.18}$$

where η_2, β_1 and β_2 are defined in Equation 3.9 and η_3 is the angle between $\overline{BC}$ and $\overline{CD}$ computed as:

$$\eta_3 = \cos^{-1}\left(\frac{L_2^2 + L_3^2 - s_1^2}{2L_2L_3}\right) \tag{3.19}$$

First order kinematic constraint equations. Fist order kinematic constraints are computed analytically differentiating the geometric constraint equations:

$$\begin{aligned} \dot{q}_2 &= \frac{L_1L_4}{2s_1^3}\sin\left(\frac{\pi}{4}+q_1\right)\left(-\frac{s_1^2+L_3^2-L_2^2}{L_2\sqrt{1-d_{21}^2}} + \frac{s_1^2+L_4^2-L_1^2}{L_1\sqrt{1-d_{22}^2}}\right)\dot{q}_1 \\ \dot{q}_3 &= \frac{L_1L_4}{L_2L_3\sqrt{1-d_3^2}}\sin\left(\frac{\pi}{4}+q_1\right)\dot{q}_1 \end{aligned} \tag{3.20}$$

where:

$$\begin{aligned} d_{21} &= \frac{L_2^2+s_1^2-L_3^2}{2L_2s_1} \\ d_{22} &= \frac{L_1^2+s_1^2-L_4^2}{2L_1s_1} \\ d_3 &= \frac{L_2^2+L_3^2-s_1^2}{2L_2L_3} \end{aligned} \tag{3.21}$$

Second order kinematic constraint equations. Equations 3.20 are differentiated once more to get second order kinematic constraints. To avoid long computations the relation between active and passive joint velocities is written as follows:

$$\dot{q}_j = W_j\dot{q}_a \tag{3.22}$$

where q_j is the j^{th} passive joint. From Equation 3.20:

$$\begin{aligned} W_2 &= \frac{L_1L_4}{2s_1^3}\sin\left(\frac{\pi}{4}+q_1\right)\left(-\frac{s_1^2+L_3^2-L_2^2}{L_2\sqrt{1-d_{21}^2}} + \frac{s_1^2+L_4^2-L_1^2}{L_1\sqrt{1-d_{22}^2}}\right) \\ W_3 &= \frac{L_1L_4}{L_2L_3\sqrt{1-d_3^2}}\sin\left(\frac{\pi}{4}+q_1\right) \end{aligned} \tag{3.23}$$

and the derivative of Equation 3.22 is:

$$\ddot{q}_j = \dot{W}_j \dot{q}_a + W_j \ddot{q}_a \tag{3.24}$$

where $\dot{W}_j$ is the only unknown value.
Consequently, passive joint accelerations are computed as follows:

$$\begin{bmatrix} \ddot{q}_2 \\ \ddot{q}_3 \end{bmatrix} = \begin{bmatrix} \dot{W}_2 \\ \dot{W}_3 \end{bmatrix} \dot{q}_1 + \begin{bmatrix} W_2 \\ W_3 \end{bmatrix} \ddot{q}_1 \tag{3.25}$$

$$\begin{aligned} \dot{W}_2 &= \frac{d}{dt}(W_2) \triangleq \frac{d}{dt}(W_{2a}(-W_{2b}+W_{2c})) = \dot{W}_{2a}(-W_{2b}+W_{2c}) + W_{2a}(-\dot{W}_{2b}+\dot{W}_{2c}) \\ \dot{W}_3 &= \frac{L_1L_4}{L_2L_3}\left(-\frac{d_3 s_1\, \dot{s}_1}{L_2L_3(1-d_3^2)^{3/2}} \sin\left(\frac{\pi}{4}+q_1\right) + \frac{1}{\sqrt{1-d_3^2}} \cos\left(\frac{\pi}{4}+q_1\right)\dot{q}_1\right) \end{aligned} \tag{3.26}$$

where:

$$\begin{aligned} \dot{W}_{2a} &= L_1L_4\left(\frac{1}{s_1}\cos\left(\frac{\pi}{4}+q_1\right)\dot{q}_1 - \frac{\dot{s}_1}{s_1^2}\sin\left(\frac{\pi}{4}+q_1\right)\right) \\ \dot{W}_{2b} &= \frac{d_{21}\dot{d}_{21}}{(1-d_{21}^2)^{3/2}}\left(\frac{s_1^2+L_3^2-L_2^2}{2L_2s_1^2}\right) + \frac{1}{\sqrt{1-d_{21}^2}}\left(\frac{\dot{s}_1(-2L_3^2+2L_2^2)}{2L_2s_1^3}\right) \\ \dot{W}_{2c} &= \frac{d_{22}\dot{d}_{22}}{(1-d_{22}^2)^{3/2}}\left(\frac{s_1^2+L_4^2-L_1^2}{2L_1s_1^2}\right) + \frac{1}{\sqrt{1-d_{22}^2}}\left(\frac{\dot{s}_1(-2L_4^2+2L_1^2)}{2L_1s_1^3}\right) \\ \dot{s}_1 &= \frac{L_1L_4}{s_1}\sin\left(\frac{\pi}{4}+q_1\right)\dot{q}_1 \end{aligned} \tag{3.27}$$

3.1.1.4 Dynamic model

The Recursive Newton-Euler Algorithm (RNEA) presented in Annex B is adopted to solve the Inverse Dynamic Model (IDM). In particular, an open-source modified version of this algorithm, based on spatial vectors, proposed by Roy Featherstone [121] and implemented by a collaboration between LAAS-GEPETTO and Aldebaran - SoftBank Group [122] has been used. The algorithm returns the vector of joint torques that are needed to track desired joint position, velocity and acceleration trajectories and to exert desired external forces on the environment. The algorithm works on serial chains and tree robots. Since the DH parameters open the four-bar linkage in a tree robot composed by two serial chains, this method computes the joint torques of the equivalent tree structure. To determine the active joint torque of the closed loop it is necessary to:

- Solve the IDM for the equivalent tree robot giving joint position, velocity and acceleration trajectories that satisfy the geometric and kinematic constraints;
- Add forces and moments between the links adjacent to the cut joints as external forces and moments.

The dynamic model has the following form:

$$\boldsymbol{\Gamma}_{cl} = \boldsymbol{\Gamma}_{tr} + \sum_{k=1}^{B}(\boldsymbol{J}_k^T \boldsymbol{F}_k - \boldsymbol{J}_{k+B}^T \boldsymbol{F}_k) \tag{3.28}$$

where:

- $\boldsymbol{\Gamma}_{cl}$: joint torques of the closed loop;
- $\boldsymbol{\Gamma}_{tr}$: joint torques of the equivalent tree structure;
- $\boldsymbol{F}_k$: external forces and torques between links adjacent to the cut joints.

with:

$$\boldsymbol{\Gamma}_{cl} = \begin{bmatrix} \boldsymbol{\tau} \\ \mathbf{0}_p \end{bmatrix} \tag{3.29}$$

where $\boldsymbol{\tau}$ is the torque vector of actuated joints in the closed loop and $\mathbf{0}_p$ is the torque vector of the passive ones.

To solve Equation 3.28 the Lagrangian-based method proposed by [114] is used. The Lagrange formulation describes the robot dynamics in terms of work and energy stored in the system. The robot Lagrangian is defined as:

$$L = E - U \tag{3.30}$$

where E is the kinetic energy and U is the potential energy. The following Lagrange equation describes the dynamic behavior of a serial robot:

$$\boldsymbol{\Gamma} = \frac{d}{dt}\left(\frac{\partial L}{\partial \dot{\boldsymbol{q}}}\right)^T - \left(\frac{\partial L}{\partial \boldsymbol{q}}\right)^T \tag{3.31}$$

To compute the active joint torques in the four-bar linkage, closed loop constraint equations ($\phi(\boldsymbol{q}_{tr}) = 0$) must be added:

$$\boldsymbol{\Gamma} = \frac{d}{dt}\left(\frac{\partial L}{\partial \dot{\boldsymbol{q}}_{tr}}\right)^T - \left(\frac{\partial L}{\partial \boldsymbol{q}_{tr}}\right)^T + \left(\frac{\partial \phi(\boldsymbol{q}_{tr})}{\partial \boldsymbol{q}_{tr}}\right)^T \boldsymbol{\lambda} \tag{3.32}$$

where $\boldsymbol{\lambda}$ is the Lagrange multiplier vector ($\boldsymbol{\lambda} = [\lambda_1, \ldots, \lambda_p]$) and p is the number of independent constraining functions of the closed loop which coincides with the number of passive joints. Lagrange multipliers are added to the Lagrangian variables (joint angles and velocities) and they represent the external forces at the cut joint required to impose the loop constraint. The equation can be rewritten as:

$$\boldsymbol{\Gamma}_{\boldsymbol{cl}} = \boldsymbol{\Gamma}_{\boldsymbol{tr}} + \left(\frac{\partial \phi(\boldsymbol{q}_{\boldsymbol{tr}})}{\partial \boldsymbol{q}_{\boldsymbol{tr}}}\right)^T \boldsymbol{\lambda} \tag{3.33}$$

Distinguishing between active and passive joints, the derivative of loop constraint equations can be written as:

$$\frac{\partial \phi(\boldsymbol{q}_{tr})}{\partial \boldsymbol{q}_{tr}} \dot{\boldsymbol{q}}_{tr} = \begin{bmatrix} \boldsymbol{W}_a & \boldsymbol{W}_p \end{bmatrix} \begin{bmatrix} \dot{\boldsymbol{q}}_a \\ \dot{\boldsymbol{q}}_p \end{bmatrix} = 0 \tag{3.34}$$

or equivalently:

$$\dot{\boldsymbol{q}}_p = -\boldsymbol{W}_p^{-1} \boldsymbol{W}_a \dot{\boldsymbol{q}}_a = \boldsymbol{W} \dot{\boldsymbol{q}}_a \tag{3.35}$$

where $\boldsymbol{W}$ coincides with the matrix obtained by rewriting Equation 3.22 in matrix form.

Then, on the base of Equation 3.34 and the virtual work principle, Equation 3.33 can be rewritten as:

$$\boldsymbol{\Gamma}_{\boldsymbol{cl}} = \begin{bmatrix} \boldsymbol{\tau}_a \\ \mathbf{0}_p \end{bmatrix} = \begin{bmatrix} \boldsymbol{\Gamma}_{tr_a} \\ \boldsymbol{\Gamma}_{tr_p} \end{bmatrix} + \begin{bmatrix} \boldsymbol{W}_a^T \\ \boldsymbol{W}_p^T \end{bmatrix} \boldsymbol{\lambda} \tag{3.36}$$

which are n equations ($n = L - B$) with N (active joint torques τ) plus p (Lagrange multipliers $\boldsymbol{\lambda}$) unknowns. Lagrange multipliers are solved using the last p equations while the first N determine the active joint torques:

$$\begin{aligned} \boldsymbol{\lambda} &= -\boldsymbol{W}_p^{-T} \boldsymbol{\Gamma}_{tr_p} \\ \boldsymbol{\tau}_a &= \boldsymbol{\Gamma}_{tr_a} - \boldsymbol{W}_a^T \boldsymbol{W}_p^{-T} \boldsymbol{\Gamma}_{tr_p} \\ &= \boldsymbol{\Gamma}_{tr_a} + \boldsymbol{W}^T \boldsymbol{\Gamma}_{tr_p} \end{aligned} \tag{3.37}$$

Rewriting $\boldsymbol{\tau}_a$ as $\boldsymbol{\tau}$, the final equation is:

$$\boldsymbol{\tau} = \begin{bmatrix} \boldsymbol{I}_N & \boldsymbol{W}^T \end{bmatrix} \begin{bmatrix} \boldsymbol{\Gamma}_{tr_a} \\ \boldsymbol{\Gamma}_{tr_p} \end{bmatrix} = \boldsymbol{G}^T \boldsymbol{\Gamma}_{tr} \tag{3.38}$$

where $\boldsymbol{I}_N$ is an identity square matrix of size N, $\boldsymbol{W}$ is the derivative of passive joint angles with respect to the actives ones and $\boldsymbol{G}$ is the derivative of $\boldsymbol{q}_{tr}$ with respect to the active joint angles ($\boldsymbol{q}_a$).
In conclusion, the IDM of the inverted four-bar linkage is solved following these steps:

1. the IDM for the equivalent tree is computed using the RNEA algorithm;
2. matrix $\boldsymbol{G}$ is determined according to loop constraints;
3. the active joint torque (q_1) is computed according to Equation 3.38.

Note that $\boldsymbol{W} = \begin{bmatrix} W_2 \\ W_3 \end{bmatrix}$, where W_2 and W_3 are defined in Equation 3.23.

3.1.2 Thumb model

The thumb has three independent DoFs. The first allows its opposition to the reminder fingers, and the second and third allow its flexion and extension. The lasts are kept independent to increase the reachability and opposability of the mechanism. The thumb is considered as the integration of a serial chain with an inverted four-bar linkage placed at the MCP joint (Figure 3.5). The serial chain is modeled using classical geometric, kinematic and dynamic models while the inverted four-bar linkage is modeled as previously explained. The DH parameters of the thumb are shown in Table 3.2. Parameters d_1 and d_2 (not shown in the picture) are the distances between the origins of R_1 (frame 1) and R_2 (frame 2) and between the origins of R_2 and R_3 respectively. As it can be seen, the four-bar linkage is modeled as a tree robot composed by two chains with a common root on R_2. Parameters L_{14}, γ_{14} and θ_{14} (shown in Figure 3.6) are necessary to locate R_4, the base of the second chain. Their values are computed as follows:

$$\begin{aligned} L_{jk} &= \sqrt{L_{ji}^2 + L_{ik}^2 - 2L_{ji}L_{ik}\cos\left(\frac{3}{4}\pi\right)} \\ \theta_{jk} &= \cos^{-1}\left(\frac{L_{jk}^2 + L_{ik}^2 - L_{ji}^2}{2L_{jk}L_{ik}}\right) \\ \gamma_{jk} &= \frac{\pi}{4} - \theta_{jk} \end{aligned} \tag{3.39}$$

j	a_j	μ_j	σ_j	γ_j	α_j	d_j	θ_j	r_j
1	0	1	0	0	0	0	q_1	0
2	1	1	0	0	$\pi/2$	d_1	q_2	0
3	2	1	0	0	0	d_2	q_3	0
4	2	0	0	$-\gamma_{14}$	0	L_{14}	$q_4 - \theta_{14}$	0
5	4	0	0	0	0	L_2	q_5	0
6	3	0	0	0	0	L_4	q_6	0
7	5	0	2	0	0	L_3	$3/4\pi$	0

Table 3.2 – Thumb DH parameters.

3.1.3 Finger model

Index, middle, ring and little fingers share all the same kinematic structure. They are modeled as complex chains composed by two four-bar linkages in cascade (Figure 3.7). The MCP joint drives the

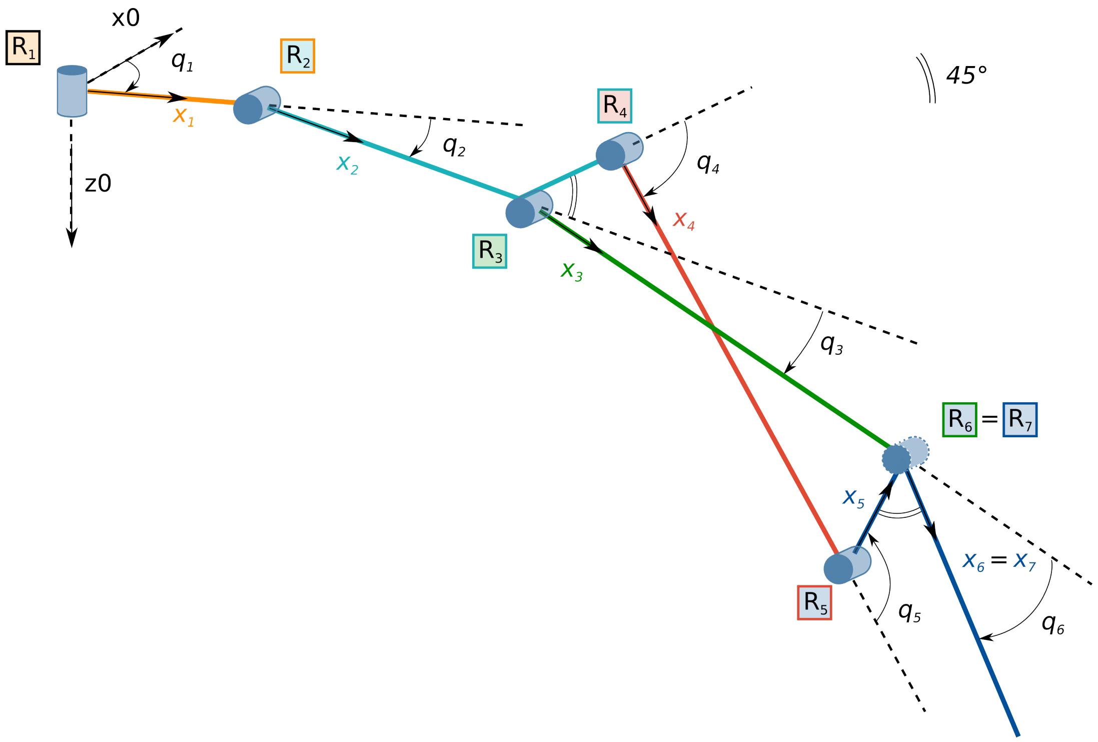

Figure 3.5 – Thumb geometric model using the modified Denavit-Hartenberg notations.

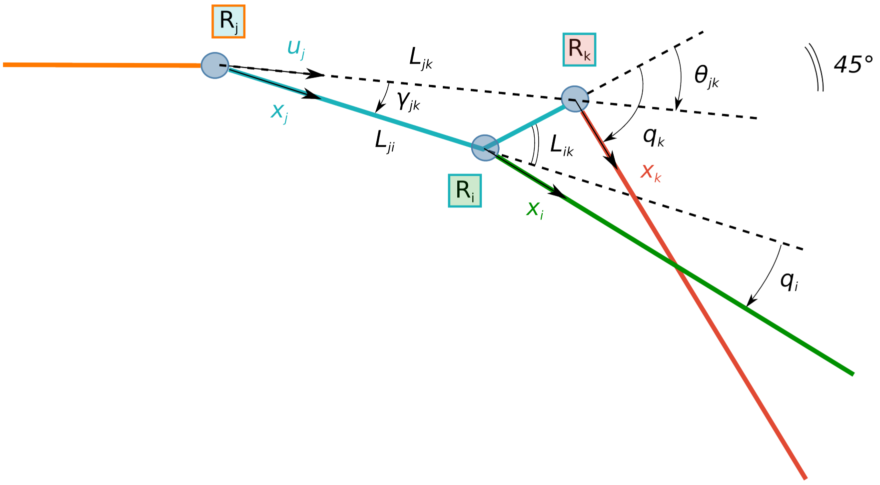

Figure 3.6 – DH parameters in case of common root.

first loop which subsequently moves the second loop. Geometric first order and second order kinematic constraints are the ones presented in Section 3.1.1, where it is simply necessary to solve the first loop to obtain the input variables for the second one. The dynamic model is computed according to Equation 3.38 where, in this case, $\boldsymbol{W}$ gathers the kinematic constraints of both loops ($\boldsymbol{W}_{\mathrm{DL}}$). Calling the first loop $1L$ and the second $2L$:

$$\begin{bmatrix}\dot{q}_2\\ \dot{q}_3\end{bmatrix} = \boldsymbol{W}_{1L}\dot{q}_1 \qquad \begin{bmatrix}\dot{q}_4\\ \dot{q}_5\end{bmatrix} = \boldsymbol{W}_{2L}\dot{q}_6 \tag{3.40}$$

and defining the derivative between q_6 and q_1 as W_6:

$$\begin{bmatrix}\dot{q}_2\\ \dot{q}_3\\ \dot{q}_4\\ \dot{q}_5\end{bmatrix} = \begin{bmatrix}\boldsymbol{W}_{1L}\\ \boldsymbol{W}_{2L}W_6\end{bmatrix}\dot{q}_1 \tag{3.41}$$

$$\dot{\boldsymbol{q}}_p = \boldsymbol{W}_{\mathrm{DL}}\ \dot{q}_a$$

where W_6 is obtained from the kinematic rotation constraint (time derivative of Equation 3.13):

$$W_6 = W_{1L_1} + W_{1L_2} - 1 \tag{3.42}$$

Note that W_{1L_1} and W_{1L_2} are the first and the second element of matrix W_{1L} respectively.
Hence, τ_a (τ_1) is computed as follows:

$$\tau_a = \begin{bmatrix}1 & \boldsymbol{W}_{\mathrm{DL}}^T\end{bmatrix}\begin{bmatrix}\Gamma_{tr_a}\\ \boldsymbol{\Gamma}_{tr_p}\end{bmatrix} = \boldsymbol{G}_{\mathrm{DL}}^T\boldsymbol{\Gamma}_{tr} \tag{3.43}$$

Table 3.3 collects the DH parameters of fingers. Note that length notations are coherent with the ones defined for the four-bar linkage structure in Figure 3.4.

j	a_j	μ_j	σ_j	γ_j	α_j	d_j	θ_j	r_j
1	0	1	0	0	0	0	q_1	0
2	0	0	0	$-\pi/4$	0	L_{1A}	q_2	0
3	2	0	0	0	0	L_{2A}	q_3	0
4	1	0	0	$-\gamma_{14}$	0	L_{14}	$q_4 - \theta_{14}$	0
5	4	0	0	0	0	L_{2B}	q_5	0
6	1	0	0	0	0	L_{4A}	q_6	0
7	6	0	0	0	0	L_{4B}	q_7	0
8	3	0	2	0	0	L_{3A}	$3/4\pi$	0
9	5	0	2	0	0	L_{3B}	$3/4\pi$	0

Table 3.3 – DH parameters for Index, Middle, Ring and Little fingers.

The resultant non-linear coupling between finger joints is shown in a series of snapshots in Figure 3.8. Figure 3.9a, 3.9b and 3.9c shows positions, velocities and accelerations of MCP, PIP and DIP joints of

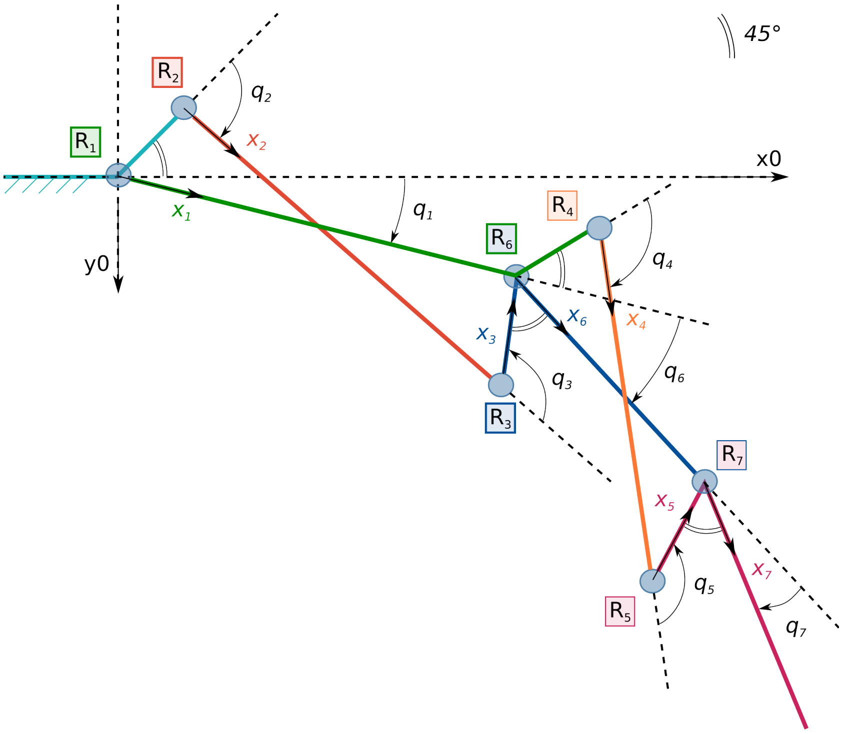

Figure 3.7 – Index, middle, ring and little fingers geometric models.

the middle finger starting from the open flat hand configuration with fingers perpendicularly stretched against gravity. The curves result from a time-constrained bang-bang trajectory with target position at 90 [deg] and a required time of 1 [s]. In this case, joint velocity and acceleration limits are chosen to show the effect of no constant velocity phase. Figure 3.9d highlights the non-linear relation between the MCP and DIP joints of the middle finger, and Figure 3.10 shows the correspondent active joint torque at the middle base computed through the previously described IDM.

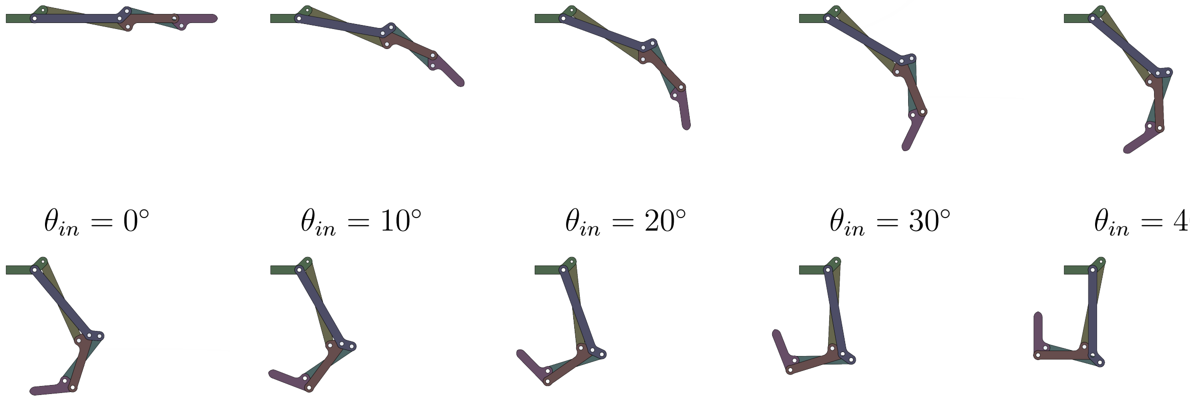

$\theta_{in} = 0°$ $\theta_{in} = 10°$ $\theta_{in} = 20°$ $\theta_{in} = 30°$ $\theta_{in} = 40°$

$\theta_{in} = 50°$ $\theta_{in} = 60°$ $\theta_{in} = 70°$ $\theta_{in} = 80°$ $\theta_{in} = 90°$

Figure 3.8 – Fully coupled finger model with non-linear reduction ratios between joints. In this series of snapshots the finger flexes from 0° - aligned configuration - to 90° - closed configuration.

3.2 Actuation

E-motion motors and associated gearboxes are sized in order to compensate finger weights at most. This choice is dictated by the fact that to perform hand gestures no high torques are necessary. In

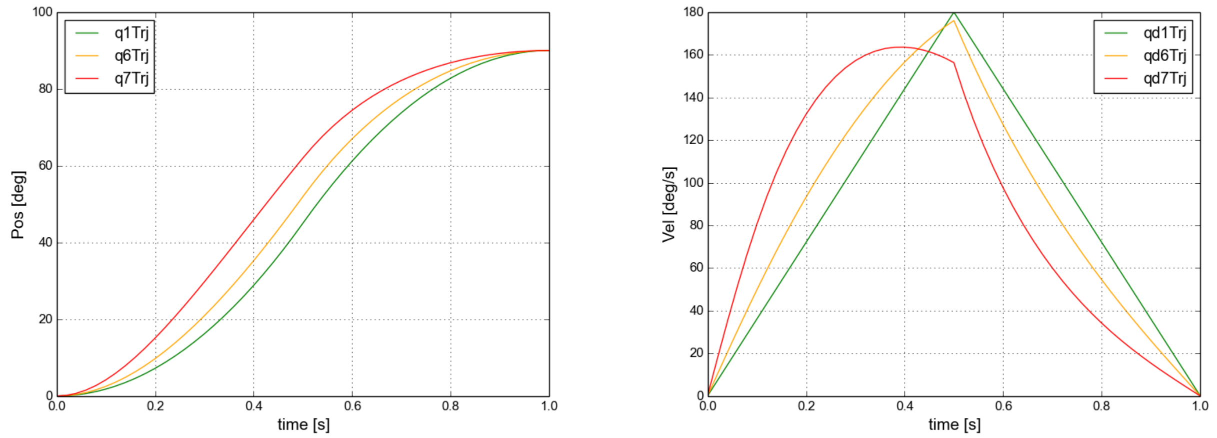

(a) Joint position trajectories.

(b) Joint velocity trajectories.

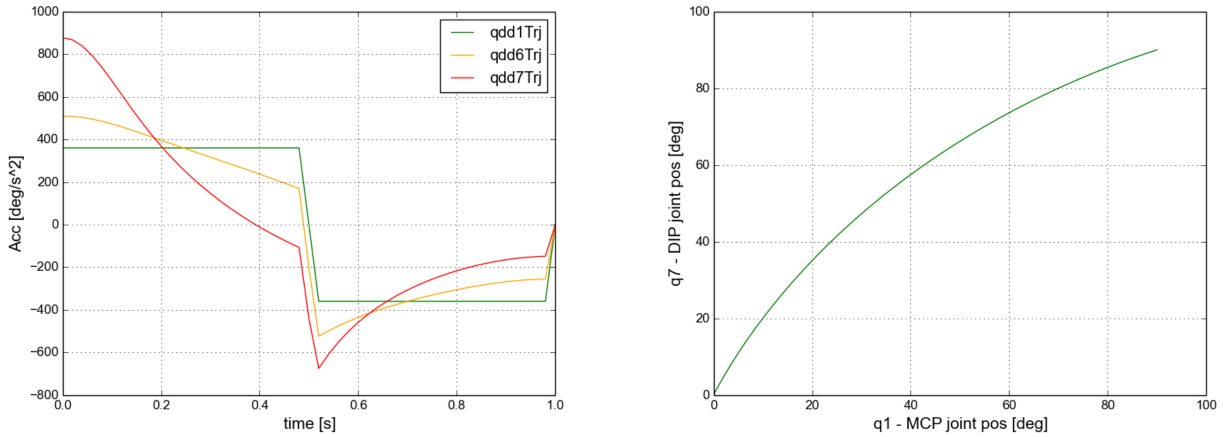

(c) Joint acceleration trajectories.

(d) MCP-DIP joint motion coupling.

Figure 3.9 – Middle finger joint trajectories during free motion - positions, velocities and accelerations curves of MCP, PIP and DIP joints are presented together with the explicit non-linear coupling between MCP and DIP joints.

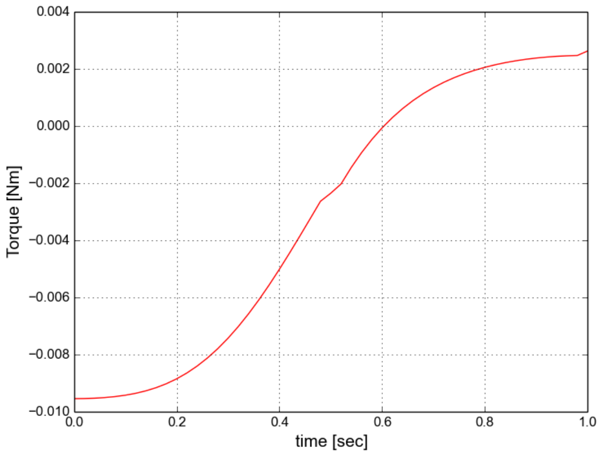

Figure 3.10 – Active joint torque trajectory.

addition, such torques can be obtained by small motors and gearboxes which ease integration and ensure sensor-less force feedback (see Annex C) - thanks to their high transparency (mechanical efficiency) which also ensures high backdrivability. E-motion motors and gearboxes are chosen in function of the minimum torque required at each active joint, their prices (which must be reasonably low) and the volume available at the finger bases and within the thumb carpal and metacarpal phalanges.

3.2.1 Required torque

Active joint torques are computed differently orienting the hand (with all digit stretched) so to impose the full weight of their kinematic chains. More specifically, joint torques at finger MCP joints and at the abduction/adduction (palm opposition) joint of the thumb are characterized by aligning the z axis of the wrist frame (shown in Figure 2.4) in opposition to gravity while, RC and MCP joint torques of the thumb are computed aligning the y axes of their frames (R_2 and R_3 in Figure 3.5) parallel to gravity. Table 3.4 collects the torques at each active joint.

	Thumb	Index/Ring	Middle	Little
$\tau_{RCabd/add}$ [mNm]	19	-	-	-
$\tau_{RCflex/ext}$ [mNm]	10	-	-	-
τ_{MCP} [mNm]	5	9	10	7

Table 3.4 – Active joint torques to compensate finger weights - rounded up to the nearest unit.

3.2.2 Motor and gearbox selection

For simplicity, e-motion motors are chosen all equal. The BLDC EC 14 flat Maxon motor is adopted for its small size and lightweight (see Table 3.5). It presents an external-rotor (outrunner) configuration: the stator coils form the center (core) of the motor, while the permanent magnets spin within an overhanging rotor which surrounds the core. This typically embeds more poles and has a higher torque at low speeds.

	Size [mm]	Power [W]	τ_n [i] [mNm]	τ_s [ii] [mNm]	weight [g]
BLDC EC 14 flat	⌀ 13.6 x 11.7 [iii]	1.5	1.81	3.8	8

[i] nominal torque [ii] stall torque [iii] shaft excluded

Table 3.5 – Characteristics of e-motion motors.

Torque requirements are satisfied by adopting custom made gearings. Bevel gears are employed at the motor shafts to re-orient actuators orthogonally with respect to the first driven joint. This is done at the finger bases and at the MCP joint of the thumb to better fit the motor within the palm and the thumb phalanx. Two stages gearboxes with 7.44 of reduction are embedded at the finger bases. As a rule of thumb, the mechanical transmission efficiency of a gearbox is about 0.9 per stage. This means that the output torque at the MCP joints is nearly 11 [mNm] in correspondence of the nominal motor torque - which is slightly larger than the maximum torque required by the middle finger. For the thumb, different reduction ratios are adopted. Their values and the theoretical torques provided at nominal motor torques are reported in Table 3.6. Figure 3.11b highlights motors and gear trains for a generic finger and the thumb.

	RC abd/add	RC flex/ext	MCP
i^{i}	17.4:1	10.2:1	3.4:1
$\hat{\tau}_n{}^{\text{ii}}$ [mNm]	25.5	15	5.5

[i] reduction ratio [ii] estimated nominal torque

Table 3.6 – Thumb theoretical active joint torques in correspondence of nominal motor torque.

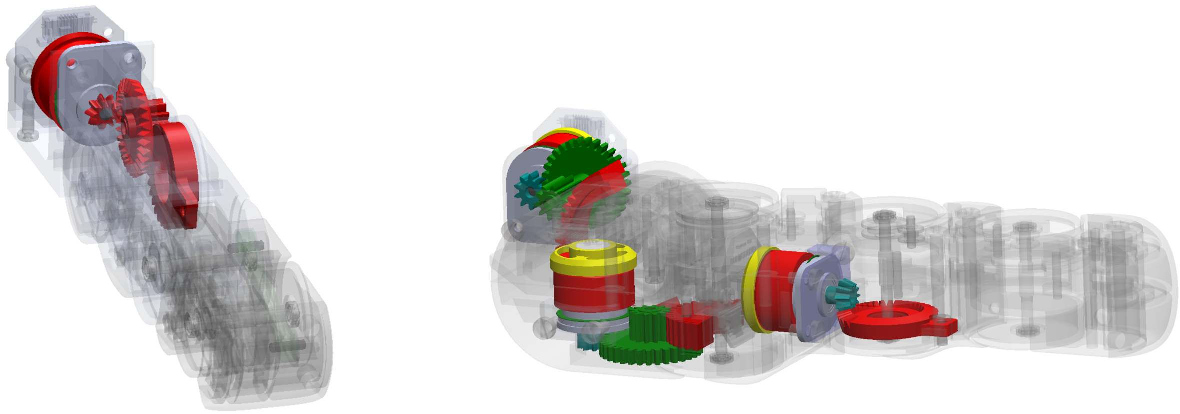

(a) Gear train for a generic finger. (b) Gearing for the three active thumb joints.

Figure 3.11 – Finger and thumb gearboxes.

3.3 Control

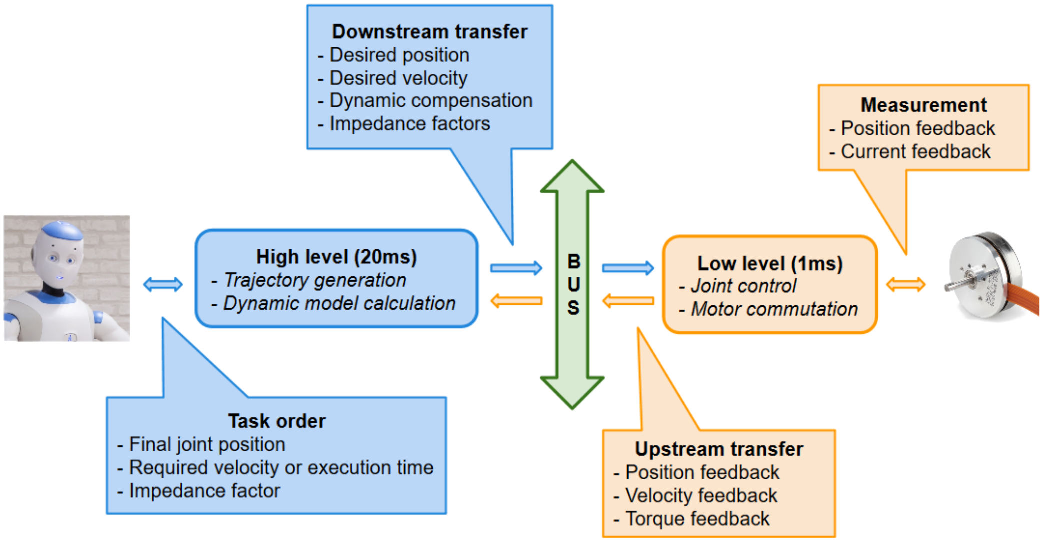

Figure 3.12 – General communication scheme of e-motion control in joint space.

The sensory apparatus of the hand is simplified to the minimum set necessary to control finger motions. No tactile sensors are applied on the fingertips, no pressure sensors on the palm and phalanges and no torque sensors at joints. Each e-motion motor is controlled at 1 [KHz] by a standard PD position controller, a torque feed-forward and an impedance controller. Positions are measured through AMS *AS5048* magnetic rotary encoders (MRE 14-bit) which provide accurate high-resolution absolute angular positions of each motor. The angle is detected through Hall sensors which measure the magnetic field of a diametric *NdFeB* magnet fixed on the outrunning rotor at an experimentally determined distance (see Annex D). Joint velocities are estimated (at low level) from encoder position measurements with linear tracking loops (a type of low-pass filter). The torque feed-forward is added to compensate the dynamic effects of finger motions in order to improve the tracking performance all along the motion range. Dynamic compensation is remotely computed on a central board (ATOM E3845) on the base of measured positions and desired velocities and accelerations, and is sent to the respective motor boards every 20 [ms]. Figure 3.12 resumes the overall communication scheme.

3.3.1 Motor commutation

A fine torque control is mandatory to efficiently exploit the actuation power. This is done by mean of the Field oriented Control (FoC) [123] implemented on the motor boards. This method, also called vector control, allows to directly control the motor through a single current input thanks to the Clark and Park transforms. These express the three-phase current from the static reference frame of the stator windings to the rotating two-axis reference frame of the rotor. The last is defined with one axis directed along the rotor magnetic field (d axis) and the other placed in quadrature (q axis), so that the coordinate change directly expresses the effects of stator currents on the output torque. With this coordinate change, torque efficiency is maximized by imposing the direct component to zero and the quadrature component to the desired torque (τ^* converted to current i_q^*). Two PI controllers ensure to track both desired values. Figure 3.13 resumes the motor commutation scheme. Even though this approach requires fast computational capabilities, since reference frame transforms (direct and inverse) have to be computed at each control cycle according to the rotor position, the FoC offers a continuous and accurate torque control at any speed. Indeed, it ensures no torque losses and ripples typical of trapezoidal control, which normally presents discontinuities and inaccuracies at low speeds. Furthermore, it has no torque losses at high speeds contrarily to the sinusoidal control, thanks to the fact that its PI controllers do not operate on time dependent signals but directly on DC currents.

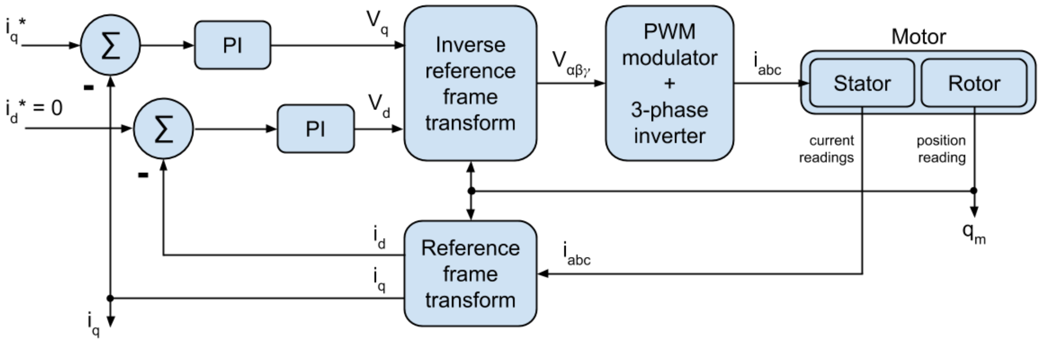

Figure 3.13 – FoC scheme - adapted from [124].

3.3.2 Joint control

Figure 3.14 shows the e-motion control scheme implemented to drive active finger joints. Hereafter, its different components are highlighted and presented.

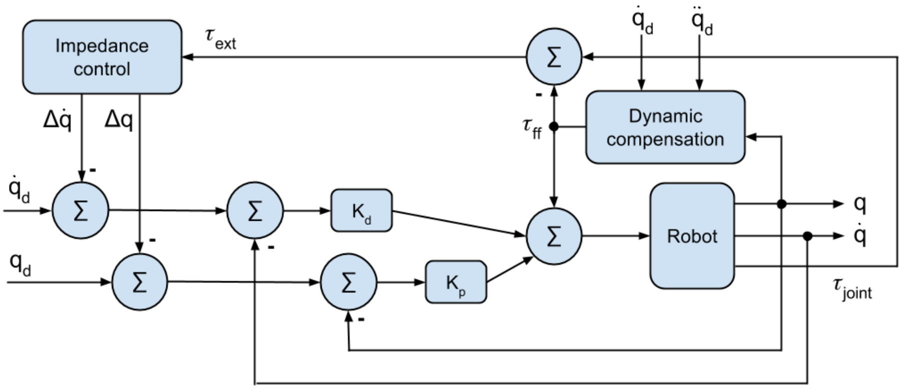

Figure 3.14 – E-motion control scheme at joint space.

PD controller with dynamic feed-forward. Joints are controlled in position and velocity by a classic PD controller with dynamic feed-forward compensation [125] as shown in Figure 3.15. Variables q_d and $\dot{q}_d$ are the desired joint position and velocity, while q and $\dot{q}$ are the current joint position and velocity. The dynamic feed-forward consists in the dynamic model compensation (IDM previously presented), which takes as input the joint trajectory (q, $\dot{q}_d$, $\ddot{q}_d$) and cancels out dynamic effects in the controller. Its effectiveness strictly depends on the model accuracy. Note that desired velocity and acceleration rather than current values are adopted to avoid noisy derivatives of measured joint positions.

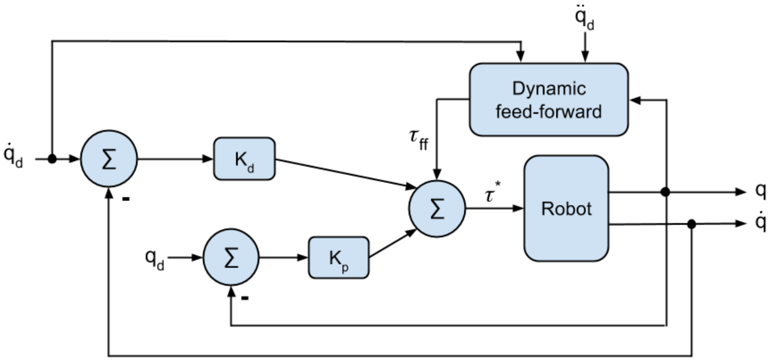

Figure 3.15 – PD control with dynamic compensation.

The Robot block. The joint torque given as input to the Robot block is converted to motor torque through an accurate gearbox model in its inverse formulation, as shown in Figure 3.16. This consists in an improved gearbox model which reliably simulates the stick-slip effects according to the sign of the power ($P = \tau\dot{q}$). Its formulation is presented in Annex C. The model is identified at $\omega = 0$ (motor angular velocity) and adopted at any motor speed, even though mesh and bearing friction coefficients are speed dependent. This is acceptable since motor speed remains low due to the small gearbox reduction ratio. To properly estimate the motor torque it is important to provide the correct power sign. This is done by using the last measured motor torque from current readings and the difference $q_d - q$, more robust than $\dot{q}$ derived from motor position measurements. The direct formulation of the gearbox model estimates the joint torque from the motor torque. The last is equal to the motor current multiplied by the torque coefficient (K_T). The motor current is measured through 10-bit ADC, based on sensing resistors in series with the motor phases.

Joint position (q) is estimated from the measured motor position (q_m). This is done dividing the motor position by the gearbox reduction ratio (i) and by counting the number of motor turns from the initial configuration. Indeed, due to the mechanical reduction more than one turn is required to completely cover the joint workspace. This requires to define an initial configuration at which the joints must be placed during the calibration process. The last is performed every time the hand controller is turned on. The initial configuration is defined by joint mechanical stops: fingers stretched (0°) and thumb aligned in the palm plane and hyper-extended (0°, -20°, 0°).

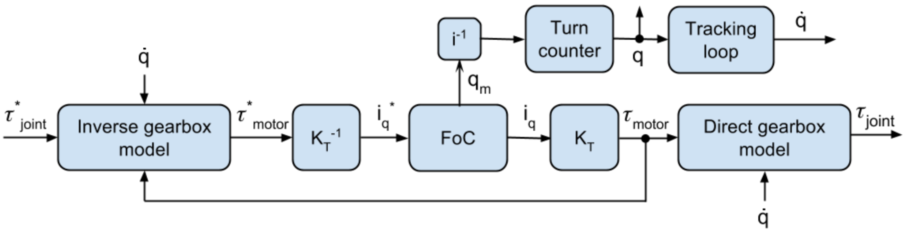

Figure 3.16 – The Robot block expanded.

Impedance control. Bring safety in physical human-robot interaction has become one of the most important topics in robotics research over the past few years. In contrast to the widely used stiff-actuators, Variable Impedance Actuators (VIA) are introduced to obtain compliant interaction for unstructured, dynamic and often unpredictable environments. There exists a large variety of different VIA design as summarized in [126]. In general, they offer safe interaction through passive or active compliance. Passive compliance contains at least one passive elastic element in series with the actuator and the end effector, providing a fast response time to impacts. Elastic elements with fixed stiffness are often cheap and simple to integrate in the mechanical design. However, they do not grant a large field of application as their are normally dimensioned for specific tasks. Elastic elements with variable stiffness solve this drawback but require additional actuators and introduce higher mechanical and control complexities. Active compliance emulates elastic behavior by software. Controllers are processed at fast rates to provide smooth and fact reactions, but no shocks can be immediately absorbed at impact due to their limited bandwidths. In addition, no energy can be stored as no physical passive elements are adopted. An advantage of active compliance is the scalability of damping and stiffness parameters which are easily adjustable to fit application requirements. One of the oldest and well-known VIA is the active impedance by control introduced by Hogan [127] which implements a dynamic relation between the end effector position and force.

The impedance action is added on top of this existing controller. It deviates position and velocity setpoints in order to provide a mass-spring-damper behavior as soon as an external torque is detected. This is expressed as:

$$\tau_{ext} = I_{AI}\Delta\ddot{q} + D_{AI}\Delta\dot{q} + K_{AI}\Delta q \tag{3.44}$$

where I_{AI}, D_{AI} and K_{AI} are respectively the active impedance coefficients of the inertia (mass), damper and spring components. These are chosen from the high-level controller according to the task to be performed. The external torque estimation (τ_{ext}) is computed subtracting the feed-forward joint torque (τ_{ff}) from the estimated joint torque as suggested in [128] and shown in Figure 3.14. Figure 3.17 shows the block scheme of the impedance controller.

Cogging torque compensation. In BLDC stator windings are wounded around ferromagnetic parts called teeth. These amplify the magnetic field generated by the coils when activated. The space between the slots in which the windings are located is called slots. Cogging torque is typical of permanent-magnet motors due to the alternation of teeth and slots. It consists in a undesired inherent torque ripple induced by the interaction between permanent magnets on the rotor and the slots on the stator. Indeed, the permanent magnets on the rotor continuously search for minimum reluctance position. Since teeth have significantly lower reluctance than slots, the rotor always tends to align with the teeth and a deviating torque is produced when permanent magnets face the slots. Cogging torque varies in function of the

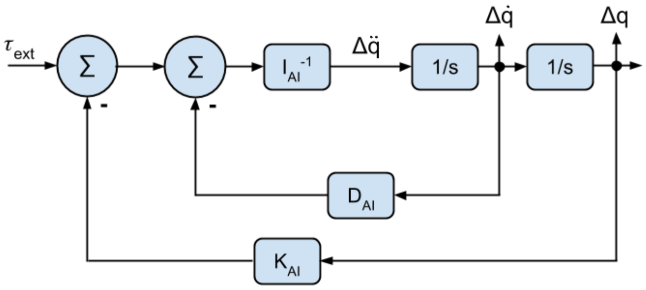

Figure 3.17 – Impedance control scheme.

rotor position and it is periodic in a mechanical turn. Its period between two slots (m) depends on the number of slots and rotor poles:

$$m = \frac{2N_p}{hcf(N_s, 2N_p)} \tag{3.45}$$

where N_p is the number of pole pairs, N_s is the number of slots and hcf is the Highest Common Factor. For the EC32 for example, $N_p = 4$ and $N_s = 6$, leading to $m = 4$ and consequently 24 cogging periods (mN_p) in a complete mechanical turn. Cogging torque is caused by the permanent magnetic field and it also exists when the stator is unexcited. Indeed, it can be felt by discrete rotor steps when the rotor is rotated by hand (see Figure 3.18). These steps can cause audible noise and mechanical vibrations.

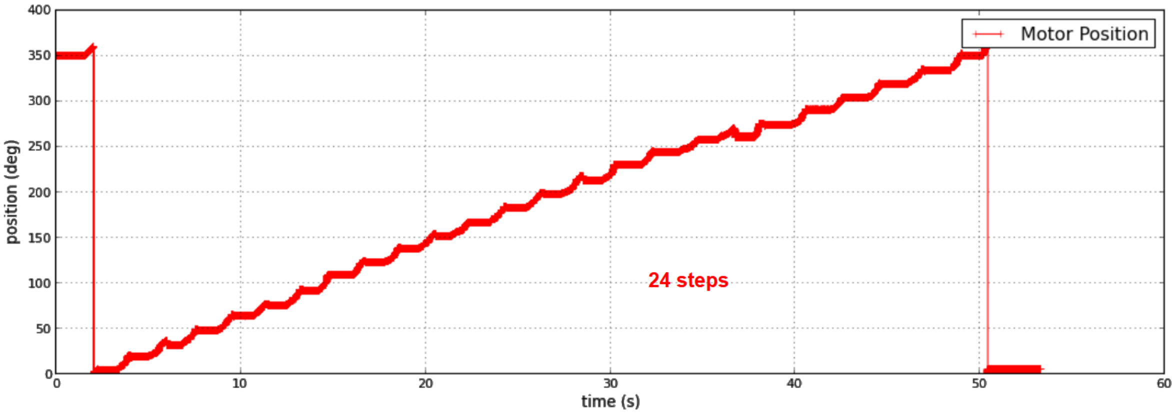

Figure 3.18 – Steps identified by moving the rotor of an EC32 Maxon motor by hand over one mechanical turn.

In practice, cogging torque is not easy to be eliminated but it can be highly reduced. Different approaches exist to reduce the cogging torque during the mechanical design of the motor, e.g. changing the shape and size of magnets, adding dummy stator slots, shifting magnets [129, 130]. In this context, since off-the-shelf Maxon motors are adopted, cogging torque is reduced by active compensation. The aim of active compensation is to increase accuracy of the overall motor control and to allow the motor to turn as smooth as possible at very low speeds. Cogging torque effects are attenuated by adding a sinusoid as torque feed-forward. Its frequency is chosen according to Equation 3.45 while its amplitude is experimentally determined. Obviously, this approach does not cancel out the undesired torque ripples but it attenuates cogging effects. Better performance might be obtained by identifying the cogging torque of each motor. However, this would require an identification process any time a motor is replaced and a large storage space on the motor board to accurately compensate it.

3.3.3 Trajectory generation

Desired joint positions and velocities are computed by a classic Bang-bang trajectory generator characterized by three phases: an acceleration phase, a constant velocity phase and a deceleration phase. These provide a trapezoidal velocity shape and a smooth position trajectory. In particular, given a target joint position, two types of trajectories are provided:

— a time constrained trajectory;
— a velocity constrained trajectory.

The first is computed to ensure the joint motion from the starting position to the target one in the desired time. It uses the maximum joint acceleration during acceleration and deceleration phases and it respects the maximum joint velocity. Figure 3.19a shows a generated joint trajectory to move from 0° to 90° in 1 [s]. When the required time imposes to reach actuation limits, the trapezoidal velocity model degenerates to a triangular shape - meaning that no constant velocity phase is adopted. If the target position cannot be reached even attaining acceleration and velocity limits, the time constraint is not respected. Maximum velocities and accelerations are still adopted to reach the demanded position in the shortest feasible time. The second type of trajectory ensures the demanded velocity during the constant speed phase. By using the maximum joint acceleration it computes the acceleration and deceleration times to move to the target position in the shortest time and at the desired speed (see Figure 3.19b). If the demanded velocity is higher than the joint velocity limit, the maximum velocity is adopted.
Joint trajectories are provided by a discretized version of the trajectory generator algorithm to the previously described controller. Samples are sent every 20 [ms].

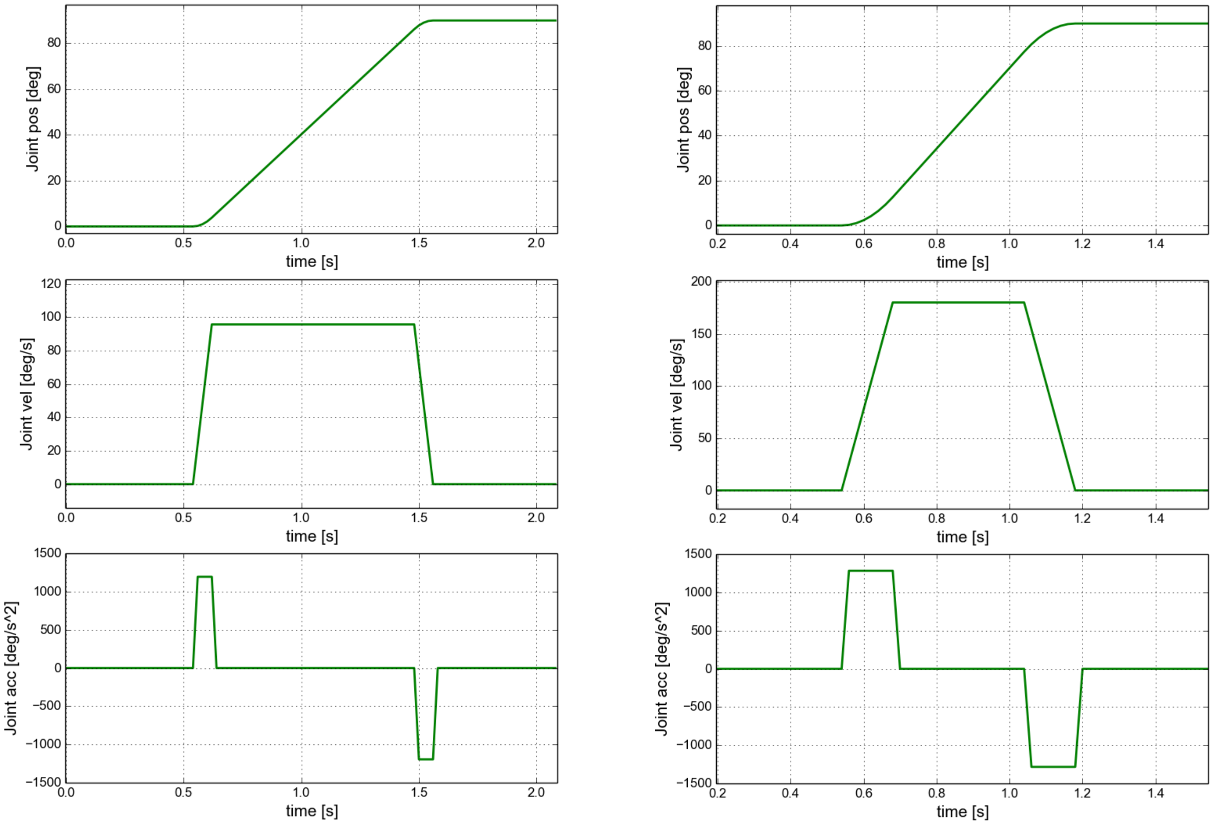

(a) Joint trajectory from 0 [deg] to 90 [deg] in 1 [s].

(b) Joint trajectory from 0 [deg] to 90 [deg] with speed 180 [deg/s].

Figure 3.19 – Joint trajectory generation using a discretized bang-bang model.

3.4 Conclusion: finger concept

Figure 3.20 shows the complete concept of the little finger. The overall structure is composed by the finger phalanges (proximal, middle and distal), the e-motion motor with its gearbox (in red) and the magnetic rotary encoder. Lateral covers are put in transparency to highlight the internal rigid bars (in green) which define the 4-bar linkage transmission. As it can be noticed, the MCP axis is vertically displaced with respect to the motor, to guarantee that the fingertips lie on the palm surface when completely closed. This offset consequently depends on the first and third phalanx lengths, varying from one finger to the other. In addition, it contributes to the arch-shaped finger base placements along the wrist frame z axis. The desired finger base placements (described in Chapter 2) are achieved by properly defining the point of attachment of the motor support to the palm. Figure 3.21 shows the thumb concept.

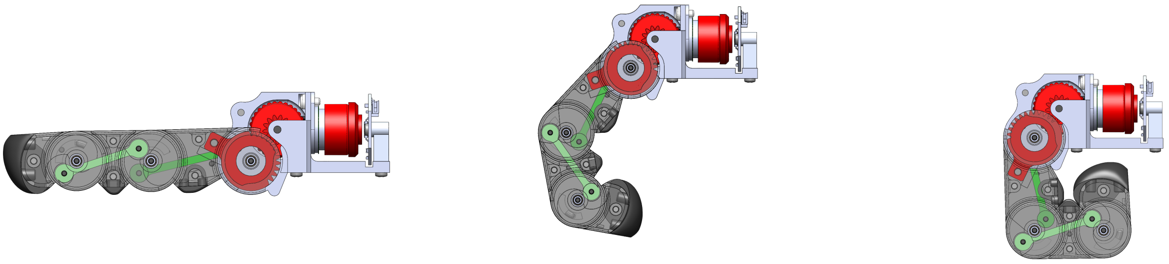

(a) MCP joint at 0 [deg]. (b) MCP joint at 45 [deg]. (c) MCP joint at 90 [deg].

Figure 3.20 – E-motion little finger concept.

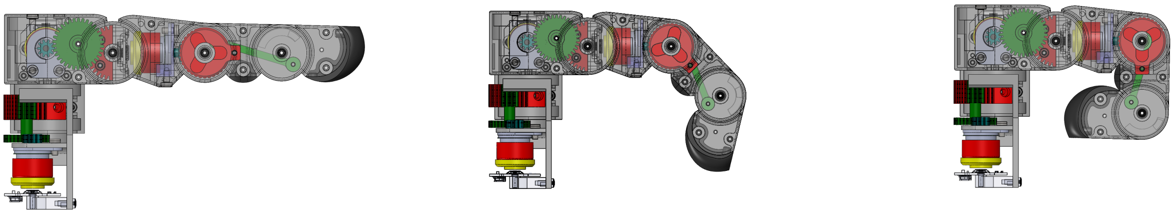

(a) MCP joint at 0 [deg]. (b) MCP joint at 45 [deg]. (c) MCP joint at 90 [deg].

Figure 3.21 – E-motion thumb concept.

4

Hand design: Grasp

In this chapter the hand is exclusively conceived for grasping. Fingers are designed to naturally adapt to the object shapes avoiding complex grasp controls. All the intelligence resides in the mechanical structure which reduces the number of actuators and the need for sensors. The design of the transmission mechanism is introduced in Section 4.1. The adopted pulley-tendon system is presented by resuming the grasp cable selection and routing (Section 4.1.1) and by describing the sizing method for the pulley radii (Section 4.1.2). Since the constant objective of this project is to keep the hand light and small, self-adaptation is also adopted between fingers by interlacing their bases to a single source placed in the forearm: the grasp motor. The actuator force is distributed to the fingers by mean of a differential mechanism, embedded in the palm, based on the sliding pulley working principle. The design of the differential mechanism is presented in Section 4.1.3 in which two different prototypes are described and tested. Then, the chapter pursues the development of the hand by outlining the sizing of the brushless DC motor (Section 4.2) and its force control (Section 4.3). Section 4.4 closes the chapter by showing finger and differential mechanism designs.

4.1 Transmission

Since the objective is to embody grasping capabilities in the hand rather than exploring new grasp models and tools for self-adaptable fingers, the design of the grasp transmission mechanism is fully based on the theoretical analysis and design of under-actuated hands proposed by Birglen, Laliberté and Gosselin in [131]. This section recalls various concepts presented in the book in order to describe the design process of the transmission mechanism, from the fingertips up to the wrist.

In general the word under-actuated defines a mechanical structure which presents less actuators than joints. In this sense the e-motion hand would commonly be considered as under-actuated because 7 motors drive the 16 DoFs of the robotic hand. For robotic hands, however, the term under-actuated is mostly used to indicate mechanisms whose joints are loosely coupled (coupled in a non-fixed way) to allow finger adaptation. In general, these mechanisms present non-actuated joints driven by passive elements when decoupled. In other words, the non-actuated joints are passive when coupled and become "active" when they leave their configurations of equilibrium. According to this difference with classical under-actuated mechanisms, in which coupled joints always remain passive and the coupling ratios fixed, the grasp hand is not defined as under-actuated but as self-adaptable, in order to avoid any confusion. Autonomous finger adaptation is obtained by introducing elastic elements in the transmission chain so that fingers can be always brought back to a known configuration. In classic designs springs keep fingers straight when not actuated thanks to mechanical stops which prevent fingers to hyper-flex (see Section 1.2). Spring stiffnesses are chosen to counterbalance finger weight and inertial effects and, at the same time, to oppose the least torque against actuation while grasping.

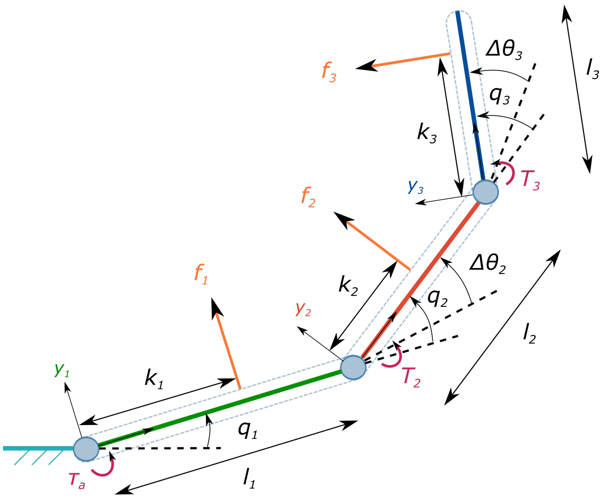

Figure 4.1 – Planar finger model: geometric and force parameter definitions.

In this context, fingers are all studied on a plane (see Figure 4.1), neglecting the abduction/adduction DoF of the thumb since it is normally used during the pre-grasping phase rather than during the grasp itself. Global grasping performance are determined by considering the grasping forces developed by each finger in contact with the object. No friction and contact geometry are involved in this analysis since the objective is to characterize the normal forces developed by the fingers according to their designs. Fingers are modeled in accordance to the quasi-static analysis proposed by Birglen and Gosselin [75]. The contact forces exerted on a fixed object by the finger phalanges are determined by mean of the virtual power principle:

$$\boldsymbol{t}^T \boldsymbol{\omega}_a = \sum_{i=1}^{3} \boldsymbol{\zeta}_i \circ \boldsymbol{\xi}_i \tag{4.1}$$

where $\boldsymbol{t}$ is the torque vector generated by the actuator and the springs, $\boldsymbol{\omega}_a$ is the input velocity vector and $\boldsymbol{\zeta}_i$ and $\boldsymbol{\xi}_i$ are respectively the planar wrench and the twist vectors at the i^{th} contact, with $\circ$ that is the scalar product between the dual spaces. The torque and velocity vectors are defined as:

$$\boldsymbol{t} = \begin{bmatrix} \tau_a \\ T_2 \\ T_3 \end{bmatrix} = \begin{bmatrix} \tau_a \\ -K_2\Delta\theta_2 \\ -K_3\Delta\theta_3 \end{bmatrix} \quad \boldsymbol{\omega}_a = \begin{bmatrix} \dot{\theta}_a \\ \dot{q}_2 \\ \dot{q}_3 \end{bmatrix} \tag{4.2}$$

where τ_a is the actuator torque, K_i is the i^{th} torsional spring constants and $\Delta\theta_i$ is the i^{th} angular spring distance from equilibrium. Developing the right hand-side of Equation 4.1 the virtual power can be rewritten as:

$$\boldsymbol{t}^T\boldsymbol{\omega}_a = \boldsymbol{f}^T\boldsymbol{J}\dot{\boldsymbol{q}} = \boldsymbol{f}^T\boldsymbol{J}\boldsymbol{T}\boldsymbol{\omega}_a \tag{4.3}$$

where $\boldsymbol{T}$ is the so called transmission matrix which relates the input velocity vector to the joint velocities: $\dot{\boldsymbol{q}} = \boldsymbol{T}\boldsymbol{\omega}_a$. Therefore, given the input torque, vector contact forces are computed as follows:

$$\boldsymbol{f} = \boldsymbol{J}^{-T}\boldsymbol{T}^{-T}\boldsymbol{t} \tag{4.4}$$

where $\boldsymbol{f}$ only collects the normal contact forces (since no torques and friction forces are assumed at contact) and $\boldsymbol{J}$ (the Jacobian matrix) is simply defined as:

$$\boldsymbol{J} = \begin{bmatrix} k_1 & 0 & 0 \\ k_2 + l_1\cos(q_2) & k_2 & 0 \\ k_3 + l_2\cos(q_3) + l_1\cos(q_2+q_3) & k_3 + l_2\cos(q_3) & k_3 \end{bmatrix} \tag{4.5}$$

where k_i is the distance between the i^{th} contact point and the base (frame origin) of the i^{th} phalanx. This formulation isolates the transmission mechanism (matrix $\boldsymbol{T}$) from the finger kinematic structure allowing to analyze the influence that transmission type and geometry exert on the grasping force.
From the results emerging from the comparison done by [75] and the fact that tendon-based transmission mechanisms are light and easy to design, pulleys and cables are used to convey the grasp force to the fingers. Hereafter, the implementation of a tendon-based transmission mechanism to drive all hand DoFs with a single actuator is depicted. At first, the transmission mechanism is introduced by showing the cable routing and the pulley radii within fingers. Then, self-adaptation between fingers is outlined by presenting the differential mechanism placed in the palm.

4.1.1 Cable selection

Tendon-based transmission mechanisms are strongly affected by frictional losses. In order to preserve good grasping performance these have to be reduced. An effective way to reduce frictions is to minimize cable re-directions and to use free-wheel pulleys (or rotating axes) rather than sliding surfaces (e.g. simple fixed axes). In fact, force loss non-linearly varies with the turning angle if the cable jointly moves with a bearing (Equation 4.6), while it varies exponentially if the cable slides on a fixed surface (Capstan equation 4.7).

$$F_{in} = F_{out}\frac{1+\cos(\frac{\pi}{2}-\frac{\beta}{2})\mu}{1-\cos(\frac{\pi}{2}-\frac{\beta}{2})\mu} \tag{4.6}$$

$$F_{in} = F_{out}\, e^{\mu\beta} \tag{4.7}$$

where F_{in} and F_{out} are the tension forces at equilibrium before and after cable bending, μ is the friction coefficient and β the angle of redirection. In the former case the friction coefficient is determined by the pulley and axis materials while, in the latter, it is determined by the cable and axis materials. Despite the fact that bearings and free-wheel pulleys highly reduce friction loss, it is not always possible to use them all along the cable routing path. For example, in the differential mechanism bearings cannot be used to guide the cable in some narrow passages. Consequently, different cable materials are tested on fixed steel axis to experimentally determine the lowest friction coefficient. Compared cable materials are the ones more commonly used on tendon-based robotic hands: steel [82][102], Kevlar [87] and Dyneema® [132][50]. Friction coefficient between cable and fixed surfaces is not the only selection criteria. Cable materials are also compared in terms of endurance, elasticity and integrability in order to study their transmission reliability and efficiency over time. A first selection is based on literature, keeping in mind that redirection radii are very small (in the order of ⌀3 [mm]). Then, the reminder materials are experimentally compared. The required cable material must have the following characteristics:

- withstand more than 80 [N] (50 [N] are required but a safety margin is added);
- resist to constant stresses (minimal wearing) continuously applied for 36000 cycles (10 [h]);
- low friction coefficient on fixed surfaces;
- withstand small bending radii;
- easy to embody in the mechanism (easy to terminate).

Regardless the first requirement, which is easy to satisfy even at small cable diameters (thanks to current cable performance), it is not trivial to satisfy all these requirements at once. Steel cables, for example, are stiff (high Young's modulus - defined in Section 5.2.2) but are difficult to terminate in limited spaces and require large bending radii [133]. In addition, their durability is shorter than polymer tendons on equivalent pulley radii [134]. Kevlar is stronger than steel, it is easier to terminate and it has higher durability if coated. However, it suffers significant strength loss when flexed with respect to Dyneema®-based fibers (experimentally confirmed by [135]). Dyneema® cables are easy to terminate (they can be spliced), they have low bending limit and are more durable than steel. They are braided polyethylene cables (identical to Spectra®) stronger and lighter than Kevlar for a given diameter. They are less stiff than steel and present strain relaxation under constant displacement [133] (named *creep*), which require dedicated closed loop control strategies to be compensated. According to cable requirements Dyneema® is the most interesting material among commonly used fibers. Even so, another high-performance cable (used in the DEXMART hand [65]) is introduced and compared: the Fast-Flight. Fast-Flight is a Dyneema®-based fiber which preserves similar bending and termination performance of its parent line. It has limited linear elasticity and a friction coefficient lower than Kevlar [135].

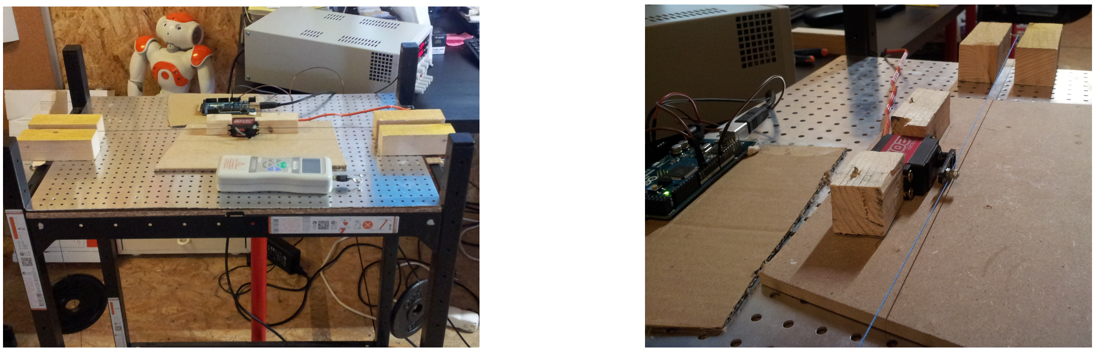

(a) Endurance test bench. The cable is kept in tension by equal loads attached at its ends.

(b) BL servomotor used to pull the cable in opposite directions.

Figure 4.2 – Cable endurance test bench. A brushless servomotor pulls the cable every second in opposite directions to constantly stress the fiber (Figure 4.2b) over the steel axes. A load of 1 [kg] is applied to each cable end (Figure 4.2a).

To determine which cable between Fast-Flight and Dyneema® has the highest durability and the lowest friction, two test benches are realized. The first consists in moving a loaded cable over two steel axes. As shown in Figure 4.2, at each cable end a load of 1 [Kg] is attached while a BL servomotor pulls the cable at the middle of its length, pulling every second in opposite directions to constantly stress the fiber. The durability is evaluated at the sliding surfaces where the cable is redirected of 90°. The effectiveness of this test is proven by testing a coated steel cable (Berkley Steelon Nylon Coated Wire - ⌀0.65 [mm] and max tensile strength of 90 [N]) and a nylon cable (Fluoro Hybrid SI - ⌀0.5 [mm] and max tensile strength of 180 [N]) which lasted about 180 cycles (≈3 [min]) and 7600 cycles (≈2 [h]) respectively before breaking. The second test bench (shown in Figure 4.3) consists in measuring the minimum force required to shift the cable over a fixed axis. Different loads are placed at one cable end while the other is attached to a free-to-move load cell placed on a slider. The cable makes a turn of 90° about the axis and the contact surface is changed between bare steel and a plastic IGUS® bearing. The turning angle has to be precisely disposed since it is used to determine the friction coefficient by mean of the Capstan equation:

$$\mu = \frac{2}{\pi} \ln(\frac{F_{\text{peak}}}{F_{\text{Load}}}) \tag{4.8}$$

where F_{peak} is the pulling force required to win the static friction and F_{Load} is the load force. The pulling force is computed as the average of 10 repeated peak forces per load and μ is averaged over the loads.

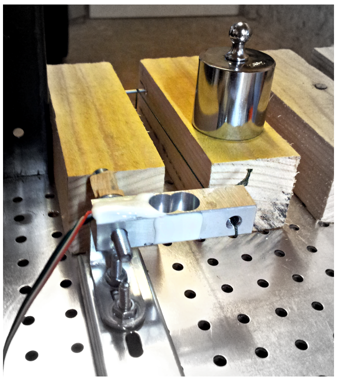

Figure 4.3 – Static friction measurement test bench. μ is indirectly obtained from the bending angle and the measured pulling force exerted by the free-to-move load cell. The picture shows the initial position in which the load (not visible) hold the load cell in contact to the mechanical stop. The weight placed beside the cable represents the calibrated loads used in this experience.

Experimental results. From the durability test it emerges that both Dyneema® ASARI Japan (⌀ 0.6604 [mm]) cable and Brownell braided Fast-Flight S (⌀ 0.7 [mm]) cable can endure 36000 pulling cycles (10 [h]) under load. However, the two lines do not withstand repeated efforts in the same way. As shown in Figure 4.4 Dyneema® wears more easily than Fast-Flight, which demonstrates a very high durability. From the friction tests, it comes out that Fast-Flight has lower static friction coefficient than Dyneema® probably thanks to its smoother surface. This result is obtained on both steel and IGUS® sliding surfaces. In case of steel, for example, the Fast-Flight friction coefficient (μ_{FF} = 0.125) is 35% smaller than the Dyneema® one (μ_D = 0.19). Experiment outcomes and literature results are merged in Table 4.1 to resume the different cable characteristics according to the required performance. From it, it emerges that Fast-Flight is the most suitable cable for this kind of application. Even though it is less stiff than steel,

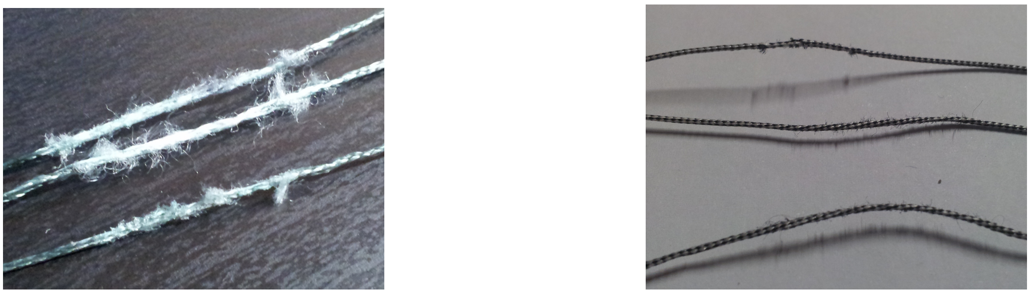

Dyneema® cable.

Fast-Flight cable.

Figure 4.4 – Cable conditions after 10 hours of stress test.

its potential deformations can be handled in the differential mechanism design by considering that cable lengths can slightly vary proportionally to the actuation force. Hence, Fast-Flight is chosen as the grasp hand tendon material and its fiber is embodied in the palm and the fingers to transmit the grasping force from the actuator to the phalanges.

	Endurance	Friction	bending limit	Termination	Stiffness[i]
Steel	-	-	-	-	+
coated Kevlar	+	-	+	+	-
Dyneema®	+	+	+	+	-
Fast-Flight	++	++	+	+	-

[i] considering the Young's Modulus and not the cable braiding

Table 4.1 – Comparison of cable characteristics with respect to the application requirements.

4.1.2 Self-adaptable finger

To transmit the grasp force to the phalanges a tendon is routed from the finger base to the fingertip through a series of free-wheel pulleys. To reduce friction losses the cable path curvature is minimized and sliding surfaces are completely avoided. Small bearings are placed between pulleys to keep the cable tangent to them in any configuration. This guarantees a constant moment arm (configuration independent) that simplifies the relation between joint and actuation torques. In this case, the transmission matrix $\boldsymbol{T}$ can be defined as follows:

$$T = \begin{bmatrix} 1 & -r_2/r_1 & -r_3/r_1 \\ 0 & 1 & 0 \\ 0 & 0 & 1 \end{bmatrix} \tag{4.9}$$

where r_1, r_2 and r_3 are the pulley radii of MCP, PIP and DIP joints respectively. Figure 4.5 presents the adopted tendon routing in the fingers. In the thumb, cable routing slightly changes at the finger base in correspondence of the additional DoF. Here, the cable passes through the center of rotation of the joint to avoid coupling between flexing and opposing motions.

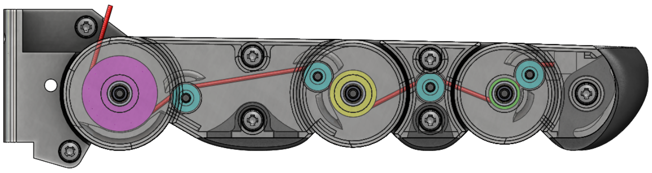

Figure 4.5 – Cable routing within a generic finger.

Recalling the relation between actuation and contact forces, one can split Equation 4.4 in to two parts:

$$\begin{aligned} \boldsymbol{\tau} &= \boldsymbol{T}^{-T}\boldsymbol{t} \\ \boldsymbol{f} &= \boldsymbol{J}^{-T}\boldsymbol{\tau} \end{aligned} \tag{4.10}$$

where the first equation shows the actuation torque distribution according to the transmission mechanism and the second one represents the effects that finger and contact geometries exert on grasping forces.

In particular, the factors which influence the contact forces are: the contact point positions, the joint configurations, the link lengths and the pulley radii. The first two depend on the object shape and the grasp type while the reminders are intrinsic to the finger design. Since link lengths are fixed by anthropomorphic constraints, pulley radii are the only mechanical parameters that are free to be tuned in order to arbitrarily vary $\boldsymbol{f}$ in function of $\boldsymbol{\tau}$.

4.1.2.1 Design example

At this stage, one could design pulley radii for a precise object shape and grasp type. A cylindrical grasp is used to hold a regular shaped object within fingers. Contact forces are equally distributed among phalanges and no contact with the palm is considered. Grasp is assumed with no planar frictions and no torques at contacts and contact positions are considered at the middle of each phalanx (Figure 4.6). For simplicity, joint angles are chosen equal for each finger except for the thumb:
— Thumb = $[80°, -20°, 30°, 30°]$
— Index = $[34°, 34°, 34°]$
— Middle = $[38°, 38°, 38°]$
— Ring = $[35°, 35°, 35°]$
— Little = $[28°, 28°, 28°]$

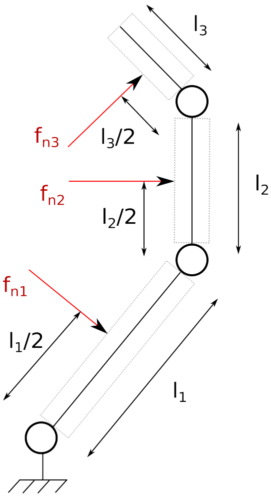

Figure 4.6 – Simple grasp state example for sizing pulley radii - contact positions are considered at the middle of each phalanx.

Considering equal force distribution while holding an object of 0.380 [kg] with vertical contact friction (μ) of 0.5, contact forces are fixed to 0.31 [N] for the finger phalanges and 1.25 [N] for the thumb phalanges. Hence, vector $\boldsymbol{f}$ is defined for each finger and vector $\boldsymbol{\tau}$ can be computed according to the Jacobian matrices. At this point, pulley radii are determined by choosing the spring constants at the second and third finger joints. These reduce the unknowns to three (τ_a, r_2/r_1 and r_3/r_1) as the number of equations (first formula in Equation 4.10). Rewriting τ_a as $f_a r_1$, where f_a is the pulling force applied to the cable before the first pulley, all unknown variables are parameterize by r_1 - which can be arbitrary chosen within a mechanically constrained range of values. Since for a given τ_a and pulley ratios (r_2/r_1 and r_3/r_1) a large r_1 implies larger pulley radii and a smaller f_a, the first pulley radius is chosen as the biggest possible. Table 4.2 shows the pulley radii and the pulling force required to grasp the object for zero spring torques. Note that, in practice, this result is not acceptable since r_3 are too small to be mechanically feasible. Sliding surfaces or two stages pulleys should be used instead.

This approach allows to attain a desired grasp for a limited set of objects which share the same shape and size. As soon as either the object geometry or the grasp type changes, grasp performance can sensibly

	Thumb	Index	Middle	Ring	Little
r_1 [mm]	6	5	5	5	4
r_2 [mm]	2.5	2	2.1	2.2	1.6
r_3 [mm]	0.7	0.6	0.6	0.6	0.5
f_a [N]	21.5	5.2	5.42	5.42	5.925

Table 4.2 – Resultant pulley radii and pulling force required to hold a cylindrical object with fixed contact forces and locations and specific joint angles.

deviate and even lead to failure. To obtain more grasp dexterity and robustness, pulley radii should be designed considering force distributions and grasp stability in various finger configurations and contact locations. Next paragraph presents a sizing approach which optimizes the pulley radii on the base of some performance and stability indexes.

4.1.2.2 Pulley radii optimization.

Finger self-adaptability does not ensure stable grasps by itself. Self-adaptable phalanges might lose contact with the grasped object and lead to object ejection in certain cases. Grasp stability is studied at the level of a single finger and it is determined by the nature of its contact forces. If a contact force is negative the corresponding phalanx loses connection with the object while it remains in contact if the force is zero or positive. In case at least one force is negative the object slides on the phalanges still in contact until one of the following event occurs:

— a stable configuration (static equilibrium) is achieved - all contact forces are non-negative (zero or positive);
— joint limits are met - self-adaptability is not exploited;
— the object is ejected - the last phalanx loses contact with the object failing the grasp.

where the last usually happens when force distribution is unbalanced leaving the last phalanx too weak to secure the grasp. To minimize the probability of object ejection and improve grasping performance, pulley radii are optimized according to four grasping indices: grasp stability, contact robustness, force isotropy and palm opposition.

Grasping indices. The grasp stability index represents the percentage of stable grasp configurations within the space ($\boldsymbol{k}^*$, $\boldsymbol{q}^*$), which collects all possible joint angles ($\boldsymbol{q}^*$) and contact positions ($\boldsymbol{k}^*$) in order to analyze contact forces for various types of grasp and different object shapes and sizes. The grasp stability index is defined as follows:

$$\mu = \frac{\int_W \delta(\boldsymbol{k}^*, \boldsymbol{q}^*) d\boldsymbol{k}^* d\boldsymbol{q}^*}{\int_W d\boldsymbol{k}^* d\boldsymbol{q}^*} \tag{4.11}$$

where

$$\delta(\boldsymbol{k}^*, \boldsymbol{q}^*) = \begin{cases} 1 & \text{if all contact forces are non-negative} \\ 0 & \text{otherwise} \end{cases} \tag{4.12}$$

with $0 < k_i < l_i$ (l_i is the i^{th} link length) and $0 < q_i < \pi/2 \; \forall \; i \in [1, 3]$ except for the RC thumb joint whose angle can vary in $[-20°, 70°]$. The grasp stability index characterizes the finger ability to generate full-phalanx grasps, however, it does not defines how much phalanges are close to lose contact. In other words, it defines the overall contact stability without evaluating the robustness of each stable grasp. Contact robustness is evaluated by the following index:

$$\eta = \frac{\int_W \min_i(f_i) \delta(\boldsymbol{k}^*, \boldsymbol{q}^*) d\boldsymbol{k}^* d\boldsymbol{q}^*}{\int_W f_a d\boldsymbol{k}^* d\boldsymbol{q}^*} \tag{4.13}$$

where $\min_i(f_i)$ is the minimum contact force for the current grasp-state configuration, f_a is the force of actuation and $\boldsymbol{k}$, $\boldsymbol{q}$ and δ are defined as in Equation 4.11. This index defines the finger capability to preserve full-phalanx grasps in case of deviations from stable configurations. Grasp stability and robustness indices characterize the quantity and the quality of full-phalanx grasps but they do not consider the force distribution between phalanges. Force distribution is not critical from the stability point of view but it might damage fragile objects if forces are strongly unbalanced and mainly concentrated in a single point. Finger force distribution is defined by the force isotropy index:

$$I = \frac{1}{mn} \sum_{j=1}^{m} \frac{\sum_{i=1}^{n} f_{i,j}}{\max_i(f_{i,j})} \delta(\boldsymbol{k}_j, \boldsymbol{q}_j) \tag{4.14}$$

where n is the number of phalanges per finger (=3 also for the thumb since its first link does not contribute to the flex) and m is the number of grasped objects. This index does not show where forces are mainly applied but it points out whether contact forces are equally distributed among phalanges. Last but not the least, better grasps can be achieved by pushing the object towards the palm. This reduces the object mobility and ensures firmer grips. The finger ability to displace the object in opposition to the palm is defined by:

$$I_{xy} = \frac{1}{m} \sum_{j=1}^{m} \frac{\min(F_{x_j}, EF_{y_j})}{f_a} \delta(F_{y_j}) \tag{4.15}$$

where E is the number of opposing fingers during the grasp (fixed to 2 in this context) and $\boldsymbol{F} = [F_x, F_y]$ is the force exerted on the object - computed as the sum of the contact forces at the finger base reference frame fixed to the palm - while $\delta(F_{y_j})$ is defined as:

$$\delta(F_{y_j}) = \begin{cases} 1 & \text{if } F_{y_j} < 0 \\ 0 & \text{otherwise} \end{cases} \tag{4.16}$$

It is worth to note the different domains in which indices are computed. Since μ and η are critical for stability they are evaluated on the whole grasp state space in order to enlarge finger grasp capabilities to different objects and grasp types. Instead, I and I_{xy} are computed for limited finger configurations and contact positions to improve grasp performance on a set of specific objects required to be grasped: a soda can, a smartphone, a glass and a pen. To determine the pulley radii which maximize the grasping indices an optimization algorithm is proposed.

Optimization algorithm. The objective of the optimization algorithm is to find the pulley radii (r_2 and r_3) which maximize the linear combination of the previously presented grasp indices for each finger. Pulley radii are directly used as optimization variables, while their relative sizes are used to graphically represent their effects on the grasp performance. Relative pulley sizes are defined as the ratio between two consecutive pulley radii: $R1 = r_2/r_1$ and $R2 = r_3/r_2$, where r_1 is fixed to the largest feasible value (see Table 4.2). Pulley ratios are only considered between $(0, 1]$ where stable designs can be obtained [75]. The effects that R_1 and R_2 have on the grasp indices can be easily identified by analyzing the two dimensional space. Figure 4.7a and 4.7b show the variation of μ and η by equally sampling both R_1 and R_2 domains. As it can be seen in both cases, better performance are obtained for small ratios which are physically unfeasible due to the reduced size of r_1 - e.g. for the middle finger $r_1 = 0.005$ [m], if $R_1 = 0.1$ and $R_2 = 0.1$ then $r_2 = 5\ 10^{-4}$ [m] and $r_3 = 5\ 10^{-5}$ [m], which are mechanically too small.

Constraints: Compact and mechanically feasible designs which reduce object ejection are ensured by defining the following optimization constraints:

1. $r_3 \leq l_3/(l_2 + l_3) r_2$;
2. $r_2 \leq r_1$ and $r_3 \leq r_2$;

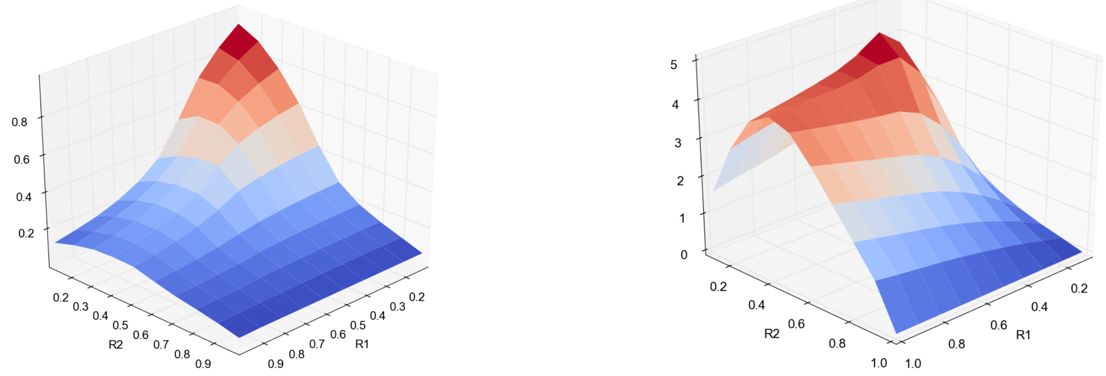

(a) Unconstrained μ index.

(b) Unconstrained η index.

Figure 4.7 – Analysis of μ and η indices in function of R_1 and R_2 over the full finger grasp state.

3. $r_2 \geq r_{2min}$ and $r_3 \geq r_{3min}$.

where $r_{2min} = 1.5\ 10^{-3}$ [m] and $r_{3min} = 1.5\ 10^{-3}$ [m]. The first constraint reduces the probability of closing-ejection by imposing the equilibrium curve to always lie on the last physical phalanx [75]. The second one avoids unstable designs and encourages compactness while the third constraint ensures mechanically feasible free-wheel pulleys. Figures 4.8a and 4.8b show the influence of the constraining equation on the grasp stability index of the middle finger. As it can be seen the full-phalanx grasp workspace drastically decreases from more than 90% (unfeasible) to 39.15%, by applying the second and the third constraints, and to 36% by applying all of them. This shows the strong influence that mechanical feasibility exerts on the final grasp performance due to the small dimensions.

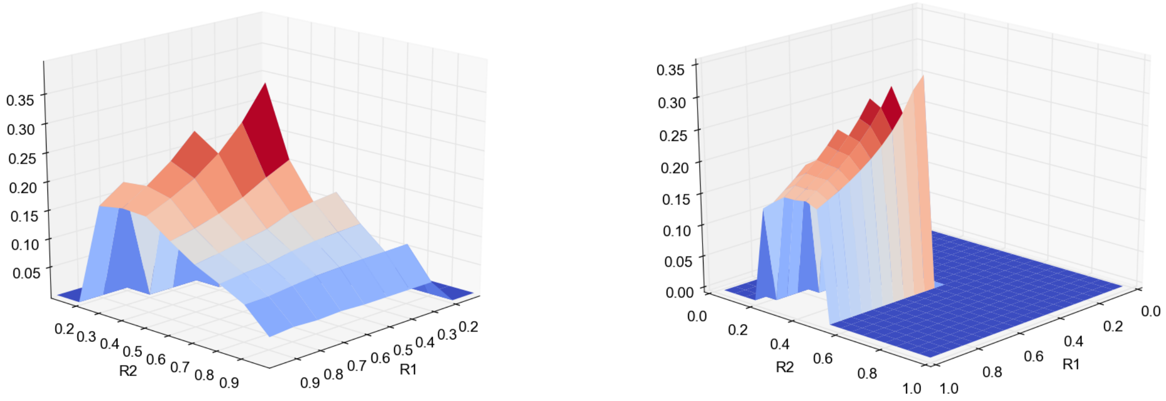

(a) μ under compactness and mechanical feasibility constraints.

(b) μ fully constrained.

Figure 4.8 – Analysis of μ under stability, compactness and mechanical feasibility constraints.

Objective function: As previously mentioned, full-phalanx stability and robustness are computed within the whole state space workspace while finger isotropy and palm opposition are analyzed for prescribed objects and specific contact positions and finger configurations provided by CAD models. By analyzing each index independently the following observations emerge:

- all indices suggest to keep the last radius pulley (r_3) as small as possible (while no hints are given for r_2);
- force isotropy does not contribute to the design since there always exists a negative force at the given joint angles and contact positions on the second phalanx for any value of r_2 and r_3.

The second point highlights that the chosen grasp-state configurations are unstable, consequently, the grasp evolution must be studied to check whether fingers reach a stable grasp or they end-up by ejecting the object. If fingers converge to a stable configuration one could optimize the force isotropy at the equilibrium state. However, since the analysis assumes no friction and single point contacts, it is likely that real stable configurations differ from the theoretical ones causing the optimization effects to be unknown. Hence, force isotropy is not included within the design criteria (grasp indices) and the objective function is defined as follows:

$$\psi = w_1\mu + w_2\eta + w_3 I_{xy} \tag{4.17}$$

where $w_1 = 1$, $w_2 = 1.5$ and $w_3 = -1.2$ (< 0 because I_{xy} is always negative due to the orientation of the finger base frame) weight the different optimization objectives: stability, robustness and palm opposition.

Results: To solve the non-linear problem the Constrained Optimization BY Linear Approximation (COBYLA) [136] algorithm is used to minimize the multi-variable scalar function. Table 4.3 collects the resultant pulley radii obtained by setting both initial pulley radii to r_1. The optimized pulley radii does not ensure stable grasps in any grasp state configuration but theoretically increase the finger grasping capabilities by reducing the probability to eject known and unknown objects. To check whether unstable grasps end up ejecting or holding the grasped object the evolution of contact trajectories is estimated and analyzed. In particular, this is done for the set of objects required to be grasped when the initial grasp state configurations present at least one negative contact force.

	Thumb	Index	Middle	Ring	Little
r_2 [mm]	2.97	2.86	2.73	2.86	2.67
r_3 [mm]	1.5	1.5	1.5	1.5	1.5

Table 4.3 – Optimized pulley radii to maximize stability and robustness in the whole grasp-state workspace and the finger ability to push specific objects towards the palm.

Stability analysis. As previously mentioned, in presence of at least one negative contact force, the grasp is said to be unstable. The phalanges corresponding to the negative forces immediately lose contact and the grasped object starts sliding on the remainder phalanges. The object keeps moving within the finger until it is ejected or a stable configuration is met (positive or zero contact forces). The convergence of the sliding motion is determined by analyzing the evolution of the grasp state from the unstable configuration. In general, a cable-driven three-phalanx finger with negligible spring torques might loose contact at the proximal or at the middle phalanx or it might loose both contacts at the same time. In this context, however, only contact losses at the middle phalanx are addressed since they are the sole occurring at some required grasp state configurations. When contact is lost at the middle phalanx the finger can be considered as a two-phalanx finger composed by middle and distal phalanges if the proximal phalanx preserves a positive contact force. The stability analysis is computed in function of q_2, q_3 and k_3 to check whether the grasp state reaches a static or a kinematic equilibrium (joint limit) or an ejection condition from the unstable configuration. Static equilibrium is defined by the grasp state configuration subset (q_2, q_3, k_3) at which the negative force is zeroed ($f_2 = 0$). Its equation is derived from Equation 4.10 and can be written as follows:

$$(r_2 - r_3)k_3 - r_3 l_2 \cos(q_3) = 0 \tag{4.18}$$

Kinematic equilibrium occurs when further motions are hindered by joint limits ($q_2 = 0°$ or $q_2 = 90°$) while object-ejection takes place if the last contact point leaves the distal phalanx ($k_3 > l_3$ or $k_3 < 0$). Static equilibrium can be represented as a surface in the subspace (q_2, q_3, k_3) while kinematic equilibrium and boundary ejection conditions as vertical and horizontal planes ($k_3 = l_3$ and $k_3 = 0$) respectively.

The grasp state trajectory is computed as follows:

$$\begin{aligned} k_{3i}\cos(q_{3i}) - k_3\cos(q_3) &= K \\ l_2(1-\cos(q_{2i}-q_2)) + k_{3i}(\cos(q_{3i}) - \cos(q_2-q_{2i}-q_{3i})) &= K \end{aligned} \tag{4.19}$$

where:

$$K = \frac{k_3^2 - k_{3i}^2}{2l_2} \tag{4.20}$$

and q_{2i}, q_{3i} and k_{3i} are the initial grasp state configuration. The direction in which the grasp state evolves along the trajectory is determined by the sign of f_2.

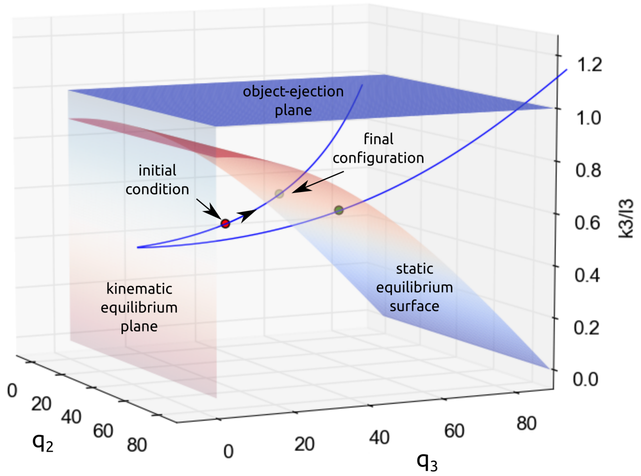

Figure 4.9 – Example of finger grasp stability analysis. To ease the representation only one kinematic equilibrium plane and object-ejection plane are shown.

Figure 4.9 shows the stability analysis conducted on the index finger while grasping a standard soda can. As it can be seen, the grasp starts moving from a given unstable initial condition (red dot) and follows the grasp state trajectory (blue curve) along which the middle phalanx undergoes an opening motion (coherently with the negative contact force) and the distal phalanx a closing one - to preserve the contact with the object. The grasp state varies until reaching a stable grasp configuration (pointed green dot) at the intersection point with the static equilibrium surface. Analogous trajectories are obtained for the other unstable finger grasps, all eventually converging to statically stable configurations.

Final pulley radii. Table 4.4 collects the pulley radii embodied in the final finger designs and shows the cable length variations (ΔL_c) required to fully close each finger. Note that the tolerance of the pulley radii is guaranteed to be 0.01 [mm] for the external radii and supposed to be similar for the internal ones, which cannot be directly measured with a standard caliper.

	Thumb	Index	Middle	Ring	Little
r_1 [mm]	6.00	5.00	5.00	5.00	4.00
r_2 [mm]	2.97	2.86	2.73	2.86	2.67
r_3 [mm]	1.50	1.50	1.50	1.50	1.50
ΔL_c [mm]	18.1	16.35	16.15	16.35	14.48

Table 4.4 – Pulley radii embodied in the final finger designs.

4.1.3 Differential mechanism

In the perspective of limiting weight, size and noise self-adaptable fingers are driven by only one motor placed in the forearm: the grasp motor. Its actuation force is distributed to the fingers through an adaptive transmission mechanism, embodied between the e-motion actuators and the dorsal side of the palm, which guarantees self-adaptation among fingers, i.e. when one or more fingers are blocked the reminders are still free to move. The transmission mechanism consists in a tree-structured composition of differential stages which split one input force in two outputs. In this context, two distinct transmission mechanisms are presented. The first one is designed to provide specific forces to each finger base while the second one is conceived to minimize friction losses and provide unbalanced forces to encourage finger closures.

4.1.3.1 Design 1: balanced force distribution

The first transmission mechanism design (inspired by [87]) relies on movable pulleys differential stages. The model of a movable pulley consists in a 2 DoFs pulley, free to rotate about its axis and to translate along only one direction (see Figure 4.10a). To avoid force losses the input force is aligned with the unconstrained translation and it is directly applied at the pulley axis. The output forces are distributed by a common tendon always tangent to the pulley circumference. Assuming no friction and constant tension along the cable, output forces are computed as follows:

$$F_{1a} = F_{2a} = \frac{F_a}{\sin(\alpha_1) + \sin(\alpha_2)} \tag{4.21}$$

where F_a is the input force, F_{1a} and F_{2a} are the two output forces and α_1 and α_2 are the output angles. In practice movable pulleys are realized by separating input and output forces on two different Teflon rings, both sliding about fixed axis connected by two plates of steel (Figure 4.10b).

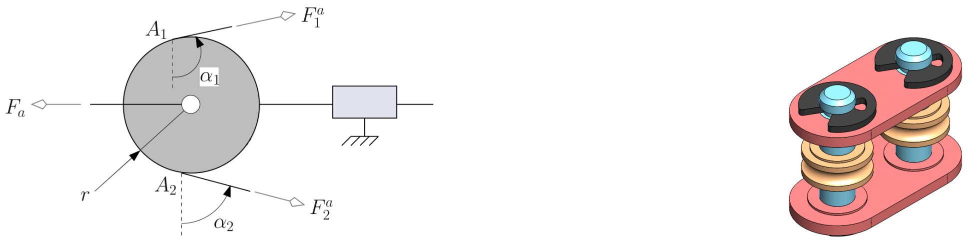

(a) Movable pulley principle taken from [137].

(b) Prototype of movable pulley embedded in the first differential mechanism design.

Figure 4.10 – Movable pulley model and prototype embedded in the first differential mechanism design.

The structure of the transmission mechanism is designed to evenly distribute the input force (F_a) among fingers. In particular, the system is conceived to constantly provide $F_a/2$ to the thumb base and $F_a/8$ to each finger base independently from the configuration of each digit. The desired constant force distribution is obtained by constraining the output angles ($\alpha_1 = \alpha_2$) to $\pi/2$, so that:

$$F_{1a_n} = F_{2a_n} = \prod_{i=1}^{n} \frac{F_a}{2} \tag{4.22}$$

where n is the number of stages in cascade. As shown in Figure 4.11a, three differential stages are implemented between the wrist and the fingers (n = 3) while one differential stage is interposed between the wrist and the thumb (n = 1). The first movable pulley decouples the motion of the thumb and the fingers and divides the force between them. Analogously, the second movable pulley splits the forces between index-middle and ring-little fingers while the last two movable pulleys (belonging to third stage) finally provide the pulling force to each digit. The length of the sliding guides belonging to the first two stages are determined by the children stages while the ones at the last stage are chosen according to the variation of the cable lengths within the fingers (see Table 4.4). Due to the thickness of the transmission mechanism (about 5 [mm]) and the space required by the thumb base, the palm width cannot be entirely used. Sliding guides are inclined to fit the available space and additional turning axis are embodied to route the cables so that the input forces remain always aligned with the pulley motions (Figure 4.11b).

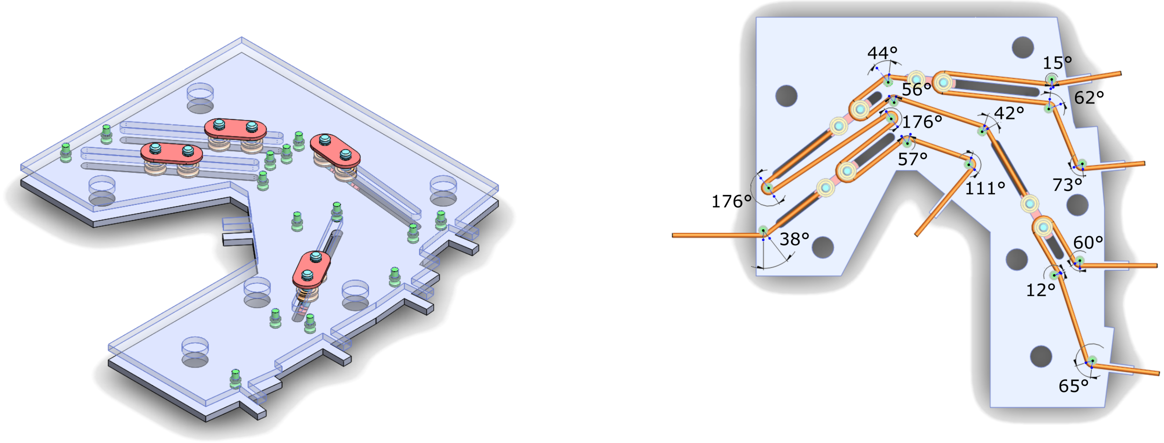

(a) Differential mechanism prototype designed to evenly distribute constant forces to the fingers.

(b) Inclined sliding guides with input and output turning axes which redirect the cable between stages.

Figure 4.11 – Differential transmission mechanism prototype with inclined sliding guides to fit the limited palm space.

Experimental results. The realization of the differential mechanism is not trivial at this scale. The prototype presents different design issues:

1. discontinuities in mechanical parts and non-smooth surfaces easily wear the cable fibers - e.g. sometimes released cables quit the pulley grooves and get damaged when put again under tension by pulley edges or by the irregular compression surfaces between the pulley and the adjacent rigid layer;
2. the fourteen small axes, which redirect the cables before and after the movable pulleys, do not always turn within their sockets due to mechanical imprecision and misalignment between the external rigid layers;
3. circlips are difficult to mount due to their small diameters (1.2 [mm]) and do not reliably hinder vertical displacements of the movable pulley axes on long terms.

The first two issues strongly affect the transmission efficiency. Worn cables increase friction coefficients on fixed surfaces and augment the probability of locking the mechanism. When stuck, small axes change the source of friction from the external layers (aluminum-steel) to the cables (aluminum-Dyneema®) completely varying friction losses (as previously mentioned). Note that Dyneema® (⌀ 0.7 [mm]) cables are adopted in this test bench since the differential mechanism was built before comparing cable performance (see Paragraph 4.1.1). The prototype is tested by redirecting the output cables of $\pi/2$ and applying to them different calibrated masses to simulate various finger contact forces (Figure 4.12). The input forces are measured by a dynamometer and averaged over ten trials per experiment. The objective of the test bench is to determine the distribution efficiency of the mechanism and check whether the desired forces are constantly provided at each output. The most evident result is obtained by applying 200 [g] on the thumb tendon and 50 [g] on the reminder output tendons. Ideally the actuation force should lift all loads at the same time by providing 3.924 [N] at the input tendon (1.962 [N] for

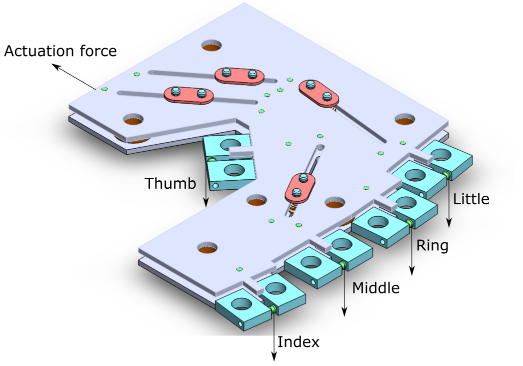

Figure 4.12 – Differential mechanism test bench: output cables are redirected by $\pi/2$ in order to attach calibrated loads.

the thumb and 0.4905 [N] for each finger). However, no motion occurs due to the strong friction forces present in the mechanism. Experimental results show that the peak force required to trigger all finger motions is about 39.4 [N], which is ten times higher than the ideal one. Force losses are mainly due to the friction contacts between:

1. blocked axes and the cable - with $\mu_{Alu-Dyneema^{\circledR}} = 0.26$ - experimentally measured with the cable slightly damaged after few tests;
2. turning axes and the external layers - with $\mu_{Alu-Steel} = 0.61$;
3. movable pulley connecting plates and the external layers - with $\mu_{Alu-Steel} = 0.61$;
4. Teflon rings and the steel axis - $\mu_{Teflon-Steel} = 0.04$ (negligible with respect to the others).

The first two factors are the ones that mostly impact the transmission efficiency. They are caused by the important amount of cable re-directions imposed by the need to preserve constant force distribution within the limited space available. Experimental results show that 17.5 [N] are necessary to only move the thumb and 39.4 [N] to move the reminder fingers from the input cable. In addition, they show that the thumb always move first with respect to the other fingers due to the less complex routing. These results are coherent with the estimated friction losses computed by assuming no-turning axes all along the cable path. Experimental results show that the original force nearly decreases of 77.5% from the differential mechanism input (root) to the thumb (83% estimated) and of 50% from the root to the second stage (89% estimated) where 9.9 [N] are necessary to lift the four fingers at once (200 [g] in total). This last measure shows an overall force loss of 80% between the second stage and each finger - estimated to 78% for the Little, 87% for the Ring, 86% for the Middle and 87% for the Index. As it can be seen the fixed axes assumption overestimates real losses, notably in correspondence of large bending angles - as disclosed between the first and second stage. Nevertheless, it explains the low mechanism efficiency and underlines the necessity to reduce the amount of cable bending angles to the least possible.

Despite the fact that well-balanced force distribution among fingers might be desirable, the conceived mechanical solution does not attain acceptable performance. The main drawbacks of this mechanisms are the numerous sources of friction induced by frequent cable deviations and sliding surfaces. In the perspective of improving the transmission efficiency and simplifying the mechanical structure another differential mechanism is designed and tested.

4.1.3.2 Design 2: optimized friction losses

The second differential mechanism design is inspired by the TUAT/Karlsruhe hand [101]. The mechanism is mainly conceived to minimize static friction forces induced by contact surfaces and cable redirections. Its design is composed by seesaw differential mechanisms with unconstrained input and output angles which reduce complexity, size, weight and costs thanks to the fact that less mechanical components are required. Similarly to movable pulleys, seesaw mechanisms are modeled as planar 2 DoFs bodies which can translate along the direction of the input force and rotate about the vector orthogonal to the plane. Force distribution depends on the geometric parameters shown in Figure 4.13a and it is deduced from the following static equilibrium equations:

$$\begin{aligned} F_{1a} &= F_{2a}\frac{\sin(\alpha_2-\alpha)a_2}{\sin(\alpha_1-\alpha)a_1} \\ F_a &= F_{1a}\sin(\alpha_1)+F_{2a}\sin(\alpha_2) \end{aligned} \tag{4.23}$$

from which:

$$\begin{aligned} F_{1a} &= F_a\frac{\sin(\alpha_2-\alpha)a_2}{\sin(\alpha_1-\alpha)a_1\sin(\alpha_2)+\sin(\alpha_2-\alpha)a_2\sin(\alpha_1)} \\ F_{2a} &= F_a\frac{\sin(\alpha_1-\alpha)a_1}{\sin(\alpha_1-\alpha)a_1\sin(\alpha_2)+\sin(\alpha_2-\alpha)a_2\sin(\alpha_1)} \end{aligned} \tag{4.24}$$

where F_{1a} and F_{2a} are the output forces, α_1 and α_2 are the output angles, α is the bar orientation with respect to the input force and a_1 and a_2 are the distances between the center of rotation and F_{1a} and F_{2a} respectively. Seesaws are realized as floating bars interconnected by tendons so that no sliding contacts exist as cables are pulled (see Figure 4.13).

(a) Seesaw model.

(b) Seesaw prototype.

Figure 4.13 – Seesaw differential unit embodied in the second differential mechanism design.

To ease and accelerate the design process the differential mechanism is conceived by mean of a 2D motion simulator called *Working Model*®. The mechanism presents several geometric parameters: bar lengths, arm lengths, initial cable lengths and angles. At first, fingers are considered to be open and the geometric parameters are chosen to equally distribute the force among outputs ($F_{1a} = F_{2a} = F_a/2$). Given the finger basis (outputs) and wrist (input) positions, bars are chosen with equal arms ($a_1 = a_2$), disposed horizontally and parallel to each others and arranged with lengths and positions so that $\alpha = 0$ and $\alpha_1 = \alpha_2 = \pi/2$. To compact the mechanism, the seesaws at the third stage are aligned and located closer to the differential output of the little finger (lowest output at the last stage) still preserving a safety distance with the corresponding bar. The same is done with the first stage where the bar is placed at a minimum distance from the differential output of the thumb. This method represents the easiest way to settle all geometric parameters of the differential mechanism but it does not take into account the limited palm space. To further minimize the occupied volume, the position of the thumb output is placed on the left side of the palm. This solves the mechanism size constraint but introduces undesired bar collisions during finger motions. At this point, feasible geometric parameters are determined through an iterative process which takes into account all possible bar configurations according to the finger postures. At each iteration the initial configuration is established by:

— aligning the center of the seesaw bars of the last stage with the middle points between Little-Ring outputs and Middle-Index outputs;

- aligning the center of the second stage bar between the centers of the two last differential units;
- aligning the center of the first stage bar between the thumb output and the center of the second stage bar.

Starting from the leaves of the differential tree, up to the root, the following steps are reiterated at each seesaw:

1. collision check: if $\max(a_1, a_2) + \epsilon$ is grater than the length of the input cable (where ϵ is the distance between the point of attach of the output cable and the edge of the bar) the current bar length is shortened to invalidate the inequality;
2. preservation of equal force distribution: a_1 and a_2 are updated according to the new output angles (see Equation 4.24);
3. exploration of the sub-tree: children stages (if present) are revisited restarting from step 1;

This method finds the largest bars possible to:

- fit within the available space in the palm - since large bars allow to explore the whole finger workspaces with wider rotations rather than displacements (that could not be attained within the palm space);
- avoid collisions;
- preserve balanced force distribution when all fingers are open.

The final design of the differential mechanism has approximately equal arms at the second and third stages while at the first one it presents unbalanced arms: the left one 8% longer than the right one. Figure 4.14 shows the simulated differential mechanism at the initial configuration, where half of the input force is provided to the thumb and the other half is evenly shared among fingers.

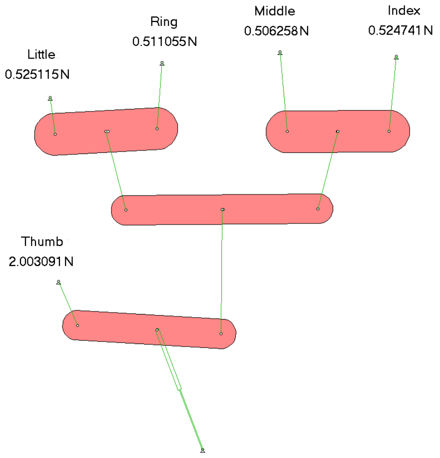

Figure 4.14 – Simulated force distribution at the initial configuration (open hand).

Experimental results. The differential mechanism is tested by realizing the tench-bench support and bars in stereolithography and by using steel axes, IGUS® pulleys and Dyneema® cables (the same used for the first differential design). Each output force is measured by a strain gauge while the input force is constantly provided by calibrated masses. Forces are averaged over 10 [s] experiments repeated at least ten times. Force distribution is measured in three different cases (see Figure 4.15):

1. all fingers open (initial condition);
2. the Thumb and the Little finger closed with the reminder fingers open;
3. a generic configuration.

Finger configurations are selected by locking the output cables of the differential mechanism. Table 4.5 shows the cable lengths relative to the initial configuration.

Table 4.6 shows the collected measurements during the tests. As it can be seen, experimental values are affected by friction losses but remain coherent with the theoretical results expected from design. The

	Thumb	Index	Middle	Ring	Little
1^{st} test [mm]	0.0	0.0	0.0	0.0	0.0
2^{nd} test [mm]	18.1	0.0	0.0	0.0	14.5
3^{th} test [mm]	18.1	5.3	9.5	8.3	14.5

Table 4.5 – Relative cable length variations with respect to the initial configuration for each experimental test.

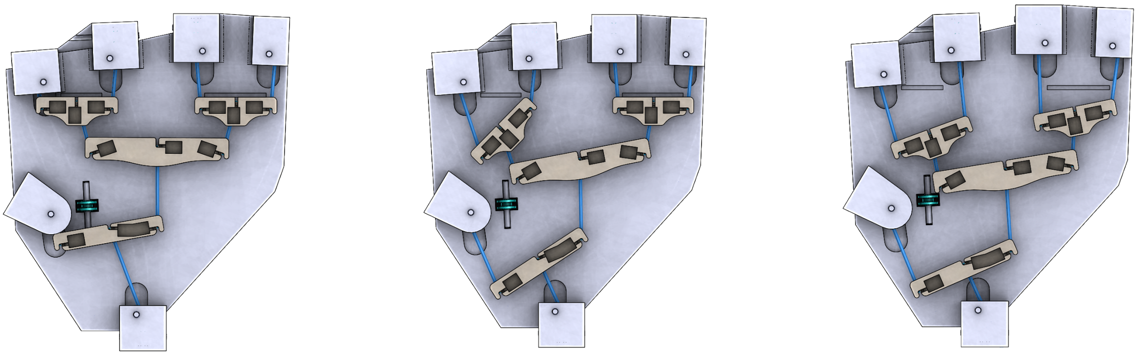

(a) 1^{st} test: open hand.

(b) 2^{nd} test: Thumb and Little finger closed, the rest open.

(c) 3^{rd} test: Random configuration.

Figure 4.15 – Differential mechanism configurations at each experimental test.

first test validates equal force distribution at the initial configuration: half of the total measured force (1.81 [N]) is provided to the Thumb and the other half is equally distributed to the fingers. The second test confirms stronger forces to more open fingers when differential angles are highly unbalanced. In this case, for example, at the first stage the 38% of the total force is provided to the Thumb base while the rest is distributed to the reminder fingers and at the third stage the 78% of the force distributed to the Ring-Little differential unit is provided to the Ring. Finally, the third test shows that finger configurations which induce small angle variations at each differential unit limitedly affect force distribution. For each experiment friction losses are computed by comparing the total output force with the input one. Averaging their values over the tests the mechanism efficiency is estimated at about 87%.

	Actuation	Thumb	Index	Middle	Ring	Little	Total F_{out}
1^{st}test [N]	1.96	0.87	0.24	0.24	0.22	0.24	1.81
2^{nd}test [N]	4.1	1.25	0.51	0.53	0.81	0.23	3.33
3^{th}test [N]	4.1	1.4	0.53	0.54	0.52	0.54	3.52

Table 4.6 – Force distribution tests of the second differential mechanism design. Experimental results (output forces) are averaged over 10 trials.

4.1.3.3 Conclusions

The two differential mechanisms present different design objectives and mechanical implementations. The first one is easier to conceive but it exhibits very low efficiency. The imposition of constant input and output angles at each differential unit requires a higher number of mechanical parts which increases force losses and the overall complexity of the system. The second differential mechanism removes these constraints, resulting more compact, lighter and efficient. Its structure is more challenging to design but it ensures equal force distribution when finger configurations are similar among each others and it provides higher forces to more stretched digits (supposed to be in contact with the object) when finger configurations are unbalanced. The first design can be revisited and improved to minimize friction losses but the reduction of contact surfaces is certainly the most reliable approach. Consequently, the transmission mechanism embodied in the palm is the second differential design. In particular, a more robust version is adopted in which:

— seesaw bars are made of steel;
— Fast-Flight cable replaces Dyneema®;
— aluminum pulleys are used to redirect the cables.

4.2 Actuation

Motor grasp is sized according to the heaviest object supposed to be grasped, a full 330 [ml] soda can (European standards) of 0.366 [Kg]. A cylindrical grasp is used to hold the object within fingers (Figure 4.16a). All fingers are involved in the grasp with all phalanges in contact. Joint configurations and contact locations are obtained through hand and object CAD models (see Table 4.7). No contact is considered at the palm. The grasp analysis is simplified to roughly define the lower bound of the grasp motor torque. Points of contacts are considered rigid with friction (Coulomb friction cone). In the vertical plane of the object, finger forces can be reduced to two opposing forces, one provided by the thumb ($\boldsymbol{f}_T$) and the other by the reminder fingers ($\boldsymbol{f}_F$) as represented in Figure 4.16. In the chosen grasp configuration, the following assumptions can be made:

— fingers exert orthogonal forces on the object surface;
— contact forces generate no torque on the object;
— contacts only occurs on hand rubber parts.

The static friction coefficient (μ) between the rubber (polyjet) on palm and phalanges and the can surface (painted aluminum) is approximately equal to 1.4 (experimentally obtained).

(a) Cylindrical grasp of a soda can.

(b) Simplified grasp in the object vertical plane.

Figure 4.16 – Chosen grasp to size the grasp motor torque.

4.2.1 Required grasp force

In order to preserve the object in the grasp, finger forces must be sufficiently important to avoid the object to slip:

$$||\boldsymbol{f}_T|| = ||\boldsymbol{f}_F|| \geq \frac{mg}{2\mu} \tag{4.25}$$

Finger	$\boldsymbol{q}$	$\boldsymbol{k}$
Thumb	(80.0°, 0.0°, 19.8°, 38.3°)	($\frac{3}{4}l_{cb}$[i], $\frac{1}{2}l_{pp}$[ii], $\frac{1}{2}l_{dp}$[iii])
Index	(50.0°, 21.6°, 44.°)	($\frac{3}{4}l_{pp}$, $\frac{1}{2}l_{mp}$[iv], $\frac{2}{3}l_{dp}$)
Middle	(55.0°, 22.6°, 48.6°)	($\frac{3}{4}l_{pp}$, $\frac{1}{2}l_{mp}$, $\frac{2}{3}l_{dp}$)
Ring	(50.0°, 27.8°, 46.2°)	($\frac{3}{4}l_{pp}$, $\frac{1}{2}l_{mp}$, $\frac{2}{3}l_{dp}$)
Little	(40.0°, 22.1°, 41.5°)	($\frac{3}{4}l_{pp}$, $\frac{1}{2}l_{mp}$, $\frac{2}{3}l_{dp}$)

[i] carpal bone length [ii] proximal phalanx length [iii] distal phalanx length [iv] middle phalanx length

Table 4.7 – Chosen grasp state configuration to size the grasp motor force.

where $\boldsymbol{f}_F = \sum_{j=1}^{4} \boldsymbol{f}_j$, with $\boldsymbol{f}_j$ representing the total force exerted by the j^{th} finger on the object. Considering each finger contact contributing in the grasp, Equation 4.25 can be rewritten as:

$$\sum_{j=1}^{4} \sum_{i=1}^{n_{cj}} \boldsymbol{f}_{ji} \cdot \boldsymbol{n}_{ji} \geq \frac{mg}{2\mu} \tag{4.26}$$

where n_{cj} is the number of point of contacts of the j^{th} finger in opposition to the thumb and $\boldsymbol{f}_{ji}\boldsymbol{n}_{ji}$ is the normal force exerted on the object by the i^{th} contact of the j^{th} finger. Normal forces can be computed through Equation 4.4 given the torque vector $\boldsymbol{t}$ of each serial chain. By defining the contact point vector $\boldsymbol{c}$ as:

$$\boldsymbol{c} = \begin{bmatrix} \delta_1 \\ \delta_2 \\ \delta_3 \end{bmatrix} \tag{4.27}$$

where:

$$\delta_i = \begin{cases} 1 & \text{if the contact forces is non-negative} \\ 0 & \text{otherwise} \end{cases} \quad i = 1, 2, 3 \tag{4.28}$$

Equation 4.26 can be written as:

$$\sum_{j=1}^{4} \boldsymbol{c}_j^T \boldsymbol{f}_j \boldsymbol{n}_j \geq \frac{mg}{2\mu} \tag{4.29}$$

By inverting and substituting Equation 4.4 in Equation 4.29, the left-hand side is equivalent to:

$$\sum_{j=1}^{4} \boldsymbol{c}_j^T \boldsymbol{J}_j^{-T} \boldsymbol{T}_j^{-T} \boldsymbol{t}_j \tag{4.30}$$

To isolate the unknown variable τ_j, namely the pulling force (f_{bj}) over the pulley at the finger base, $\boldsymbol{t}_j$ can be replaced by:

$$\boldsymbol{t}_j = \boldsymbol{B}_j \boldsymbol{x}_j \tag{4.31}$$

where:

$$\boldsymbol{B}_j = \begin{bmatrix} r_{1j} & 0 \\ 0 & -K_2 \Delta\theta_2 \\ 0 & -K_3 \Delta\theta_3 \end{bmatrix} \tag{4.32}$$

and

$$\boldsymbol{x}_j = \begin{bmatrix} f_{bj} \\ 1 \end{bmatrix} \tag{4.33}$$

where r_{1j} is the first pulley radius of the j^{th} finger and f_{bj} is the pulling force at j^{th} finger base provided by the differential mechanism in the palm. This is done to separate the unknown f_{bj} from the transmission design parameters (r_{1j}, K_2, K_3) and the spring deviation from their equilibrium ($\Delta\theta_2$, $\Delta\theta_3$). Equation 4.30 can be restated as:

$$\sum_{j=1}^{4} \boldsymbol{c}_j^T \boldsymbol{J}_j^{-T} \boldsymbol{T}_j^{-T} \boldsymbol{B}_j \boldsymbol{x}_j \tag{4.34}$$

Considering that in grasping the soda can finger joints are similar to each others, the floating bars of the differential mechanism remain approximatively parallel to the initial configuration distributing the motor force equally among finger bases. Consequently,

$$\boldsymbol{x}_j = \boldsymbol{x} = \begin{bmatrix} F_{mf}/4 \\ 1 \end{bmatrix} = \frac{1}{4} \begin{bmatrix} F_{mf} \\ 4 \end{bmatrix} \tag{4.35}$$

where F_{mf} is the motor force distributed towards the fingers (thumb excluded). In Equation 4.29:

$$\sum_{j=1}^{4} (\boldsymbol{c}_j^T \boldsymbol{J}_j^{-T} \boldsymbol{T}_j^{-T} \boldsymbol{B}_j) \boldsymbol{x} \geq \frac{2mg}{\mu} \tag{4.36}$$

naming the sum of four (1 x 2) matrices as $\boldsymbol{v}^T$, the system is solved as follows:

$$\begin{aligned} \boldsymbol{v}^T \boldsymbol{x} &\geq \frac{2mg}{\mu} \\ \boldsymbol{v}\boldsymbol{v}^T \boldsymbol{x} &\geq \boldsymbol{v}\frac{2mg}{\mu} \\ \boldsymbol{x} &\geq (\boldsymbol{v}\boldsymbol{v}^T)^{-1}\boldsymbol{v}\frac{2mg}{\mu} \equiv \boldsymbol{v}^{+T}\frac{2mg}{\mu} \end{aligned} \tag{4.37}$$

from which F_{mf} is obtained if $\boldsymbol{v}$ is full row rank. The same equation applies to the thumb, also studied in the plane by fixing the palm opposition DoF at the base. In this case, equations simplify getting rid of the sum ($\sum_{j=1}^{4}$) since only one finger is considered. The sum of the force required for the fingers (F_{mf}) and the thumb (F_{mt}) is adopted as the demanded force to the motor grasp.

Results. Even though the chosen grasp state configuration is actually unstable - in the sense that the middle phalanx of each finger tends to open at the initial configuration (negative normal force) - contact point are considered fixed (the object does not move) and the grasp stably guaranteed by the first and third phalanges. The minimal motor force required to hold the can is about 50 [N]. This value was obtained at early design stages, when no elastic elements were embedded in finger mechanisms ($K_2 = K_3 = 0$). This obviously imposes an underestimation of the grasp motor force required in the hand prototype (see Chapter 5), since no passive opposing torques are taken into account.

4.2.2 Motor and gearbox selection

The minimum grasp force can be provided either by a low power motor with a big gearbox or, on the contrary, by a high power motor with a small gearbox. Following the same approach adopted for the e-motion motors (see Section 3.2), a small reduction is preferred over a big one in order to sense the output torque from current readings rather than from additional torque or force sensors. On these terms, no gearbox is installed after the motor output and a high power motor is selected: the EC 45 flat Maxon motor (characteristics shown in Table 4.8). This motor is chosen according to its size, so to fit in the robot forearm, its good power-to-weight ratio and limited price (about 100 €). A steel pulley is mounted on the motor shaft to pull the grasp tendon. The tendon is passed from the inside to the outside of the pulley through a small hole (on one side of the pulley) and fixed to the pulley by a simple knot applied at the cable end. The pulley radius is determined to provide the minimum grasp force and its width is designed so that the cable is rolled without superposing. This avoids arm length variations that would undesirably affect the output force. Cable superposition is dodged by selecting a pulley radius sufficiently large to completely roll the cable, from the open hand configuration to the closed one, in at most one turn. Given that at the differential input the maximum length variation of the tendon to close all fingers is about 15 [mm], the pulley diameter is appointed to 5 [mm] in order to provide more than 50 [N] at nominal torque (51.2 [N]) and fully roll the cable in about one turn.

	Size [mm]	Power [W]	τ_n [Nm]	weight [Kg]
BLDC EC 45 flat	⌀ 42.8 x 47.3	70	0.128	0.141

Table 4.8 – Characteristics of the chosen grasp motor.

4.3 Control

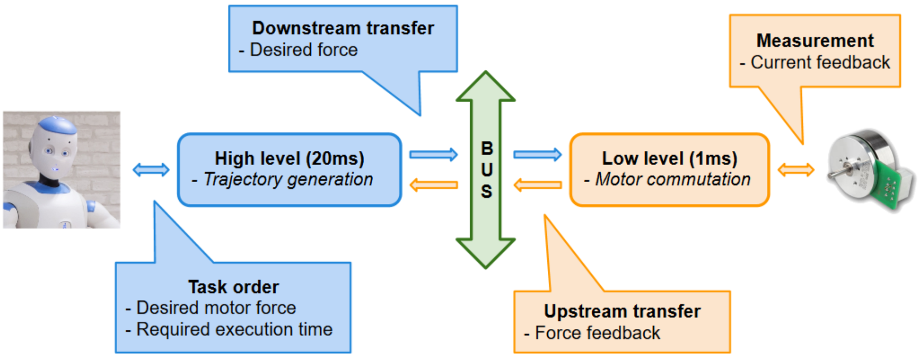

Figure 4.17 – Global communication scheme of grasp motor.

The grasp motor is controlled in force at 1 [KHz] through the Field oriented Control (FoC) presented in Section 3.3.1. Differently from e-motion motors, no outer control loops are implemented since the motor commutation already implements a PI controller to drive the motor output torque to the desired one. A magnetic rotary encoder (AMS *AS5048*) is used to detect the absolute angular position of the rotor, even though no position control is performed. This because the FoC requires the rotor orientation to compute the phase frame transforms. The desired pulling force is given every 20 [ms] from a high level task to the motor controller. This is converted to the desired torque (τ^*) and current (i^*) knowing the arm at the pulley (R_P) and the motor torque constant (K_T). The arm is computed as the pulley radius plus half of the cable diameter, while the motor torque constant is taken from the motor data-sheet. No torque sensors at the output shaft and cable tension sensors are used (according to the same policy adopted for the e-motion actuation system). However, since in this case no close loop is performed on force - but only on torque - cable tensioning is highly affected by the knowledge of the real radius and torque constant parameters. Figure 4.18 shows the control scheme. The gains R_P and K_T^{-1} before the FoC controller are the ones affecting control performance. The ones after the FoC controller have the only use to provide feedback at the higher level. Figure 3.12 resumes the communication scheme between higher and lower level modules.

Figure 4.18 – Grasp motor control scheme.

4.3.1 Cogging torque: Identification and Compensation

The undesired cogging torque characteristic of BLDC motors [138] is identified and compensated [139] via torque feed-forward. The identification is performed over a complete mechanical turn through a simple position control loop. Indeed, the current required by a PI controller to preserve a desired rotor position at no load is directly related to the cogging torque - since the motor would need no current to preserve the attained rotor position in absence of external forces. A stair-like position reference trajectory is provided to identify the cogging torque at discrete intervals (Figure 4.19). According to the desired number of torque samples the step amplitude is adjusted. At each step, the command (expressed in duty cycles) given to the controller is stored as the transient phase is completed. The gains of the PI controller are not trivial to be identified since at each step the rotor suffers different external forces. Gains are chosen in function of the worst case at which the rotor is asked to stabilize: close to a stator slot (cogging peak). To improve cogging torque estimation, collected data are filtered to reduce high frequency noise and they are averaged over repeated tests.

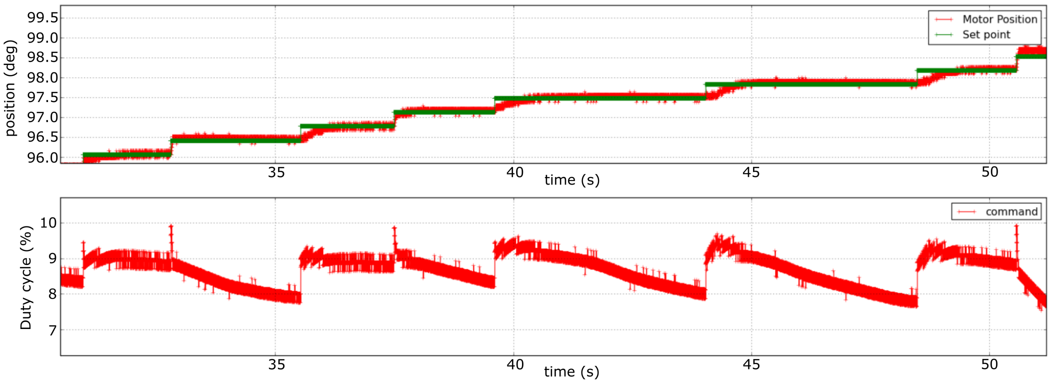

Figure 4.19 – Position control to characterize the cogging torque over a complete mechanical turn.

For the EC 45 Maxon motor, 48 cogging torque periods exist in a mechanical turn - 6 in an electrical one (since E45 has 8 pairs of poles). Since the cogging torque is similar at each electrical turn, their values are averaged to identify a general cogging torque per electrical turn (dashed black curve in Figure 4.20a). This allows to store a smaller number of points on the motor card which presents a limited storage. The 8 curves are identified by rotating the motor in both direction and averaging their values to eliminate static friction effects. The identification process requires about 45 minutes to collect data for a full mechanical turn. Figure 4.20b shows the two collected (and averaged) curves over an electrical turn.
Curve offsets are subtracted from the respective curves and their average is taken as the friction bearing current offset. Figure 4.21 compares the originally collected curves (dashed blue and red curves) with the ones obtained by adding the estimated bearing friction to the stored cogging curve (blue and red curves). The no load current ($i_0 = 234$ [mA]) reported on the motor data-sheet is also represented (green dashed lines) to show that it is defined by the motor constructor to overcome friction bearing and cogging torque with a safe margin. Finally, Figure 4.22 highlights the identified cogging torque values (signed 8 bit) stored on the motor board. A cubic interpolation is traced to visually reconstruct the cogging torque shape.

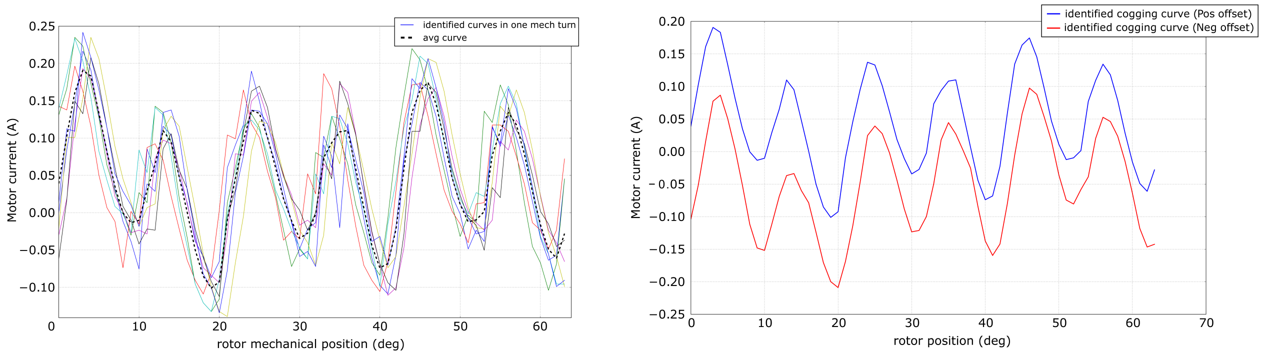

(a) Averaged motor currents on an electrical turn. Data are acquired in a complete mechanical turn.

(b) Averaged motor currents over two mechanical turns of opposing directions.

Figure 4.20 – Cogging torque identification for the EC 45 Maxon motor in an electrical turn.

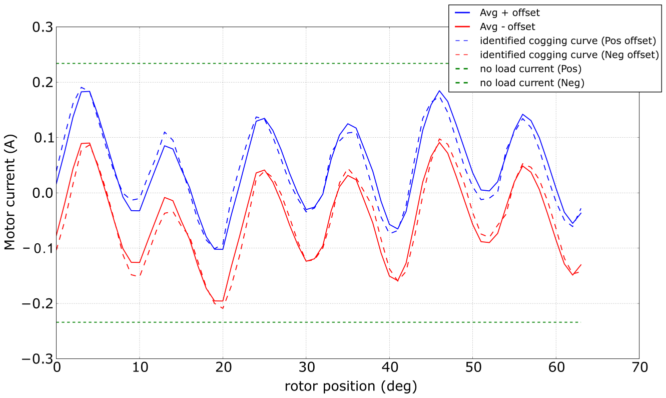

Figure 4.21 – Comparison between the cogging torque identified, the one stored (plus the estimated bearing friction) and the no load current motor.

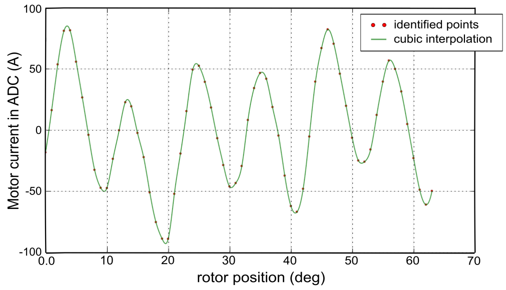

Figure 4.22 – Values stored on the motor board and added to i_q^* to compensate cogging torque effects.

4.3.2 Trajectory generation

The desired pulling force is generated at high level by a Bang-bang trajectory generator which takes as inputs the desired target force and execution time. Trajectories are computed as described in Section 3.3.3, where in this case smoothness and continuity are ensured for the force and a trapezoidal (or triangular) model is provided to its derivative.

4.3.3 Experimental results

To investigate the performance of the force control, a dynamometer is used to measure the pulling force at the cable as shown in Figure 4.23.

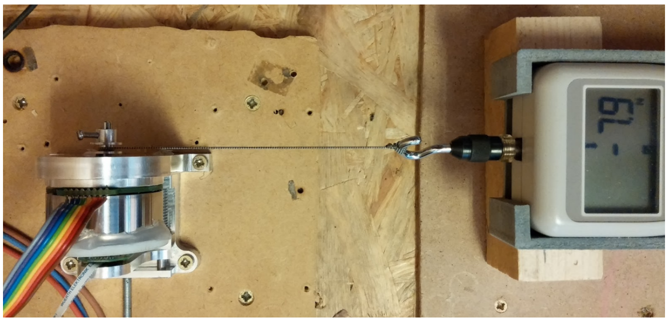

Figure 4.23 – Force control experimental test bench for the grasp motor.

No torque feed-forward. At first, the analysis is conducted without injecting the identified cogging torque in the controller. As it can be seen in Figure 4.24a, the output force does not coincide with the measured one. This is an expected result since the force is controlled in open loop. Several factors might be the cause, such as the inaccurate knowledge of the arm length (real pulley and cable radii) or of the motor parameters (K_T and the Shunt resistor). However, none of them would cause the important offset and oscillatory trend which characterize the measured force. By looking at rotor position trajectory (during experimental tests), it is observed that the rotor still presents small slow motions at constant motor currents. These motions, due to the knot elasticity at the cable end, induce cogging torque variations which explain the oscillatory behavior of the tensioning force. The remaining offset, instead, is mainly due to frictional losses and partially caused by model inaccuracies. These are grouped and identified as a general torque dependent friction loss through the gearbox formulation presented in Annex C. Once identified the cogging torque (as explained in Section 4.3.1) and the frictional losses, the estimated force from current measurements is post-processed taking into account both effects. Figure 4.24b shows the clear match between the measured force and the resultant estimated force. In particular, the blue curve represents the estimated force subtracted of friction losses while the green one is the estimated force considering both friction and cogging torque effects.

Torque feed-forward. At this point, frictional and cogging torque effects are feed-forwarded to the desired motor torque. Figure 4.25a shows the desired force (green curve), the effect of the identified cogging torque on the output force (yellow curve) and the force given as input to the controller (red curve). The last results from estimated frictional and cogging torque feed-forwards and improves the control performance by reducing force oscillations and offset, as shown in Figure 4.25. Error still exists due to the roughly identified cogging torque and since the controller is in open loop on the force reference. Minor errors might be achieved by identifying the cogging torque over a complete mechanical turn and with more points. Nevertheless, limited advantages would be obtained since the controller would still lack of force feedback at the cable.

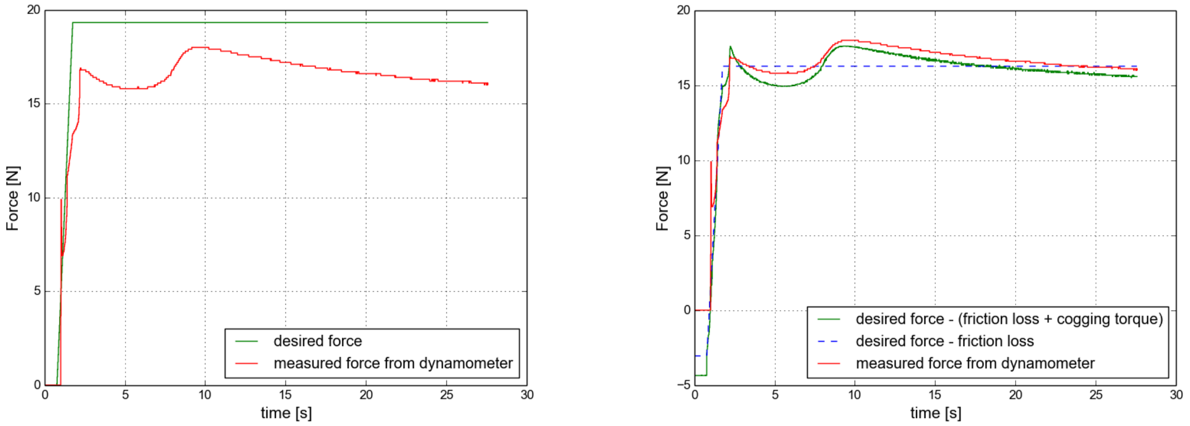

(a) Force control performance without torque feed-forward.

(b) Identification of disturbance factors on the output pulling force.

Figure 4.24 – Early experimental force control results and identification of force disturbances.

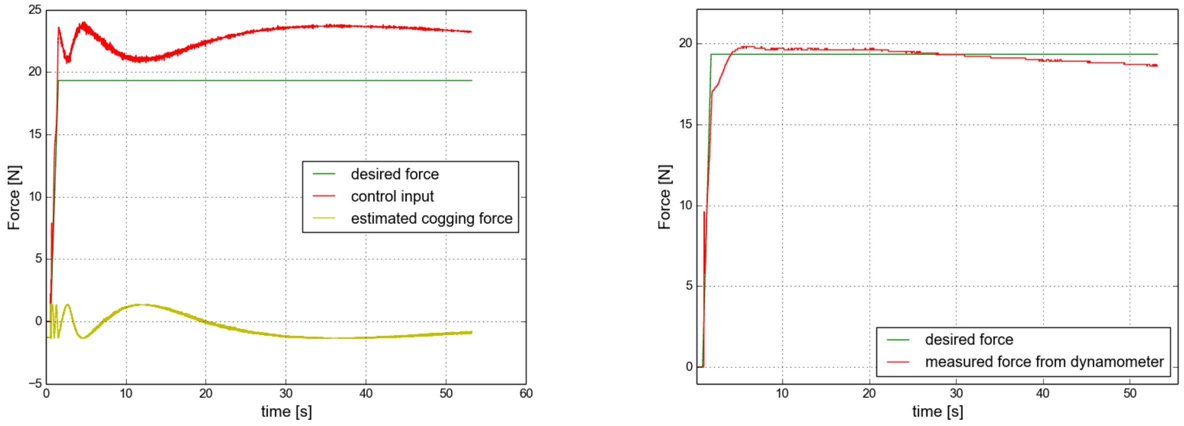

(a) Desired force, estimated cogging force and force given as input to the controller (f^*_{cable}) after torque feed-forward (obtained from current readings).

(b) Comparison between the measured force and the desired one.

Figure 4.25 – Torque feed-forward effects on the open loop force control.

Experimental results show that a force control can be achieved with active friction and cogging compensation. Even without considering successive frictional losses in the mechanical transmission chain, they highlight the need for higher motor torques with respect to the one required.

4.4 Conclusion: finger concept

In this section, the final finger and differential mechanism designs are presented. Figure 4.26 shows a generic finger concept in the stretched configuration and at other possible configurations dictated by the presence of external forces. Lateral covers are left transparent to highlight the tendon-based transmission mechanism. Pulleys placed at the joint rotational axes are the ones designed in Section 4.1.2.2 to improve grasping capabilities. Figure 4.27 presents the differential mechanism in a random configuration with input and outputs highlighted.

(a) Stretched.

(b) Last phalanx decoupling in presence of an external force at the middle phalanx.

(c) All phalanx decoupled.

(d) Second phalanx decoupled in presence of an external force at the proximal phalanx.

Figure 4.26 – Generic finger grasp prototype.

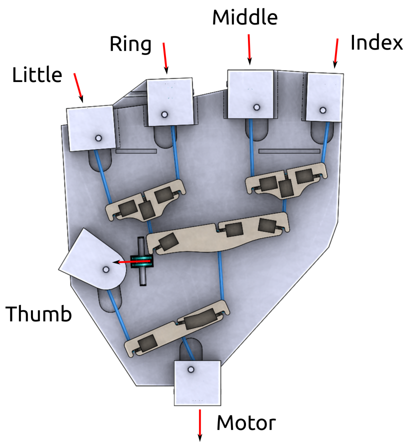

Figure 4.27 – Dorsal view of the differential mechanism prototype.

5

Hand design: ALPHA

The designs presented in Chapters 3 and 4 can be integrated in the same hand by dealing with the opposing nature of their transmission mechanisms. In fact, the capability of fingers to gesture and self-adapt as presented, cannot coexist without intervening on the e-motion transmission mechanism. This chapter presents the mechanical interface devised to switch between motion and grasp functionalities. The main challenge consists in preserving the characteristics of both transmission mechanisms while limiting potential losses caused by their coexistence. The switch between e-motion and grasp is realized by opening and closing finger couplings. In order to choose where and how kinematic closed loops can be opened, Section 5.1 analyzes the internal efforts at the four-bar linkages. After, Section 5.2 proposes some mechanisms for decoupling finger phalanges and, then, Section 5.3 presents the adopted solution and shows the final hand design: the ALPHA design (ALdebaran Parallel HAnd).

5.1 Force analysis

The dynamic model presented in Section 3.1.1.4 computes the joint torques that are needed to track desired joint position, velocity and acceleration trajectories for a closed loop mechanism. The algorithm solves the IDM for the equivalent tree robot and, then, closes the loop by adding contact wrenches between the links at which the closure is performed. Constraining forces are added to the Lagrange equations using the Lagrange multipliers ($\boldsymbol{\lambda}$) and active joint torques are efficiently computed by using Equations 3.36 - 3.38. This approach uses the constraining forces to simplify the active torques calculation without developing the effects of the closing loop on the coupling mechanism, ensuring good performances in real-time. In order to characterize the internal efforts caused by the kinematic closed loop, contact forces have to be explicitly determined and propagated in the whole chain. The first line of Equation 3.37 determines the p Lagrange multipliers which constrain the loop at the cut revolute joints. These external forces have to be projected on the cut joint frames and applied (added or subtracted) to the connected links. At this point, internal efforts are determined by propagating the constraining forces to the common root of the tree robot. Internal efforts analysis is necessary to determine the nature of the kinematic switching interface and to size its locking force.

5.1.1 Thumb analysis

The thumb model presents only one four-bar linkage in its chain, which means that $\boldsymbol{\lambda}$ is a (2 x 1) vector. Its components correspond to the planar force exerted at the cut joint (q_6) due to the closed loop constraint. Their values are computed according to:

$$\boldsymbol{\lambda} = -\boldsymbol{W}_p^{-T}\boldsymbol{\Gamma}_{tr_p} \tag{5.1}$$

where $\boldsymbol{W}_p$ is obtained from the kinematic constraint equations:

$$\boldsymbol{J}\dot{\boldsymbol{q}} = 0 \tag{5.2}$$

which can be rewritten as:

$$\begin{bmatrix} \boldsymbol{W}_a & \boldsymbol{W}_p & \boldsymbol{0} \\ \boldsymbol{W}_{ac} & \boldsymbol{W}_{pc} & \boldsymbol{W}_{cc} \end{bmatrix} \begin{bmatrix} \dot{\boldsymbol{q}}_a \\ \dot{\boldsymbol{q}}_p \\ \dot{\boldsymbol{q}}_c \end{bmatrix} = \boldsymbol{0} \tag{5.3}$$

In particular, for the thumb model $\boldsymbol{J} = \boldsymbol{J}_6 - \boldsymbol{J}_7$ since:

$$\boldsymbol{J}_6 \begin{bmatrix} \dot{q}_3 \\ \dot{q}_6 \end{bmatrix} = \boldsymbol{J}_7 \begin{bmatrix} \dot{q}_4 \\ \dot{q}_5 \end{bmatrix} \tag{5.4}$$

and the matrix $\boldsymbol{W}_p$ is obtained by rewriting Equation 5.4 in the same form of Equation 5.3, considering that q_3 is the active joint, q_4 and q_5 are the passive ones and q_6 is the cut joint.

5.1.2 Finger analysis

The same approach applies to the finger model where, this time, two four-bar linkages in series are present. Each loop cannot be solved independently since the calculation would neglect the influence that the proximal loop exerts on the distal one. Hence, both closed loops are solved at the same time rewriting Equation 3.28 as follows:

$$\boldsymbol{\Gamma}_{cl} = \begin{bmatrix} \tau_a \\ 0 \\ 0 \\ 0 \\ 0 \end{bmatrix} = \boldsymbol{\Gamma_{tr}} + (\boldsymbol{J}_6 - \boldsymbol{J}_8)^T\boldsymbol{\lambda}_1 + (\boldsymbol{J}_7 - \boldsymbol{J}_9)^T\boldsymbol{\lambda}_2 \tag{5.5}$$

where the second term expresses the kinematic constraint at the first loop:

$$\boldsymbol{J}_6 \begin{bmatrix} \dot{q}_1 \\ \dot{q}_6 \end{bmatrix} = \boldsymbol{J}_8 \begin{bmatrix} \dot{q}_2 \\ \dot{q}_3 \end{bmatrix} \tag{5.6}$$

and third terms expresses the kinematic constraint at the second one:

$$\boldsymbol{J}_7 \begin{bmatrix} \dot{q}_1 \\ \dot{q}_6 \\ \dot{q}_7 \end{bmatrix} = \boldsymbol{J}_9 \begin{bmatrix} \dot{q}_1 \\ \dot{q}_4 \\ \dot{q}_5 \end{bmatrix} \tag{5.7}$$

in which q_1 is the active joint, q_2 to q_5 are the passive ones, q_6 is the cut joint at the first loop and q_7 is the cut joint at the second one. Note that, in the second loop, q_6 is replaced by q_1, q_2 and q_3 according to the kinematic constraint equation of the first loop, consequently contributing to the computation of $\boldsymbol{W}_p$ for the second loop ($\boldsymbol{W}_{2p}$). Both $\boldsymbol{W}_{1p}$ and $\boldsymbol{W}_{2p}$ matrices are identified rewriting Equations 5.6 and 5.7 in the same form of Equation 5.3. According to the virtual work principle (Equation 3.36) and the last p equations of Equation 5.5, the following relation holds:

$$\boldsymbol{\Gamma}_{\boldsymbol{tr}} = - \begin{bmatrix} \boldsymbol{W}_{1p}^T & \boldsymbol{W}_{2p}^T \end{bmatrix} \begin{bmatrix} \boldsymbol{\lambda}_1 \\ \boldsymbol{\lambda}_2 \end{bmatrix} \tag{5.8}$$

where the constraining force $\boldsymbol{\lambda}_1$ exerted at joint q_6 and the constraining force $\boldsymbol{\lambda}_2$ exerted at joint q_8 are computed using Equation 5.1.

5.1.3 Conclusion

Once constraining forces are computed at each cut joint and projected in their frames, they are applied at each link connected to the cut joints and, then, propagated in the tree robot up to the root (as in the backward recursion of the RNEA B.1). This method allows to completely characterize the internal efforts in the closed loop chain. At this point, forces can be studied at any desired point of the chain to merge e-motion and grasp designs in one hand. Simulation results of internal efforts at the e-motion coupling bars are reported in Section 5.3.2.

5.2 Merging designs

Finger self-adaptability and gestures are obtained by contrasting transmission couplings. The former is ensured by a transmission mechanism that does not restrain finger DoFs while, the latter, is assured by joint couplings that reduce finger DoFs to the number of actuators. In order to preserve both functionalities it is necessary to design an interface mechanism that switches from one coupling system to the other. Since the gesture capability has higher priority than the grasping one, the fusion of the hand designs starts from preserving the double inverted four-bar linkages. To open and close the kinematic loops active or passive elements can be adopted. Passive elements are classified in triggered (or discrete) and continuous elements [140]. A triggered element is a mechanical element like a spring or a friction component, which allow joint motion after a minimum joint force or torque is reached while, a continuous element is a mechanical element, like a dumper or a mass (or inertia), which admits joint motions in direct dependence to the joint force or torque. In this context, since coupling has to be preserved during e-motion triggered elements are used to decouple finger joints. Force thresholds are determined in function of the estimated efforts in the transmission mechanisms, while driving active joints from 0° to 90° in 1 [s]. Two types of passive decoupling mechanisms are developed: a friction-based locking mechanism and an elastic link. Both mechanisms are designed to satisfy the following specifications:

— joint coupling has to be ensured with a negligible angle error during e-motion (see Section 5.3.1);
— passive elements have to exert a bounded opposing force during grasping.

This section is structured as follows. The analysis of some active and passive locking mechanisms is firstly presented in Section 5.2.1. Here, a brief introduction about electromagnetic and bi-stable locking devices is given, together with the description of developed passive locking mechanism prototypes. Even though the lasts solve the transition between e-motion and grasp, they are not designed to autonomously couple back the original transmission. Furthermore, they are complex and non-trivial to industrialize. Hence, rather than opening and closing finger transmissions through locking-unlocking devices, linkage couplings are transformed to elastic transmissions replacing rigid bars by elastic elements. This approach, presented in Section 5.2.2, is mechanically simple, easy to be industrialized and it solves both loop opening and closure (joint decoupling and re-coupling). Even if it introduces slight angle errors during quasi-static motions and uncontrollable finger configurations during high dynamic motions, this solution respects the given requirements.

5.2.1 Locking devices

Locking-unlocking devices can be divided in three main categories: mechanical, friction and singularity. Mechanical locks are obtained by getting stuck two mechanical components according to their relative position. A classical example is a latch with one locking position in which a pawl hinders the motion of the hook when it gets blocked in the socket. Singularity locks are based on singular mechanism configurations in which a high locking force is generated and a low unlocking forces is required. Friction locks are characterized by two surfaces that transmit motion when in contact. Their locking forces (or torques) depend on the friction coefficient and the normal force between the two surfaces. The main advantage of friction-based locking devices is that they can be easily released under load with respect to the other categories. On the other hand, their locking torques are limited by the maximal normal force between the two surfaces in contact. Locking devices belonging to any of these categories can be active or passive. Active locking devices change their state (locked-unlocked) by mean of a controller while passive ones do not require any regulation.

Active friction-based locks. Among friction-based active locking devices electromagnetic brakes are commonly used. These brakes modulate the normal force between the contact surfaces by controlling the magnetic field induced in a electromagnet or coil that interacts with a permanent magnet. These devices are easy to control and simple to conceive but they consume a large amount of energy every time they are active (to preserve a desired unstable position). In order to reduce power consumption bi-stable brakes can be used. Such devices present two equilibrium positions (locked-unlocked) and one unstable position in between, and require energy only to change their state. An example is represented by the Bi-stable Linear Moving Magnet (BLMM) where the two stable positions are created by opposite electromagnets. This device controls the linear position of a short shaft that can be alternatively used to lock and unlock a mechanical latch. In this case, possible locking positions are reduced to one and the locking force (torque) is no more related to the normal force between the contact surfaces. Although this idea could be used to establish or relax mechanical constraints, ready-to-use active brakes require more space than the one available in the fingers.

Passive friction-based locks. Passive friction-based locking devices present locking torques that cannot be controlled. As stated before locking torques are limited by the maximal normal force between the two surfaces in contact. Nevertheless, this could be either a disadvantage or an advantage. In fact, if locking is only needed under a certain force, the limit can be carefully tuned during the design phase to obtain the disengagement when desired. Rather than adopting solutions proposed in literature [141], a custom friction-based magnetic brake is developed on the base of this principle.

5.2.1.1 Friction-based magnetic lock

The friction force between surfaces is generated by the attracting force between a permanent magnet and a ferromagnetic material. To choose the structure of the locking mechanism different magnet shapes and relative displacements between them are analyzed. Electromagnetic problems are addressed in 2D with FEMM (Finite Element Method Magnetics) a finite element solver which includes a CAD-like program to inspect magnetic interactions between arbitrary contours. Supposing to integrate both elements at level of the joints, or bars of the transmission mechanism, three cases are investigated:

1. rectangular (1 x 0.5 [mm]) magnets 1 [mm] thick axially displaced;
2. rectangular (1 x 0.5 [mm]) magnets 1 [mm] thick laterally displaced;
3. circular (D_{1ext} = 2.05 [mm], D_{2ext} = 1.5 [mm]) magnets 0.5 [mm] thick axially displaced.

In each case, one magnet is fixed while the other one is displaced along a constrained trajectory as if attached to a sliding joint. The objective of these simulations is to qualitatively characterize the force of attraction exerted on the moving part according to its shape and position. Figure 5.1 shows the attraction force behavior for each case. In the first case (Figure 5.1a) the force decreases in a quadratic way as one magnet gets farther from the other. The peak force is at contact and the force of attraction completely vanishes after some distance. In the second case (Figure 5.1b), instead, the contact between surfaces does not constraint their relative motions leading to an elastic effect in its neighborhood. The same happens for the third case (Figure 5.1c) in which two concentric magnets are involved: the contact is stable but not constrained, which means that even a small force can displace the movable magnet. In addition, they experience undesired slight repulsion forces before attraction. The second and third cases allow a continuous decoupling rather than an on/off effect. In the contact neighborhoods they behave exactly like elastic elements, but their attraction forces are weaker compared to springs of the same size. In addition, they completely loose connection if an effort stronger than their maximum attraction force is attained. Since for a locking mechanism an on/off behavior is desired, the first solution is used to develop the passive friction-based locking device. Henceforth two designs are proposed. Both improve the maximum locking force by means of additional friction surfaces and take advantage of the radial displacement to help re-coupling. A composition of neodymium, iron and boron (NdFeB) permanent magnets are used in both prototypes. The two designs allow finger decoupling by stretching and shortening the rigid bar of the four-bar linkage (see Chapter 3.4).

First version. The first version of the magnetic friction-based locking device is composed by a permanent magnet wrapped by a non-magnetic cap and a free-to-move ferromagnetic shaft as shown in Figure 5.2a. The device is placed on a stereoscopic mechanism composed by a sliding bar and a guiding rectangular tube (Figure 5.2b). The stereoscopic mechanism replaces the aluminum bar presented in the e-motion design and ensures the coupling by securing the sliding bar to the tube with the locking mechanism. The cap of the lock is fixed to the tube while the shaft is in a cylindrical socket placed in the bar, in which it can limitedly move along its axis. As soon as the shaft gets close to the cap, the permanent magnet pulls the shaft partially out of its socket, consequently locking the bar to the tube. At this point, the coupling is ensured by the friction force between the shaft and the cap. If an external force stronger than maximum locking force is applied, the shaft disengages from the magnet and returns into the socket. The contact between shaft and cap is modeled in 2D as shown in Figure 5.3. In static conditions the following equations hold :

$$\begin{aligned} \boldsymbol{F}_T &= \boldsymbol{F}_w + \boldsymbol{F}_B + \boldsymbol{F}_{ext} \\ F_n &= -\,\boldsymbol{F}_T\cos(\beta) \\ F_f &= -\,\boldsymbol{F}_T\sin(\beta) \end{aligned} \tag{5.9}$$

where

— F_f: friction force tangent to contact (y axis);

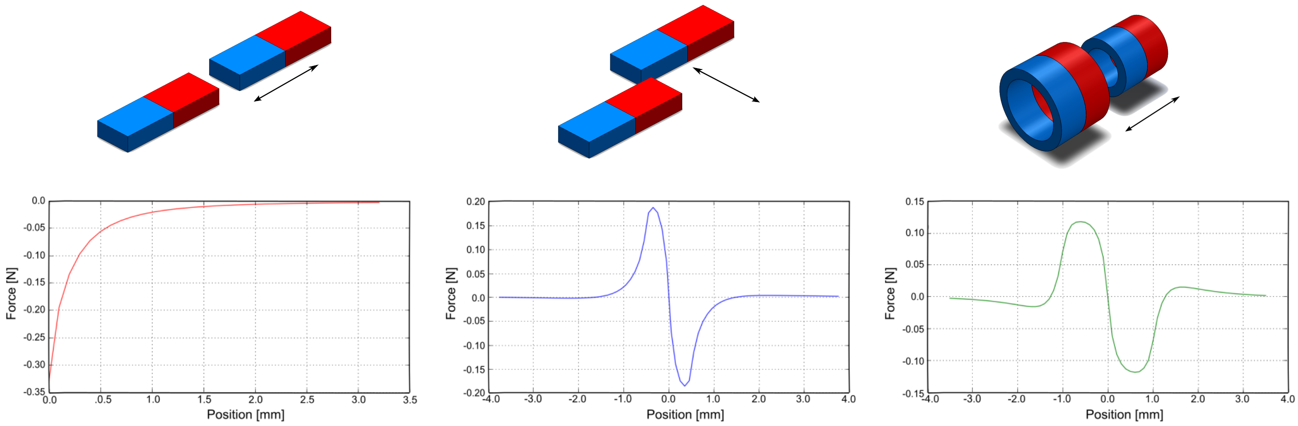

(a) Attraction force behavior as the movable magnet is axially displaced.

(b) Attraction force behavior as the movable magnet is laterally displaced.

(c) Attraction force behavior as the movable magnet is axially displaced.

Figure 5.1 – Characterization of the attraction force exerted on the moving magnet according to its shape and position. Three cases are here analyzed: rectangular magnets axially and laterally displaced and ring magnets axially displaced.

- F_n: normal contact force (x axis);
- $\boldsymbol{F}_T$: total force exerted on the chamfer surface;
- $\boldsymbol{F}_w$: shaft weight;
- $\boldsymbol{F}_B$: magnetic attraction force exerted by the magnet on the shaft;
- $\boldsymbol{F}_{ext}$: external force exerted on the shaft always orthogonal to $\boldsymbol{F}_B$ and $\boldsymbol{F}_w$ by design;
- β: angle between $\boldsymbol{F}_T$ and the normal vector to the chamfer surface.

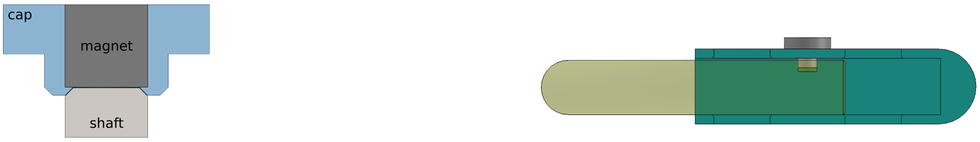

(a) Magnetic friction-based locking device.

(b) Stereoscopic transmission mechanism composed by a sliding bar and a guiding rectangular tube.

Figure 5.2 – Friction-based locking device and transmission mechanism to decouple finger joints.

Using the Coulomb friction model no sliding happens if:

$$F_f \leq \mu F_n \tag{5.10}$$

where μ is the friction coefficient between the surfaces in contact.
The parameters which characterize the locking mechanism are:

- the magnetic attraction force of the permanent magnet ($\boldsymbol{F}_B$) which can be tuned changing the shape and material of the magnet and ferromagnetic shaft;
- the weight of the shaft ($\boldsymbol{F}_w$);
- the chamfer angle of the cap (α);
- the friction coefficient between the cap and the shaft (μ).

The external force applied on the bar ($\boldsymbol{F}_{ext}$) is the only variable in the system. Its intensity varies angle β and consequently triggers the sliding. The transition happens when $F_f = \mu F_n$, which means that:

$$\begin{aligned} \mu F_n &= -\boldsymbol{F}_T \sin(\beta) \\ -\mu \boldsymbol{F}_T \cos(\beta) &= -\boldsymbol{F}_T \sin(\beta) \\ \beta &= \tan^{-1}(\mu) \end{aligned} \tag{5.11}$$

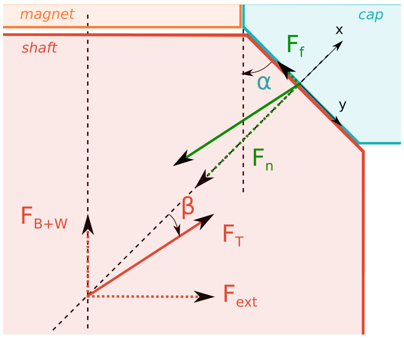

Figure 5.3 – 2D contact point model between the friction surfaces of the locking device.

$\boldsymbol{F}_{ext}$ can be a consequence of the finger dynamics during e-motion or it can be generated while grasping. The locking device has to hold the coupling during hand gestures and it is supposed to release the paring as finger adaptation is needed. The maximum locking force of the mechanism is tuned in function of the previously mentioned parameters. Since gravity influences the normal force to the contact two cases are considered. In the first one, the attraction force and the weight of the shaft have the same direction and sign as shown in Figure 5.3 :

$$\begin{aligned} \tan(\alpha - \beta) &= \frac{F_B + F_w}{F_{ext}} \\ F_{ext} &= \frac{F_B + F_w}{\tan(\alpha - \beta)} \end{aligned} \tag{5.12}$$

the external force unlock the mechanism when:

$$F_{ext} = \frac{F_B + F_w}{\tan(\alpha - \tan^{-1}(\mu))} = \max(F_{\text{lock}}) \tag{5.13}$$

where α is the chamfer angle. In this scenario the locking force is the maximum possible and it is used to set the lower boundary of decoupling external force.

In the second case, the attraction force and the weight of the shaft are opposite to each others. The locking force is weaker than before and it is used to size the locking device parameters in order to preserve finger coupling during motion:

$$F_{ext} = \frac{F_B - F_w}{\tan(\alpha - \tan^{-1}(\mu))} = \min(F_{\text{unlock}}) \tag{5.14}$$

where F_B and F_w depend on the permanent magnet and shaft materials and volumes while μ on the shaft and cap surface materials. These parameters are constrained by little material choice and limited space in the fingers while the chamfer angle can be arbitrarily chosen in the interval $(0, \pi/2)$.

Note that at this scale F_w is negligible with respect to F_B (< 0.01$\%$) leading $\max(F_{\text{lock}})$ to basically coincide with $\min(F_{\text{unlock}})$.

Figure 5.4 shows the passive locking device prototype and the test bench which allows to measure the efforts exerted on it. A screw is used to push the bar inside the rectangular tube and a load cell, attached to the tube, is used to record the transmitted force. As it can be seen from the experimental curve in Figure 5.5, the mechanism remains locked until the pushing force triggers the decoupling. The curve presents two spikes before the triggering force which prove that the bar is still locked and it presents an offset after the triggering force due to the sliding friction between the bar and the tube.

This friction-based locking device offers an on/off behavior that guarantees no opposing force to the grasping actuator once the mechanism is released. However, its realization is not trivial due to small dimension of the mechanical parts. Quality and precision of fabrication of the cap strongly influence the chamfer accuracy and, consequently, the lock sizing according to the desired maximum locking force. These limits hinder the fruitful employ of this mechanism imposing the conception of a different version,

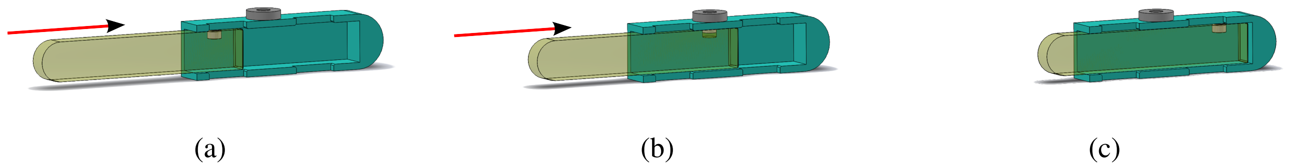

Figure 5.4 – The friction-based locking device test bench consists in pushing the sliding bar in the rectangular tube fixed to a load cell. Transition from (a) to (b) checks whether the magnet properly pulls the shaft out of its socket, locking the mechanism. Transition from (b) to (c) evinces the triggering force required to unlock the device.

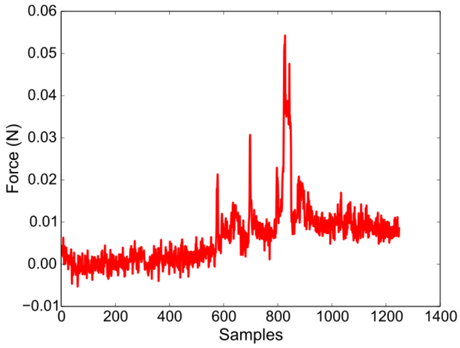

Figure 5.5 – Experimental force threshold. The maximum peak represents the triggering force after which the locking device is unlocked.

easier to manufacture and design.

Second version. The second prototype is based on the same working principle: the magnetic attraction between a permanent magnet and a ferromagnetic element. This time, however, the locking mechanism is located at one joint of the four-bar linkage rather than at the main link. The aluminum bar which couples finger phalanges maintains its shape and length but it is no more hinged to a fixed axis. The connection between bar and phalanx is ensured by the locking mechanism composed of a magnetic sphere and non-ferromagnetic and ferromagnetic (iron) layers stacked one on top of the other (Figure 5.6). The sphere is attached to the end of the bar while the plates are fixed to the successive phalanx. A circular hole on the non-ferromagnetic material locks the mechanism at the desired coupling transmission. To avoid mechanical play, an air gap between the sphere and the iron place is preserved so that the magnetic ball perfectly fits in the hole. Analogously to the previous prototype, external forces exerted on the bar unlock the mechanism as they exceed the maximum locking force. The contact model is the same as before (Equations from 5.9 to 5.14) where the contact points are between the sphere and the hole edge rather than the chamfered surfaces, and where:

- α is the inclination of the tangent to the sphere surface passing at the point of contact;
- $\boldsymbol{F}_w$ is the weight of the magnetic sphere.

Again, α is the parameter which affects the most the locking force. It can be adjusted by varying the hole diameter between the interval $(0, D_{\text{sphere}})$. The thickness of the non-ferromagnetic layer also influences the locking force but it is limited by two antagonistic constraints:

- keep the sphere always in contact to the non-magnetic material when the mechanism is unlocked;
- avoid mechanical play by preserving an air gap between the sphere and the magnet when the mechanism is locked.

The thickness of the non-ferromagnetic layer and the hole diameter impose a vertical displacement of the sphere. To allow this additional motion, the joint at the bar base is transformed to a 2 DoFs spherical joint. In order to help the sphere to easily find back the hole once the mechanism is unlocked, the non-ferromagnetic plate is designed so that the magnet is restrained to follow a circular trajectory.

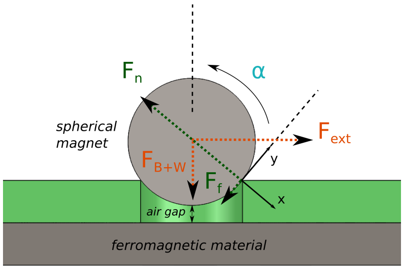

Figure 5.6 – Contact model of the friction-based locking mechanism composed of a magnetic sphere and non-ferromagnetic and ferromagnetic (iron) plates stacked one on top of the other.

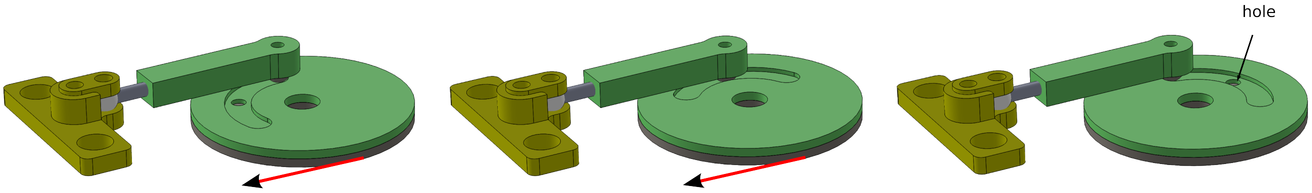

(a) (b) (c)

Figure 5.7 – Test bench of the friction-based locking mechanism. Transition from (a) to (b) checks whether the spheres gets stuck in the circular gap, locking the mechanism. Transition from (b) to (c) evinces the triggering force required to unlock the device.

The system used to test the prototype is shown in Figure 5.7. The external force is provided by a screw and it is transmitted through a load cell and a cable-pulley mechanism to the locking device. The force measured by the load cell (F_{exp}) refers to the pulling tension on the cable and it is used to indirectly compute the force applied on the magnetic sphere (F_{ext}) according to the pulley geometry:

$$F_{ext} = \frac{F_{\text{exp}} R}{d} \tag{5.15}$$

where d is the distance between the center of rotation of the pulley and the center of the hole and R is the pulley radius. Measurements are repeated ten times then filtered and averaged for different hole diameters. As shown in Figure 5.8 theoretical and experimental results present some differences but globally follow the same trend. At each tested hole diameter a point is highlighted on the experimental and theoretical curves. Differences are mainly due to mechanical inaccuracies since the test bench is hand-made. In addition, friction coefficient is experimentally estimated on a smooth flat surface while unlocking is experienced on imperfect hole edges.

This friction-based locking mechanism preserves the advantages of the previous version and solves the sizing problem. Nevertheless, its mechanics remains still complex for production. In addition, a locking device does not solve the finger coupling-decoupling by itself. A re-coupling strategy or mechanism have to be integrated to finally settle the problem.

5.2.1.2 Re-coupling with locking devices

The presented locking mechanisms answer the need for constraining the relative motions between two components at one desired point. However, once one component is free to move with respect to the other, decoupling endures in absence of external forces. Integrating the locking devices in the fingers, restorative forces which lock back the mechanisms can be provided by:

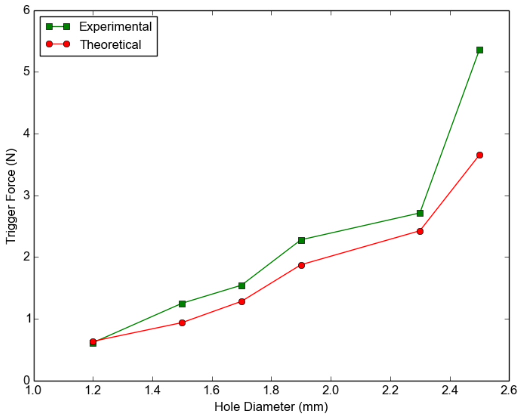

Figure 5.8 – Experimental and theoretical maximum locking forces for the second version of friction-based locking mechanism. Triggering forces are compared for different hole diameters.

1. gravity or other external forces applied on phalanges;
2. the grasp cable;
3. a cable routed in opposition to the grasp cable integrated in the fingers;
4. elastic elements integrated in the fingers.

Gravity can be used in any situation to couple back finger phalanges. If its contribution is not adequate to realign the fingers, mass inertia or the surrounding environment can be used for completing the task. Yet, this method requires the hand to follow predetermined trajectories each time an object is released. The re-coupling procedure would consist in releasing the grasp cable, move the e-motion motors back to the initial position and execute arm-wrist predefined movements. Another method consists in using the grasp cable to couple fingers back. Based on the fact that locking positions can be naturally reached at the joint limits, re-coupling is obtained by pulling the grasp cable once the object is released. In absence of obstacles all joints are driven to their mechanical stops and e-motion motors can re-establish the coupling by moving to 90°. A different approach solves the re-coupling problem through a position control strategy of e-motion motors. Once the object is released, e-motion actuators are driven from 0° to 90° as many times as the number of locking devices in series (two for the fingers and one for the thumb). Like in the previous methods, this approach assumes that the object is easily released simply relaxing the grasping cable and it needs additional finger movements to close back the four-bar linkages. A cable attached at the fingertip and straightly passed on the dorsal part of the finger is used in different robotic hand designs. It does not demand any additional finger motions but it requires a supplementary motor or a more complex reeling mechanism and more space in the fingers. Alternatively, elastic elements can be integrated to the locking devices to easily locate the coupling point. This solution opposes to the grasp actuator a restoring force proportional to the joint deflection (difference between the coupled angle and the current decoupled configuration) but provides a natural and effective re-coupling.

5.2.1.3 Conclusions

In this section locking devices have been presented as a solution to the decoupling problem. Two friction-based mechanism have been conceived, adapted to the context and tested. As it has been shown they over satisfy the design requirements providing no opposition to the grasp actuation and no joint angle errors once the mechanism is locked. However, they lack in attractive solutions for re-coupling. In addition, they present mechanisms that are too complex to be embodied on robot which aims to be produced in series. Since decoupling specifications are more relaxed than the results obtained with the locking devices, the decoupling mechanics can be simplified to single elastic component. Properly sizing their elastic behavior they can solve decoupling and re-coupling problems respecting the design specifications at the same time.

5.2.2 Decoupling mechanism

Transmission decoupling and re-coupling can be obtained by replacing the rigid aluminum bar connecting two adjacent links with an elastic element. Elasticity allows a natural variation in the transmission ratio as the bar length changes and it preserves coupling under certain stress. To respect the e-motion coupling the resting position of elastic bar coincides with the length of the replaced rigid bar. Elastic properties are designed studying the efforts exerted on the bars in different scenarios. A qualitatively analysis is performed by considering two adjacent coupled links and opposing decoupling forces (Figure 5.9). Decoupling forces are external forces which aims to open or close the finger with respect to its coupled (or equilibrium) configuration. Due to the geometry of the transmission mechanism (Chapter 3.1) closing forces squeeze the bar while opening forces stretch it.

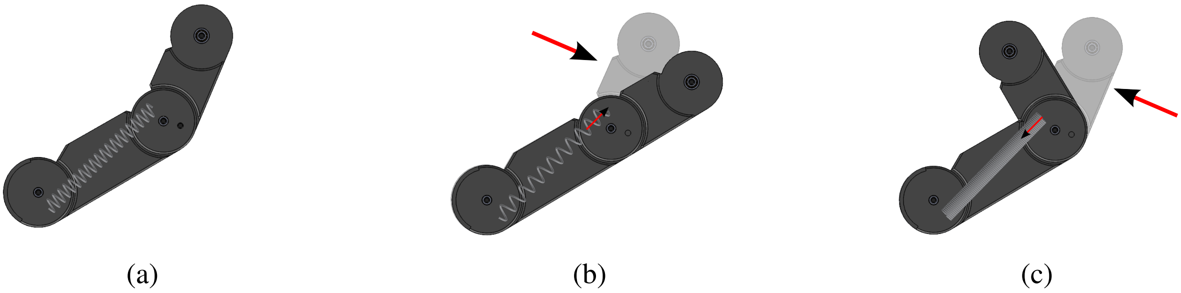
(a) (b) (c)

Figure 5.9 – (a) Adjacent coupled links (b) opened and (c) closed by external opposing forces. According to the transmission geometry closing forces squeeze the bar while opening forces stretch it.

Decoupling forces derive from the opposition between actuation efforts and the following elements: gravity, mass inertia and external forces. Gravity and mass inertia are both present during e-motion tasks and are taken into account in the dynamic model. Compression and tension forces on the bar, estimated as presented in Chapter 5.1, have to be supported by the elastic bar rigidity to ensure finger coupling during motion. External forces are usually generated by contacts with objects or, more generally, with people and the environment. Contact with objects are necessary for finger self-adaption: when a link enters in contact with the environment the successive one keeps moving as the grasping actuation exceeds the opposing elastic force. To support self-adaptation and, in particular, object wrapping, grasping forces have to be opposed the least possible by the elastic bar. Hereafter, elastic property of materials are analyzed and a solution to this problem is presented.

Elastic properties. The Young's Modulus (E) expresses the resistance to elastic deformation that an object has once subjected to an external force:

$$E = \frac{\sigma}{\epsilon} \tag{5.16}$$

where σ is the tensile stress and ϵ is the strain. The tensile stress is the internal restorative force that the material has over a unit area while the strain is the relative deformation:

$$\begin{aligned} \sigma &= \frac{F}{A_0} \\ \epsilon &= \frac{\Delta L}{L_0} \end{aligned} \tag{5.17}$$

where ΔL is the distance from the equilibrium (resting) position, L_0 is the original length of the material and A_0 is the cross sectional area through which F is applied. Young's Modulus denotes the resistance to deformation which means that a stiff (or rigid) material has a high (or infinite) coefficient. For linear-elastic materials the Young's Modulus is the constant slope of the stress-strain curve and it can be used as proportionality factor in the Hook's Law:

$$\begin{aligned} E &= \frac{FL_0}{A_0 \Delta L} \\ F &= -k\Delta L = -\frac{EA_0}{L_0}\Delta L \end{aligned} \tag{5.18}$$

The range of linear-elasticity is limited for any kind of material. Out of the linear region, at large stresses or strains, some failure modes can be experienced: buckling, non-reversible changes (plastic deformations) or even rupture. Buckling is characterized by a lateral collapse of the sample caused by a high compression stress. The force which triggers the buckling, called critical force, is known from classical theory:

$$F = \frac{\pi^2 EI}{(K_b L)^2} \tag{5.19}$$

where E is the Young's Modulus, I is the area momentum of inertia of the cross section of the material, L is the length of the component supporting the compressing force F and K_b is the column effective length factor, which depends on the ends mobility:

$$K_b = \begin{cases} 1 & \text{if ends are free to rotate} \\ 0.5 & \text{if ends are fixed} \end{cases} \tag{5.20}$$

Once a material buckles the restorative stress no more depends on the strain remaining fixed to the critical force (see Section 5.2.2.2). Even though buckling is normally undesired, the effect to have a known bounded force perfectly suits the need to limit the grasping force opposition while grasping. Note that since buckling occurs in compression only closing adaptability is encouraged. Fingers can adapt to different shapes but opening efforts, which stretch the bars, are opposed by restoring forces proportional to the distance from the coupled configuration.

Design constraints. To avoid mechanical changes in the finger design bar geometries has to respect the following constraints:

- length (L_0) must coincide with the aluminum bar length to preserve coupling;
- height (h) and width (b) have to fit in the fingers.

Elastic bars have to allow both compression and extension. Extension has no design constraints while compression has to withstand dynamic motions, where the maximum coupling error (ΔL_{err}), chosen in Section 5.3.1, establishes the lower boundary for the elastic constant:

$$k \geq \frac{\max(F_{dyn})}{\Delta L_{err}} \tag{5.21}$$

where $\max(F_{dyn})$ is the maximum force experienced during dynamic motions.

In the next sections two elastic materials are proposed: classical springs and elastomers. According to the desired critical force (F_c) the following parameters are determined:

- geometric parameters (coil diameter, number of turns, etc.) for springs;
- Young's modulus (E) for elastomers.

5.2.2.1 Spring bars

Linear coil springs are mainly divided in compression springs and tension springs. The former resist compressing forces and are used to keep components far from meeting. They normally have flat ends and they need to be guided by shafts or contained in a hole to be properly integrated in a mechanism. The latter resist extension forces and are normally used to hold two elements together. They present various end types designed to ease the link between the spring and the mechanism, and tightly wounded coils to ensure the connection with a certain preload. In this context, compression and extension are both necessary to couple two adjacent phalanges. Hence, tension springs with zero initial load (non-zero pitch) are used.

Spring design. To design a spring, different parameters have to be taken into account:

— L_a: spring length at equilibrium (ends included);
— L_0: spring active length at equilibrium (ends excluded);
— D_e: external diameter of the spring;
— d: coil diameter;
— D: average diameter ($= D_e - d$);
— w: winding ratio ($= D_e/d$);
— G: shear module (transverse elastic module) - which depends on the material and the spring shape;
— n: number of coils;
— p: spring pitch - distance between two successive coils.

European standards constrain w between [4, 20], while the available space in the fingers limits the spring length and diameter. The elastic parameter (k) is constant both in compression and in extension and it is computed as follows:

$$k = \frac{Gd^4}{8nD^3} \tag{5.22}$$

As it can be seen from the equation, coil and spring diameters play a fundamental role in the spring rigidity. Since D_e is fixed by design, d remains the dominant parameter:

$$d = \frac{D}{w} \tag{5.23}$$

where w is arbitrarily chosen within the interval provided by the constructor (normally contained in the European standards). Further variations in the elastic constant can be obtained by changing the spring material (which determines the shear modulus G), and the number of coils:

$$n = \frac{L_0}{p} \tag{5.24}$$

where the pitch (p) is generally limited within (0.2 D, 0.4 D). Considering that efforts exerted on the full loop ends tension spring are important with respect to its size, the design is oriented to obtain a high rigidity. The minimum boundary of the elastic coefficient is defined by Equation 5.21 while its value is computed according to Equation 5.22, where D_e and L_0 are given and parameters w, p and G are tuned according to the production feasibility. In compression, the spring behaves like a column under load, failing once a certain force is attained. Since the geometry is different from a full column the equation differs from the one presented in the previous section. The critical axial force (F_c) that leads a spring to buckle can be approximately computed as follows:

$$F_c = kL_0\alpha \tag{5.25}$$

where α is a buckling factor depending on the ratio L_0/D. Note that this equation also implies that if $L_0\alpha > \Delta L_{err}$ the critical force is superior to the maximal effort experienced during motion.

5.2.2.2 Elastomer bars

Elastomers are elastic materials composed by long-chain polymers. These chains are interconnected by cross-linking chemical bonds obtained through a process called vulcanization. Cross-linkings enhance the mechanical properties of the material and contribute to determine its elasticity (memory property). Elastomers can be classified according to their resistance to permanent deformation known as indentation hardness. This is measured applying a constant compression load on the material with a sharp object. The scale commonly used is the Shore measured by a hardness tester called Durometer. The durometer measures the depth indentation induced by a force exerted with tool on the material. The depth depends on the hardness and the viscoelastic properties of the sample, the shape of the tool and the duration of the test. For this reason, the Shore is measured by standard procedures (e.g. ISO 868) which fix all these parameters together with the size and shape of the sample. The Shore scale is divided between A and D. The former comprehends soft, medium and hard (with almost no flexibility) flexible rubbers while the latter only measures hard rubbers, semi-rigid and hard plastics. Among all types of elastic polymers Polyurethanes (PUs) are the ones used in this context. PUs are the most known elastomers and they are currently used in large variety of applications, e.g. as flexible foam in many domestic and automotive appliances (carpet, sofas, car seats, etc.) and as rigid foam in thermal insulations, mechanical seals and shoes. PUs have high tensile, abrasion and tear strength. In addition, they are cheap to produce (low-pressure injection molding) and can be precisely cut by laser or high pressure water jet.

Elastomer elastic characterization. Elastomer materials present a non-linear stress/strain behavior (see Figure 5.10). This implies that Equation 5.18 is still valid if E is no more constant: $E = E(\epsilon)$. For this reason, elastomer elasticity is described by the tensile stress at given strains (e.g. at 10%, 100%, 200%) rather than being the slope of the stress/strain curve. A typical characteristic of elastomers behavior is the stress difference ($\Delta\sigma$) between loading and unloading phases. This is due to internal material frictions that occurs while elastomers are compressed or extended.

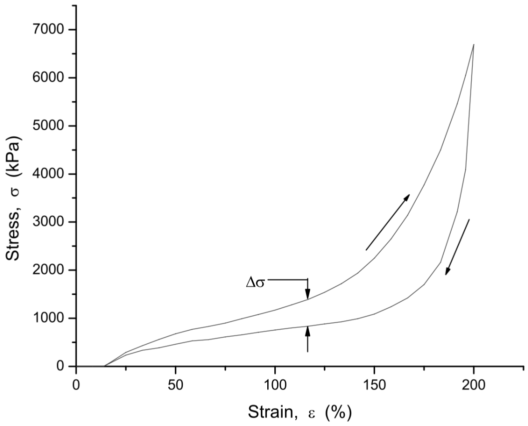

Figure 5.10 – General non-linear stress/strain curve of elastomers. The curve highlights the hysteresis induced by internal frictions during extension and compression. This picture is taken by [142].

Unfortunately, manufacturers do not always provide tensile stress (or the Young's Modulus) at different strains. Sometimes they only provide the elastomer Shore hardness or the tensile stress at strain intervals far from the one of interest. When the polymer durometry is the only data available the elastic modulus can be determined either experimentally or analytically, by converting the indentation measurement according to the geometry of the indenter [143]. Kunz and Studer [144], for example, convert Shore to Young's Modulus using Equation 5.26 when the indenter shape is a truncated cone (ISO 868):

$$E = \frac{1-\mu^2}{2RC_3}\frac{C_1 + C_2 Sh_A}{100 - Sh_A} \tag{5.26}$$

where μ is the Poisson's ratio, R is the radius of the indenter while C_1, C_2 and C_3 are parameters which describe the linear relationship between the depth of the penetration and the Shore hardness and between depth penetration and the indenting force of the durometer. This equation approximately converts Shore A between 30 and 95 to the modulus of elasticity in compression and it can be modified by a correction function to take into account neglected phenomena and different specimen thicknesses. The limit of this approach is that Young's Modulus is estimated from compressing the material rather than expanding it. In order words this method estimates the elastic modulus only for small elongations, where the stress/strain behavior remains linear in both compression and extension.

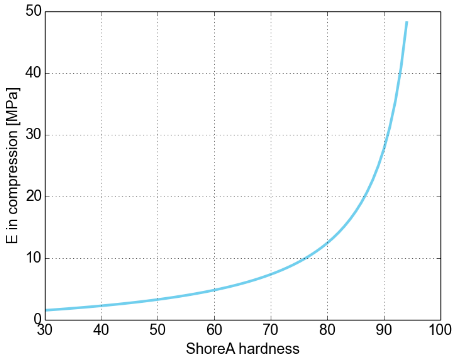

Figure 5.11 – Conversion from Shore A to Modulus of Elasticity in compression using Equation 5.26.

Whether the analytical conversion is not sufficient to characterize the material elasticity, the stress/strain curve can be experimentally identified. In this context, the test bench shown in Figure 5.12 is realized to trace the general stress/strain curve of elastomer samples and to analyze the restorative forces generated by the elastic bars in traction and compression. The test bench consists in a lead screw that pushes and pulls a linearly guided movable part to which one elastomer end is attached. Since the other end of the elastomer is fixed to ground, the specimen (or elastomer bar) is stretched or compressed according to the lead screw position. The strain is measured by a digital caliper while the stress is measured by a strain gauge (Phidgets) placed between the elastomer and the sliding part. Measurements are taken at discrete strain intervals keeping the position fixed during the force collection. Strain gauge readings are collected every 8 [ms] and averaged over 5 [s] of acquisition.

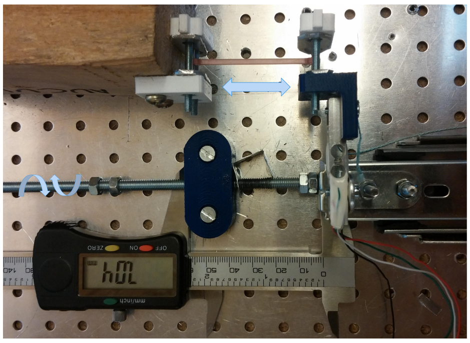

Figure 5.12 – Elastomer traction/compression test bench.

Samples used to determine the elastomer elasticity have the same shape and size of the dumb-bells defined in ISO 37:2011. Their form is chosen to concentrate the material elongation only in the thinnest part of the sample, the so called test length, so that tensile forces remain orthogonal to the cross section during the experiment. Since only small elongation/contractions are attained in our application, the tensile stress is analyzed at strains within 10%.

In this interval experimental results show that the elastomer preserve a linear behavior both in extension and in compression (Figure 5.13a). More precisely, in compression the slope remains constant if the sample is far from buckling, otherwise the slope decreases as the stress approaches the critical force - at which the curve flattens (Figure 5.13b). Another phenomena observed during the experiments is the elastomer length variation induced by constant stresses held in time. This effect, called creep, is detected

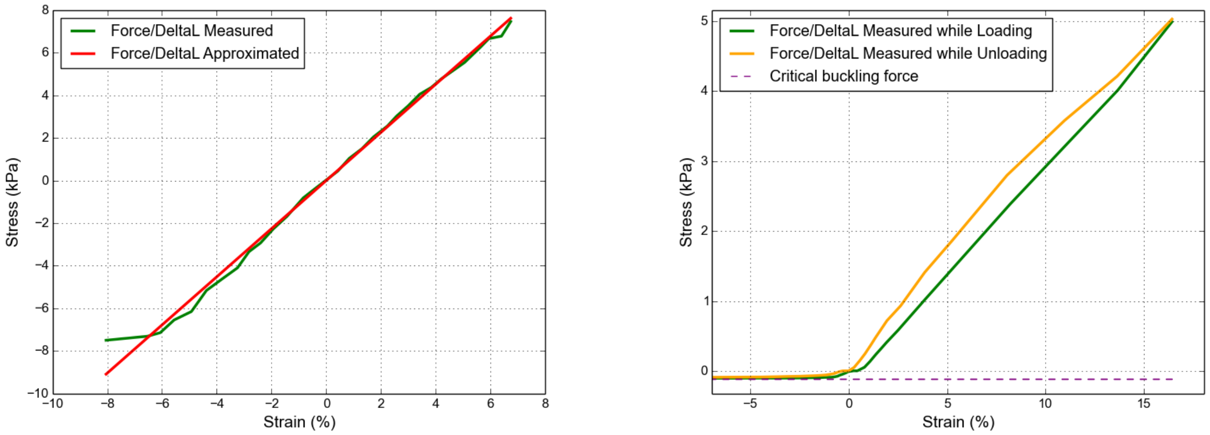

(a) Stress/strain curve of the dumb-bell during loading.

(b) Stress/strain curve of a SH80 PU elastomer sized for the middle proximal bar.

Figure 5.13 – Elastomer elastic characterization: linearity (a), hysteresis and buckling phenomena (b).

by reaching zero stress at positive strain after extension and at negative strain after compression (Figure 5.14). This is not the only time dependent behavior that elastomers have: at any time the strain is held constant the stress decreases during loading and increases during unloading. This behavior, called stress relaxation, occurs under both constant deformation and cyclic deformation. This behavior is not visible in our context since the average value of the measured forces is collected at each holding period. Despite the time dependence, experimentally acquired strain are coherent with the data provided by the supplier and are used to size the bars in the fingers (Section 5.3.2).

As mentioned before, the stress/strain curve is linear both in compression and in extension and the experimental elasticity can be used to estimate the forces exerted by the elastomer at arbitrary deformations if the elastomer is far from buckling. On the contrary, when the sample is close to buckle this is no more possible. In fact, the curve slope decreases as the bar starts to bend and the Hook's law, based on the linear E, overestimates the real pushing force. For this reason, the test bench is also used to verify the restorative internal force of the coupling bars at different small strains and to characterize the non-linear curve before buckling. Experimental results are used to confirm whether the classical Equation 5.19, used for columns, applies for elastomers (Figure 5.14) and to design the elastomer bars for each finger.

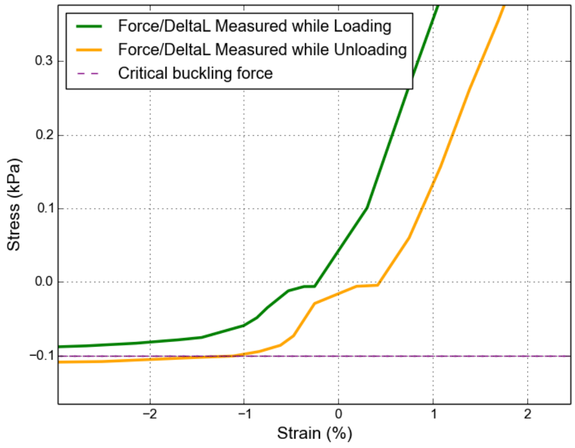

Figure 5.14 – Creep phenomenon on the elastomer bar induced by constant stresses held in time. This curve also shows the reliable critical force estimation of Equation 5.19 on elastomer bars.

Elastomer bar design. Ideally, elastomer bars should be as rigid as the aluminum ones when gestures are required and be perfectly transparent when an object has to be grasped. These two requirements are obviously in contrast. Indeed, for a given bar shape, the elastic stiffness and the buckling force are both proportional to the Young's Modulus. This means that a high E coefficient implies a more rigid bar which buckles at stronger efforts and increases the opposition to the grasping force. In order to save energy, the opposing force has to be the least possible but strong enough to handle finger dynamics. Rewriting Equation 5.19:

$$E \geq \frac{\max(F_{dyn})(K_b L_0)^2}{\pi^2 I} \tag{5.27}$$

where I is chosen to be:

$$I = \min(I_x, I_y) \tag{5.28}$$

to avoid buckling about the thinnest side. Since the cross section is rectangular I_x and I_y are simply defined as:

$$\begin{aligned} I_x &= \frac{bh^3}{12} \\ I_y &= \frac{b^3h}{12} \end{aligned} \tag{5.29}$$

where b and h are the height and the width of the bar cross section, K_b (= 1) is the column effective length factor, L_0 is the bar length at rest, I is the weakest area moment of inertia of the bar cross section and F_{dyn} is the compression force that the elastomer experiences during motion. The compression force exerted on each bar is computed according to the finger dynamics as described in Chapter 5.1. Equation 5.27 represents the minimum value to avoid buckling and defines the lower bound to design the bar elasticity. To respect the maximum angle error E is sized for an arbitrary critical force (F_c^*) higher than $\max(F_{dyn})$:

$$E^* = \frac{F_c^*(K_b L_0)^2}{\pi^2 I} \tag{5.30}$$

A safety margin of about two times the maximum compression force experienced during motion is experimentally proven to largely satisfy the joint angle error constraint. Consequently, elastomer shores are chosen according to the E^* of each finger bar.

5.2.2.3 Comparison

Thanks to their linear elastic behavior with no hysteresis and creep phenomena coil springs are the common choice when an elastic elements are required. In this context, however, strong mechanical constraints hinder their practical use. The limited space in the finger imposes small external diameters which, in turn, bound coil diameters, drastically limiting the elastic constant (Equation 5.22). Even varying the design parameters (G, w, p) transmission bars are not sufficiently stiff to bear finger weights. In addition, all consulted manufacturers provide a length accuracy between (0.1, 0.5] [mm] which is inadequate considering that a length variation of 0.2 [mm] already outweighs the required angle error.

Elastomers have undesired time dependent behaviors, hysteresis and a non-linear elastic constant. The last has to be characterized if the manufacturer does not provide stresses at different strains. Nevertheless, experiments show that undesired phenomena are negligible in our working domain and stress at 10% is the only data necessary for designing the coupling bars. Elastomers present a large variety of elastic constants (or Shore) and are less affected by the mechanical constraints thanks to their structure. All finger bars can be designed using PU with Shore A within SH60-SH97. In addition, their shapes can be precisely obtained by laser or water cutting using the same aluminum bar drawings. Last but not the least, a single elastomer plate from which several dozens of bars can be made costs far less than a single customized spring.

Table 5.1 resumes pros and cons about springs and elastomers. Even though weight is an important factor in the hand design its contribution is not added in the comparison since both solutions lighten the finger structure (steel spring of 63% and SH80 PU elastomer of 53%). In order to meet force requirements with coil springs, bar geometries should be changed together with finger drawings.

	length accuracy	elastic module (G or E)	elastic behavior	cost
Springs	low	soft and limited	linear and constant	expensive (design on demand)
Elastomers	high	adequate and varied	linear with hysteresis and time dependent	cheap (a single elastomer sheet + laser cutting)

Table 5.1 – Springs and elastomers pros and cons.

5.3 Prototype

Previous sections introduced the main merging issues and selected, among different mechanical devices analyzed and tested, the mechanism that ensures the best trade-off between e-motion and grasping performances. Hereafter, the experimental realization of this solution is described. Firstly, the acceptable coupling error and the method adopted to size the decoupling components are presented. Afterwards, the finger and thumb prototypes and the complete ALPHA design are shown.

5.3.1 Acceptable coupling error

The output angle in the four-bar transmission mechanism is highly sensitive to slight geometrical inaccuracies. Even when the whole structure is rigid, small angle errors can be induced by imperfections in the bar length or important mechanical plays. In presence of elastic bars its is necessary to define the maximum output angle error in order to size the elastic constant of the flexible elements. Acceptable angle errors are determined by studying the strongest finger deflection and its impact on the human perception. Slightly flexed fingers resemble naturally relaxed human fingers causing no perturbation to the human senses. Experimentally varying the bar lengths it is proven that a ΔL of 1% on both proximal and distal bars deflects the distal phalanx of about 20° with respect to the palm (the proximal bar is the bar coupling proximal and middle phalanges, and the distal bar is the bar coupling middle and distal phalanges). This angle is too large to be accepted. After some tests, an angle of about 10° has been accepted imposing a ΔL of 0.5% on both bars.

5.3.2 Elastomer bar sizing

Forces exerted on the rigid bars are computed for a closing finger motion, from a fully stretched to a completely flexed configuration, lasting 1 [s]. Calculations are performed according to Chapter 5.1. Efforts are analyzed at the point of connection between the bar and the successive phalanx (see Figure 5.15). In particular, they are inspected at joint 5 and projected on R_4 for the thumb model (see Figure 3.5) while, for the fingers, they are inspected at joint 3 and 5 and projected on R_2 and R_4 respectively (see Figure 3.7). These frames are practical to analyze compression and extension stresses exerted on the bar since their x axes are always aligned with the bars. In addition, on their y axis the forces which generate the motion can be observed. Figure 5.16 shows the mechanical stress computed at the coupling bar in the thumb, when the last is stretched against gravity (worst case scenario). In the figure, a positive sign refers to a stretching force while a negative sign refers to a compressing one.

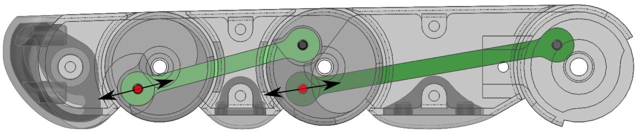

Figure 5.15 – Points of connection at which the force analysis is performed.

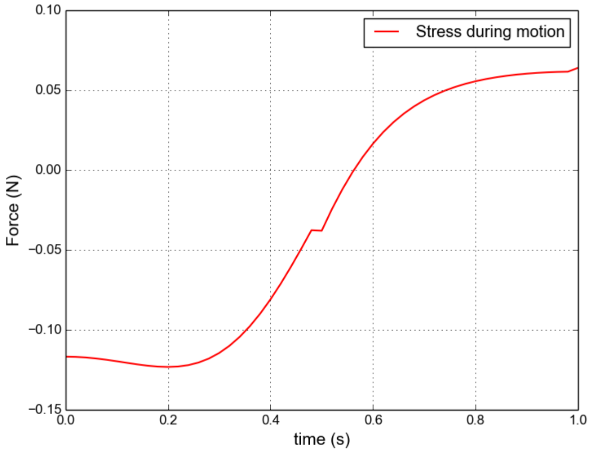

Figure 5.16 – Compression-extension force exerted at the coupling bar of the thumb.

The axial force varies from compression to extension according to the finger configuration. As discussed in Section 5.2.2, the bar is squeezed any time an external force tries to close the finger with respect to its coupled configuration. On the contrary, it is stretched when an external force pushes the finger to open. In this case, for example, the gravity forces the finger to close when its phalanges are aligned, and to open when all phalanges are completely flexed. Obviously, the same applies when two closed loops are applied in series. Figure 5.17 shows the compression and extension forces at the proximal and distal bars of the middle finger. The experience conducted is exactly the same adopted for the thumb: the finger starts from a fully stretched configuration and flexes till 90° in 1 [s]. As it can be observed, the trend does not change from one loop to the other, while the force strongly increases as the bar gets closer to the base of the chain. Finger coupled motions are driven by second order trajectories based on the trapezoidal velocity model presented in Section 3.3.3. These motions require accelerations which slightly impact internal efforts at the bars (about 10%). Their effect are barely visible in the graphs, except for the small variation between the interval [0.48-0.52] [s] induced by the transition from positive to negative accelerations. Basically, it is the gravity force the main component which affects compression and extension forces at the bars.

The maximum compression force experienced during motion drives the elastomer sizing. In Table 5.2 the maximum compression force estimated at each bar are reported. Elastomer bars preserve the same

Bar / Finger	Thumb	Index / Ring	Middle	Little
Proximal	x	0.83 [N]	0.89 [N]	0.76 [N]
Middle	0.17 [N]	0.15 [N]	0.16 [N]	0.14 [N]

Table 5.2 – Maximum compression forces experienced during motion at each finger bar.

length (L_0) and height (h) of the aluminum ones. Their width (b), instead, are imposed by the elastomer plate thicknesses and they are limited by the available space in the finger (less than 3.5 [mm]). Due to the injection molding tolerance elastomer plates range between [1.9, 2.3] [mm] and [3.1, 3.4] [mm] rather

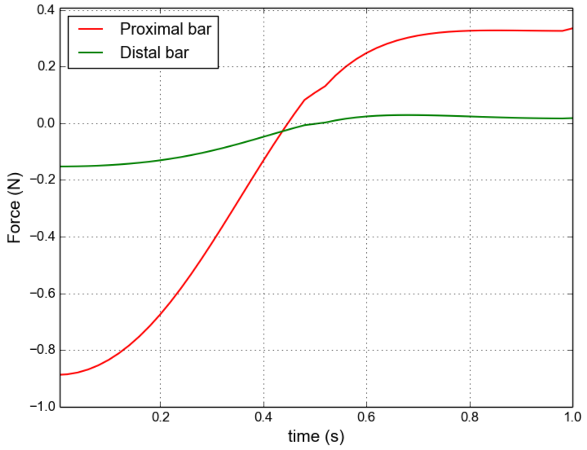

Figure 5.17 – Forces exerted at the proximal and distal coupling bars of the middle finger during motion.

than being precisely 2 [mm] and 3 [mm] thick. Since the critical buckling force is sensitive to height and width variations (see Equation 5.19) the minimum stress at 10% strain is computed for each plate thickness (see Equation 5.27). Table 5.3 lists the candidate elastomers showing their thicknesses, Shores and stresses at 10% strain.

Shore	SH70	SH80	SH90	SH95	SH97
Stress at 10% strain [MPa]	1.0	1.6-1.8	3.4-3.7	6.1	10.5
Thickness [mm]	1.9	2.3	2.0, 3.4	2.1, 3.1	1.9, 3.2

Table 5.3 – Candidate PU elastomers to replace aluminum coupling bars.

Materials are selected by choosing the elastomer width and Shore which generate the desired critical force (F_c^*) arbitrarily chosen between (β, 2β] - where $\beta = \max(F_{dyn})$. Table 5.4 shows the elastomer materials which theoretically solve the coupling-decoupling problem. However, SH97 elastomers present a high viscosity with respect to the others. The material slowly reacts to the external forces, remaining contracted after compression and stretched after elongation for a relatively long time. Hence, SH97 bars are all replaced by softer SH95 3.1 [mm] elastomers which still withstand the maximum compression forces but with a reduced safety margin.

Bar / Finger	Thumb	Index / Ring	Middle	Little
Proximal	x	SH97 (1.9[mm])	SH97 (1.9[mm])	SH90 (2[mm])
Middle	SH70	SH70	SH70	SH70

Table 5.4 – Selected elastomer materials for the elastic coupling bars.

5.3.3 ALPHA finger concepts

The final finger and thumb designs are shown in Figure 5.18 and Figure 5.19. They preserve gesture and grasping functionalities by integrating the two independent actuation systems in parallel. The e-motion brushless DC motor and transmission system composed by gears and elastic bars are highlighted in red while the grasp cable and pulleys are presented in blue. Screws, stereolithographic parts (phalanx covers) and soft parts (rubber) are put in transparency to ease the representation. The two transmission mechanisms are embedded one beside the other all along finger structures. This solution imposes a minimum width which slightly exceeds anthropometric finger widths (see Section 2.2), particularly for the little finger.

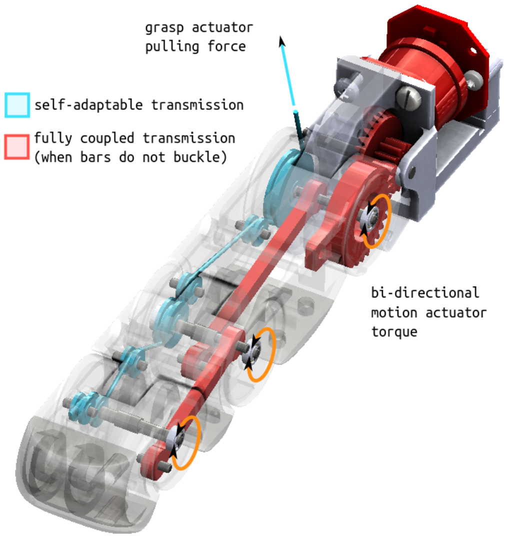

Figure 5.18 – ALPHA finger design: parallel e-motion and grasp transmission mechanisms. The e-motion brushless DC motor, gears and elastic coupling bars are highlighted in red while the grasp cable and pulleys are presented in blue.

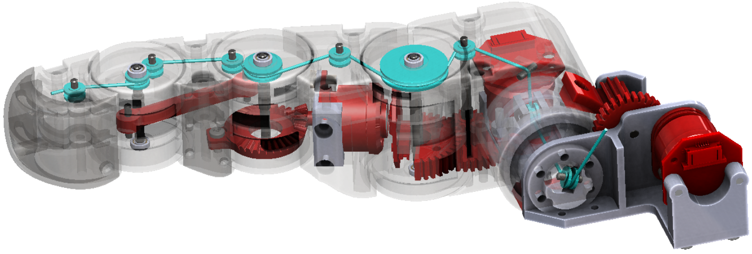

Figure 5.19 – ALPHA thumb design: parallel e-motion and grasp transmission mechanisms. The e-motion brushless DC motors, gears and elastic coupling bar are highlighted in red while the grasp cable and pulleys are presented in blue.

Differently from aluminum bars, elastomer bars have holes with diameters of 1.6 [mm] rather than 1.5 [mm]. This is done to avoid high friction contacts between the elastomer and the axes of steel. Small aluminum rings with 1.5 [mm] of internal diameters are placed in the bar holes so that the static friction coefficient (μ) is reduced from 0.7 (PU on steel) to 0.4 (aluminum on steel). Note that the internal diameter of aluminum rings has to be accurate to avoid mechanical play which would increase the joint angle error. No further changes are applied to the e-motion and grasp mechanisms.

5.3.4 ALPHA prototype

Figure 5.20 shows the ALPHA prototype during its mounting process. As it can be seen, the e-motion actuation system is completely hosted in the palmar side of the hand (Figure 5.20a) while the differential mechanism is located in the dorsal one (Figure 5.20b). The grasp motor is placed outside the palm together with motor boards (one per motor) and the central unit hosted in the Pepper's head shown in Figure 5.21. The prototype weighs 540 [g], considering the whole hand plus the motor in the forearm and excluding the non-optimized electronics outside of the palm. The overall system is arranged to test and validate ALPHA.

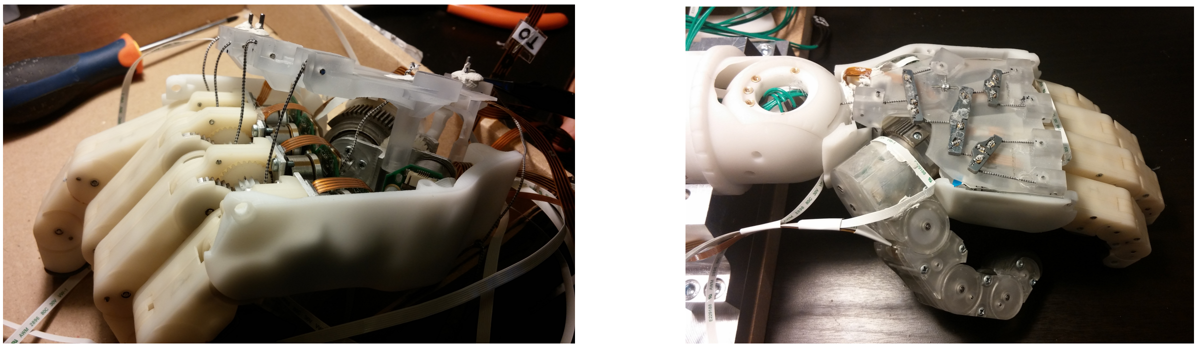

(a) E-motion actuation system embedded within the palm.

(b) Differential mechanism mounted at the dorsal side of the palm.

Figure 5.20 – Prototype palm assembly.

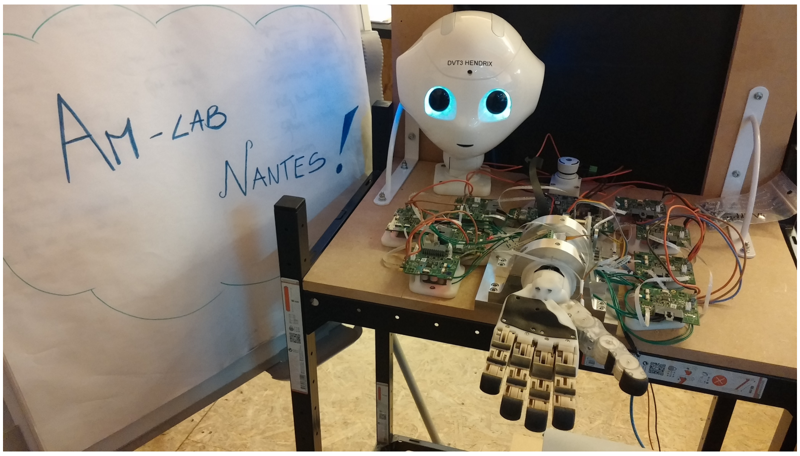

Figure 5.21 – Overall ALPHA prototype.

5.4 Validation

During normal motion the system behaves as the e-motion hand described in Chapter 3. This is useful to perform gestures and to pre-shape the hand before grasping. Limited errors at joint angles do not impact human perception and affect grasping performance. At contact, fingers autonomously self-adapts when the grasp motor is activated. In this case, the system behaves as the grasp hand described in Chapter 4. Differently from classic self-adaptable fingers (presented in Chapter 1.2) return torques exist when phalanges are deviated from their coupled configurations - rather than the straight configurations at their mechanical stops. They oppose the grasp force with approximately constant torques for angles bigger than the equilibrium angle. While, they help the grasp force with spring-like torques for angles smaller than the equilibrium angle. This particular design hinders caging strategies by sweeping [145] but it allows to reduce energy consumption while grasping.

5.5 Conclusion

The final structure of the ALPHA finger is similar to the e-motion transmission mechanism based on fixed coupling. The fundamental difference between them is that an elastic element is added in the transmission chain to vary the bar length and, consequently, the coupling ratio. The elastomer allows the relative motion between phalanges when external forces are applied on the links. They stretch when opening forces oppose the joint torques, e.g. while adapting to the object shape, and they shorten till buckling when closing forces are applied, e.g. when using the grasp actuator after contact on the first or second phalanx. This solution enhances grasping capabilities thanks to the possibility to adapt to the object shapes. On the other hand it requires more efforts at the design stage to size the stiffnesses of elastic elements. In conclusion, this approach ensures a good compromise between gesture and grasping capabilities while respecting mechanical design constraints.

6

Experiments and Validation

This chapter is devoted to the analysis and evaluation of the ALPHA prototype. Firstly, the control strategies adopted to test the hand are briefly introduced. Then, the tests performed to analyze its anthropomorphism, gesture and grasping capabilities are presented. These are intended to both check mechanical and functional requirements and to characterize its general performance. Finally, some conclusions are drawn about experimental results. The hand design is validated in terms of the thesis objectives and the limits of its implementation are highlighted.

6.1 Experiments

Hand performances are experimentally validated on the base of:
— hand anthropomorphism;
— e-motion capabilities;
— grasping capabilities.
These are conducted by developing the remote control methods described hereafter.

6.1.1 High level control

Desired hand configurations and grasp forces are achieved by remotely controlling e-motion and grasp actuators through a GUI and a dataglove.

6.1.1.1 The Graphical User Interface

The Graphical User Interface (GUI - shown in Figure 6.1) allows the turning on and off of the motors, defines target positions for each active joint and establishes the desired force at the grasp motor. It also allows the recording of joint postures and play gestures as a sequence of selected configurations.

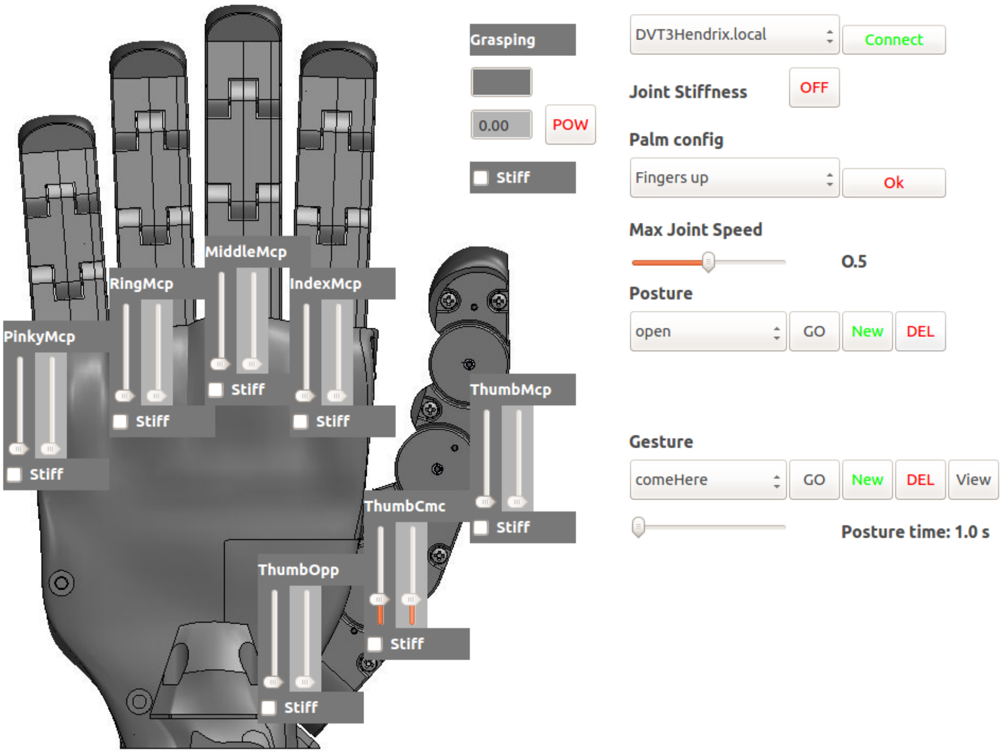

DVT3Hendrix.local

Joint Stiffness: OFF

Palm config: Fingers up

Max Joint Speed: 0.5

Posture: open

Gesture: comeHere

Posture time: 1.0 s

Figure 6.1 – Developed GUI to control ALPHA from remote.

6.1.1.2 Dataglove

The developed GUI is useful to record and play specific finger configurations. However, it is ineffective and time-consuming to reproduce natural motions, or pre-shape the hand according to different configurations and objects. In this sense, better performance is obtained by controlling the hand through motion capture devices. At first, a recently developed hand tracker device is adopted: the Leap Motion Controller [146]. This tracks human hands through infrared cameras at up to 200 [fps]. It is easy to install and interact with. By simply placing the hand over it, the software quickly recognizes the human hand structure and tracks the joint configurations. The camera properly tracks hand motions when the last is placed with the palm facing the device. This means that limited wrist rotations are allowed (not relevant in this context since no wrist is implemented) and, more importantly, thumb motions in opposition are poorly estimated. This is shown in Figure 6.2 where it is highlighted the inability to detect proper thumb configurations when in opposition to the palm. In addition, it sometimes returns badly estimated angles leading to undesired postures or unrecognizable gestures. This would need a fault detection algorithm to protect the mechanics of the robotic hand.

A more robust approach to track joint motions consists in using datagloves (or cybergloves). Datagloves are wearable devices often used in virtual reality environments. With respect to the Leap Motion Controller, they slightly constrain hand natural motions and require calibration to adapt to different users. In contrast, they precisely estimate joint angles and are not affected by occlusion. The dataglove adopted

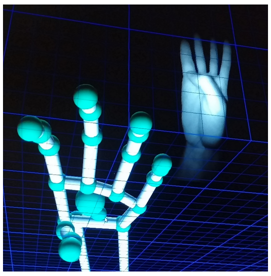

Figure 6.2 – Thumb posture false detection with Leap Motion Controller.

in this context is the 5DT dataglove 14 ultra [147]. The data is filtered by a low-pass filter.

Calibration. The calibration process identifies sensor values corresponding to minimum and maximum human joint angles. Every time a new user wears the dataglove, calibration is required to adapt data acquisition according to their hand size and proportions. Since datagloves undergo small motions over the skin during operation, human calibration postures are chosen close, but not coinciding, to real human joint limits. For example fingers are not perfectly stretched to identify their minimum angle but are kept slightly bent in a more natural and relaxed posture (Figure 6.3). This avoids the operators stressing their tendon and ligaments. In correspondence of minimum and maximum calibrated positions, sensor values are set to 0 and 1 respectively.

Figure 6.3 – Dataglove calibration postures. From left to right: thumb and finger minimum joint angles, thumb maximum joint angle and finger maximum joint angles.

Kinematic mapping. The 5DT dataglove 14 ultra has 14 optical sensors, two per finger plus one placed between two adjacent fingers. The former detects MCP and PIP/DIP flexing motions, while the latter detects abduction/adduction motions (see Figure 6.4 and Table 6.1). However, no neat separation exists between the acquired data and finger motions. Indeed, sensors are placed so that there exists mutual influence between distinct movements. In particular, the ones detecting MCP flexions are affected by skin artifacts induced by relative flexion of adjacent fingers, while the ones detecting MCP abductions are placed so that any relative flexion is perceivable. Since the robotic hand has only 1 DoF per finger (thumb excluded), direct mapping is performed between sensors at the DIP/PIP human joints (IF, MF, RF, LF - not affected by relative motions of their neighborhood) and the MCP joint of the robotic hand. The mapping of the three independent DoFs of the robotic thumb to the sensors detecting the posture of its human counterpart are experimentally determined. The robotic MCP joint is directly associated to the distal sensors placed on the thumb (TF), while the first joint of the robotic thumb chain is directly related to the sensor between the thumb and the index (TI). A less intuitive solution is adopted to control the flexing motion of the second joint of the robotic thumb. Rather than directly mapping the sensor at the base of the human thumb (TN) to the robotic RC flexing joint, TF is adopted as a weighing factor. This is because the TN is highly affected by abduction/adduction thumb movements and a damping factor is necessary to avoid undesired robotic thumb base flexions during pure human thumb abductions (palm opposition). This imposes the operators to keep their distal phalanx of the thumb straight to avoid undesired flexion movements of the robotic thumb during abduction/adduction motions and to flex their MCP and DIP joints together when flexion of robotic thumb is desired.

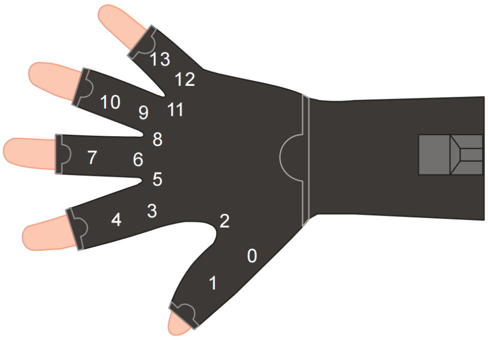

Figure 6.4 – Location of dataglove optic sensors. Picture taken from [147].

Sensor	Description	Name	Used
0	Thumb flexure at MCP	TN (Thumb Near)	✓
1	Thumb flexure at DIP	TF (Thumb Far)	✓
2	Thumb-Index abduction	TI (Thumb-Index)	✓
3	Index flexure at MCP	IN (Index Near)	✗
4	Index flexure at PIP	IF (Index Far)	✓
5	Index-Middle abduction	IM (Index-Middle)	✗
6	Middle flexure at MCP	MN (Middle Near)	✗
7	Middle flexure at PIP	MF (Middle Far)	✓
8	Middle-Ring abduction	MR (Middle-Ring)	✗
9	Ring flexure at MCP	RN (Ring Near)	✗
10	Ring flexure at PIP	RF (Ring Far)	✓
11	Ring-Little abduction	RL (Ring-Little)	✗
12	Little flexure at MCP	LN (Little Near)	✗
13	Little flexure at PIP	LF (Little Far)	✓

Table 6.1 – Dataglove sensor nomenclature.

To resume:

- Thumb RC abduction/adduction = (1 - TI) $\pi/2$;
- Thumb RC flexion/extension = α TN TF $\pi/2$ - 20/180 π;
- Thumb MCP = TF $\pi/2$;
- Index MCP = IF $\pi/2$;
- Middle MCP = MF $\pi/2$;
- Ring MCP = RF $\pi/2$;
- Little MCP = LF $\pi/2$.

where α is an experimentally determined scaling coefficient. Before passing these values to motion interpolators, the obtained joint angles are clipped to correspondent mechanical limits. This mapping does not obviously ensure a proper correspondence between human and artificial hands but it does provide an effective control for testing purposes.

Persistent task for motion. To reproduce human motions recorded by the dataglove, dedicated interpolators are activated and reinitialized any time new data are provided to the trajectory generator (every 20 [ms]). These interpolators are persistent tasks defined to reach the desired position with the maximum velocity - from current position and velocity to ensure continuity. Figure 6.5 shows a motion example of the index robotic finger controlled through the dataglove.

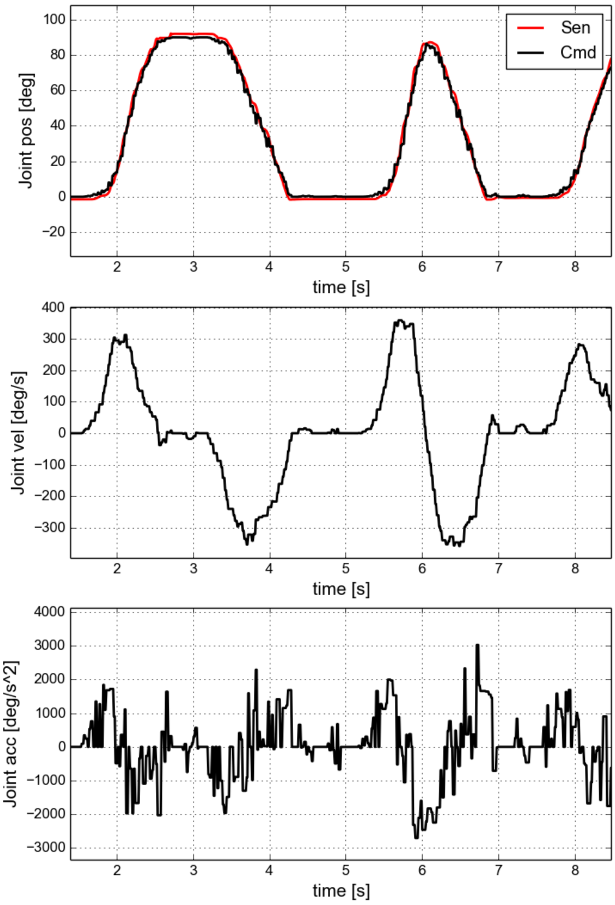

Figure 6.5 – Example of finger motion remotely controlled through the dataglove.

6.1.2 Hand anthropomorphism

Hand anthropomorphism is evaluated according to a surgical test reformulated in Section 2.2.3.6 which analyses the thumb dexterity and opposability by reaching a set of predefined locations on the reminder fingers. The thumb is required to reach 8 positions to be considered fully functional: all bases and fingertips of the opposing digits. Required configurations are reached by remotely controlling the hand through the GUI previously presented, and they are accepted by direct visual feedback. Figure 6.6 shows the distinct hand configurations achieved. This test confirms a human-like thumb opposability and dexterity which enhances hand anthropomorphism.

Figure 6.6 – Thumb opposition validation through the reformulated Kapandji test.

6.1.3 E-motion tests

Gesture capabilities are tested by controlling the prototype through the GUI. At first, it is checked if the hand is capable of opening and closing in 1 [s]. This is done by analyzing the behavior of each finger. Figure 6.7 shows the position, velocity and acceleration trajectories at the MCP joint of the second digit. Green curves represent the desired trajectories while the red one is the measured joint position estimated from the rotor position. Note that no sensor velocity is reported since it is too noisy. As it can be seen, the finger performs a closing and opening motion in less than 1 [s]. However, small tracking errors exist along the desired trajectory due to low PD gains, gear train imprecisions and the motor cogging torque. Gear trains present misaligned meshes due to both manufacturing and deflection errors. These alter the location of contact on the tooth flank and lead to large stresses and an increased transmission noise. The last does not affect the overall robot gesture capabilities, nevertheless, it induces some important side effects. At low dynamics fingers experience small oscillations which strongly affect motion smoothness (see Figure 6.7b), while at high dynamics joint position inaccuracies lead fingers to bounce at their mechanical stops when stretched back. This phenomena is visible in Figure 6.7a at the end of motion. More importantly, transmission noise hinders an effective external force estimation from current readings. Indeed, motor currents no more resemble the ones estimated from finger dynamics and high thresholds have to be adopted to detect contact forces at fingers.
Afterwards, it is verified whether the hand is capable of performing the hand gestures for which it has been explicitly designed for (see Section 2.1). These gestures consist of common signs that are normally used to provide a service (cupped hand and pointing), convey information (counting up to five and "telephone"), spring emotions ("ok" and "thumbs-up") and express personal feelings ("twiddling thumbs" and a closed fist). The ones that can be achieved by one limb are successfully performed by the hand (a collection of these is shown in Fig. 6.8) while the ones which require two hands, such as twiddling the thumbs or mimicking the shape of a heart, cannot be effectively tested.

6.1.4 Grasping tests

Grasp capabilities are explored on the base of the comprehensive grasp taxonomy of the human hand presented by [38]. The identified 33 grasp types are tested with both actuation mechanisms to analyze their performance and limits. Tests are conducted by two subjects, the first remotely controls the hand while the second provides and fetches the objects to the prototype. The objects are light 3D printed ABS objects filled at 15% of their volume. They respect the proportions of the item proposed in the taxonomy, and the heaviest object weighs 91 [g]. For power and intermediate grasps remote control is performed via the dataglove to accelerate grasp phases. On the contrary, precision grasps are executed on the base of stored force closure configurations due to the kinematic differences between the human hand

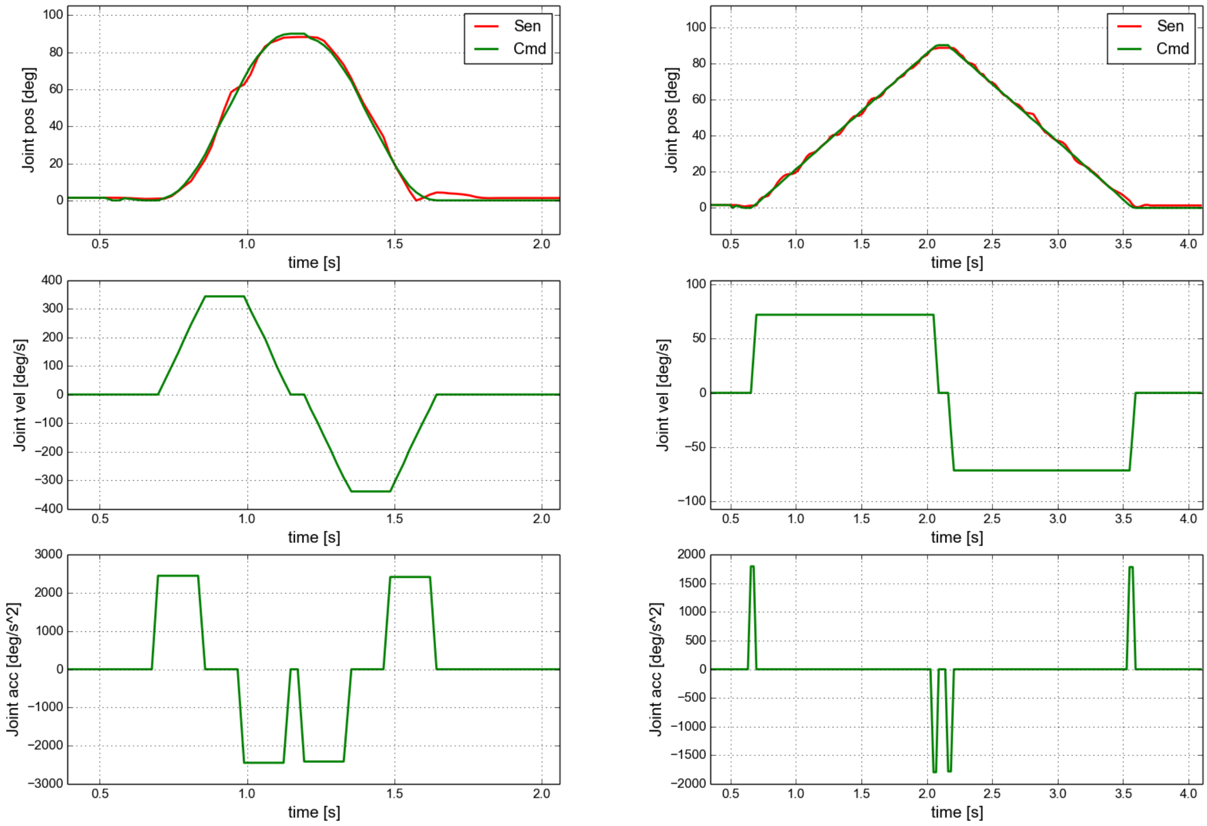

(a) Open/close finger motion under 1 [s].

(b) Slow finger motion.

Figure 6.7 – Index finger motion under e-motion control. Red curves represent sensor (Sen) data and the green ones the desired command (Cmd) trajectories.

and the robotic one. Experimental tests show that the e-motion actuation system can perform 90% of grasp types (3% failed due to unreachable force closure and 6% failed because of the amount of weight and its distribution) while the self-adaptable transmission mechanism achieves 39% of them. This is because the latter is designed to bring the object toward the palm and to involve all fingers left open while approaching the grasp. This is clearly shown in Fig. 6.9 where objects are initially grasped with the e-motion actuation mechanism and then seized by the grasp actuation mechanism, by turning off the first and activating the second system. Indeed, 94% of the failed gesture types involve pads and 57% involve the hand side in opposition. All grasp types which use palm in opposition are achieved (some examples shown in Fig. 6.10) except one (Index Finger Extension [38]), during which the index finger acts as a second virtual finger, rather then a third, due to the differential mechanism which autonomously balances forces among fingers. Even though at a first glance the e-motion mechanism seems to have better grasp performance, it is important to recall that grasp tests have been performed on very light objects and force closures have been achieved by visual feedbacks (some examples shown in Fig. 6.11). Even implementing force closure by adding appropriate perception capabilities (e.g. tactile sensing) and complex grasp planning strategies, grasp performance remains limited by design. In fact, the fingers cannot provide high grasp forces and cannot adapt to different object shapes to secure the grasp (e.g. on the power grasp of a disk - Fig. 6.9a). Experimentally, the maximal grasp force provided by the e-motion actuation mechanism is about 0.8 [N]. The adaptable actuation system instead, does not require any grasp planning and can hold objects up to 3.6 [N]. Figure 6.12 shows a subset of grasped objects.

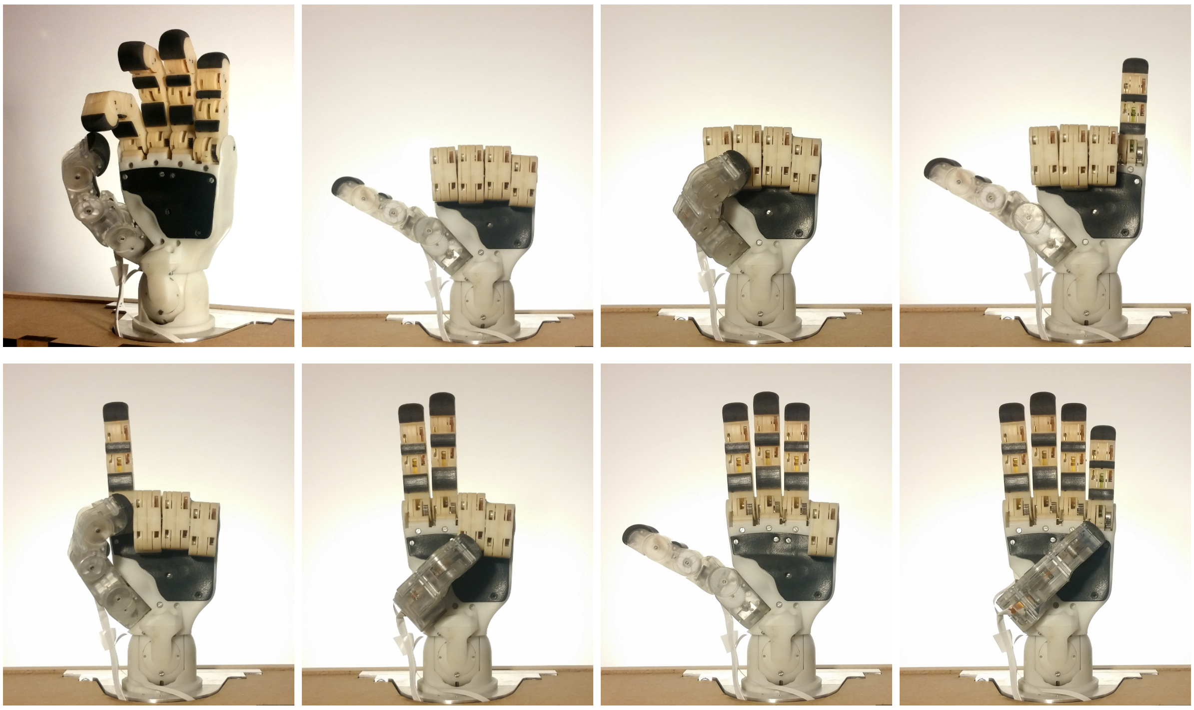

Figure 6.8 – E-motion test: examples of feasible hand gestures.

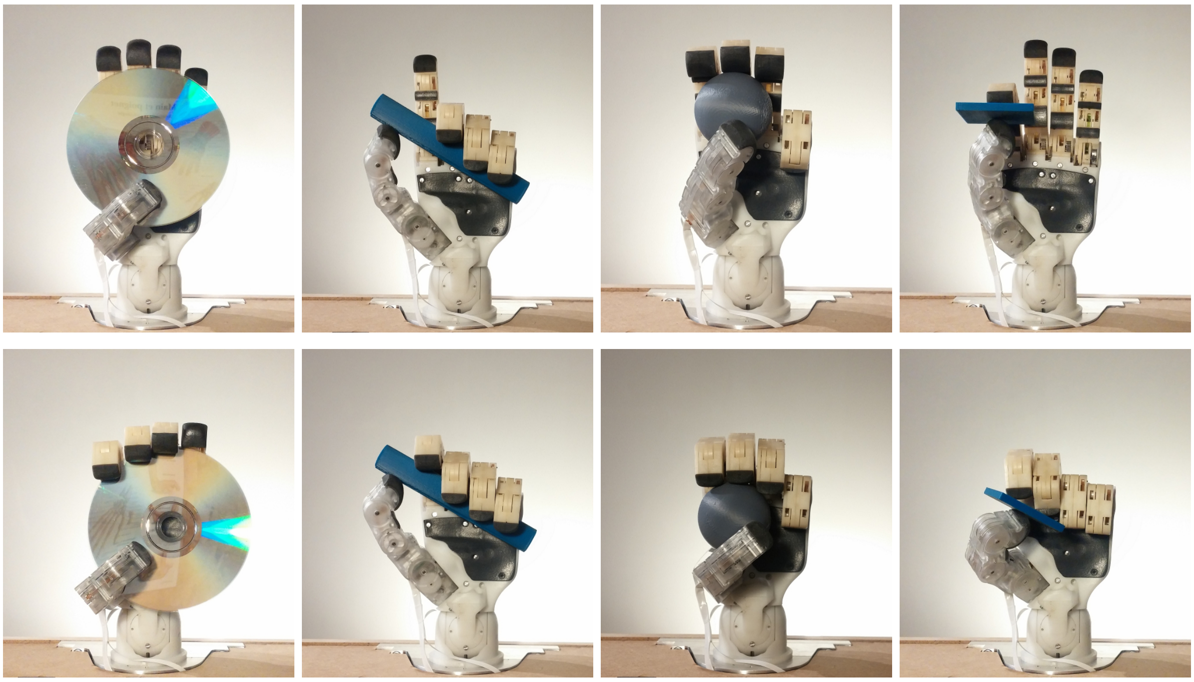

(a) (b) (c) (d)

Figure 6.9 – Examples of grasp transition between the two actuation systems. The first row shows the initial grasp configurations achievable with the e-motion actuation. The second row shows the final grasp state once the motor in the forearm is activated.

6.2 Validation

ALPHA is validated according to the thesis objectives presented in Section 1.4. Tables 6.2, 6.3 and 6.4 summarize the mechanical and functional specifications and shows whether the prototype satisfies each requirement.

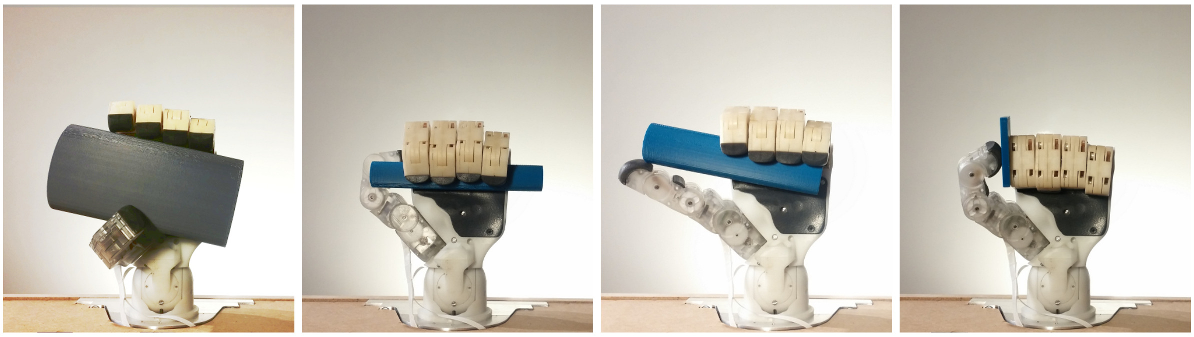

Figure 6.10 – Examples of grasp types that can be achieved by the grasp actuation mechanism.

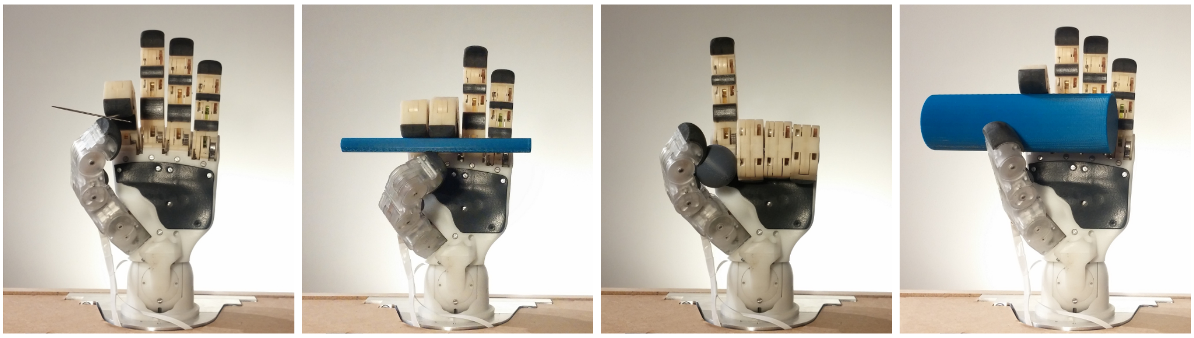

Figure 6.11 – Examples of grasp types that can be achieved by the e-motion actuation mechanism.

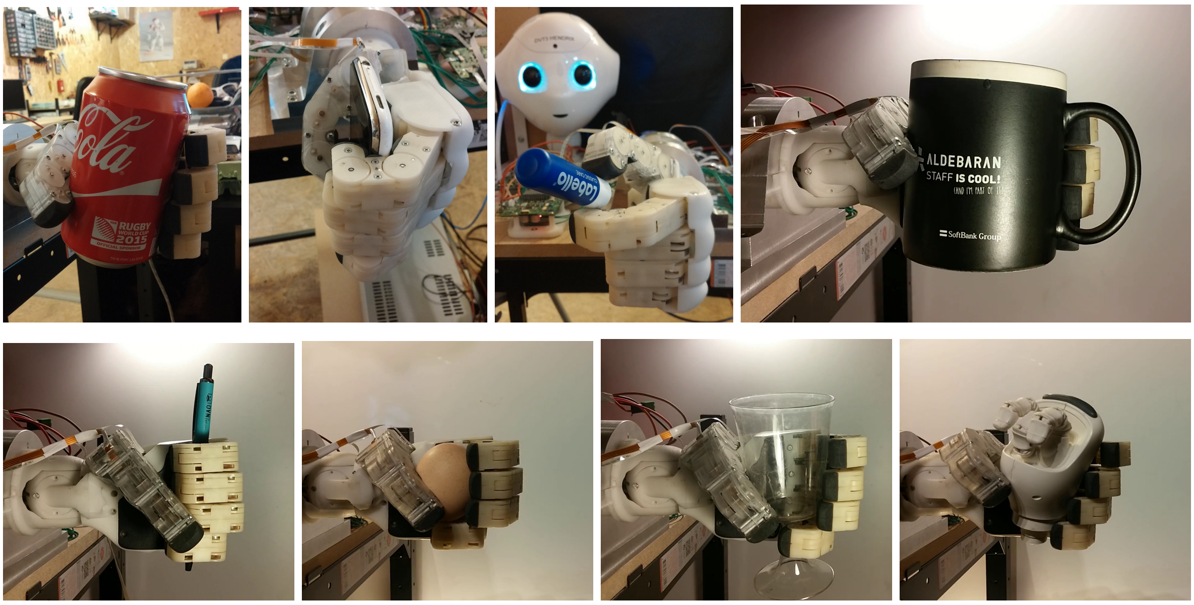

Figure 6.12 – Selection of small and light objects grasped by ALPHA.

ALPHA highly simplifies the human hand kinematics but preserves several anthropomorphic aspects. With respect to the anthropometric data proportioned to a 1.4 [m] young man, the total hand length (from the wrist to the middle fingertip) is 23% longer, mainly due to the palm which is 35% longer than the human palm. The hand is 24% wider than the human hand and it is ≈ 40 [mm] thick. Fingers respect human proportions and are dimensioned according to the robot body. They are placed as to resemble the human hand shape and flexion convergence. In addition, ALPHA presents a highly opposable thumb which strongly enhances hand anthropomorphism even though only 7 DoFs are adopted. The overall system weighs 540 [g], excluding the electronic boards placed outside the palm together with the grasp motor. These components are supposed to be placed in Romeo's forearm to preserve the human-like

Mechanical specifications	Respected
anthropomorphic design	✓
self-contained	≈
weigh less than 600 [g]	✓
safe	✓
back-drivable	✓
open/close in less than 1 [s]	✓
low-cost	✓
robust[i]	✓
energy-efficient	✓
coherent actuation technology[ii]	✓
silent	✓

[i] actuation system protection from undesired mechanical stresses [ii] electromagnetic actuators

Table 6.2 – Validation of mechanical specifications.

hand shape and size. ALPHA is designed to be safe. Even though sensor-less active compliance loses its meaning due to noisy gear trains, human-robot interaction is still preserved thanks to low torque e-motion actuators and a highly backdrivable transmission mechanism. Safety is also ensured during grasping since the developed force is limited to hold objects which weigh less than 400 [g]. The system is also robust against undesired mechanical stresses notably thanks to elastic couplings. These preserve a desired non-linear coupling in absence of external forces and allow deflection during grasp so that no energy is consumed to fight return forces during normal motion. High backdrivability is ensured through low gearbox reduction ratios which allow fast and silent movements. The cost of the prototype is less than 8k€, where nearly half of it is spent for gears manufacturing and a third of it for pulleys, axes and bars. The production cost of the hand is about 250€ (approximatively 30 times smaller the prototype cost) excluding the electronic boards. This is evaluated considering most of the mechanical parts in plastic, except for motor supports, axes, differential bars, finger and palm soft parts and the first train gear at the base of the thumb. The estimation is based on the cost of similar parts currently embedded on Aldebaran's humanoid robots. Since the production volume is unpredictable the cost (and relative depreciation) of plastic molds is not taken into account. As shown in Figure 6.13, thanks to the industrialization process the charge of gear manufacturing drastically drops while MAXON motors become the main cost factor (nearly two-third of the final price).

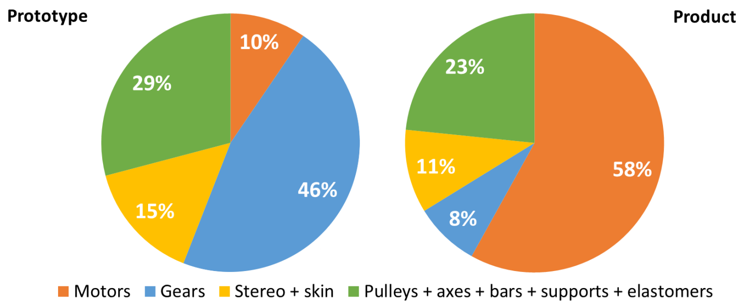

Figure 6.13 – Detailed cost factors of ALPHA prototype and product.

Expressive hand gestures	Priority	Achieved
thumb-up	high	✓
OK	high	✓
"give me" (cupped hand)	high	✓
point at	high	✓
shake and handle the hand of a man	high	✓
"come here"	high	$\approx$
mimic the shape of a heart	high	n/a
count up to 5 in two different ways	middle	✓
telephone	middle	✓
twiddling thumbs	middle	n/a
closed fist	low	✓
"blah-blah"	low	✗
"stop" (with the hand at the level of the throat)	low	✗

Table 6.3 – Validation of required expressive hand gestures.

Not all hand gestures can be performed. This is due to the simplified kinematic structure chosen at design stages (see Section 2.1). High priority gestures can all be performed and easily recognized, except the "come here" gesture which, for some, it only involves MCP joint motions with the DIP and PIP joints immobile. Mimicking the shape of a heart and twiddling thumbs cannot be verified since they involve two hands. Only two gestures are not validated. These are the low priority "blah-blah" gesture and the "stop" gesture which strictly need MCP joints to be independent from PIP and DIP ones, requiring four additional actuators in the palm.

Objects	Weight [g]	Grasped
full beverage can	366	$\approx$
full small bottle (33cl)	330	✓
glass (plastic, wine)	100	✓
pencil and pen	20	✓
smartphone	140	✓
switching the light	n/a	n/a
holding a box	n/a	n/a

Table 6.4 – Validation of required object to be grasped.

All small and lightweight objects required to be grasped can be held stably (Table 6.4). However, a full beverage can is grasped only in a specific configuration within the palm. Experimental results show that the can is brought to the center of the hand (as desired) but not all contacts occur on rubber surfaces when the object is proposed orthogonal to the hand sagittal plane. Indeed, the object is held in the upper part of the palm close to the finger bases where no rubber is present. Here, the static friction coefficient drops down to 0.14 (experimentally measured), leading to grasp failure (the can slip from the grasp).

On the contrary, the can stably remains within the grasp by manually bending the object (as shown in Figure 6.12) in contact with the palm soft parts. This shows that the grasp actuation force has been properly sized and that the palm shape should be redesigned. Switching the light and holding a box cannot be validated. The former requires the displacement of the whole test bench while the latter needs a cooperating opposite hand.

6.3 Prototype limits

The ALPHA prototype serves as a proof of concept. Its anthropomorphic design based on two distinct actuation systems globally solves mechanical and functional requirements. Nevertheless, its realization presents some defects and its control requires some improvement. This discussion is structured according to the functional aspects to better identify each matter.

E-motion.

— *operation over nominal torque*: e-motion motors work nearly at their stall torques when fingers are stretched against gravity. This is because of the model inaccuracies, frictions and a lower than expected efficiency of gearboxes. Actuation should have been sized with a larger safety margin;

— *manufacturing and mounting inaccuracies at gearboxes*: gearbox inaccuracies lead to additional stresses and noise in the transmission chain. External forces can be estimated from current sensing only after an important threshold which yields active compliance to be peripheral. Since safety is still guaranteed by high backdrivability and low motor torques, impedance control has been disabled. In addition, gear meshes at the MCP joint of the thumb sometimes lose contact after grasp. Thumb gears are in stereo-lithography rather than steel (as the ones adopted for the other fingers) because of their better manufacture. To avoid all these problems, gears should be better manufactured and embedded in the transmission chain for further developments;

— *external cable routing at thumb*: all flexible flat cables are passed outside the thumb covers due to the several cut occurred during experimental tests. Another routing solution needs to be found and implemented.

Grasp.

— *limited self-adaptability*: fingers present less self-adaptability with respect to sweep-based hand designs. This is because phalanges are coupled for gesturing and because decoupling is more encouraged in one direction. In addition, stiffnesses have been chosen in order to limit energy consumption without taking into account the decoupling process. This results in a stiffer coupling between proximal and middle phalanges which respect to middle and distal phalanges. Consequently, distal phalanges close before middle ones when proximal phalanges enter in contact at first;

— *no cable unwinding*: after grasp, e-motion motors are supposed to unwind the grasp cable by opening the fingers. However, their torques and elastomers stiffnesses are not sufficiently strong enough to perform this action. To solve this problem, the grasp motor is activated on the opposite direction for a very short time to autonomously unwind the cable;

— *no proper re-coupling of the thumb distal phalanx*: after several tests the chosen elastomer turned out to be too soft to restore the coupling ratio - probably due to frictions in the differential mechanism;

— *sub-optimal pulley radii*: adopted pulley radii have been computed in absence of return torques. Their values should be changed as to consider the elastic effects at the finger joints;

— *non-constant return torque at buckling*: elastomers touch finger covers when buckling, consequently increasing the resistance to grasp;

— *absence of rubber at the top of the palm*: palm shape should be redesigned to increase the extension of the soft parts ensuring higher friction coefficients at contact.

7

Conclusions and future works

7.1 Context

In this thesis a novel human-inspired robotic hand for a humanoid robot has been presented. The hand is designed to enhance the integration of social humanoid robots in our society by providing valuable services and more engaging interaction. At present, the diffusion of humanoid robots is paradoxically hindered by their aspect. Indeed, the human shape instils high expectations about robot capabilities which can cause rejection and deception if failed. In addition, humanoid robots are generally too expensive to be adopted in everyone's home. To contain prices, some social humanoid robots adopt very simple manipulators or five-fingered hands only for aesthetic purposes. In this sense, it is necessary to conceive of low-cost anthropomorphic robotic hands capable of providing fundamental functionalities; namely gesturing and grasping. The former to strengthen empathy through non-verbal communication in human-robot interaction and the latter to provide basic services such as fetching, holding and providing common household objects.

The design of such device involves three main challenges:

1. define the geometry and kinematics which preserve anthropomorphism and ensure the required functional capabilities;
2. achieve desired motion dexterity and grasp power while preserving a compact and lightweight structure and respecting integration constraints (mechanical, energetic, technological, price, etc.);
3. implement a functional prototype which provides safe human-robot interaction.

The first has been addressed in Chapter 2 and it has been solved from direct inspiration and simplification of the human hand. The others have been confronted in Chapters 3-5 and tackled through a novel hybrid design.

7.2 Summary

Geometry and kinematic definition. The definition of the hand geometry and kinematics has been dictated by the functional requirements and the need for keeping the number of actuators to a minimum. Independent DoFs have been considered driven by dedicated actuators without the adoption of locking devices to distribute the action of a single actuators to different outputs. Indeed, one could have argued that one motor could have been used to independently drive more joints at deferred intervals. However, this would have induced undesired asynchronous motions for gesturing. The hand kinematics have been inspired from the human hand and incrementally defined on the base of prioritized hand gestures. Even though its structure highly simplifies the human counterpart, anthropomorphism has been ensured in terms of finger placements, proportions and sizes. A numerical methodology to compute finger and thumb geometries and bases has been developed. While existing models are usually the result of successive parameter adjustments, the proposed method determines fingers placements by means of empirical tests based on anthropometric data. Moreover, a surgery test and a workspace analysis of the whole hand are used to find the best thumb position and orientation according to the hand kinematics and structure. In literature, there are few numerical methods for the finger placement of human-inspired robotic hands. In particular, there are no numerical methods for the thumb placement, that aim to improve the hand dexterity and grasping capabilities by keeping the hand design close to the human one.

Hybrid hand design. To obtain a compact, light-weight robotic hand able to perform common gestures and self-adaptable grasps, a novel hybrid design has been proposed. This solution mixes the advantages of two types of hands, a fully-coupled and a self-adaptable hand, in a unique design. It answers the need for precise finger postures and sensor-less force feedback when performing gestures and for finger adaptation when grasping. The adjective *hybrid* arises from the fact that the hand behaves as a self-adaptable hand by alternatively using two distinct actuation systems, placed in parallel within the palm and the fingers. Up to the author's knowledge, robotic hands which embody dual actuation systems are driven by different objectives from the one presented in this context (e.g. gross and fine manipulation, or precise and power grasp) and their coexistence (actuation cooperation or independence) is often solved by control. Variable finger kinematics is ensured by an elastic transmission mechanism which offers sufficient coupling rigidity to perform fast finger motions and limited restoring force to allow finger adaptation with reduced actuation energy. Elastomers, rather than classical tension springs, are used as passive elements in the fingers, thanks to their high elastic coefficient at reduced sizes and strains. The actuation system dedicated to perform hand gestures is designed with low power small motors and gearboxes with very low reduction ratios. This because gestures require at least seven motors to be embedded within the palm and the fingers. These contribute to a compact and lightweight hand and ensure fast motions. The actuation system dedicated to grasping compensates the lack of grasp force. It is conceived to hold small and light objects and it implements self-adaptability among phalanges and fingers to autonomously adapt to different object shapes without the need for grasp planning. The grasp force is provided by only one high power motor placed in the forearm, sized to grasp objects up to the weight of a soda can. Aldebaran - SoftBank Groups is currently applying for a patent to protect the elastomer-based transmission mechanism design.

Prototype realization. To validate the proposed hybrid design a functional prototype has been implemented. This globally respects the design constraints required to be embedded on Romeo, a 1.4 [m] social humanoid robot, and attains the expected functional objectives (and even more in terms of grasping). The prototype is also developed to evaluate its robustness and safe human-robot interaction. The last is primarily guaranteed by sensor-less impedance control during normal motion and by a bounded actuation force (by current limits) during grasp. In addition, the e-motion actuation system is conceived to be highly backdrivable (barely no reduction ratio) and delicate - with just sufficient power to counterbalance the effects of gravity - which guarantee a second degree of safety in case of active compliance failures. No contact (or force) sensors are adopted to contain costs and avoid unreliable contact detection - either due to malfunctioning after damage or to uncovered finger parts. Finally, mechanical integrity is provided by the elastic elements in the transmission mechanisms which protect the actuation system from shocks and erratic interactions far from the joint limits.

7.3 Future works

The prototype is the first version of ALPHA (ALdebaran Parallel HAnd). It presents some implementation defects and needs some improvements to be effectively embedded on the robot. First of all, gears need to be improved to reduce transmission noise and guarantee current-based force feedback. This would allow an effective contact detection for active compliance and an autonomous transition between e-motion and grasp. Gear transmissions can be improved by design, i.e. adopting helical gears which are stronger (due to the longer and thicker tooth form) and more quiet (thanks to the additional contact ratio) than the equivalent spur gears, or by construction. For example, more reliable mesh contacts at bevel gears can be ensured by adding springs, such as conical spring washers at their axes. Another important improvement consists of redesigning the palm as to provide a larger rubber layer for grasping. Better grasping performance can be also encouraged by implementing abduction/adduction motions at the finger bases. Without embedding any additional actuators, these motions might be left passive to enhance self-adaptability, and with return springs to restore the initial configuration. To further reduce the cost of the hand, the thumb kinematic can be simplified to two independent DoFs by coupling the flexing motion of the RC joint to the MCP one. This would certainly reduce hand anthropomorphism in terms of opposability and thumb dexterity. Indeed, the thumb would probably not be capable of reaching the little finger base and fingertip. The thumb base may be replaced to guarantee equal interaction with all opposing fingers (using the approach presented in Chapter 1) but this would probably lead to a very small distance between the thumb and the reminder finger bases, strongly limiting the size of the palm and of graspable objects. Other future works include the optimization of electronic component sizes and shapes. Currently, most electronic components are placed outside the hand and, a part of them, should be integrated in the palm for a proper integration on the robot arm. Further steps consist in designing a 3 DoFs wrist and improving the overall aesthetics of the hand, in accordance to Aldebaran's style. The hand also needs to be adapted for the industrialization process. Most of the parts will be replaced by plastic and, probably, some will need to be simplified or transformed. Moreover, the hand will be subjected to an evaluation process to determine its reliability under repeated motions and stress tests. Last but not the least, postural synergies should be implemented to simplify grasp planning and control [148].

ALPHA represents an important step towards compact, lightweight and low-cost anthropomorphic robotic hands, for humanoid robots supposed to gesture and grasp.

A

Robotic hands details

A.1 Highly dexterous hands

Name	DoFs		Joints (DoMs)[i] distribution					
	Joints	**Independent**	T	I	M	R	L	Palm
DLR Hand Arm System [50]	21	19	4	4	4	4(3)	4(3)	1
Shadow hand [52]	22	18	5	4(3)	4(3)	4(3)	4(3)	1
CEA hand [53]	22	18	5	4(3)	4(3)	4(3)	4(3)	1
Gifu hand III [55]	20	16	4	4(3)	4(3)	4(3)	4(3)	-
SBC [57]	20	16	4	4(3)	4(3)	4(3)	4(3)	-
UB hand IV [56]	20	15	4(3)	4(3)	4(3)	4(3)	4(3)	-
DLR/HIT hand II [54]	20	15	4(3)	4(3)	4(3)	4(3)	4(3)	-
Sonoda and Golder hand [58]	18	14	3	4(3)	3	4(3)	4(3)	-
Robonaut 2 hand [51]	18	12	4	4(3)	4(3)	3(1)	3(1)	-

[i] if different from the number of joints

Table A.1 – Highly actuated robotic hands: Joint and independent DoFs.

Name	Actuators	Actuator distribution					
		T	I	M	R	L	Palm
DLR Hand Arm System [50]	38	8	8	8	6	6	2
Shadow hand [52]	18[i]	5	3	3	3	3	1
	36[ii]	10	6	6	6	6	2
CEA hand [53]	18	5	3	3	3	3	1
Gifu hand III [55]	16	4	3	3	3	3	-
SBC [57]	32	8[iii]	6	6	6	6	-
UB hand IV [56]	20	4	4	4	4	4	-
DLR/HIT hand II [54]	15	3	3	3	3	3	-
Sonoda and Golder hand [58]	15	4	3	2	3	3	-
Robonaut 2 hand [51]	17	5	4	4	2	2	-

[i] Smart Motors [ii] Air Muscles [iii] supposed - not defined in the paper

Table A.2 – Highly actuated robotic hands: number of actuators.

A.2 Hands with reduced DoMs

A.2.1 Fixed joint couplings

Name	DoFs		Joints (Actuators)[i] distribution					
	Joints	**Ind.**	T	I	M	R	L	Palm
Schunk Gripping hand [73]	20	9	4(1+α)	4(2+β)	3(2)	4(1+β)	4(1+β)	α
HRP-4C hand [74]	13	2	1	3(α)	3(α)	3(α)	3(α)	-

α and β are independent motors shared among different joints

[i] if different from the number of joints

Table A.3 – Robotic hands with fixed joint couplings.

A.2.2 Self-adaptation within fingers

Name	DoFs		Joints (Actuators)[i] distribution					
	Joints	**Ind.**	T	I	M	R	L	Palm
Cyber Hand [76]	16	6	3(2)	3(1)	3(1)	3(1)	3(1)	-
Alpes Instruments hand [77]	15	6	3(2)	3(1)	3(1)	3(1)	3(1)	-
InMoov hand [78]	17	5	3(1)	3(1)	3(1)	3(α)	3(β)	2($\alpha + \beta$)
Harada hand [79]	14	5	2(1)	3(1)	3(1)	3(1)	3(1)	-

α and β are independent motors shared among different joints

[i] if different from the number of joints

Table A.4 – Robotic hands with self-adaptable fingers.

A.2.3 Self-adaptation among and within fingers

Name	DoFs		Joints (Actuators)[i] distribution					
	Joints	**Ind.**	T	I	M	R	L	Palm
iCub hand [82]	19	9	4(3)	4(2+α)	3(2)	4($\alpha + \beta$)	4($\alpha + \beta$)	-
FRH-4 hand [83]	11	8	2	2	2	2(α)	2(α)	1
IH2 Azzurra hand[84]	11	5	3(2)	2(1)	2(1)	2(α)	2(α)	-
Smart hand [85]	16	4	3(2)	3(1)	3(α)	3(α)	3(α)	-
Nazarbayev Universtiy (NU) hand [86]	10	4	2	2(1)	2(α)	2(α)	2(α)	-
15-dof underactuated hand [87]	16	1	4(α)	3(α)	3(α)	3(α)	3(α)	-
Pisa/IIT soft hand [88]	19	1	3(α)	4(α)	4(α)	4(α)	4 (α)	-
The Delft Cylinder Hand [89]	13	1	1(0)	3(α)	3(α)	3(α)	3(α)	-

α and β are independent motors shared among different joints

[i] if different from the number of joints

Table A.5 – Robotic hands with differential mechanisms to distribute finger actuation.

B

Inverse Dynamic model

This annex presents the Inverse Dynamic Model for serial and tree rigid multi-body systems. It summarizes the main concepts necessary to the reader for a better understanding of Chapters 3 and 5. The notations adopted here are the ones used by Khalil in [149]. For further details about rigid body dynamics of serial/tree robots the reader is invited to read [150] and [121].

The Inverse Dynamic Model (IDM) computes the joint torques and forces in terms of joint positions, velocities, accelerations. Its general formulation for a rigid robot is written as follows:

$$\boldsymbol{\Gamma} = \boldsymbol{f}(\boldsymbol{q}, \dot{\boldsymbol{q}}, \ddot{\boldsymbol{q}}, \boldsymbol{F_e}) \tag{B.1}$$

where:

- $\boldsymbol{\Gamma}$: vector of joint torques (if revolute joint) or forces (if prismatic joint);
- $\boldsymbol{q}$: vector of joint positions;
- $\dot{\boldsymbol{q}}$: vector of joint velocities;
- $\ddot{\boldsymbol{q}}$: vector of joint accelerations;
- $\boldsymbol{F_e}$: vector of forces and moments exerted by the robot on the environment (6 x 1 vector).

The IDM is defined as inverse model since it computes input robot variables (joint torques or forces) in function of output robot variables (joint positions, velocities and accelerations): the desired robot state variables. The IDM of a robot composed by n active joints can be written using the following Lagrange formulation:

$$\boldsymbol{\Gamma} = \boldsymbol{A}(\boldsymbol{q})\ddot{\boldsymbol{q}} + \boldsymbol{C}(\boldsymbol{q}, \dot{\boldsymbol{q}})\dot{\boldsymbol{q}} + \boldsymbol{Q}(\boldsymbol{q}) \tag{B.2}$$

where:

- $\boldsymbol{A}(\boldsymbol{q})$: ($n$ x n) symmetric positive definite robot inertia matrix. Its elements are function of the joint positions $\boldsymbol{q}$;
- $\boldsymbol{C}(\boldsymbol{q}, \dot{\boldsymbol{q}})$: ($n$ x n) matrix computed using Christoffel symbols;
- $\boldsymbol{C}(\boldsymbol{q}, \dot{\boldsymbol{q}})\dot{\boldsymbol{q}}$: ($n$ x 1) vector which represents the Coriolis and centrifugal forces;
- $\boldsymbol{Q}(\boldsymbol{q})$: vector of gravity forces.

To determine $\boldsymbol{A}$, $\boldsymbol{C}$ and $\boldsymbol{Q}$ the kinetic and potential energies of all the robot links have to be symbolically computed. Lagrange approach sees the multi-body robot as a whole. The constraint (internal) reaction forces between the links are automatically eliminated because they do not perform work. This method is best suited for the study of dynamic properties and the analysis of control schemes.

B.1 Newton-Euler formulation

The most efficient approach to solve the IDM in real time is the Newton-Euler algorithm. Its formulation is based on the classical Newton-Euler equations which compute the total forces and torques acting on link j at the point O_j:

$$\begin{aligned}\boldsymbol{F}_j &= M_j\dot{\boldsymbol{V}}_j + \dot{\boldsymbol{\omega}}_j \times \boldsymbol{MS}_j + \boldsymbol{\omega}_j \times (\boldsymbol{\omega}_j \times \boldsymbol{MS}_j)\\ \boldsymbol{M}_j &= \boldsymbol{J}_j\dot{\boldsymbol{\omega}}_j + \boldsymbol{MS}_j \times \dot{\boldsymbol{V}}_j + \boldsymbol{\omega}_j \times (\boldsymbol{J}_j\boldsymbol{\omega}_j)\end{aligned} \tag{B.3}$$

where:

— O_j:the origin of frame R_j
— $\boldsymbol{F}_j$: vector of total forces acting on link j;
— M_j: mass of link j;
— $\dot{\boldsymbol{V}}_j$: linear acceleration vector of link j;
— $\boldsymbol{M}_j$: vector of total moments acting on link j about O_j;
— $\boldsymbol{S}_j$: position of the CoM of link j equal to $\boldsymbol{O}_j\boldsymbol{G}_j = (\boldsymbol{G}_j - \boldsymbol{O}_j)$;
— $\boldsymbol{MS}_j$: first moment of link j equal to $M_j\boldsymbol{S}_j$;
— $\boldsymbol{J}_j$: inertia matrix of link j about O_j;
— $\boldsymbol{\omega}_j$: angular velocity vector of link j;
— $\dot{\boldsymbol{\omega}}_j$: angular acceleration vector of link j.

The Newton-Euler algorithm, also known as RNEA (Recursive Newton-Euler Algorithm), computes $\boldsymbol{\Gamma}$ through two recursive computations (forward and backward recursion) avoiding the calculation of $\boldsymbol{A}$, $\boldsymbol{C}$ and $\boldsymbol{Q}$ matrices. The forward recursion computes link velocities and accelerations from the robot base to the terminal links in order to deduce the dynamic wrenches (total force and moment) of each link. Afterwards, the backward recursion provides the reaction wrenches on the links developing the computation from the last link of the chains (multiple in case of a tree robot) to the base.

Forward computation To compute the dynamic wrench for each link j (for j = 1, 2, . . ., n) using Equations B.3 $\boldsymbol{\omega}_j$, $\dot{\boldsymbol{\omega}}_j$ and $\dot{\boldsymbol{V}}_j$ are needed. For a serial robot these velocities are recursively computed as follows:

$$\begin{aligned}\boldsymbol{\omega}_j &= \boldsymbol{\omega}_{j-1} + \bar{\sigma}_j\dot{q}_j\boldsymbol{a}_j\\ \boldsymbol{V}_j &= \boldsymbol{V}_{j-1} + \boldsymbol{\omega}_{j-1} \times \boldsymbol{L}_j + \sigma_j\dot{q}_j\boldsymbol{a}_j\end{aligned} \tag{B.4}$$

where

$$\begin{cases}\sigma_j = 0 & \textit{if j revolute}\\ \sigma_j = 1 & \textit{if j prismatic}\end{cases} \tag{B.5}$$

and $\boldsymbol{L}_j$ is the distance vector between the origin of the precedent frame R_{j-1} (O_{j-1}) and the origin of the current frame R_j (O_j).

Linear and angular accelerations are directly obtained from the derivative of Equations B.4:

$$\begin{aligned}\dot{\boldsymbol{\omega}}_j &= \dot{\boldsymbol{\omega}}_{j-1} + \bar{\sigma}_j(\ddot{q}_j\boldsymbol{a}_j + \boldsymbol{\omega}_{j-1} \times \dot{q}_j\boldsymbol{a}_j)\\ \dot{\boldsymbol{V}}_j &= \dot{\boldsymbol{V}}_{j-1} + \dot{\boldsymbol{\omega}}_{j-1} \times \boldsymbol{L}_j + \boldsymbol{\omega}_{j-1} \times (\boldsymbol{\omega}_{j-1} \times \boldsymbol{L}_j) + \sigma_j(\ddot{q}_j\boldsymbol{a}_j + 2\boldsymbol{\omega}_{j-1} \times \dot{q}_j\boldsymbol{a}_j)\end{aligned} \tag{B.6}$$

For a robot with a fixed base the algorithm starts from j = 1 with the following initial conditions: $\boldsymbol{\omega}_0 = 0$, $\dot{\boldsymbol{\omega}}_0 = 0$, $\boldsymbol{V}_0 = 0$ and $\dot{\boldsymbol{V}}_0 = 0$.

Backward computation It computes the Newton-Euler equations at the origin O_j for each link j, for j = $n, \ldots, 1$:

$$\begin{aligned}\boldsymbol{F}_j &= \boldsymbol{f}_j - \boldsymbol{f}_{j+1} + M_j\boldsymbol{g} - \boldsymbol{f}_{ej}\\ \boldsymbol{M}_j &= \boldsymbol{m}_j - \boldsymbol{m}_{j+1} - \boldsymbol{L}_{j+1} \times \boldsymbol{f}_{j+1} + \boldsymbol{S}_j \times M_j\boldsymbol{g} - \boldsymbol{m}_{ej}\end{aligned} \tag{B.7}$$

where:

- $\boldsymbol{F}_j$ and $\boldsymbol{M}_j$ vectors represent the dynamic wrench of link j computed with the Newton-Euler equations;
- $\boldsymbol{f}_j$: force exerted by link j-1 on link j;
- $\boldsymbol{f}_{j+1}$: force exerted by link j on link j+1;
- $\boldsymbol{f}_{ej}$: force exerted by link j on the environment;
- $\boldsymbol{m}_j$: moment about O_j exerted by link j-1 on link j;
- $\boldsymbol{m}_{j+1}$: moment about O_j exerted by link j on link j+1;
- $\boldsymbol{m}_{ej}$: moment about O_j exerted by link j on the environment.

Note that if $\dot{\boldsymbol{V}}_0$ is set to $-g$, there is no need to compute the gravity force term $\boldsymbol{S}_j \times M_j \boldsymbol{g}$. External forces ($\boldsymbol{f}_{ej}$) and moments ($\boldsymbol{m}_{ej}$) are assumed to be known while $\boldsymbol{f}_{n+1} = 0$ and $\boldsymbol{m}_{n+1} = 0$ at the last link.
If $\dot{\boldsymbol{V}}_0 = -g$:

$$\begin{aligned} \boldsymbol{F}_j &= \boldsymbol{f}_j - \boldsymbol{f}_{j+1} - \boldsymbol{f}_{ej} \\ \boldsymbol{M}_j &= \boldsymbol{m}_j - \boldsymbol{m}_{j+1} - \boldsymbol{L}_{j+1} \times \boldsymbol{f}_{j+1} - \boldsymbol{m}_{ej} \end{aligned} \tag{B.8}$$

obtaining that:

$$\begin{aligned} \boldsymbol{f}_j &= \boldsymbol{F}_j + \boldsymbol{f}_{j+1} + \boldsymbol{f}_{ej} \\ \boldsymbol{m}_j &= \boldsymbol{M}_j + \boldsymbol{m}_{j+1} + \boldsymbol{L}_{j+1} \times \boldsymbol{f}_{j+1} + \boldsymbol{m}_{ej} \end{aligned} \tag{B.9}$$

From which the joint torque (or force) is computed projecting $\boldsymbol{m}_j$ (or $\boldsymbol{f}_j$) on the joint axis:

$$\boldsymbol{\Gamma}_j = (\sigma_j \boldsymbol{f}_j + \bar{\sigma}_j \boldsymbol{m}_j)^T \boldsymbol{a}_j \tag{B.10}$$

To solve the IDM for a tree robot the algorithm has to be slightly modified. Instead of proceeding from link j to $j-1$, the robot is visited starting from the last links (leaves) to the base passing through the antecedent ($ant(j)$) of each link.

B.2 Dissipation phenomena

To improve the dynamic model dissipation phenomena and the presence of actuators on the robot have to be taken into account.

B.2.1 Friction

In general, three kind of frictions are considered: Coulomb friction, static friction, viscous friction. The Coulomb friction is a constant friction force independent from the velocity magnitude. The static friction is the friction force necessary to initiate the motion. The viscous friction is generally simplified to be a friction force proportional to the body velocity (the so called Stribeck effect phenomenon is usually neglected). The most used friction model only includes the Coulomb and the viscosity frictions:

$$\Gamma_{Fr_j} = F_{C_j} sign(\dot{q}_j) + F_{V_j} \dot{q}_j \tag{B.11}$$

where:

- Γ_{Fr_j}: friction torque of joint j;
- F_{C_j}: Coulomb friction coefficient at joint j;
- F_{V_j}: viscous friction coefficient at joint j.

To keep them into account in the dynamic model, they can be directly added on the right hand side of Equation B.10 for each joint j. Note that these effects are referred to the actuators and transmission frictions and not to other external frictions (e.g. between links).

B.2.2 Rotor inertia of actuators

The rotors of electric motors are very small compared to the other robot parts therefore their mass is usually neglected. However, if links are not directly actuated motor rotors attain higher speeds than the bodies they are driving and can, in consequence, considerably influence the whole robot dynamics. What is commonly done in robotics is to model the actuator (motor and gearbox) as an ideal electric motor that develops N_j times the torque of the real motor and runs at $1/N_j$ times the speed and has N_j^2 times the rotor inertia of the real motor plus the gearbox inertia, where N_j is the gear ratio. These fictitious inertia is added to the diagonal elements of the robot inertia matrix ($\boldsymbol{A}$) to keep into account rotor dynamic effects on the robot structure. In the Newton-Euler algorithm, the rotor inertia effect (Ia_j) is added to the right hand side of Equation B.10: $Ia_j\ddot{q}_j$.

C

Force sensing from current readings

This annex presents the work done by Florian Armange, a colleague at the AM-Lab Nantes of Aldebaran - SoftBank Group, about the suitability of external torque estimation based on current feedback for active impedance control. The analysis is performed on three distinct actuation blocks with nearly equivalent output torques characterized by different motors and gearboxes. This is done to study the influence of reduction ratio on torque estimation. To compare experimental results, the estimation is considered suitable for active compliance when its error is less than 10% of the real output torque.

C.1 Experimental setup

To characterize the precision of the torque feedback a constant load is applied to the actuation mechanism. The actuation mechanism is composed of a brushless motor and a gearbox, while the load consists of a calibrated weight attached to a pulley. The pulley is placed at the gearbox output shaft and the weight is hung onto the pulley with a non-elastic cable. Figure C.1 shows the experimental setup principle. The torque is sensed at the motor through current readings provided by shunt resistors.

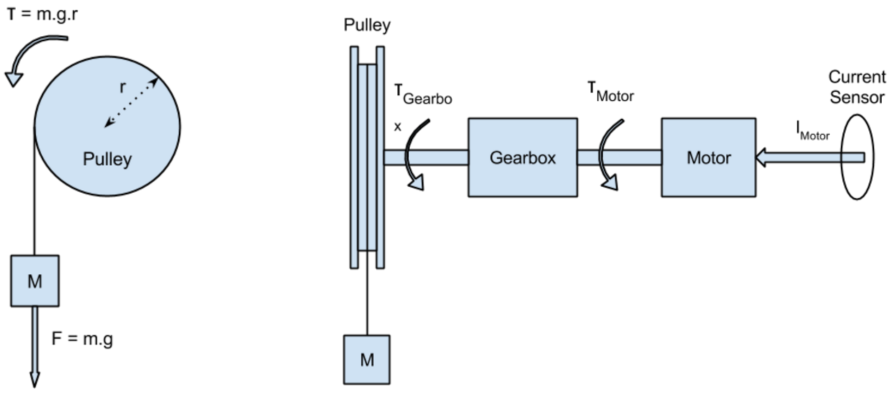

Figure C.1 – Current sensing experimental setup.

Three actuation systems, characterized by different motors and gearboxes, are compared (see Table C.1):
- — High Power motor (Maxon EC 45 flat) and Low Reduction ratio (HPLR);
- — Middle Power motor (Maxon EC 32 flat) and Middle Reduction ratio (MPMR);

— Low Power motor (Maxon EC 20 flat) and High Reduction ratio (LPHR).

A quick and simplified description of each configuration is : These configurations have similar output torques according to the well-known simplified gearbox model:

$$\tau_B = i\,\eta\,\tau_A \tag{C.1}$$

where τ_B is the gearbox output torque, τ_A is the motor torque at the gearbox input, i is the gearbox ratio and η is the gearbox efficiency. For each drive configuration, torque losses due to the gearbox efficiency can be easily computed:

$$\Delta\tau = \tau_B - \, i\,\tau_A \tag{C.2}$$

	HPLR	MPMR	LPHR
Nominal motor torque [mNm]	128	25.5	7.74
Gear ratio (i)	3.5:1	21:1	89:1
Gearbox efficiency (η)	0.9	0.81	0.59
Nominal joint torque[i] [mNm]	403.2	441.1	405.5
Torque loss at nominal[ii] [mNm]	44.8	103.5	281.8

[i] computed from Equation C.1 [ii] computed from Equation C.2

Table C.1 – Three motor and gearboxes configurations adopted to analyze torque estimation from motor currents.

C.2 Gearbox characterization

The simplified gearbox model roughly approximates the friction loss taking place in the gearbox. In order to better estimate the output load, an improved model is adopted. This is based on the work of Pelchen et al. [151] which includes bearing friction, mesh friction and power flow direction. It takes into consideration the influence of gear wheel sticking and sliding due to Coulomb friction between gear teeth, leading to load-dependent torque losses. This allows reliable simulation of stick-slip effects in gearboxes. A general overview of this model is here presented.

C.2.1 Improved model

By defining τ_A and ω_A as the torque and angular velocity at the input shaft of the gearbox and τ_B and ω_B as the torque and angular velocity at the output shaft of the gearbox, the following equation holds:

$$\tau_B = i(\hat{\eta}_{mf}(|\omega_A|)\,\tau_A - \hat{\tau}_{bf}(\omega_A)) \tag{C.3}$$

where $\hat{\eta}_{mf}(|\omega_A|)$ represent mesh frictions and $\hat{\tau}_{bf}(\omega_A)$ bearing frictions as function of the angular speed at the input shaft. The definitions of $\hat{\eta}_{mf}$ and $\hat{\tau}_{bf}$ change according to the sign of τ_A and ω_A and for $\omega_A = 0$. For simplicity, Equation C.3 can be rewritten as:

$$\tau_B = i(\tau_A - \Delta\tau) \tag{C.4}$$

where:

$$\Delta\tau = \begin{cases} (1-\hat{\eta}_{mf}(|\omega_A|))\,\tau_A + \hat{\tau}_{bf}(\omega_A) & \text{for } \omega_A \neq 0 \\ \text{so that } \dot{\omega}_A = 0 & \text{otherwise} \end{cases} \tag{C.5}$$

Torque loss ($\Delta\tau$) can be divided in four quadrants depending on desired angular speed direction $\dot{q}_d$ and torque sign as shown in Figure C.2. Its value lies on the upper or lower limiting line according to the power flow when gears slide ($\omega_A \neq 0$), while it is bounded between them when gears are stuck ($\omega = 0$) due to bearing and mesh frictions.

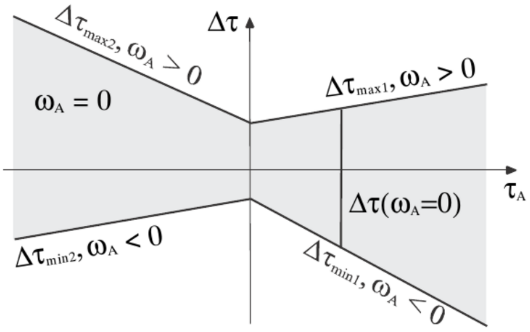

Figure C.2 – Torque loss according to the power flow. Picture taken from [151].

C.2.2 Experimental identification

For a given angular velocity, bearing and mesh friction components can be estimated with at least two distinct loads. Indeed, given one fixed load, Equation C.3 still presents two unknown. Consequently, bearing and mesh friction coefficients are determined by using different loads and correspondent input torques (to characterize positive and negative power flows) through a least mean square fitting (as proposed by [151]). In this context, measurement are performed at the transition between stuck and sliding gears. This is done by triggering positive and negative power flows from static configurations. Static configurations are obtained by applying the τ_A correspondent to each load (so that $\omega = 0$). Negative power is triggered by augmenting the load until the last falls, while positive power is triggered by increasing the motor torque until the charge is lifted. Figure C.3 compares the gearbox models for each drive configuration. The blue and red lines describe the improved gearbox model with the experimental efficiency for positive power ($\tau_A\omega_A > 0$ - named "Motor" mode) and negative power ($\tau_A\omega_A < 0$ - named "Brake" mode) flows respectively. The cyan and purple dotted lines represent the simplified gearbox model with the theoretical efficiency provided by constructors for positive and negative power flows respectively.

C.3 Load estimation

To properly estimate the joint torque (load) the sign of the power flow must be known. In the test bench loads are always placed to induce positive motor torques, consequently, the power sign is equivalent to the sign of the angular velocity of the motor. Since motor velocity is normally obtained from position measurements, it is possible to wrongly estimate the sign of the power flow at $\omega_A \approx 0$. To evaluate its impact on the final result, joint torques are estimated on angular velocities with correct and wrong signs. Figure C.4 shows the experimental mass estimation obtained from the improved gearbox model for MPMR and HPLR configurations and Figure C.5 expresses the estimation error in percentage of nominal joint torques. The LPHR configuration is characterized by small currents highly affected by noise which compromise their use for torque estimation. As it can be seen, when the good model is used to compute the nominal joint torque, the error is acceptable (lower than the 10% of the nominal joint torque) for both MPMR and HPLR configurations. However, if wrong model is considered, torque estimation exceeds the validation criteria at higher loads in the HPLR configuration and strongly exceeds the validation criteria at any load in the MPMR configuration. By interpolation, LPHR configuration would tend to be worst of the two presented.

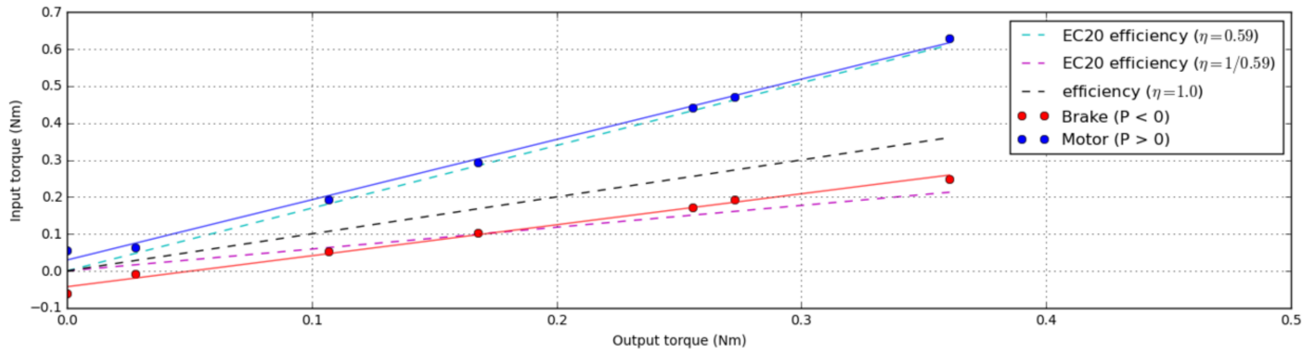

(a) LPHR.

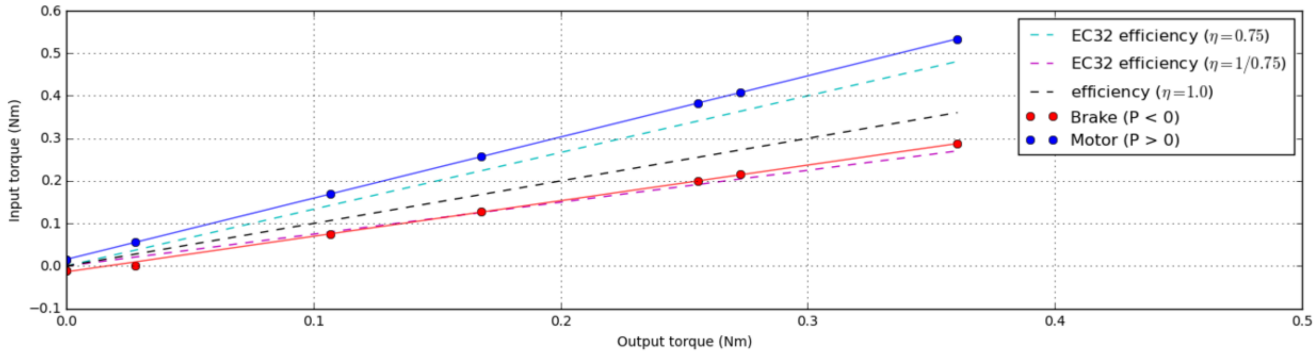

(b) MPMR.

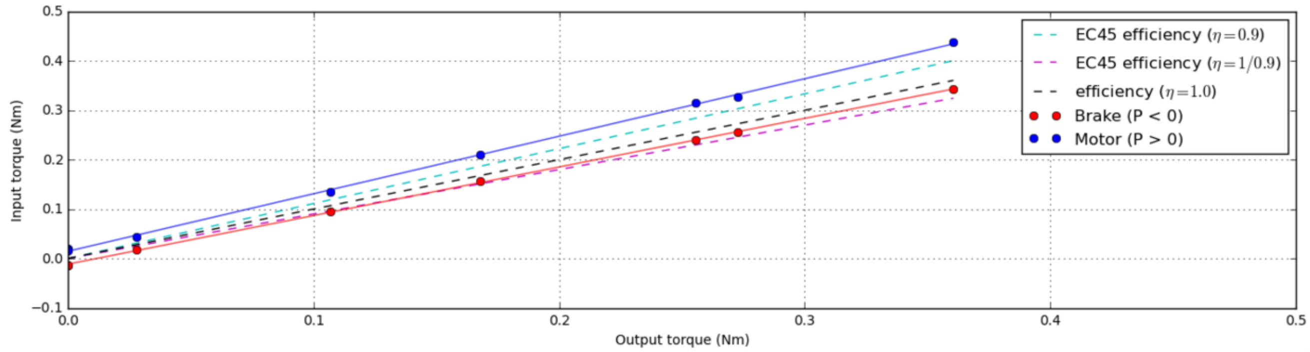

(c) HPLR.

Figure C.3 – Comparison between the simplified gearbox model (with theoretical efficiency) and the improved gearbox model (with experimental efficiency). The comparison is shown for each drive configuration.

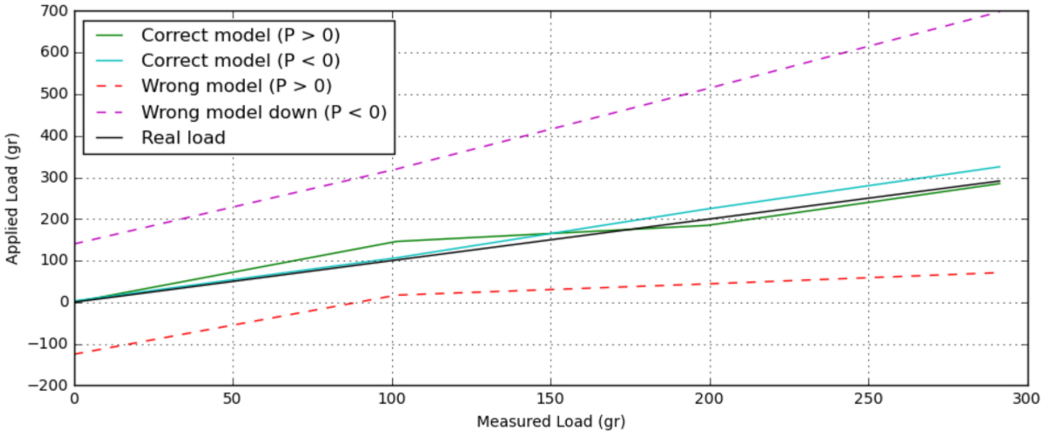

(a) MPMR.

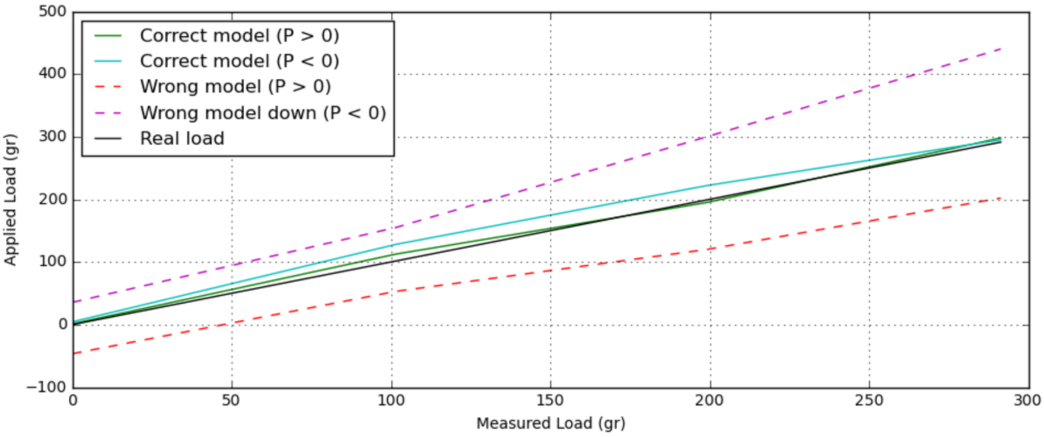

(b) HPLR.

Figure C.4 – Absolute load estimation.

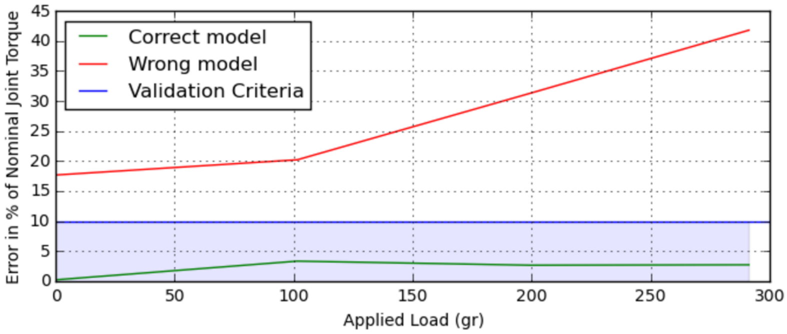

(a) MPMR.

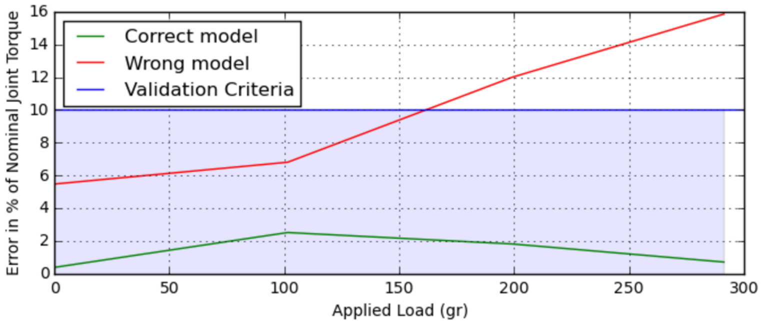

(b) HPLR.

Figure C.5 – Load estimation percentage error with respect to the nominal motor torque.

C.4 Conclusion

This study shows that torque sensing through motor current is possible with low and middle gear ratio configurations by adopting an improved gearbox model. However, the risk of torque estimation error caused by bad direction detection has to be limited in order to guarantee safe physical human-robot interaction. In this perspective, the HPLR configuration is preferred since more robust than the MPMR and LPHR solutions.

D

MRE placement

To reduce the volume occupied by the motors within the palm, the distance between MREs (Magnetic Rotary Encoders) and rotors is reduced. Motor angular position is obtained by the MRE through a cylindrical diametrically magnetized magnet glued on the rotor. According to AMS specifications, the recommended distance (z) interval between the magnet and the package surface is [0.5 mm, 2.5 mm] for a magnet of dimension ($\varnothing$6 [mm] x 3 [mm]). In this context, two magnets of smaller thicknesses (2.5 [mm] and 1.0 [mm]) are attached to the rotor, and the distance interval at which they can be placed to preserve comparable measurement performance is here determined. To verify within which interval a MRE can be placed in front of the magnet, the noise and the linearity of the sensor (AMS AS5048) are tested at various distances. For both magnets, the gap between the magnet and the rotor is fixed to 2 [mm] to avoid magnetic interference of the motor on the magnetic field of the permanent magnet.

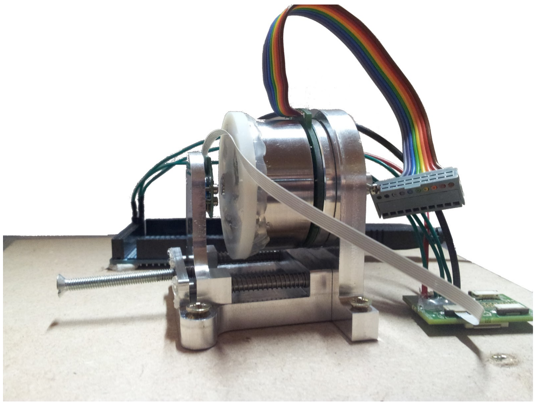

Figure D.1 – MRE placement test bench. A moving plate is used to precisely displace the MRE from the magnet surface. A 3D-printed support fixed on the rotor diameter ensures a centered magnet position.

D.1 Noise measurement

MRE signal is acquired at constant rotor positions to characterize the Gaussian noise at different MRE distances. Noise evaluation is based on standard deviation of the collected samples mean: $SD_x = \sigma/\sqrt{n}$, where σ is the standard deviation of the distribution and n is the number of collected samples. More than 250 samples are taken at each z position of the MRE from the magnet surface. In

Figure D.2 the resultant standard deviation distributions of both magnets are compared. From the two curves it can be seen that the noise with the 1 [mm] magnet is stronger than the 2.5 [mm] magnet at distances greater than 1.8 [mm] (as expected) because of the weaker electromagnetic field. On the other hand, the 2.5 [mm] magnet is more noisy at very short distances (e.g. 0.2 [mm]).
Recognized the possibility to adopt a thinner magnet on the rotor, its linearity is characterized to determine whether it can effectively replace the standard magnet.

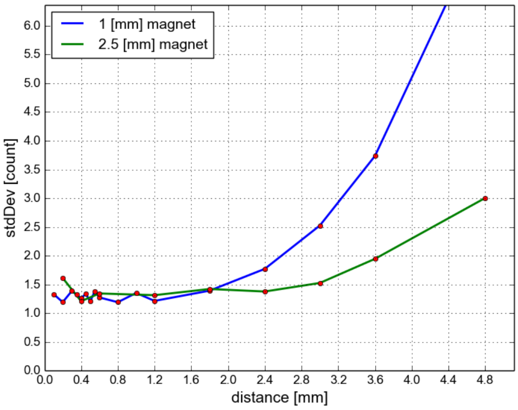

Figure D.2 – SD_x magnets comparison.

D.2 Sensor linearity

The linearity test consists in characterize the MRE at various rotor configurations in a complete mechanical turn. To pass from one configuration to another, the motor is controlled switching the three phases with an Arduino board and a h-bridge (Figure D.3). Since the adopted motor (EC 45) has 8 pole pairs, for each step eight mechanical positions can be achieved in a turn. This is equivalent to say that 48 positions can be attained cycling the six step open loop controller 8 times. The MRE signal is collected every 100 [ms] while the rotor position is changed every second. Post-processing on the acquired data is used to select the samples once the rotor is stable (after the transient phase). To evaluate the MRE performance in one turn, it is checked that at each motor step the measured displacement is coherent with the theoretical one (no absolute reference is used). Linearity is characterized in function of the mean of the step errors and its standard deviation at each MRE z distance. From this test it comes out that error rapidly increases at distances less than 0.5 [mm] for the 1 [mm] magnet.

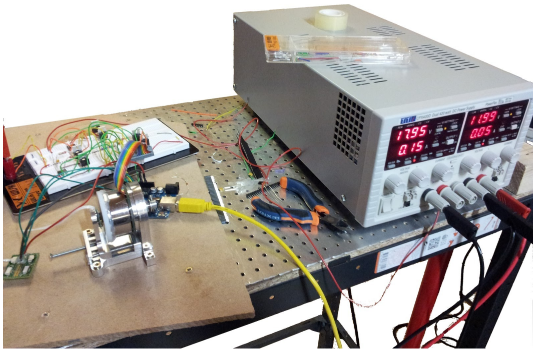

Figure D.3 – Linearity characterization.

D.3 Conclusions

In conclusion, a (⌀6 [mm] x 1 [mm]) magnet can replace the one recommended by AMS specifications by placing the MRE package surface within the interval [0.5, 1.8] [mm] from the magnet. Consequently, MRE motor supports are designed at the closest distance in order to reduce the volume required by e-motion actuators within the palm.

E

ALPHA Documentation

E.1 Dimensions, Joint RoMs and Geometry

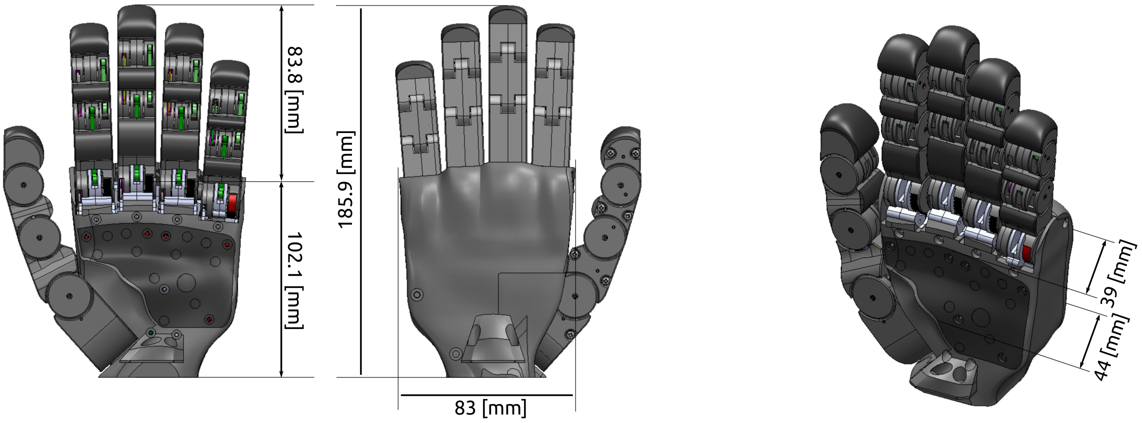

Figure E.1 – ALPHA length, width and thickness.

Finger	Joint	Extension/Flexion	Abduction/Adduction
Thumb	RC	-20° / 70°	0° / 90°
	MCP	0° / 90°	0°
	IP	0° / 90°	0°
I, M, R, L	MCP	0° / 90°	0°
	PIP	0° / 90°	0°
	DIP	0° / 90°	0°

Table E.1 – Joint range of motions. I, M, R, L are respectively index, middle, ring and little fingers.

Finger	Link	Length [mm]	Width [mm]
Thumb	Carpometacarpal[i]	53[ii]	29
	Proximal phx	25.9	23
	Distal phx	28	20
Index and Ring	Proximal phx	33.3	18
	Middle phx	22.2	18
	Distal phx	21.8	18
Middle	Proximal phx	37.0	18
	Middle phx	24.0	18
	Distal phx	22.8	18
Little	Proximal phx	26.8	18
	Middle phx	20.0	18
	Distal phx	19.7	18

[i] separated into two links since abduction/adduction axes do no intersect but present an offset of 22 [mm]

[ii] in default configuration: 22 (offset) + 31

Table E.2 – ALPHA link lengths and widths.

Finger	Base position [mm] (x, y, z)	Base orientation [deg]
Thumb	(32.0, 24.0, -2.0)	42°
Index	(100, 26.7, -3.7)	2.25°
Middle	(102, 7, 0.0)	0°
Ring	(100, -12.7, -3)	-2.25°
Little	(94, -32.4, -8.5)	-4.5°

Table E.3 – ALPHA finger base positions and orientations with respect to the wrist frame.

E.2 Masses, CoMs and Inertia matrices

E.2.1 Thumb

E.2.1.1 ThumbOpp

Mass $[kg]$ =

$$0.04101019 \tag{E.1}$$

CoM $[m]$ =

$$\begin{bmatrix} 0.00022840 & 0.00731984 & -0.00138019 \end{bmatrix} \tag{E.2}$$

I $[Kg\, m^2]$ =

$$\begin{bmatrix} 0.00000750 & -0.00000102 & 0.00000006 \\ = Ixy & 0.00000460 & -0.00000057 \\ = Ixz & = Iyz & 0.00000792 \end{bmatrix} \tag{E.3}$$

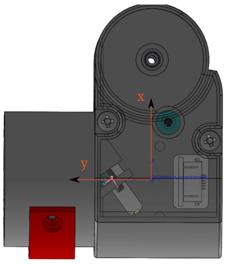

Figure E.2 – *ThumbOpp* Mass, CoM and Inertia matrix.

E.2.1.2 ThumbCmc

Mass $[kg]$ =

$$0.02706976 \tag{E.4}$$

CoM $[m]$ =

$$\begin{bmatrix} 0.00964431 & -0.00034946 & -0.00502263 \end{bmatrix} \tag{E.5}$$

I $[Kg\, m^2]$ =

$$\begin{bmatrix} 0.00000237 & -0.00000012 & -0.00000077 \\ = Ixy & 0.00000697 & 0 \\ = Ixz & = Iyz & 0.00000598 \end{bmatrix} \tag{E.6}$$

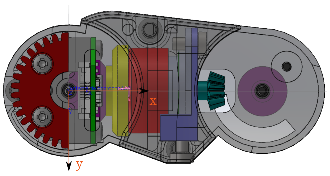

Figure E.3 – *ThumbCmc* Mass, CoM and Inertia matrix.

E.2.1.3 ThumbMcp

Mass $[kg]$ =

$$0.00749488 \tag{E.7}$$

CoM $[m]$ =

$$\begin{bmatrix} 0.01124022 & -0.00022062 & -0.00073156 \end{bmatrix} \tag{E.8}$$

I $[Kg\ m^2]$ =

$$\begin{bmatrix} 0.00000074 & 0 & 0.00000007 \\ = Ixy & 0.00000222 & 0 \\ = Ixz & = Iyz & 0.00000201 \end{bmatrix} \tag{E.9}$$

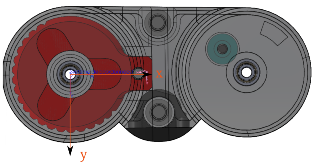

Figure E.4 – *ThumbMcp* Mass, CoM and Inertia matrix.

E.2.1.4 hThumbMcp

Mass (aluminum) $[kg]$ =

$$0.00072555 \tag{E.10}$$

Mass (SH70) $[kg]$ =

$$0.00032579 \tag{E.11}$$

CoM $[m]$ =

$$\begin{bmatrix} 0.01352137 & 0 & 0 \end{bmatrix} \tag{E.12}$$

I $[Kg\ m^2]$ =

$$\begin{bmatrix} 0 & 0 & 0 \\ = Ixy & 0.00000020 & 0 \\ = Ixz & = Iyz & 0.00000021 \end{bmatrix} \tag{E.13}$$

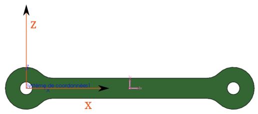

Figure E.5 – *hThumbMcp* Mass, CoM and Inertia matrix.

E.2.1.5 hThumbDip

Mass $[kg]$ =

$$0.00625829 \tag{E.14}$$

CoM $[m]$ =

$$\begin{bmatrix} -0.00264419 & 0.00852321 & 0.00085899 \end{bmatrix} \tag{E.15}$$

I $[Kg\, m^2]$ =

$$\begin{bmatrix} 0.00000099 & -0.00000027 & 0 \\ = Ixy & 0.00000054 & 0.00000005 \\ = Ixz & = Iyz & 0.00000113 \end{bmatrix} \tag{E.16}$$

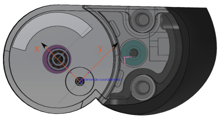

Figure E.6 – *hThumbDip* Mass, CoM and Inertia matrix.

E.2.2 Index/Ring

E.2.2.1 IndexMcp/RingMcp

Mass $[kg]$ =

$$0.01094632 \tag{E.17}$$

CoM $[m]$ =

$$\begin{bmatrix} 0.01244612 & 0.00180044 & 0.00017102 \end{bmatrix} \tag{E.18}$$

I $[Kg\, m^2]$ =

$$\begin{bmatrix} 0.00000065 & -0.00000006 & 0.0 \\ = Ixy & 0.00000394 & 0.0 \\ = Ixz & = Iyz & 0.00000409 \end{bmatrix} \tag{E.19}$$

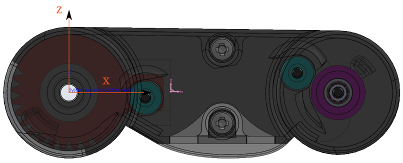

Figure E.7 – *IndexMcp/RingMcp* Mass, CoM and Inertia matrix.

E.2.2.2 hIndexMcp/hRingMcp

Mass $[kg]$ =

$$0.00024041 \tag{E.20}$$

CoM $[m]$ =

$$\begin{bmatrix} 0.01697844 & 0.0 & 0.0 \end{bmatrix} \tag{E.21}$$

I $[Kg\, m^2]$ =

$$\begin{bmatrix} 0.0 & 0.0 & 0.0 \\ = Ixy & 0.00000025 & 0.0 \\ = Ixz & = Iyz & 0.00000025 \end{bmatrix} \tag{E.22}$$

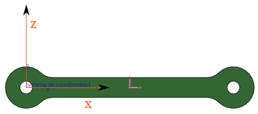

Figure E.8 – *hIndexMcp/hRingMcp* Mass, CoM and Inertia matrix.

E.2.2.3 hIndexPipProx/hRingPipProx

Mass $[kg]$ =

$$0.00402642 \tag{E.23}$$

CoM $[m]$ =

$$\begin{bmatrix} -0.00441519 & -0.00070241 & -0.00911525 \end{bmatrix} \tag{E.24}$$

I $[Kg\, m^2]$ =

$$\begin{bmatrix} 0.0000006 & 0.0 & 0.00000025 \\ = Ixy & 0.00000077 & 0.00000003 \\ = Ixz & = Iyz & 0.00000035 \end{bmatrix} \tag{E.25}$$

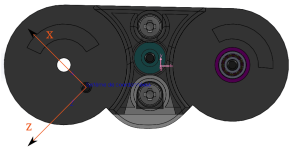

Figure E.9 – *hIndexPipProx/hRingPipProx* Mass, CoM and Inertia matrix.

E.2.2.4 hIndexPipDist/hRingPipDist

Mass $[kg]$ =

$$0.00019541 \tag{E.26}$$

CoM $[m]$ =

$$\begin{bmatrix} 0.01164946 & 0.0 & 0.0 \end{bmatrix} \tag{E.27}$$

I $[Kg\, m^2]$ =

$$\begin{bmatrix} 0.0 & 0.0 & 0.0 \\ = Ixy & 0.00000009 & 0.0 \\ = Ixz & = Iyz & 0.00000009 \end{bmatrix} \tag{E.28}$$

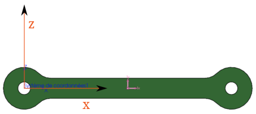

Figure E.10 – *hIndexPipDist/hRingPipDist* Mass, CoM and Inertia matrix.

E.2.2.5 hIndexDip/hRingDip

Mass $[kg]$ =

$$0.00375430 \tag{E.29}$$

CoM $[m]$ =

$$\begin{bmatrix} -0.00095401 & -0.00058359 & -0.00595724 \end{bmatrix} \tag{E.30}$$

I $[Kg\, m^2]$ =

$$\begin{bmatrix} 0.00000041 & 0.0 & 0.00000008 \\ = Ixy & 0.00000041 & 0.0 \\ = Ixz & = Iyz & 0.00000028 \end{bmatrix} \tag{E.31}$$

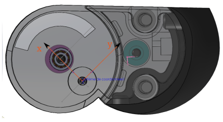

Figure E.11 – *hIndexDip/hRingDip* Mass, CoM and Inertia matrix.

E.2.3 Middle

E.2.3.1 MiddleMcp

Mass $[kg]$ =

$$0.0114633 \tag{E.32}$$

CoM $[m]$ =

$$\begin{bmatrix} 0.01401769 & 0.00172090 & 0.00014836 \end{bmatrix} \tag{E.33}$$

I $[Kg\, m^2]$ =

$$\begin{bmatrix} 0.00000069 & -0.00000007 & 0.0 \\ = Ixy & 0.00000504 & 0.0 \\ = Ixz & = Iyz & 0.00000519 \end{bmatrix} \tag{E.34}$$

E.2.3.2 hMiddleMcp

Mass $[kg]$ =

$$0.00025990 \tag{E.35}$$

CoM $[m]$ =

$$\begin{bmatrix} 0.01877165 & 0.0 & 0.0 \end{bmatrix} \tag{E.36}$$

I $[Kg\, m^2]$ =

$$\begin{bmatrix} 0.0 & 0.0 & 0.0 \\ = Ixy & 0.00000033 & 0.0 \\ = Ixz & = Iyz & 0.00000033 \end{bmatrix} \tag{E.37}$$

E.2.3.3 hMiddlePipProx

Mass $[kg]$ =

$$0.00428849 \tag{E.38}$$

CoM $[m]$ =

$$\begin{bmatrix} -0.00536012 & -0.00072722 & -0.00964955 \end{bmatrix} \tag{E.39}$$

I $[Kg\, m^2]$ =

$$\begin{bmatrix} 0.00000071 & 0.0 & 0.00000033 \\ = Ixy & 0.00000094 & 0.0 \\ = Ixz & = Iyz & 0.00000043 \end{bmatrix} \tag{E.40}$$

E.2.3.4 hMiddlePipDist

Mass $[kg]$ =

$$0.00020431 \tag{E.41}$$

CoM $[m]$ =

$$\begin{bmatrix} 0.01241471 & 0.0 & 0.0 \end{bmatrix} \tag{E.42}$$

I $[Kg\, m^2]$ =

$$\begin{bmatrix} 0.0 & 0.0 & 0.0 \\ = Ixy & 0.00000011 & 0.0 \\ = Ixz & = Iyz & 0.00000011 \end{bmatrix} \tag{E.43}$$

E.2.3.5 hMiddleDip

Mass $[kg]$ =

$$0.00389066 \tag{E.44}$$

CoM $[m]$ =

$$\begin{bmatrix} -0.00172983 & -0.00048440 & -0.00621472 \end{bmatrix} \tag{E.45}$$

I $[Kg\, m^2]$ =

$$\begin{bmatrix} 0.00000045 & 0.0 & 0.00000012 \\ = Ixy & 0.00000047 & 0.0 \\ = Ixz & = Iyz & 0.00000031 \end{bmatrix} \tag{E.46}$$

E.2.4 Little

E.2.4.1 LittleMcp

Mass $[kg]$ =

$$0.00933904 \tag{E.47}$$

CoM $[m]$ =

$$\begin{bmatrix} 0.00840320 & 0.00217919 & 0.00032894 \end{bmatrix} \tag{E.48}$$

I $[Kg\, m^2]$ =

$$\begin{bmatrix} 0.00000058 & 0.0 & 0.00000006 \\ = Ixy & 0.00000193 & 0.0 \\ = Ixz & = Iyz & 0.00000208 \end{bmatrix} \tag{E.49}$$

E.2.4.2 hLittleMcp

Mass $[kg]$ =

$$0.00018020 \tag{E.50}$$

CoM $[m]$ =

$$\begin{bmatrix} 0.01378913 & 0.0 & 0.0 \end{bmatrix} \tag{E.51}$$

I $[Kg\, m^2]$ =

$$\begin{bmatrix} 0.0 & 0.0 & 0.0 \\ = Ixy & 0.00000013 & 0.0 \\ = Ixz & = Iyz & 0.00000013 \end{bmatrix} \tag{E.52}$$

E.2.4.3 hLittlePipProx

Mass $[kg]$ =

$$0.00416395 \tag{E.53}$$

CoM $[m]$ =

$$\begin{bmatrix} -0.00220090 & -0.00084261 & -0.00689923 \end{bmatrix} \tag{E.54}$$

I $[Kg\, m^2]$ =

$$\begin{bmatrix} 0.00000046 & 0.0 & 0.00000016 \\ = Ixy & 0.00000057 & 0.0 \\ = Ixz & = Iyz & 0.00000028 \end{bmatrix} \tag{E.55}$$

E.2.4.4 hLittlePipDist

Mass $[kg]$ =

$$0.00016669 \tag{E.56}$$

CoM $[m]$ =

$$\begin{bmatrix} 0.01053779 & 0.0 & 0.0 \end{bmatrix} \tag{E.57}$$

I $[Kg\, m^2]$ =

$$\begin{bmatrix} 0.0 & 0.0 & 0.0 \\ = Ixy & 0.00000007 & 0.0 \\ = Ixz & = Iyz & 0.00000007 \end{bmatrix} \tag{E.58}$$

E.2.4.5 hLittleDip

Mass $[kg]$ =

$$0.00352536 \tag{E.59}$$

CoM $[m]$ =

$$\begin{bmatrix} -0.00053825 & -0.00052020 & -0.00524245 \end{bmatrix} \tag{E.60}$$

I $[Kg\; m^2]$ =

$$\begin{bmatrix} 0.00000034 & 0.0 & 0.00000006 \\ = Ixy & 0.00000033 & 0.0 \\ = Ixz & = Iyz & 0.00000025 \end{bmatrix} \tag{E.61}$$

Bibliography

[1] L. A. Jones and S. J. Lederman, *Human hand function*. Oxford University Press, 2006. 2

[2] J. R. Napier and R. H. Tuttle, *Hands*. Princeton University Press, 1993. 2

[3] J. R. Napier and P. H. Napier, *natural history of the primates*. MIT Press, 1994. 2

[4] R. W. Young, "Evolution of the human hand: the role of throwing and clubbing," *Journal of Anatomy*, vol. 202, no. 1, pp. 165–174, 2003. 2

[5] L. Da Vinci, *Leonardo on the human body*. Courier Corporation, 2013. 2, 6

[6] M. Kemp, *Leonardo da Vinci: the marvellous works of nature and man*. OUP Oxford, 2006, no. plate 33. 2

[7] F. van der Hulst, S. Schatzle, C. Preusche, and A. Schiele, "A functional anatomy based kinematic human hand model with simple size adaptation," in *IEEE International Conference on Robotics and Automation (ICRA), St. Paul, MN, USA*, May 2012, pp. 5123–5129. 3, 7, 33

[8] A. Barr and J. Bear-Lehman, "Biomechanics of the wrist and hand," *Basic Biomechanics of the Musculoskeletal System*, pp. 358–387, 2001. 4

[9] D. Giurintano, A. Hollister, W. Buford, D. Thompson, and L. Myers, "A virtual five-link model of the thumb," *Med. Eng. Phys.*, vol. 17, pp. 297–303, 1995. 4, 33

[10] I. Kapandji, "The Physiology of the Joints, Volume I, Upper Limb." *American Journal of Physical Medicine & Rehabilitation*, vol. 50, no. 2, p. 96, 1971. 4

[11] M. Grebenstein, M. Chalon, G. Hirzinger, and R. Siegwart, "A Method for Hand Kinematics Designers 7 Billion Perfect Hands," in *1st International Conference on Applied Bionics and Biomechanics ICABB, Venice, Italy*, 2010. 4, 33, 34

[12] M. Grebenstein, "Approaching human performance: The functionality driven Awiwi robot hand," Ph.D. dissertation, ETH Zurich, 2012, pp. 39-63. 4

[13] C. C. Norkin and P. K. Levangie, *Joint structure & function a comprehensive analysis*, 2nd ed. Philadelphia Davis, 1992, includes bibliographical references and index. 5

[14] J. Lin, Y. Wu, and T. S. Huang, "Modeling the constraints of human hand motion," in *Workshop on Human Motion*. IEEE, 2000, pp. 121–126. 5, 33

[15] S. Cobos, M. Ferre, M. A. Sánchez-Urán, and J. Ortego, "Constraints for realistic hand manipulation," *Proc. Presence 2007*, pp. 369–370, 2007. 5

[16] C. C. Norkin and D. J. White, *Measurement of joint motion: a guide to goniometry*. FA Davis, 2009. 5

[17] N. A. Davidoff and A. Freivalds, "A graphic model of the human hand using CATIA," *International Journal of Industrial Ergonomics*, vol. 12, no. 4, pp. 255–264, 1993. 6

[18] S. Cobos, M. Ferre, M. Sanchez Uran, J. Ortego, and C. Pena, "Efficient human hand kinematics for manipulation tasks," in *IEEE/RSJ International Conference on Intelligent Robots and Systems* , Sept 2008, pp. 2246–2251. 6, 33

[19] L. A. Galea, R. Gatt, and C. Sciberras, "Hand and wrist configurations in patients with Carpal Tunnel Syndrome," *Malta Med J*, vol. 19, no. 02, pp. 32–34, 2007. 6, 44

[20] A. Freivalds, *Biomechanics of the upper limbs: mechanics, modeling and musculoskeletal injuries*. CRC Press, 2011. 7

[21] B. Alexander and K. Viktor, "Proportions of hand segments," *Int. J. Morphol*, vol. 28, no. 3, pp. 755–758, 2010. 7

[22] Y. Isobe, "Hand Position," *Book of Orthopaedics*, vol. No. 38, pp. 24–34, 1985. 8, 45

[23] T. Greiner, *Hand Anthropometry of U.S. Army Personnel*, ser. Technical report (U.S. Army Natic Laboratories. Development Engineering Center). U.S. Army Natick Research, Development & Engineering Center, 1991. [Online]. Available: http://books.google.fr/books?id=JlimSgAACAAJ 8, 44

[24] B. Buchholz and T. J. Armstrong, "An Ellipsoidal Representation of Human Hand Anthropometry," *Human Factors: The Journal of the Human Factors and Ergonomics Society*, vol. 33, no. 4, pp. 429–441, July 1991. 8, 44

[25] S. Komandur, P. Johnson, R. Storch, and M. Yost, "Relation between index finger width and hand width anthropometric measures," in *Annual International Conference of the IEEE Engineering in Medicine and Biology Society (EMBC), Minnesota, USA*, Sept 2009, pp. 823–826. 8, 44

[26] A. Kapandji, "Cotation clinique de l'opposition et de la contre-opposition du pouce," *Annales de Chirurgie de la Main*, vol. 5, no. 1, pp. 67–73, 1986. 8, 9, 47

[27] I. M. Bullock and A. M. Dollar, "Classifying human manipulation behavior," in *Rehabilitation Robotics (ICORR), 2011 IEEE International Conference on*, June 2011, pp. 1–6. 9, 10

[28] F. Bacon, *The advancement of learning*, 4th ed. Oxford University Press, 1891, no. 2. 9

[29] J. Nespoulous and A. R. Lecours, "Gestures: Nature and function," *Biological Foundations of Gestures: Motor and Semiotic Aspects*, pp. 49–62, 1986. 9

[30] A. Kendon, "Gesture and speech: How they interact," *Nonverbal interaction*, vol. 11, pp. 13–45, 1983. 9

[31] B. Koechlin and D. Efron, *Gesture, race and culture: a tentative study of some of the spatio-temporal and" linguistic" aspects of the gestural behavior of Eastern Jews and Southern Italians in New York City, living under similar as well as different environmental conditions*. JSTOR, 1975. 11

[32] P. Turchet, *The Secrets of Body Language: An Illustrated Guide to Knowing what People are Really Thinking and Feeling*. Skyhorse Publishing Inc., 2012. 11

[33] R. M. Krauss, Y. Chen, and P. Chawla, "Nonverbal behavior and nonverbal communication: What do conversational hand gestures tell us?" *Advances in experimental social psychology*, vol. 28, pp. 389–450, 1996. 11

[34] B. Rime and L. Schiaratura, *Fundamentals of nonverbal behavior*. Cambridge University Press, 1991, ch. Gesture and Speech. 11

[35] I. G. Schlesinger, "Der mechanische aufbau der künstlichen glieder," in *Ersatzglieder und Arbeitshilfen*. Springer, 1919, pp. 321–661. 11

[36] J. R. Napier, "The prehensile movements of the human hand," *Bone & Joint Journal*, vol. 38, no. 4, pp. 902–913, 1956. 12

[37] M. Cutkosky, "On grasp choice, grasp models, and the design of hands for manufacturing tasks," *IEEE Transactions on Robotics and Automation*, vol. 5, no. 3, pp. 269–279, 1989. 12

[38] T. Feix, R. Pawlik, H.-B. Schmiedmayer, J. Romero, and D. Kragic, "A comprehensive grasp taxonomy," in *Robotics, Science and Systems: Workshop on Understanding the Human Hand for Advancing Robotic Manipulation*, 2009, pp. 2–3. 12, 136, 137

[39] T. Feix, J. Romero, H.-B. Schmiedmayer, A. M. Dollar, and D. Kragic, “The GRASP taxonomy of human grasp types,” *IEEE Transactions on Human-Machine Systems*, vol. 46, no. 1, pp. 66–77, 2016. 12

[40] M. Santello, M. Flanders, and J. F. Soechting, “Postural hand synergies for tool use,” *The Journal of Neuroscience*, vol. 18, no. 23, pp. 10 105–10 115, 1998. 13, 28

[41] M. Santello, G. Baud-Bovy, and H. Jörntell, “Neural bases of hand synergies,” *Frontiers in computational neuroscience*, vol. 7, p. 23, 2013. 13

[42] E. J. Weiss and M. Flanders, “Muscular and postural synergies of the human hand,” *Journal of Neurophysiology*, vol. 92, no. 1, pp. 523–535, 2004. 13

[43] F. Ficuciello, G. Palli, C. Melchiorri, and B. Siciliano, “Postural synergies of the UB Hand IV for human-like grasping,” *Robotics and Autonomous Systems*, vol. 62, no. 4, pp. 515–527, 2014. 13

[44] D. Flavigné and V. Perdereau, “A learning-free method for anthropomorphic grasping,” in *IEEE/RSJ International Conference on Intelligent Robots and Systems*, 2013. 13

[45] M. Ciocarlie, C. Goldfeder, and P. Allen, “Dimensionality reduction for hand-independent dexterous robotic grasping,” in *IEEE/RSJ International Conference on Intelligent Robots and Systems*. IEEE, 2007, pp. 3270–3275. 13

[46] C. Y. Brown and H. H. Asada, “Inter-finger coordination and postural synergies in robot hands via mechanical implementation of principal components analysis,” in *IEEE/RSJ International Conference on Intelligent Robots and Systems*, Oct 2007, pp. 2877–2882. 13

[47] M. Santello and J. F. Soechting, “Force synergies for multifingered grasping,” *Experimental Brain Research*, vol. 133, no. 4, pp. 457–467, 2000. 13

[48] A. Bicchi, M. Gabiccini, and M. Santello, “Modelling natural and artificial hands with synergies,” *Philosophical Transactions of the Royal Society of London B: Biological Sciences*, vol. 366, no. 1581, pp. 3153–3161, 2011. 13

[49] H. Mnyusiwalla, P. Vulliez, J.-P. Gazeau, and S. Zeghloul, “A New Dexterous Hand Based on Bio-Inspired Finger Design for Inside-Hand Manipulation,” *IEEE Transactions on Systems, Man, and Cybernetics: Systems*, vol. 46, no. 6, pp. 809–817, 2016. 13

[50] M. Grebenstein, A. Albu-Schaffer, T. Bahls, M. Chalon, O. Eiberger, W. Friedl, R. Gruber, S. Haddadin, U. Hagn, R. Haslinger, H. Hoppner, S. Jorg, M. Nickl, A. Nothhelfer, F. Petit, J. Reill, N. Seitz, T. Wimbock, S. Wolf, T. Wusthoff, and G. Hirzinger, “The DLR hand arm system,” in *IEEE International Conference on Robotics and Automation (ICRA), Shanghai, China*, 2011, pp. 3175–3182. 14, 15, 82, 149, 150

[51] L. Bridgwater, C. Ihrke, M. Diftler, M. Abdallah, N. Radford, J. M. Rogers, S. Yayathi, R. S. Askew, and D. Linn, “The Robonaut 2 hand - designed to do work with tools,” in *IEEE International Conference on Robotics and Automation (ICRA), St. Paul, MN, USA*, 2012, pp. 3425–3430. 14, 19, 20, 149, 150

[52] Shadow hand. Website. Shadow Robot Company LTD. (Accessed 27 Feb 2016). [Online]. Available: http://www.shadowrobot.com/products/dexterous-hand/ 14, 15, 149, 150

[53] J. Martin and M. Grossard, “Design of a fully modular and backdrivable dexterous hand,” *The International Journal of Robotics Research*, vol. 33, no. 5, pp. 783–798, 2014. 14, 15, 16, 149, 150

[54] H. Liu, K. Wu, P. Meusel, N. Seitz, G. Hirzinger, M. Jin, Y. Liu, S. Fan, T. Lan, and Z. Chen, “Multisensory five-finger dexterous hand: The DLR/HIT Hand II,” in *IEEE/RSJ International Conference on Intelligent Robots and Systems, Nice, France*, 2008, pp. 3692–3697. 14, 18, 149, 150

[55] T. Mouri, H. Kawasaki, K. Yoshikawa, J. Takai, and S. Ito, "Anthropomorphic Robot Hand: Gifu Hand III," in *International Conference on Control, Automation and Systems (ICCAS), Jeonbuk, Korea*, Oct. 2002, pp. 1288–1293. 14, 16, 47, 49, 149, 150

[56] C. Melchiorri, G. Palli, G. Berselli, and G. Vassura, "Development of the UB Hand IV: Overview of Design Solutions and Enabling Technologies," *Robotics Automation Magazine, IEEE*, vol. 20, no. 3, pp. 72–81, 2013. 14, 17, 18, 149, 150

[57] K.-J. Cho, J. Rosmarin, and H. Asada, "SBC Hand: A Lightweight Robotic Hand with an SMA Actuator Array implementing C-segmentation," in *IEEE International Conference on Robotics and Automation, Roma, Italy*, 2007, pp. 921–926. 14, 17, 149, 150

[58] T. Sonoda and I. Godler, "Multi-fingered robotic hand employing strings transmission named Twist Drive," in *IEEE/RSJ International Conference on Intelligent Robots and Systems (IROS)*, 2010, pp. 2527–2528. 14, 18, 19, 149, 150

[59] M. Grebenstein, M. Chalon, G. Hirzinger, and R. Siegwart, "Antagonistically driven finger design for the anthropomorphic DLR Hand Arm System," in *10th IEEE-RAS International Conference on Humanoid Robots (Humanoids)*, Dec 2010, pp. 609–616. 14

[60] G. K. Klute, J. M. Czerniecki, and B. Hannaford, "McKibben artificial muscles: pneumatic actuators with biomechanical intelligence," in *Proceedings IEEE/ASME International Conference on Advanced Intelligent Mechatronics*. IEEE, 1999, pp. 221–226. 15

[61] F. Daerden and D. Lefeber, "Pneumatic artificial muscles: actuators for robotics and automation," *European journal of Mechanical and Environmental Engineering*, vol. 47, pp. 10–21, 2000. 15, 55

[62] H. Kawasaki, H. Shimomura, and Y. Shimizu, "Educational–industrial complex development of an anthropomorphic robot hand'Gifu hand'," *Advanced Robotics*, vol. 15, no. 3, pp. 357–363, 2001. 16

[63] H. Kawasaki, T. Komatsu, and K. Uchiyama, "Dexterous anthropomorphic robot hand with distributed tactile sensor: Gifu hand II," *IEEE/ASME Transactions On Mechatronics*, vol. 7, no. 3, pp. 296–303, 2002. 16

[64] H. Kawasaki, T. Mouri, and S. Ito, "Toward next stage of kinetic humanoid hand," in *Proceedings World Automation Congress, 2004.* 16

[65] G. Palli, C. Melchiorri, G. Vassura, U. Scarcia, L. Moriello, G. Berselli, A. Cavallo, G. De Maria, C. Natale, S. Pirozzi, C. May, F. Ficuciello, B. Siciliano, *et al.*, "The DEXMART hand: Mechatronic design and experimental evaluation of synergy-based control for human-like grasping," *The International Journal of Robotics Research*, vol. 33, no. 5, pp. 799–824, 2014. 17, 82

[66] G. Palli, U. Scarcia, C. Melchiorri, and G. Vassura, "Development of robotic hands: The UB hand evolution," in *IEEE/RSJ International Conference on Intelligent Robots and Systems (IROS)*, Oct 2012, pp. 5456–5457. 17

[67] G. Berselli, G. Borghesan, M. Brandi, C. Melchiorri, C. Natale, G. Palli, S. Pirozzi, and G. Vassura, "Integrated mechatronic design for a new generation of robotic hands," in *Proc. IFAC Symposium on Robot Control, Gifu, Japan*, vol. 480, 2009. 17

[68] G. Borghesan, G. Palli, and C. Melchiorri, "Design of tendon-driven robotic fingers: Modeling and control issues," in *IEEE International Conference on Robotics and Automation (ICRA)* . Ieee, 2010, pp. 793–798. 17

[69] G. Palli, C. Natale, C. May, C. Melchiorri, and T. Wurtz, "Modeling and control of the twisted string actuation system," *IEEE/ASME Transactions on Mechatronics*, vol. 18, no. 2, pp. 664–673, 2013. 17

[70] G. Hirzinger, J. Butterfass, M. Fischer, M. Grebenstein, M. Hahnle, H. Liu, I. Schaefer, and N. Sporer, "A mechatronics approach to the design of light-weight arms and multifingered hands," in *Proceedings. ICRA IEEE International Conference on Robotics and Automation*, vol. 1, 2000, pp. 46–54 vol.1. 18

[71] Maxon motor Moves Humanoid Robotic Hand. Website. Maxon motor. (Accessed 03 March 2016). [Online]. Available: http://www.maxonmotor.com/medias/sys_master/8808033943582/2013-01-en-humaoid-robotic-hand.pdf?attachment=true 18

[72] J. T. Belter and A. M. Dollar, "Performance characteristics of anthropomorphic prosthetic hands," in *IEEE International Conference on Rehabilitation Robotics (ICORR)*, vol. 29. IEEE, 2011, pp. 1–7. 19, 20

[73] Servo-electric 5-Finger Gripping Hand. Website. Schunk GmbH & Co. KG. (Accessed 25 Feb 2016). [Online]. Available: http://mobile.schunk-microsite.com/en/produkte/produkte/servo-electric-5-finger-gripping-hand-svh.html 20, 21, 150

[74] K. Kaneko, F. Kanehiro, M. Morisawa, T. Tsuji, K. Miura, S. Nakaoka, S. Kajita, and K. Yokoi, "Hardware improvement of Cybernetic Human HRP-4C for entertainment use," in *IEEE/RSJ International Conference on Intelligent Robots and Systems (IROS)*, Sept 2011, pp. 4392–4399. 20, 21, 22, 150

[75] L. Birglen and C. Gosselin, "Kinetostatic analysis of underactuated fingers," *IEEE Transactions on Robotics and Automation*, vol. 20, no. 2, pp. 211–221, April 2004. 22, 28, 80, 81, 87, 88

[76] M. C. Carrozza, G. Cappiello, S. Micera, B. B. Edin, L. Beccai, and C. Cipriani, "Design of a cybernetic hand for perception and action," *Biological cybernetics*, vol. 95, no. 6, pp. 629–644, 2006. 22, 23, 151

[77] E. Matheson, Y. Aoustin, E. Le Carpentier, A. Leon, and J. Perrin, *New Trends in Medical and Service Robots*, P. Wenger, C. Chevallereau, D. Pisla, H. Bleuler, and A. Rodić, Eds. Springer, 2016. 23, 151

[78] G. Langevin. InMoov - Open Source 3D printed life-size robot. [Online]. Available: http://inmoov.fr/ 23, 151

[79] D. Keymeulen and C. Assad, "Investigation of the Harada robot hand for space," in *IEEE RAS International Conference on Humanoid Robots, Tokyo, Japan*, November 2001. 23, 24, 151

[80] A. Villoslada, A. Flores-Caballero, D. Copaci, D. Blanco, and L. Moreno, "High-displacement fast-cooling flexible Shape Memory Alloy actuator: application to an anthropomorphic robotic hand," in *14th IEEE-RAS International Conference on Humanoid Robots (Humanoids)*. IEEE, 2014, pp. 27–32. 23

[81] G. A. Bekey, R. Tomovic, and I. Zeljkovic, "Control architecture for the Belgrade/USC hand," in *Dextrous robot hands*. Springer, 1990, pp. 136–149. 24

[82] A. Schmitz, U. Pattacini, F. Nori, L. Natale, G. Metta, and G. Sandini, "Design, realization and sensorization of the dexterous iCub hand," in *10th IEEE-RAS International Conference on Humanoid Robots (Humanoids), Nashville, TN, USA*, 2010, pp. 186–191. 24, 25, 82, 151

[83] I. Gaiser, S. Schulz, A. Kargov, H. Klosek, A. Bierbaum, C. Pylatiuk, R. Oberle, T. Werner, T. Asfour, G. Bretthauer, and R. Dillmann, "A new anthropomorphic robotic hand," in *8th IEEE-RAS International Conference on Humanoid Robots, Daejeon, South Korea*, 2008, pp. 418–422. 25, 26, 151

[84] IH2 AZZURRA series. Website. Prensilia Srl. (Accessed 03 March 2016). [Online]. Available: www.prensilia.com 25, 27, 151

[85] C. Cipriani, M. Controzzi, and M. C. Carrozza, "The SmartHand transradial prosthesis," *Journal of neuroengineering and rehabilitation*, vol. 8, no. 1, p. 1, 2011. 25, 26, 27, 151

[86] Z. Kappassov, Y. Khassanov, A. Saudabayev, A. Shintemirov, and H. Varol, "Semi-anthropomorphic 3D printed multigrasp hand for industrial and service robots," in *IEEE International Conference on Mechatronics and Automation (ICMA)*, 2013, pp. 1697–1702. 25, 27, 151

[87] C. Gosselin, F. Pelletier, and T. Laliberte, "An anthropomorphic underactuated robotic hand with 15 dofs and a single actuator," in *IEEE International Conference on Robotics and Automation, 2008*, May 2008, pp. 749–754. 25, 27, 28, 82, 91, 151

[88] M. G. Catalano, G. Grioli, E. Farnioli, A. Serio, C. Piazza, and A. Bicchi, "Adaptive synergies for the design and control of the Pisa/IIT SoftHand," *The International Journal of Robotics Research*, vol. 33, no. 5, pp. 768–782, 2014. 25, 28, 29, 151

[89] G. Smit, D. H. Plettenburg, and F. C. van der Helm, "The Lightweight Delft Cylinder Hand: First Multi-Articulating Hand That Meets the Basic User Requirements," *Neural Systems and Rehabilitation Engineering, IEEE Transactions on*, vol. 23, no. 3, pp. 431–440, 2015. 25, 29, 151

[90] A. Kargov, H. Breitwieser, H. Klosek, C. Pylatiuk, S. Schulz, and G. Bretthauer, "Design of a modular arm robot system based on flexible fluidic drive elements," in *IEEE 10th International Conference on Rehabilitation Robotics, 2007*. IEEE, 2007, pp. 269–273. 26

[91] S. Schulz, C. Pylatiuk, and G. Bretthauer, "A new ultralight anthropomorphic hand," in *Proceedings ICRA. IEEE International Conference on Robotics and Automation*, vol. 3, 2001, pp. 2437–2441 vol.3. 26

[92] S. Schulz, C. Pylatiuk, A. Kargov, R. Oberle, and G. Bretthauer, "Progress in the development of anthropomorphic fluidic hands for a humanoid robot," in *4th IEEE/RAS International Conference on Humanoid Robots*, vol. 2, 2004, pp. 566–575. 26

[93] I. N. Gaiser, C. Pylatiuk, S. Schulz, A. Kargov, R. Oberle, and T. Werner, "The FLUIDHAND III: A Multifunctional Prosthetic Hand," *Journal of Prosthetics and Orthotics*, vol. 21, no. 2, pp. 91–96, 2009. [Online]. Available: http://journals.lww.com/jpojournal/Fulltext/2009/04000/The_FLUIDHAND_III__A_Multifunctional_Prosthetic.5.aspx 26

[94] A. Kargov, C. Pylatiuk, H. Klosek, R. Oberle, S. Schulz, and G. Bretthauer, "Modularly designed lightweight anthropomorphic robot hand," in *Multisensor Fusion and Integration for Intelligent Systems, 2006 IEEE International Conference on*, Sept 2006, pp. 155–159. 26

[95] C. Cipriani, M. Controzzi, and M. C. Carrozza, "Progress towards the development of the SmartHand transradial prosthesis," in *Rehabilitation Robotics, 2009. ICORR 2009. IEEE International Conference on*. IEEE, 2009, pp. 682–687. 26

[96] C. Cipriani, F. Zaccone, G. Stellin, L. Beccai, G. Cappiello, M. C. Carrozza, and P. Dario, "Closed-loop controller for a bio-inspired multi-fingered underactuated prosthesis," in *Robotics and Automation, 2006. ICRA 2006. Proceedings 2006 IEEE International Conference on*. IEEE, 2006, pp. 2111–2116. 26

[97] S. A. Dalley, T. E. Wiste, H. A. Varol, and M. Goldfarb, "A multigrasp hand prosthesis for transradial amputees," in *Engineering in Medicine and Biology Society (EMBC), 2010 Annual International Conference of the IEEE*. IEEE, 2010, pp. 5062–5065. 27

[98] B. Hillberry and J. A. Hall, "Rolling contact joint," US Patent 3,932,045, 1976. 28

[99] J.-M. Boucher and L. Birglen, "Underactuated Finger Closing Motion Control Using Dual Drive Actuation," in *ASME 2015 International Design Engineering Technical Conferences and Computers and Information in Engineering Conference*. American Society of Mechanical Engineers, 2015, pp. V05BT08A005–V05BT08A005. 30

[100] Y. Lee and C. Cho, "A biomimetic hand employing a dual actuation scheme," *Journal of mechanical science and technology*, vol. 26, no. 12, pp. 4131–4139, 2012. 30

[101] N. Fukaya, S. Toyama, T. Asfour, and R. Dillmann, “Design of the TUAT/Karlsruhe humanoid hand,” in *Proceedings IEEE/RSJ International Conference on Intelligent Robots and Systems (IROS 2000). Takamatsu, Japan*, vol. 3, 2000, pp. 1754–1759 vol.3. 30, 93

[102] Y.-J. Kim, Y. Lee, J. Kim, J.-W. Lee, K.-M. Park, K.-S. Roh, and J.-Y. Choi, “RoboRay hand: A highly backdrivable robotic hand with sensorless contact force measurements,” in *Robotics and Automation (ICRA), 2014 IEEE International Conference on*, May 2014, pp. 6712–6718. 30, 31, 82

[103] A. Crawford, J. Molitor, A. Pérez Gracia, S. Chiu, *et al.*, “Design of a robotic hand and simple EMG input controller with a biologically-inspired parallel actuation system for prosthetic applications,” in *ASME 2010, IDETC/CIE 2010*. 30, 32

[104] N. Fukaya, T. Asfour, R. Dillmann, and S. Toyama, “Development of a five-finger dexterous hand without feedback control: The TUAT/Karlsruhe humanoid hand,” in *Intelligent Robots and Systems (IROS), 2013 IEEE/RSJ International Conference on*. IEEE, 2013, pp. 4533–4540. 30, 31

[105] L. Biagiotti, F. Lotti, C. Melchiorri, and G. Vassura, “How Far Is the Human Hand? A Review on Anthropomorphic Robotic End-effectors,” 2004. 32, 33

[106] D. M. Cocchiarella, A. M. Kociolek, C. T. Tse, and P. J. Keir, “Toward a realistic optoelectronic-based kinematic model of the hand: representing the transverse metacarpal arch reduces accessory rotations of the metacarpophalangeal joints,” *Computer methods in biomechanics and biomedical engineering*, pp. 1–9, 2015. 33

[107] J. H. Buffi, J. J. Crisco, and W. M. Murray, “A method for defining carpometacarpal joint kinematics from three-dimensional rotations of the metacarpal bones captured in vivo using computed tomography,” *Journal of biomechanics*, vol. 46, no. 12, pp. 2104–2108, 2013. 33

[108] O. A. van Nierop, A. van der Helm, K. J. Overbeeke, and T. J. Djajadiningrat, “A natural human hand model,” *The Visual Computer*, vol. 24, no. 1, pp. 31–44, 2008. 33

[109] L. Y. Chang and N. S. Pollard, “Robust estimation of dominant axis of rotation,” *Journal of biomechanics*, vol. 40, no. 12, pp. 2707–2715, 2007. 33

[110] M. Vande Weghe, M. Rogers, M. Weissert, and Y. Matsuoka, “The ACT Hand: design of the skeletal structure,” in *IEEE International Conference on Robotics and Automation (ICRA), Barcelona, Spain*, vol. 4, April 2004, pp. 3375–3379. 33, 34

[111] Z. Xu and E. Todorov, “Design of a Highly Biomimetic Anthropomorphic Robotic Hand towards Artificial Limb Regeneration,” in *in review for IEEE International Conference on Robotics and Automation, 2016 (ICRA’16)*. 33

[112] E. Ouellette, J. McAuliffe, and R. Carneiro, “Partial-hand amputations: Surgical principles,” *Atlas of limb prosthetics: Surgical, prosthetic, and rehabilitation principles. St. Louis (MO): Mosby Year Book*, 1992. 34

[113] H. Wang, S. Fan, and H. Liu, “An anthropomorphic design guideline for the thumb of the dexterous hand,” in *International Conference on Mechatronics and Automation (ICMA), Chengdu, China*, Aug 2012, pp. 777–782. 34, 50

[114] W. Khalil and J. Kleinfinger, “A new geometric notation for open and closed-loop robots,” in *Robotics and Automation. Proceedings. 1986 IEEE International Conference on*, vol. 3. IEEE, 1986, pp. 1174–1179. 41, 65

[115] E. Y. S. Chao, K.-N. An, W. P. Cooney III, and R. L. Linscheid, *Biomechanics of the hand. A basic research study*. World Scientific, 1989, vol. 59, no. 1. 43

[116] G. Elert, “as Size of a Human: Body Proportions,” *The Physics Factbook*, 2006. 43

[117] NAOqi Framework. Website. Aldebaran SoftBank Group. (Accessed 1 Oct 2014). [Online]. Available: https://community.aldebaran-robotics.com/doc/1-14/dev/naoqi/index.html 52

[118] J. M. Jani, M. Leary, A. Subic, and M. A. Gibson, “A review of shape memory alloy research, applications and opportunities,” *Materials & Design*, vol. 56, pp. 1078–1113, 2014. [Online]. Available: http://www.sciencedirect.com/science/article/pii/S0261306913011345 55

[119] J. B. Rosmarin, “The design of a hybrid DC motor/SMA actuated robotic hand based on physiological and anatomical synergies,” Master’s thesis, DSpace@MIT: Massachusetts Institute of Technology, 2008. 55

[120] K. Andrianesis, A. Tzes, G. Nikolakopoulos, and Y. Koveos, *Experimental study of a shape memory alloy actuation system for a novel prosthetic hand.* INTECH Open Access Publisher, 2010. 55

[121] R. Featherstone, “Rigid Body Dynamics Algorithms.” Secaucus, NJ, USA: Springer-Verlag New York, Inc., 2007, pp. 89–99. 64, 153

[122] M. Naveau, J. Carpentier, S. Barthelemy, O. Stasse, and P. Souères, “METAPOD Template META-programming applied to dynamics: CoP-CoM trajectories filtering,” in *International Conference on Humanoid Robotics*, Madrid, Spain, Nov. 2014. [Online]. Available: https://hal.archives-ouvertes.fr/hal-01122475 64

[123] J. John, S. Kumar, and B. Jaya, “Space Vector Modulation based Field Oriented Control scheme for Brushless DC motors,” in *Emerging Trends in Electrical and Computer Technology (ICETECT), 2011 International Conference on*, March 2011, pp. 346–351. 73

[124] STM32F PMSM single/dual FOC SDK v4.2. STMicroelectronics. (Accessed Sept 2015). [Online]. Available: http://www2.st.com/content/ccc/resource/technical/document/user_manual/5e/5e/d2/cb/07/35/45/a6/CD00298474.pdf/files/CD00298474.pdf/jcr:content/translations/en.CD00298474.pdf 73

[125] R. Kelly, V. S. Davila, and J. A. L. Perez, *Control of robot manipulators in joint space*. Springer Science & Business Media, 2006. 74

[126] B. Vanderborght, A. Albu-Schäffer, A. Bicchi, E. Burdet, D. G. Caldwell, R. Carloni, M. Catalano, O. Eiberger, W. Friedl, G. Ganesh, *et al.*, “Variable impedance actuators: A review,” *Robotics and autonomous systems*, vol. 61, no. 12, pp. 1601–1614, 2013. 75

[127] N. Hogan, “Impedance control: An approach to manipulation,” in *American Control Conference, 1984*. IEEE, 1984, pp. 304–313. 75

[128] D. Tsetserukou, R. Tadakuma, H. Kajimoto, N. Kawakami, and S. Tachi, “Towards Safe Human-Robot Interaction: Joint Impedance Control of a New Teleoperated Robot Arm,” in *Robot and Human interactive Communication, 2007. RO-MAN 2007. The 16th IEEE International Symposium on*, Aug 2007, pp. 860–865. 75

[129] L. Dosiek and P. Pillay, “Cogging torque reduction in permanent magnet machines,” *Industry Applications, IEEE Transactions on*, vol. 43, no. 6, pp. 1565–1571, 2007. 76

[130] N. Bianchi and S. Bolognani, “Design techniques for reducing the cogging torque in surface-mounted PM motors,” *Industry Applications, IEEE Transactions on*, vol. 38, no. 5, pp. 1259–1265, 2002. 76

[131] L. Birglen, T. Lalibert, and C. M. Gosselin, *Underactuated Robotic Hands*, 1st ed. Springer Publishing Company, Incorporated, 2008. 80

[132] M. Chalon, A. Wedler, A. Baumann, W. Bertleff, A. Beyer, J. Butterfaß, M. Grebenstein, R. Gruber, F. Hacker, E. Kraemer, *et al.*, “Dexhand: a space qualified multi-fingered robotic hand,” in *Robotics and Automation (ICRA), 2011 IEEE International Conference on*. IEEE, 2011, pp. 2204–2210. 82

[133] W. Friedl, M. Chalon, J. Reinecke, and M. Grebenstein, “FAS A flexible antagonistic spring element for a high performance over actuated hand,” in *IEEE/RSJ International Conference on Intelligent Robots and Systems (IROS)*, Sept 2011, pp. 1366–1372. 82

[134] J. Reinecke, M. Chalon, W. Friedl, and M. Grebenstein, “Guiding effects and friction modeling for tendon driven systems,” in *IEEE International Conference on Robotics and Automation (ICRA)*, May 2014, pp. 6726–6732. 82

[135] G. Palli, G. Borghesan, and C. Melchiorri, “Tendon-based transmission systems for robotic devices: Models and control algorithms,” in *IEEE International Conference on Robotics and Automation (ICRA)*, May 2009, pp. 4063–4068. 82

[136] R. E. Perez, P. W. Jansen, and J. R. Martins, “pyOpt: a Python-based object-oriented framework for nonlinear constrained optimization,” *Structural and Multidisciplinary Optimization*, vol. 45, no. 1, pp. 101–118, 2012. 89

[137] L. Birglen and C. M. Gosselin, “Force Analysis of Connected Differential Mechanisms: Application to Grasping,” *Int. J. Rob. Res.*, vol. 25, no. 10, pp. 1033–1046, Oct. 2006. 91

[138] A. Hartman and W. Lorimer, “Cogging torque control in brushless dc motors,” *Incremental Motion Control Syst. And Devies, 29Th Annu. Syrup. Proc*, pp. 237–243, 2000. 101

[139] M. Piccoli and M. Yim, “Cogging torque ripple minimization via position-based characterization,” in *Proceedings of robotics: science and systems*, 2014. 101

[140] L. Birglen, “Type Synthesis of Linkage-Driven Self-Adaptive Fingers,” *ASME Journal of Mechanisms and Robotics*, vol. 1, no. 2, pp. 809–816, 2009. 109

[141] M. Plooij, G. Mathijssen, P. Cherelle, D. Lefeber, and B. Vanderborght, “Lock Your Robot: A Review of Locking Devices in Robotics,” *Robotics Automation Magazine, IEEE*, vol. 22, no. 1, pp. 106–117, March 2015. 110

[142] J. T. Bauman, “Rubber Stress-Strain Behavior,” in *Rubber Components*, J. T. Bauman, Ed. Hanser, 2008, pp. 9–18. [Online]. Available: http://www.sciencedirect.com/science/article/pii/B9783446416819500030 120

[143] A. Giacomin and A. Mix, “Standardized polymer durometry,” *Journal of Testing and Evaluation*, vol. 39, no. 4, pp. 1–10, 2011. 120

[144] J. Kunz and M. Studer, “Determining the Modulus of Elasticity in Compression via the Shore A Hardness,” *Kunststoffe*, vol. 6, p. 6, 2006. 120

[145] L. U. Odhner, L. P. Jentoft, M. R. Claffee, N. Corson, Y. Tenzer, R. R. Ma, M. Buehler, R. Kohout, R. D. Howe, and A. M. Dollar, “A compliant, underactuated hand for robust manipulation,” *The International Journal of Robotics Research*, vol. 33, no. 5, pp. 736–752, 2014. 128

[146] L. Motion, “Leap motion controller,” 2014. 132

[147] 5DT Data Glove 14 Ultra. Website. 5DT. Accessed 06 May 2016. [Online]. Available: http://www.5dt.com 133, 134

[148] F. Ficuciello, A. Federico, V. Lippiello, and B. Siciliano, “Synergies Evaluation of the SCHUNK S5FH for Grasping Control,” in *Advances in Robot Kinematics : Proceedings of the 15th international conference on Advances in Robot Kinematics*, 2016, pp. 229–237. 147

[149] W. Khalil, “Dynamic Modeling of Robots Using Newton-Euler Formulation,” in *Informatics in Control, Automation and Robotics (ICINCO)*, ser. Lecture Notes in Electrical Engineering, J. Cetto, J.-L. Ferrier, and J. Filipe, Eds. Springer Berlin Heidelberg, 2011, vol. 89, pp. 3–20. [Online]. Available: http://dx.doi.org/10.1007/978-3-642-19539-6_1 153

[150] E. Dombre and W. Khalil, *Robot manipulators: modeling, performance analysis and control.* John Wiley & Sons, 2013. 153

[151] C. Pelchen, C. Schweiger, and M. Otter, “Modeling and simulating the efficiency of gearboxes and of planetary gearboxes,” in *Proceedings of 2nd International Modelica Conference*, 2002, pp. 257–266. 158, 159

l'université
nantes
angers
le mans
COMMUNAUTÉ D'UNIVERSITÉS ET ÉTABLISSEMENTS

Centrale
Nantes

Thèse de Doctorat

Giulio CERRUTI

Conception et Contrôle d'une Main Robotique anthropomorphique et dextre

Design and Control of a Dexterous Anthropomorphic Robotic Hand

Résumé

Cette thèse présente la conception et la commande d'une main robotique légère et peu onéreuse pour un robot compagnon humanoïde. La main est conçue pour exprimer des émotions à travers des gestes et pour saisir de petits objets légers. Sa géométrie est définie à l'aide de données anthropométriques. Sa cinématique est simplifiée par rapport à la main humaine pour réduire le nombre d'actionneurs tout en respectant ses exigences fonctionnelles. La main préserve son anthropomorphisme grâce aux nombres et au placement de la base des doigts et à une bonne opposabilité du pouce. La mécatronique de la main repose sur un compromis entre des phalanges couplés, qui permettent de bien connaître la posture des doigts pendant les gestes, et des phalanges capable de s'adapter à la forme des objets pendant la saisie, réunis en une conception *hybride* unique. Ce compromis est rendu possible grâce à deux systèmes d'actionnement distincts placés en parallèle. Leur coexistence est garantie par une transmission compliante basée sur des barres en élastomère. La solution proposée réduit significativement le poids et la taille de la main en utilisant sept actionneurs de faible puissance pour les gestes et un seul moteur puissant pour la saisie. Le système est conçue pour être embarqué sur *Romeo*, un robot humanoïde de 1.4 [m] produit par Aldebaran. Les systèmes d'actionnements sont dimensionnés pour ouvrir et fermer les doigts en moins de 1 [s] et pour saisir une canette pleine de soda. La main est réalisée et contrôlée pour garantir une interaction sûre avec l'homme mais aussi pour protéger l'intégrité de la mécanique. Un prototype (ALPHA) est réalisé pour valider le conception et ses capacités fonctionnelles.

Mots clés

Robot Compagnon Humanoïde, Main Robotique à Cinq Doigts, Anthropomorphisme, Double Actionnement, Gestes, Saisie Auto-Adaptable.

Abstract

This thesis presents the design and control of a low-cost and lightweight robotic hand for a social humanoid robot. The hand is designed to perform expressive hand gestures and to grasp small and light objects. Its geometry follows anthropometric data. Its kinematics simplifies the human hand structure to reduce the number of actuators while ensuring functional requirements. The hand preserves anthropomorphism by properly placing five fingers on the palm and by ensuring an equilibrated thumb opposability. Its mechanical system results from the compromise between fully-coupled phalanges and self-adaptable fingers in a unique *hybrid* design. This answers the need for known finger postures while gesturing and for finger adaptation to different object shapes while grasping. The design is based on two distinct actuation systems embodied in parallel within the palm and the fingers. Their coexistence is ensured by a compliant transmission based on elastomer bars. The proposed solution significantly reduces the weight and the size of the hand by using seven low-power actuators for gesturing and a single high-power motor for grasping. The overall system is conceived to be embedded on *Romeo*, a humanoid robot 1.4 [m] tall produced by Aldebaran. Actuation systems are dimensioned to open and close the fingers in less than 1 [s] and to grasp a full soda can. The hand is realized and controlled to ensure safe human-robot interaction and to preserve mechanical integrity. A prototype (ALPHA) is realized to validate the design feasibility and its functional capabilities.

Key Words

Social Humanoid Robot, Five-Fingered Robotic Hand, Anthropomorphism, Dual Actuation, Gestures, Self-Adaptable Grasping.